Dissertation
zur Erlangung der Doktorwürde
an der

Gesamtfakultät für Mathematik,
Ingenieur- und Naturwissenschaften
der
Ruprecht-Karls-Universität Heidelberg

Thema:

Forces and Transport in Biological Media

vorgelegt von:
Ing. Lucie Motyčková

Juli 2025

Gutachter:
Professor Dr. Peer Fischer
Professor Dr. Christine Selhuber-Unkel

Diese Fassung wurde gemäß den Empfehlungen des Betreuers überarbeitet und entspricht nicht der ursprünglich zur Prüfung eingereichten Fassung.

Abstract

Forces are fundamental to the function of living systems, driving natural processes such as tissue morphogenesis and locomotion, as well as our ability to interact with living matter, for instance, in the context of therapeutic interventions. Magnetic fields, in particular, offer distinct advantages in biomedical applications due to their ability to penetrate tissues non-invasively and exert forces remotely. Beyond delivering mechanical stimuli, magnetic fields can facilitate the transport of objects through biological media.

This work spans several approaches to generate forces using magnetism at the nano- and microscale, including magnetic field gradients, rotating magnetic fields, and homogeneous magnetic fields. These strategies are applied in various biomedical contexts to enable characterization, manipulation, and transport of nano- and microscale objects. Furthermore, when direct mechanical forces alone are insufficient to achieve the desired outcomes, the thesis investigates an alternative strategy to locally disrupt a principal biological barrier, thereby facilitating transport within complex biological environments.

The thesis begins with a quantitative analysis of the force ranges achievable through different magnetic strategies and their implications for biomedical applications. Subsequently, a method is developed to quantify the magnetic properties of individual particles suspended in liquid using magnetic field gradients. Magnetic stimuli are then applied to cells with the aim of developing tools to investigate mechanotransduction. In this context, cell monolayers are mechanically stimulated using embedded ferrofluid droplets, which serve as magnetically responsive actuators under homogeneous magnetic fields. This platform is subsequently enhanced by introducing a magnetizable probe that locally perturbs the uniform magnetic field, thereby generating spatially confined magnetic field gradients at the microscale. A similar microscale gradient strategy is employed in a separate experimental setup to guide the sprouting of cells that have internalized magnetic nanoparticles, offering a tool for applications in tissue engineering. The final section of the thesis explores the transport of nano- and microscale objects for ophthalmological applications, with the aim of enabling targeted delivery of drugs or therapeutic genes within the eye. The work first addresses transport through potential vitreous substitutes, which are relevant in the treatment of eye conditions. Using magnetic field gradients, suitable hyaluronic acid–based formu-

lations are identified that permit the penetration of nano- and microparticles. Building on these findings, the thesis demonstrates the active propulsion of helical nano- and micropropellers within these materials using rotating magnetic fields, thereby establishing the feasibility of magnetically guided delivery systems in hydrogels that are designed to replace the vitreous body. Finally, the thesis investigates targeted nanoscale transport to retinal cells, where the successful delivery of therapeutic genes holds promise for treating a range of retinal disorders that can lead to blindness. Initial experiments using *ex vivo* porcine models are used to asses the property of natural barriers impeding nanoscale transport. To address limited permeability, a more refined strategy is introduced, in which enzymes are attached to microparticles to enable localized degradation of the primary biological barrier, thereby facilitating access to the retina. This approach results in enhanced nanoparticle transport across the barrier.

Collectively, this work establishes methods for magnetic-field based force application, targeted manipulation, and controlled transport at the nano- and microscale within complex biological environments. This work introduces novel tools and strategies that advance both mechanobiology and targeted ocular delivery systems.

Zusammenfassung

Kräfte sind grundlegend für die Funktion lebender Systeme, und bestimmen natürliche Prozesse wie die Gewebemorphogenese und Fortbewegung. Kräfte sind essentiell für die Fähigkeit, mit lebender Materie zu interagieren und im Zusammenhang mit therapeutischen Interventionen. Insbesondere magnetische Felder bieten in biomedizinischen Anwendungen besondere Vorteile, da sie Gewebe nicht-invasiv durchdringen und Kräfte aus der Ferne übertragen können. Über die mechanische Stimulation hinaus ermöglichen magnetische Felder auch den Transport von Objekten durch biologische Medien.

Diese Arbeit untersucht verschiedene Ansätze, die zur Erzeugung von Kräften mittels Magnetismus im Nano- und Mikrometermaßstab genutzt werden können, u.a. magnetische Feldgradienten, sowie rotierende und homogene Magnetfelder, die durch magnetische Materialien verändert werden. Diese unterschiedlichen Methoden werden in der Dissertation für verschiedene biomedizinische Anwendungen eingesetzt, um die Charakterisierung, Manipulation und den Transport von mikro- und nanoskaligen Objekten zu ermöglichen. Darüber hinaus wird untersucht, wie eine biologische Barriere gezielt lokal abgebaut werden kann, um den Transport durch die Barriere zu ermöglichen.

Diese Dissertation beginnt mit einer quantitativen Analyse verschiedener magnetischer Kräfte, sowie deren Bedeutung für biomedizinische Anwendungen. Anschließend wird eine Methode vorgestellt, mit der sich die magnetischen Eigenschaften einzelner, in Flüssigkeit suspendierter Partikel mithilfe magnetischer Magnetfeldgradienten bestimmen lassen. In der Arbeit werden auch magnetische Werkzeuge zur Untersuchung der Mechanotransduktion vorgestellt. Es wird beschrieben, wie eine Einzellage von Zellen mit eingebetteten Ferrofluidtröpfchen mechanisch, mittels eines homogenen Magnetfelds, stimuliert werden kann. Diese Plattform wird anschließend durch die Einführung einer magnetisierbaren Sonde erweitert, die das ursprünglich homogene Magnetfeld lokal stört und so mikroskalige magnetische Feldgradienten erzeugt. Eine ähnliche Strategie wird in einem separaten Versuchsaufbau eingesetzt, um das Sprießen von Zellen zu steuern, die zuvor magnetische Nanopartikel internalisiert haben, was für Anwendungen in Gewebekulturen von Interesse ist. Der letzte Teil der Dissertation befasst sich mit dem Transport nano- und mikroskaliger Objekte für ophthalmologische Anwendungen, mit der Vision, eine gezielte Verabreichung

von Medikamenten oder die Gentherapie innerhalb des Auges zu ermöglichen. Dabei wird zunächst die mikroskalige Fortbewegung durch potenzielle Glaskörperersatzstoffe untersucht, die für die Behandlung verschiedener Augenerkrankungen von Bedeutung sind. Unter Verwendung magnetischer Feldgradienten werden geeignete, auf Hyaluronsäure basierende Gele identifiziert, die eine Penetration von Nano- und Mikropartikeln erlauben. Darauf aufbauend wird die aktive Fortbewegung helikaler Nano- und Mikropropeller in diesen Materialien unter rotierenden Magnetfeldern demonstriert. Dies zeigt die Umsetzbarkeit magnetisch gesteuerter Transportsysteme in Hydrogelen, die als Ersatz für den Glaskörper im Auge konzipiert sind. Abschließend wird der gezielte nanoskalige Transport zu Netzhautzellen untersucht, bei dem die erfolgreiche Einschleusung therapeutischer Gene ein vielversprechender Behandlungsansatz für verschiedene Netzhauterkrankungen, die zur Erblindung führen können, darstellt. Erste Experimente mit ex vivo Schweinemodellen dienen zur Untersuchung der Eigenschaften natürlicher Barrieren, die den nanoskaligen Transport einschränken. Um deren begrenzte Durchlässigkeit zu erhöhen, wird untersucht, wie Enzyme die an Mikropartikel gekoppelt werden, lokal die biologische Barriere abbauen können und es somit ermöglichen, den Transport in die Netzhaut zu erleichtern. Es wird gezeigt werden, dass ein erhöhter Transport von Nanopartikeln durch die Barriere hinweg erzielt werden kann.

Insgesamt werden in dieser Arbeit Methoden zur magnetfeldbasierten Krafteinwirkung realisiert, die eine gezielte Manipulation und den kontrollierten Transport im Nano- und Mikrobereich innerhalb komplexer biologischer Systeme ermöglicht. Dabei werden neue Werkzeuge und Strategien vorgestellt, die sowohl die Mechanobiologie als auch den gerichteten Wirkstofftransport für die Augenheilkunde vorantreiben.

Contents

Preface

Life is strongly tied to forces. From the earliest stages of development, a dynamic interplay between mechanical forces and genetic information shapes the formation of the organism [1]. Even when the embryo is merely a simple sphere of cells, mechanical cues begin to influence how cells divide, migrate, and organize into progressively more complex structures [1]. Far from being passive, cells actively sense, respond to, and generate forces [1]. Through mechanotransduction, cells convert physical inputs into biochemical signals that guide key decisions during development. The type, magnitude, frequency, and duration of mechanical stimuli have all been shown to steer mesenchymal stem cell fate, directing differentiation into bone, cartilage, or muscle cells [2, 3]. Importantly, mechanical forces are indispensable in guiding proper organ morphogenesis [1]. Mechanical forces remain essential throughout life. In adulthood, they regulate dynamic physiological processes, supporting the body's ability to cope with diseases and to repair tissue following injury [1]. Furthermore, mechanical inputs are deeply embedded in everyday physiological functions such as muscle contraction [4] or the constant stretching of lung tissue during breathing [5].

Biological systems also sense mechanical forces originating from outside the organism. For example, sensory modalities such as touch and hearing rely on the ability to detect and interpret external mechanical stimuli [4]. In the context of development, maternal movements and muscular activity transmit mechanical signals that are crucial for normal skeletal formation in the developing embryo [6, 7]. Beyond naturally occurring forces, mechanical stimuli are purposefully applied to biological systems *in vitro*, *ex vivo* and *in vivo*. It is therefore of interest to gain deeper insights into how living systems interpret and respond to mechanical inputs and how such forces can be harnessed to promote healing, mitigate disease progression, or develop novel therapeutic strategies.

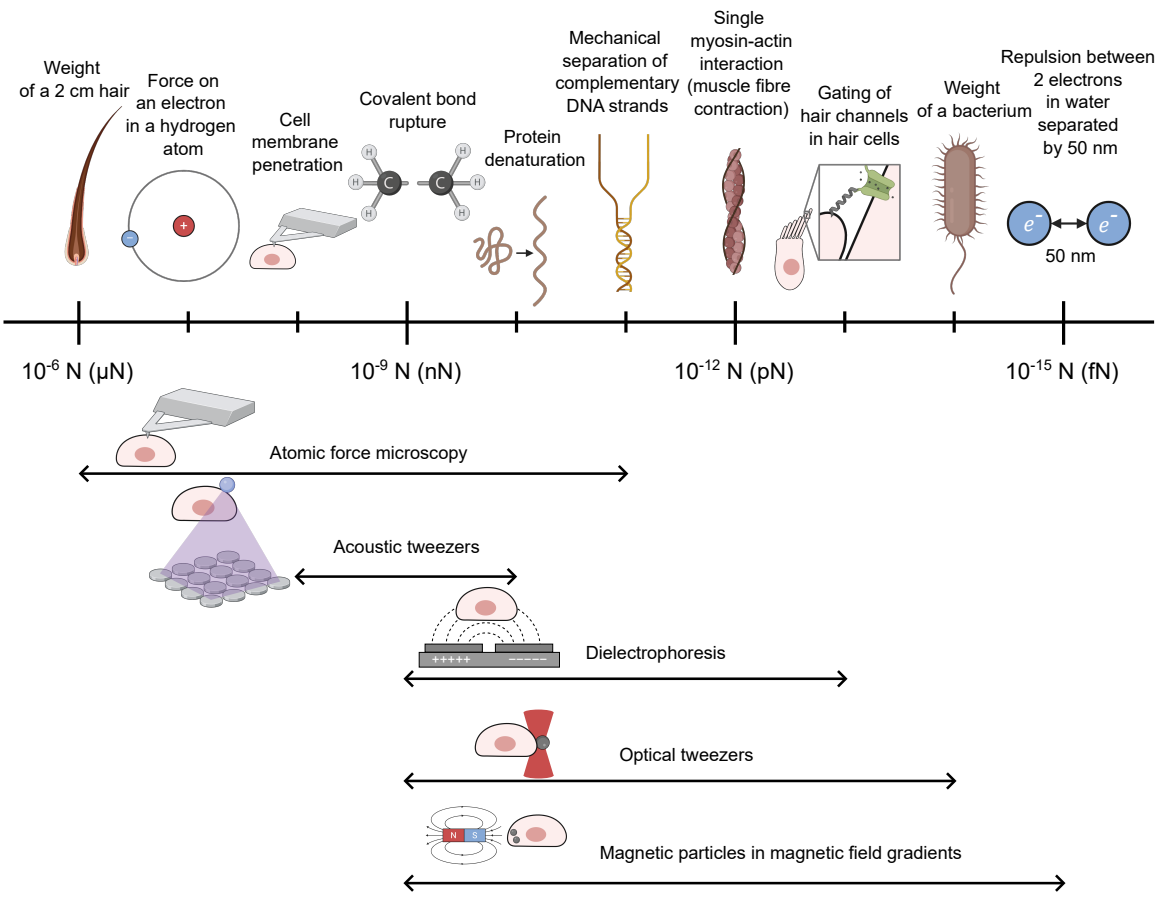

Figure 0.1. Force range scale from micronewtons to femtonewtons on a logarithmic scale. The figure highlights experimental techniques and the typical force ranges they can apply at the single-cell level [8–12], together with representative biological phenomena occurring within each relevant order of magnitude [13–22].

Most techniques for the precise application of physical forces have been developed for *in vitro* settings, where experimental conditions can be precisely controlled. In this context, we highlight methods capable of delivering well-defined physical stimuli to individual cells. These techniques differ in both the type and magnitude of forces applied. Figure 0.1 illustrates the typical force ranges associated with each modality, along with representative biological phenomena that occur within each corresponding order of magnitude. Mechanical forces, for example, are applied using atomic force microscopy (AFM) cantilevers, which engage primarily with membrane-level mechanics and can access intracellular structures only upon membrane disruption [14]. Acoustic forces are employed in acoustic tweezers to manipulate single cells either directly [23] or indirectly via microbubbles attached to the cell membrane [24], enabling high-throughput, selective, and contact-free control, while acoustic radiation forces generated through acoustic holographic assemblies provide advanced spatial manipulation capabilities [25]. Electric forces are utilized in dielectrophoresis, which leverages non-uniform electric fields to manipulate individual cells based on their dielectric

properties in a label-free manner [11]. Optical forces, generated by focused laser beams in optical tweezers, enable precise trapping and manipulation of particles either internalized within cells or positioned on the cell surface [26]. Magnetic forces, generated by spatially varying magnetic fields acting on magnetic particles attached to or internalized within cells, enable precise, non-contact manipulation of cells and subcellular structures and are employed in techniques such as magnetic tweezers [27]. While these represent some of the main modalities, numerous other physical force–based approaches are under active investigation to further enhance control at the single-cell scale [12].

Among the various physical modalities, magnetism offers distinct advantages due to its ability to penetrate biological media without scattering or absorption, unlike acoustic or optical forces, while also avoiding the unwanted ionization associated with electric fields, yet still enabling remote control. Consequently, a major focus of this thesis is the generation and application of magnetic forces at the nano- and microscale across diverse biomedical contexts.

Chapter 1 introduces several strategies for force generation using magnetic field gradients, rotating magnetic fields, and homogeneous magnetic fields, along with estimations of the forces involved. These methods are then employed throughout the thesis across increasingly complex environments, spanning from Newtonian fluids to cellular monolayers and hydrogels designed as vitreous substitutes. A critical review of the biomedical literature on the use of magnetic forces at small scales is also provided. In Chapter 2, I present a technique to measure the magnetic moment of single particles in liquid, a parameter essential for precise force calibration. This approach is applied to commercially available particles, custom-fabricated monodisperse particles, and Janus particles designed for smart cargo delivery. Chapter 3 investigates the use of magnetic forces to apply mechanical stimuli to cells in monolayers. A platform based on ferrofluid droplets that deform under magnetic fields is developed and characterized. These droplets are subsequently integrated into cell cultures, where both homogeneous magnetic fields and magnetic field gradients are used to transmit mechanical forces from the synthetic magnetic cells to adjacent biological cells. Additionally, I design a platform to guide magnetically labeled cellular sprouts using localized magnetic field gradients. Chapter 4 shifts focus to opthalmological applications. We begin with a magnetism-based investigation into the porosity of hyaluronic acid-based gels, proposed as vitreous humor substitutes, by investigating the ability of magnetic particles to penetrate these gels under field gradients generated by a permanent magnet. We further demonstrate the controlled navigation of helical microswimmers through these gels using rotating magnetic fields, advancing the concept of targeted intraocular drug delivery through such biomimetic vitreous replacement.

While the application of physical forces offers powerful capabilities, stronger stimuli are not always beneficial. Excessive force can cause tissue damage, inflammation, or functional loss. Conversely, weaker stimuli may fail to achieve the desired therapeutic effect, requiring more refined strategies. The final part of Chapter 4 addresses this challenge in the context of delivering materials to porcine retinas. After initial attempts disrupted retinal integrity, we investigate passive diffusion across the retina using novel *ex vivo* porcine eye models. We further demonstrate that retinal permeability can be enhanced by enzymatic digestion of its principal barrier, achieved by localizing the enzyme on the surface of microbeads. We envision that integrating these findings will ultimately enable the development of helical propellers capable of delivering therapeutic cargo to retinal cells.

The results presented in this thesis are being prepared for publication.

Chapter 2

- V. Mihali, X. Huang, L. Motyčková, N. Moreno Gomez, M. Skowicki, C.-A. Schoenenberger, P. Fischer, C. G. Palivan, ”Multiplex Modular Nanorobots with Programmable Self-organization and Magnetic Control”, manuscript submitted.

Chapter 3

- J. De Lora, L. Motyčková (shared first autorship), S. Pashapour, P. Fischer, and J. P. Spatz, ”Building mechanoresponsive hybrid cell cultures comprising E-Cadherin functionalized synthetic magnetic cells (symcells) and natural cells”, manuscript prepared for submission.
- A manuscript is planned on sprouting assisted by magnetic nanoparticles:
  H. K. Senapati, L. Motyčková *et al.*

Chapter 4

- A manuscript is planned on nanopropeller propulsion through hydrogels:
  M. Hammer, L. Motyčková *et al.*
- A manuscript on enzyme-driven transport to the retina has been submitted to the journal *Small* and is available as a preprint on *bioRxiv*: L. Motyčková, F. Peter (shared first authorship) *et al.* Enzyme-functionalized microparticles to open the vitreoretinal interface. *bioRxiv* (2026). doi:10.64898/2026.01.12.699029.

Declaration of Generative Artificial Intelligence (AI) Use:

I hereby declare that generative AI tools were employed during the preparation of this thesis. In particular, *ChatGPT* and *Perplexity* were used to support language refinement of text originally written by the author and to assist in the literature survey process. The scientific content presented in this thesis remains the sole responsibility of the author.

Image Credits:

I used *BioRender* to create the following figures: Fig. 0.1, Fig. 1.5, Fig. 1.6, Fig. 1.12, Fig. 2.2, Fig. 2.7, Fig. 3.1, Fig. 3.4, Fig. 3.5, Fig. 3.10, Fig. 3.12, Fig. 3.13, Fig. 3.14, Fig. 4.1, Fig. 4.2, Fig. 4.5, Fig. 4.7, Fig. 4.10, Fig. 4.11, Fig. 4.12, Fig. 4.14, Fig. 4.15, Fig. 4.16, Fig. 4.17 and Fig. 5.1.

I used *Blender* to create Fig. 2.4.

All remaining illustrations were created in *Inkscape*, with all figures finalized in *Inkscape*, including those initially drafted in other software.

All plots were generated using *Python 3.10.9*.

Chapter 1

Magnetic Strategies for Force Generation

Despite many research proposals emerging every year, effective magnetic guidance of therapeutic vectors or magnetic force stimulation at the nano-/microscale within the human body has not reached clinical use [28, 29]. A primary challenge in magnetic targeting lies in its common dependence on high magnetic field gradients, typically generated by permanent magnets. However, the generation of sufficiently strong magnetic field gradients within the spatial constraints of the human body remains challenging [30], due to the rapid spatial decay of magnetic field gradients with increasing distance from the magnet. As a result, the corresponding magnetic forces diminish rapidly, often becoming negligible compared to thermal fluctuations. At first glance, this may suggest that magnetic methods are inherently unsuitable for remote force generation at small scales, such as those required in *in vivo* environments. Fortunately, alternative magnetic strategies exist that can circumvent these limitations and offer more scalable solutions for nano- and microscale biomedical applications. A careful evaluation of the achievable forces is essential to assess the feasibility of these magnetic approaches and to guide the development of practical applications.

Author Contributions

I performed all calculations presented in this chapter. The calculations related to real magnetic helical propellers actuated by rotating magnetic fields were based on velocity measurements published by V. Kadiri *et al.* [31].

Scope of the Chapter

This chapter provides a theoretical background and quantitative analysis of the magnetic forces achievable through different magnetic actuation strategies. It first focuses on the conventional approach of using magnetic field gradients generated by permanent magnets and evaluates the feasibility of selected biomedical applications frequently proposed in the literature that rely on this principle. Subsequently, an alternative strategy for creating magnetic field gradients by perturbing homogeneous magnetic fields is introduced, followed by a discussion of approaches based on rotating magnetic fields and the use of ferrofluid droplets in homogeneous magnetic fields. The strategies outlined in this chapter form the basis for the magnetic actuation concepts applied in the subsequent chapters of this thesis.

1.1 Forces Opposing Active Propulsion

Moving objects inevitably experience resistance from the surrounding medium. Whether moving through viscous fluids, porous materials, or complex biological tissues, such motion is opposed by dissipative forces that arise from interactions with the environment. While the nature of the resistance can be complex and highly nonlinear in biological or heterogeneous media, they are well understood in the case of incompressible Newtonian fluids, where analytical descriptions exist.

At the microscale, fluid flows often occur at low velocities such that viscous forces dominate over inertial forces, even in low-viscosity fluids like water. This regime is characterized by low Reynolds numbers, which express the ratio of inertial to viscous forces, and the fluid dynamics in this regime are governed by the Stokes equation [32, 33]

$$-\nabla p + \eta \nabla^2 \mathbf{u} = 0, \tag{1.1}$$

where p is the pressure, η is the dynamic viscosity of the fluid, and $\mathbf{u}$ is the flow velocity. The velocity field $\mathbf{u}$ of an incompressible Newtonian fluid also satisfies the equation of continuity [33]

$$\nabla \cdot \mathbf{u} = 0. \tag{1.2}$$

Due to the absence of time derivatives in Eq. (1.1) and Eq. (1.2), the external force $\mathbf{F}$ and the external torque $\boldsymbol{\tau}$ acting on the object depend linearly on its translational and angular velocities [34]

$$\begin{pmatrix} \mathbf{F} \\ \boldsymbol{\tau} \end{pmatrix} = \begin{pmatrix} \mathbf{A} & \mathbf{C}^\intercal \\ \mathbf{C} & \mathbf{D} \end{pmatrix} \begin{pmatrix} \mathbf{v} \\ \boldsymbol{\omega} \end{pmatrix}, \tag{1.3}$$

where $\begin{pmatrix} \mathbf{A} & \mathbf{C}^\intercal \\ \mathbf{C} & \mathbf{D} \end{pmatrix}$ is the 6×6 propulsion matrix of the object, $\mathbf{v}$ is the translation velocity of the object, and $\boldsymbol{\omega}$ is the angular velocity of the object. The translation resistance tensor

$\mathbf{A}$, the translation-rotation coupling tensor $\mathbf{C}$ and the rotation resistance tensor $\mathbf{D}$ are 3×3 matrices proportional to the fluid viscosity η and they depend otherwise only on the shape and size of the object. The matrix $\mathbf{C}^\intercal$ is the transpose of the translation-rotation coupling tensor $\mathbf{C}$.

The resistance tensors $\mathbf{A}$, $\mathbf{C}$ and $\mathbf{D}$ have been analytically expressed for objects of regular shapes such as a sphere [34, 35]

$$\mathbf{A}_\mathrm{S} = 6\pi\mu R_\mathrm{S}\mathbf{I}, \mathbf{C}_\mathrm{S} = \mathbf{0}, \mathbf{D}_\mathrm{S} = 8\pi\mu R_\mathrm{S}^3\mathbf{I}, \tag{1.4}$$

where $\mathbf{I}$ is a unity matrix, $\mathbf{0}$ is a null matrix and R_S is the hydrodynamic radius. Similar solutions exist for an ellipsoid [34, 35]. As for particles of arbitrary shapes, the analytical solutions for the resistance tensors generally do not exist, and the determination thereof usually relies on methods in which the hydrodynamic properties of the particle of interest are calculated from models composed of spherical elements [35, 36].

Although the coupling tensor $\mathbf{C}$ vanishes for highly symmetric objects, the translational resistance tensor $\mathbf{A}$ is always non-zero. Thus, any object in a viscous medium experiences a drag force opposing its motion

$$\mathbf{F}_{\mathrm{D},\mathbf{v}} = -\mathbf{A} \cdot \mathbf{v}. \tag{1.5}$$

This drag force opposes the object's active propulsion, such as that induced by magnetic actuation, meaning that the resistance tensor $\mathbf{A}$ significantly influences the achievable velocity of the object in the fluid.

1.2 Magnetic Field Gradients

In a magnetic field, any magnetizable object experiences a magnetic force, provided the magnetic field varies in space; in other words, when a magnetic field gradient exists. The magnetic force $\mathbf{F}_\mathrm{m}$ acting on the magnetizable object of interest in an applied magnetic field $\mathbf{B}$ is then given by [37]

$$\mathbf{F}_\mathrm{m} = (\mathbf{m} \cdot \nabla)\mathbf{B}, \tag{1.6}$$

where $\mathbf{m}$ is the magnetic moment of the particle. The magnetic force $\mathbf{F}_\mathrm{m}$ can be rewritten as

$$\mathbf{F}_\mathrm{m} = V \cdot \begin{pmatrix} M_x\frac{\partial B_x}{\partial x} + M_y\frac{\partial B_x}{\partial y} + M_z\frac{\partial B_x}{\partial z} \\ M_x\frac{\partial B_y}{\partial x} + M_y\frac{\partial B_y}{\partial y} + M_z\frac{\partial B_y}{\partial z} \\ M_x\frac{\partial B_z}{\partial x} + M_y\frac{\partial B_z}{\partial y} + M_z\frac{\partial B_z}{\partial z} \end{pmatrix}, \tag{1.7}$$

where V is the volume of the particle and $\mathbf{M} = \frac{\mathbf{m}}{V}$ is its magnetization.

The magnetic force $\mathbf{F}_\mathrm{m}$ depends solely on the gradient of the magnetic field, not on the magnetic field directly (Eq. (1.7)). However, the magnetization $\mathbf{M}$ of the particle depends on the external field $\mathbf{B}$, meaning that $\mathbf{B}$ influences the force $\mathbf{F}_\mathrm{m}$ through its effect on $\mathbf{M}$. This dependence follows the material's magnetization curve, which varies across substances.

A strong magnetic field gradient, essential for generating forces of high magnitude (see Eq. (1.7)), can be achieved through the following methods, as will be shown in detail below:

(i) Permanent magnets can be placed near the magnetic particle. However, this approach requires the particle to be located very close to the magnet, as the magnetic gradient decreases rapidly with distance from the surface of the magnet. For example, at a distance equal to the lateral dimension of the magnet, the gradient is only a very small fraction of its value at the magnet's surface.

(ii) Localized magnetizable bodies can be introduced into a homogeneous magnetic field near the magnetic particle of interest, thereby producing localized magnetic field gradients. In this case, the particle must be in the vicinity of the magnetizable body to experience the gradient.

In the following subsections, I provide force estimations for magnetic nano- and microparticles within the magnetic field gradients produced by the two aforementioned approaches.

1.2.1 Permanent Magnets

The magnetic field $\mathbf{B}$, generated solely by permanent magnets (and not by currents), can be derived from the magnetic scalar potential ϕ [38]

$$\mathbf{B} = -\mu_0 \nabla \phi, \tag{1.8}$$

where μ_0 is the vacuum permeability, historically defined as $4\pi \times 10^{-7}\ \mathrm{H/m}$ and now experimentally determined following the recent revision of the SI (International System of Units) [39]. For simpler, symmetrical geometries, the magnetic scalar potential ϕ at a point $\mathbf{r}$ can be analytically determined by integrating the contributions from the infinitesimal dipoles over the volume V of the permanent magnet

$$\phi(\mathbf{r}) = \int_V d\phi(\mathbf{r}) = \int_V \frac{1}{4\pi} \frac{(\mathbf{r} - \mathbf{r}') \cdot \mathbf{M}}{|\mathbf{r} - \mathbf{r}'|^2}\, \mathrm{d}^3\mathbf{r}', \tag{1.9}$$

where $\mathbf{r}'$ denotes the location of the elementary magnetic dipole [40, 41]. By applying Eqs. (1.8) and (1.9), the magnetic field can be analytically derived for simple magnet geometries. In the present analysis, I focus on two common shapes: cylindrical and block magnets.

Cylindrical Magnets

Cylindrical magnets are typically magnetized along their axial direction. Neglecting edge effects, the strongest magnetic force is exerted on a sample positioned along the magnet's long symmetry axis, denoted as z (see Fig. 1.1). On this axis, the magnetic field $\mathbf{B}$ has only a z-component, which can be determined using Eq. (1.8) and Eq. (1.9) [40]

$$B_z = \frac{B_\mathrm{r}}{2}\left(\frac{h+z}{\sqrt{R^2+(h+z)^2}} - \frac{z}{\sqrt{R^2+z^2}}\right), \tag{1.10}$$

where h is the height of the cylinder (along the symmetry axis), R is the radius of the cylinder and z is the distance from a pole face on the symmetry axis. B_r is the remanent field, which depends on the material of the magnet.

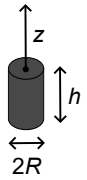

Figure 1.1. Schematic of a cylindrical magnet illustrating key parameters.

All magnets considered in this thesis, both for calculations and experiments, are made of NdFeB, the strongest commercially available permanent magnetic material. Their performance is characterized by the maximum energy product, which represents twice the maximum magnetic energy stored in the magnetic field produced surrounding unit volume of an optimally shaped permanent magnet [38]. The maximum energy product can be expressed as $-\frac{1}{2}\int_V \mu_0 \mathbf{B}\mathbf{H}_\mathrm{d}\,\mathrm{d}^3\mathbf{r}$, where $\mathbf{H}_d$ denotes the demagnetizing field and the integration is performed over the volume V of the magnet [38]. This quantity is typically reported in units of megagauss-oersted (MGOe), with a conversion of $100\,\mathrm{kJ/m^3} = 12.57\,\mathrm{MGOe}$ [38]. Based on this energy product, magnets are classified into different grades. The minimum and maximum remanent fields B_r for each NdFeB magnet grade are listed in Table 1.1 [42].

Magnet grade	minimum B_r [T]	maximum B_r [T]
N30	1.08	1.12
N33	1.14	1.17
N35	1.17	1.21
N38	1.22	1.26
N40	1.26	1.29
N42	1.29	1.32
N45	1.32	1.37
N48	1.37	1.42
N50	1.40	1.46
N52	1.42	1.47

Table 1.1. Remanent magnetic field B_r ranges for various NdFeB magnet grades. Data adapted from [42].

The magnetic field gradient along the z-direction on the symmetry axis is given by

$$\frac{\partial B_z}{\partial z} = \frac{1}{2} B_\mathrm{r} R^2 \left(\frac{1}{\left(R^2 + (h+z)^2\right)^{\frac{3}{2}}} - \frac{1}{\left(R^2 + z^2\right)^{\frac{3}{2}}} \right). \tag{1.11}$$

As an example, I present the magnetic field gradient for selected magnets of grade N48. I consider a real permanent magnet (N48, $h = 8\,\mathrm{mm}$, $R = 1.5\,\mathrm{mm}$) available from *Webcraft GmbH* [43], producing one of the highest gradients among the magnets offered by this company. First, I fix the radius of the magnet R and examine how the magnetic field gradient varies with distance from the magnet's surface for different magnet heights (see Figure 1.2a). As the height increases from $0.1h$ to h, the magnetic field gradient also increases. However, beyond h, further increase in height no longer enhances the gradient significantly. Moreover, as the height-to-radius ratio (h/R) decreases, the location of the maximum magnetic field gradient shifts farther from the magnet surface, caused by enhanced magnetic flux concentration near the cylinder's periphery. Next, I fix the magnet's height h and analyze the magnetic field gradient as a function of distance for different radii (see Figure 1.2b). As the radius R from $10R$ to $0.1R$, the magnetic field gradient at the magnet's surface increases. However, it also decays more rapidly, leading to a lower gradient at greater distances. Therefore, to achieve the highest possible magnetic field gradient for a given application, it is crucial to optimize the distance between the magnet's surface and the particle of interest. For simplicity, I neglect the effect of the magnet's coating (typically Ni-Cu-Ni with a thickness of $12\,\mu\mathrm{m}$ [44]) in the plots.

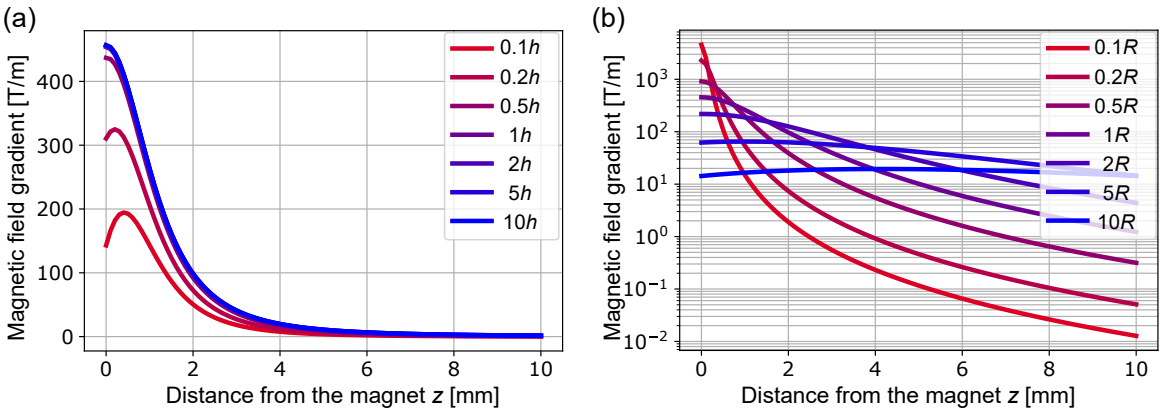

Figure 1.2. Magnetic field gradient vs. distance from the surface of a N48 magnet with: (a) the radius $R = 1.5\,\mathrm{mm}$ and a variable height, (b) the height $h = 8\,\mathrm{mm}$ and a variable radius.

The simplest way to asses the force acting on a particle on the symmetry axis of a cylindrical magnet is to calculate the force analytically. In a good approximation, $M_z \frac{\partial B_z}{\partial z} \gg M_x \frac{\partial B_z}{\partial x} + M_y \frac{\partial B_z}{\partial y}$ and thus Eq. (1.7) can be rewritten as

$$F_z = V M_z(B_z) \frac{\partial B_z}{\partial z}, \tag{1.12}$$

where $M_z(B_z)$ is the magnetization derived from the hysteresis behavior as a function of the magnetic field B_z (see Eq. (1.10)) and $\frac{\partial B_z}{\partial z}$ is the magnetic field gradient from the Eq. (1.11).

As an example, Fig. 1.3 shows magnetic hysteresis curves for bulk soft iron and iron-oxide beads. The curve for soft iron was obtained from the COMSOL Multiphysics® material library (see Fig. 1.3a), while the iron-oxide data were taken from the measurements of R. J. S. Derks *et al.* [45] for Dynabeads MyOne from *Thermo Fisher Scientific* (see Figure1.3b). These spherical beads have a diameter of $1.05\,\mu\mathrm{m}$ and contain approximately 37 % ferrites (26 % elemental iron). I use these magnetic properties to estimate the magnetic forces acting on iron and iron-oxide particles.

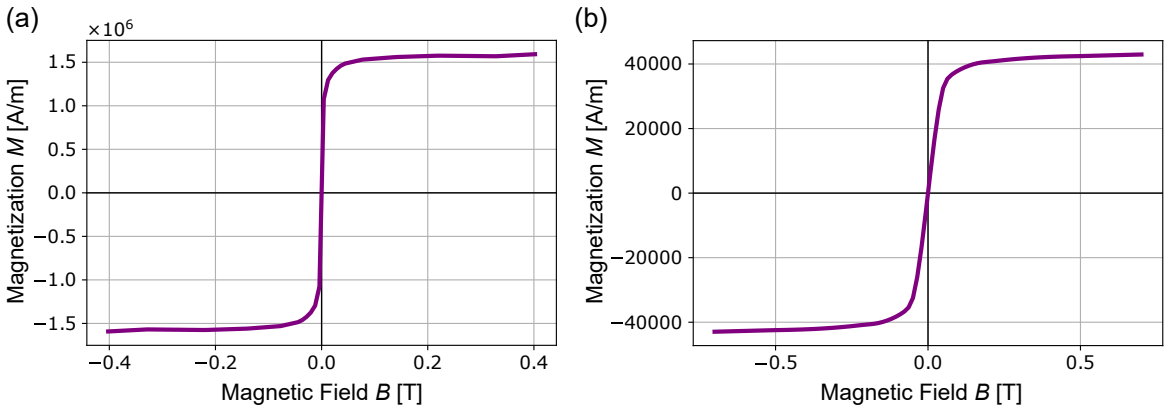

Figure 1.3. Magnetization vs. magnetic field curves for (a) soft bulk iron adapted from the built-in material library in COMSOL Multiphysics®; b) a high concentrated bulk solution of iron-oxide beads as measured using a vibrating sample magnetometer (VSM) [45].

It is important to note that at the nano- and micrometer scales, magnetic behavior deviates from that of bulk materials due to size- and shape-dependent effects [38]. While the saturation magnetization, the magnetization achieved when all magnetic moments in the material are aligned in the same direction, typically remains unchanged unless a phase transformation occurs (as in materials like FePt, discussed later), the shape of the magnetization curve differs between bulk and nanoscale systems [38]. In particular, magnetic nanoparticles often exhibit enhanced effective magnetic anisotropy, arising from surface and shape contributions that define preferred directions of magnetization and influence its reversal behavior [38]. Moreover, particle size plays a critical role in determining magnetic domain structure [38]. Below a critical diameter (typically around 20 nm, depending on the material), particles tend to become single-domain and thus more susceptible to thermal fluctuations, a regime characterized by superparamagnetic behavior [38]. These effects are not accounted for in the following estimations, where I directly apply these magnetic hysteresis curves from bulk soft iron and Dynabeads to particles of different sizes.

The magnetic force as a function of the vertical distance z above a cylindrical magnet (grade N48, height $h = 8\,\mathrm{mm}$, radius $R = 1.5\,\mathrm{mm}$) is shown in Fig. 1.4a for iron particles of different sizes, and in Fig. 1.4b for iron-oxide beads.

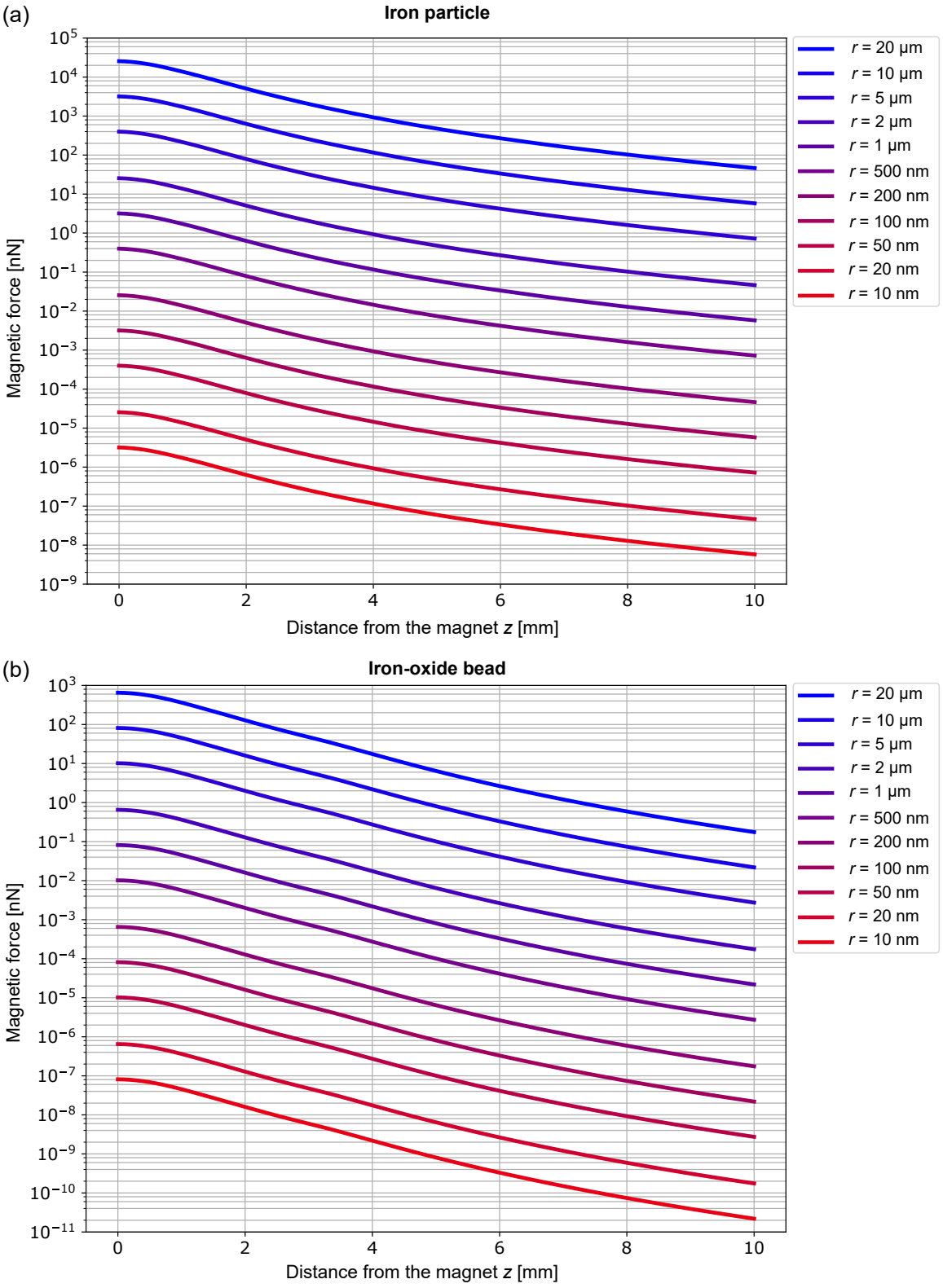

Figure 1.4. Magnetic force on (a) an iron particle and (b) an iron-oxide bead, both of radius r and positioned at height z above a cylindrical NdFeB magnet (N48, $h = 8\,\mathrm{mm}$, $R = 1.5\,\mathrm{mm}$).

Block Magnets

Similarly, the magnetic field on the symmetry axis z in the north-south pole direction above a block magnet can be also derived from Eq. (1.8) and Eq. (1.9) [40]

$$B_z = \frac{B_\mathrm{r}}{\pi}\left[\mathrm{arctg}\left(\frac{a_1 a_2}{2z\sqrt{4z^2+a_1^2+a_2^2}}\right) - \mathrm{arctg}\left(\frac{a_1 a_2}{2(h+z)\sqrt{4(h+z)^2+a_1^2+a_2^2}}\right)\right], \tag{1.13}$$

where h is the height of the magnet along the symmetry axis, a_1 and a_2 are the remaining two sides of the block and z is the distance from a pole on the symmetry axis.

The magnetic gradient in the z-direction on the symmetry axis is given by

$$\frac{\partial B_z}{\partial z} = B_\mathrm{r} a_1 a_2 \Bigg[-\frac{2\left(a_1^2+a_2^2+8z^2\right)}{\pi\left(a_1^2+4z^2\right)\left(a_2^2+4z^2\right)\sqrt{a_1^2+a_2^2+4z^2}} + \frac{2\left(8h^2+16hz+a_1^2+a_2^2+8z^2\right)}{\pi\left(4h^2+8hz+a_1^2+4z^2\right)\left(4h^2+8hz+a_2^2+4z^2\right)\sqrt{4h^2+8hz+a_1^2+a_2^2+4z^2}}\Bigg]. \tag{1.14}$$

The magnetic force in the z-direction on the symmetry axis can again be approximated by Eq. (1.12). However, I do not show force calculations for magnetic particles above block magnets, as their magnitudes do not differ substantially from those obtained for cylindrical magnets of comparable dimensions. A detailed discussion of block magnets arranged in a Halbach configuration will be presented later in this thesis, in Chapter 3.

1.2.2 Critical Review of Magnetic Targeting in Biomedicine

Assessing whether a magnetic stimulus can effectively influence a magnetically responsive object within a biological setting remains challenging. This difficulty arises because motion generated by magnetic forces on magnetic particles is not only opposed by viscous drag, as discussed in Section 1.1, but is also hindered by the complex, and often unknown properties of surrounding biological environments, including cells and tissues.

Nonetheless, the expected magnetic forces can be evaluated under simplified conditions, such as assuming motion in a Newtonian fluid like water. These approximations may provide a first indication of whether magnetic forces are sufficient to affect the object of interest. Yet, in numerous published studies, the magnetic potential energy exerted on the targeted objects is, in fact, orders of magnitude lower than the thermal energy, implying that stochastic thermal fluctuations, rather than magnetic forces, predominantly govern particle behavior. Interestingly, many of these studies report that magnetic fields were successfully used to induce biological effects at the cellular or tissue level, raising questions about the plausibility of the claimed outcomes.

One illustrative example can be found in magnetogenetics, a field aiming to genetically engineer specific cells, such as neurons, to enable external magnetic control of their activity [46]. Several studies have reported successful modulation of biological molecules and cellular processes using magnetic fields, with these findings published in leading scientific journals [47–49]. However, subsequent critical evaluations have demonstrated that these claims often conflict with fundamental physical principles, with discrepancies spanning five to ten orders of magnitude [46, 50, 51].

In this context, motivated by the ultimate goal of achieving gene delivery to the retina using magnetic helical propellers as described later in Chapter 4, I present a similarly critical review of the use of permanent magnets in two research areas closely related to our work. First, I review the use of magnetic forces in magnetofection studies, where magnetic fields are used to enhance gene transfection. Subsequently, I analyze three selected studies that employed permanent magnets to target retinal cells *in vivo*.

Magnetofection

The concept of magnetic targeting for site-specific drug delivery within the human body was first introduced nearly fifty years ago by K. Widder *et al.* [52]. Building upon this foundation, the technique of magnetofection, gene delivery and transfection facilitated by magnetic fields, was first established over two decades ago by F. Scherer *et al.* [53]. They demonstrated the conjugation of vectors carrying genetic information with superparamagnetic nanoparticles, enabling targeting sites of interest using permanent magnets, both *in vitro* and *in vivo* [53]. Since then, a substantial number of studies have investigated the potential of magnetic targeting for biomedical applications. However, despite this extensive research, magnetic targeting using nanoscale materials has not been translated into clinical practice. In the following, I critically examine the underlying challenges contributing to this translational gap, with a particular focus on the forces involved in magnetofection.

A typical magnetofection complex is designed to deliver genetic material to cells for therapeutic purposes. It generally consists of a magnetic nanoparticle core conjugated with a gene delivery vector, either viral or nonviral, along with the corresponding nucleic acid payload [54]. In earlier studies, the hydrodynamic diameter of such complexes was often in the range of several hundred nanometers, with some reports indicating sizes as large as 1.5 µm [55]. More recent efforts, particularly in the context of non-viral magnetofection, have shifted toward significantly smaller complexes, with diameters typically ranging from 100 nm to 250 nm [56–63]. While reducing the complex diameter decreases the ratio of magnetic force (scaling with the cube of the magnetic core diameter, as indicated by the volume term in Eq. (1.7)) to the drag force (scaling with the diameter of the whole complex, as described by Eqs. (1.4) and (1.5)), and thus can diminish magnetic targeting efficiency, this reduction in size is also motivated by the more efficient cellular uptake of smaller particles through endocytosis. Specifically, particles up to approximately 200 nm are efficiently internalized by cells through clathrin-mediated endocytosis, whereas larger particles, up to 500 nm, are internalized via caveolae-mediated endocytosis [64], a pathway generally considered to have lower capacity in most cell types [65, 66].

For generating the magnetic field gradients required to exert force on such complexes, many *in vitro* studies rely on commercially available magnetic plates [67–69], which consist of regularly arranged arrays of permanent magnets. However, these systems are generally insufficiently characterized; key parameters such as magnetic field strength and gradient values are often not disclosed on the manufacturers' websites, making it difficult to evaluate the magnetic forces applied in experiments using these devices.

To address this limitation and enable a more accurate force assessment in magnetofection studies, I experimentally characterized the magnetic properties of commonly used magnetic plate systems, focusing in particular on plates from *Chemicell* and *OZ Biosciences*. The

magnetic field was measured using a magnetometer (*MAGSYS* HGM09s) mounted on a manual micromanipulator. I recorded the magnetic field and calculated the corresponding gradients above the magnets in the *Chemicell* MagnetoFACTOR-24 plate (containing 24 magnets), the *Chemicell* MagnetoFACTOR-96 plate (96 magnets), and the *OZ Biosciences* Super Magnetic Plate (see Fig. 1.5a–c). Despite its name, the latter also contains 24 magnets but exhibits lower magnetic field strengths and gradients compared to the *Chemicell* 24-magnet plate. This reduction is attributable to an additional plastic housing layer that encloses the magnet array, obscuring the internal configuration and offering no transparency regarding its design. All tested plates featured magnet arrays with alternating polarity.

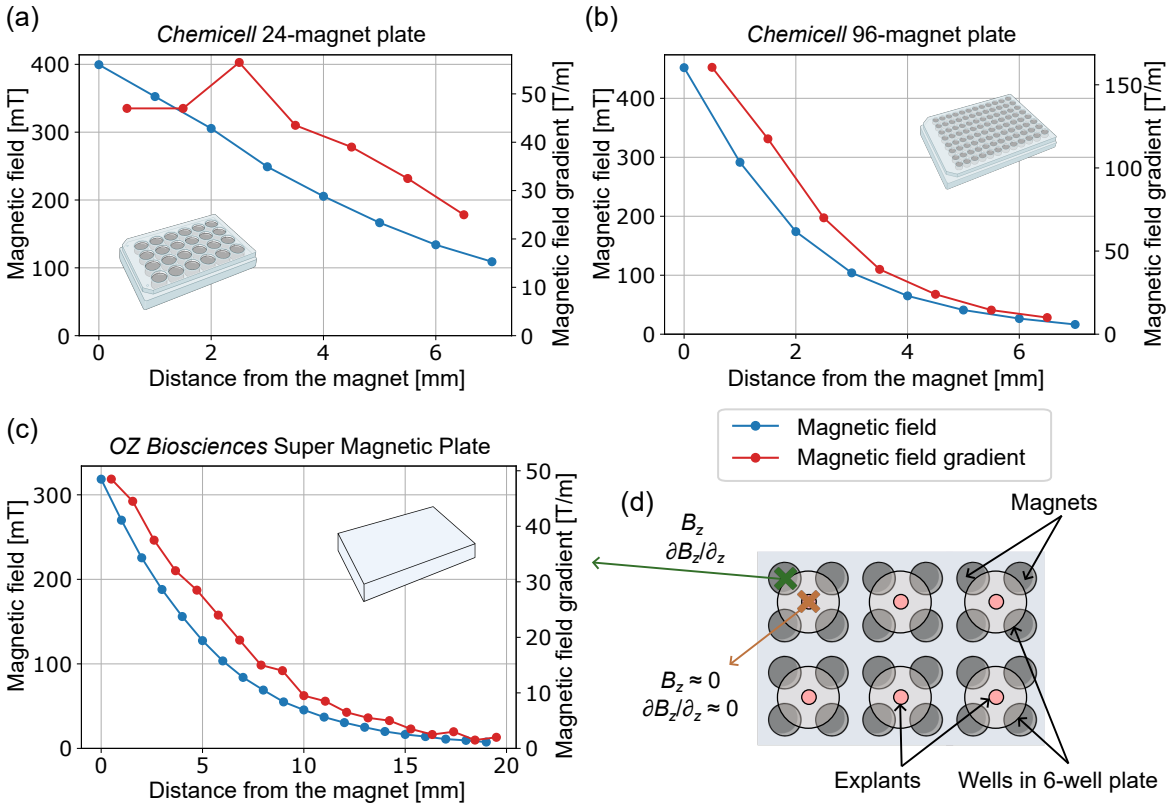

Figure 1.5. Characterization of standard magnetofection plates: (a) magnetic field and gradient as functions of vertical distance above a single magnet in the *Chemicell* 24-magnet plate; (b) magnetic field and gradient as functions of vertical distance above a single magnet in the *Chemicell* 96-magnet plate; (c) magnetic field strength and gradient as functions of vertical distance above a single magnet in the *OZ Biosciences* Super Magnetic Plate; (d) schematic of the experimental setup for ”Reverse Magnetofection” [70, 71], illustrating the magnetic field and gradient above individual magnets as shown in (c), and the zero magnetic field and gradient between magnets, corresponding to the explant positions in the study by Sen *et al.* [71]. Magnetic field and gradient values in (a)–(c) represent averages over two magnets.

When standard cell culture plates are positioned above these magnetic arrays, the vertical separation between the culture surface and the magnets is approximately 5 mm. At this distance above a single magnet in the array, I calculated the magnetic forces acting on 200 nm particles across all three characterized magnetofection plates. These calculations considered three distinct magnetic material properties:

(i) Iron oxide beads with 26 % iron content, as shown in Fig. 1.3b.

(ii) Pure magnetite (Fe_3O_4), the most magnetically responsive iron oxide phase, surpassing its oxidized form, maghemite (γ-Fe_2O_3), and weakly magnetic hematite (α-Fe_2O_3) [72]. The hysteresis curve was obtained by normalizing the data from Fig. 1.3b and scaling it to the saturation magnetization of pure magnetite (480 kA/m) [73, 74].

(iii) Bulk iron, as depicted in Fig. 1.3a.

The resulting magnetic forces are summarized in Table 1.2. Assuming particle motion in a medium with water-like viscosity, the drift velocities induced by these magnetic forces were estimated using Eqs. (1.5) and (1.4). The calculated velocities span from slightly above 1 µm/s to over 100 µm/s, as detailed in Table 1.2. For context, the root mean square displacement of a spherical particle due to thermal diffusion can be estimated using the diffusion coefficient [75]

$$D = \frac{kT}{6\pi\mu R_{\mathrm{S}}}, \tag{1.15}$$

where k is the Boltzmann constant, T is the absolute temperature, μ is the dynamic viscosity of the medium, and R_{S} is the particle radius. Considering motion along a single spatial dimension, specifically the *z*-axis, along which the nanoparticle is drawn toward the magnet, the 1D root mean square displacement after a time t is given by [75]

$$\sqrt{\langle z^2 \rangle} = \sqrt{2Dt}. \tag{1.16}$$

For a 200 nm nanoparticle in water at room temperature, this yields a root mean square displacement in *z*-direction of approximately 2 µm after one second. As a result, only particles composed of pure magnetite or iron exhibit magnetic forces sufficient to induce displacements significantly (by approximately an order of magnitude) greater than those caused by Brownian motion (see Table 1.2 for a comparison of drift velocities relative to the 2 µm displacement over one second). Magnetofection complexes, however, are not composed exclusively of magnetic materials. As previously discussed, they also incorporate gene delivery vectors and nucleic acid payloads, which reduce the relative proportion of magnetic content and thereby further decrease the ratio of magnetically induced drift to Brownian motion. Even when magnetic forces are sufficient to overcome diffusion and concentrate complexes near the target cell layer, it is important to recognize that these forces do not disrupt the cell membrane. Forces in the nanonewton range are typically required to induce

membrane penetration [14], which exceed those generated by magnetic attraction under standard magnetofection conditions by several orders of magnitude, as shown in Table 1.2. Thus, effective gene delivery still relies on the subsequent uptake of the complexes by the target cells through endocytic pathways, consistent with the conclusion by C. Plank that the internalization mechanisms in magnetofection do not differ from those in non-magnetic nucleic acid delivery [54].

		24-magnet plate	96-magnet plate	Super Magnetic Plate
Iron-oxide beads	Force	6 fN	2.3 fN	4 fN
	Velocity	3 µm/s	1.2 µm/s	2.3 µm/s
Pure magnetite	Force	70 fN	26 fN	49 fN
	Velocity	36 µm/s	14 µm/s	26 µm/s
Bulk iron	Force	234 fN	119 fN	171 fN
	Velocity	124 µm/s	63 µm/s	91 µm/s

Table 1.2. Magnetic force and corresponding drift velocity in water for 200 nm particles positioned 5 mm above standard magnetofection plates: *Chemicell* 24-magnet plate, *Chemicell* 96-magnet plate, and *OZ Biosciences* Super Magnetic Plate. Particle magnetic properties considered include iron oxide beads (26 % iron content, as depicted in Fig. 1.3b), pure magnetite (normalized hysteresis from Fig. 1.3b, scaled by the saturation magnetization of pure magnetite), and bulk iron (as shown in Fig. 1.3a).

The Super Magnetic Plate has also been employed in a less effective configuration referred to as ”Reverse Magnetofection”, where the magnetic plate was positioned above the culture dish to attract magnetofection complexes upward toward *ex vivo* explants [70, 71]. In this setup, the distance between the magnetic complexes and the magnetic plate exceeds 17 mm. At this axial position, the magnetic field gradient is only 2.5 T/m (see Fig. 1.5c). For a complex with a diameter of 200 nm composed of iron oxide, and using magnetic properties from Fig. 1.3, the resulting magnetic force is approximately 84 aN. For comparison, if the complex were made of pure magnetite or iron, the force would be about 1.1 fN and 12 fN, respectively. Based on Eq. (1.4), this corresponds to drift velocities of roughly 45 nm/s for iron oxide composites, 560 nm/s for magnetite particles, and 6 µm/s for iron particles, resulting in displacements of only 45 nm, 560 nm, and 6 µm, respectively, after one second. For iron oxide, as reported in the referenced studies, magnetic drift is considerably smaller than the displacement due to diffusion (2 µm after one second), rendering the magnetic effect negligible. Even for particles with the magnetic properties of bulk iron, the displacement is only marginally greater than that caused by thermal diffusion, indicating that Brownian motion substantially limits the effectiveness of magnetic manipulation under these condi-

tions. Moreover, Sen *et al.* [71] report the use of standard 6-well plates placed above the Super Magnetic Plate, which consists of 24 individual magnets (see schematic in Fig. 1.5d). As a result, the explants in this study were likely located in the regions between individual magnets. However, due to the alternating polarity arrangement of the magnets within the plate, the magnetic field and corresponding gradient at these inter-magnet positions are effectively zero. This fact further undermines the reliability of the magnetic targeting strategy reported in the study.

Magnetofection has also been investigated in *in vivo* contexts [57, 58, 60–62, 76–80]. However, detailed reporting on the magnetic field strengths and gradients employed is often lacking. In many studies, only a general reference to the use of a permanent magnet is provided [60–62, 77], occasionally accompanied by a specification of the magnetic field strength at the magnet surface [57, 58, 76, 78–80]. The reported magnetic field strengths at the magnet surface, and where available, the corresponding gradients, typically do not exceed those generated by standard *in vitro* magnet arrays [58, 76, 78]. Moreover, in *in vivo* applications, the distance between the magnet and the target site is generally much larger than the standard 5 mm separation used in *in vitro* setups. Magnetofection complexes must also navigate through a substantially more complex biological environment compared to the aqueous medium of cell culture systems. Additionally, in typical magnetofection formulations with hydrodynamic diameters ranging from 100 nm to 250 nm, the magnetite core rarely exceeds 100 nm in diameter [57,60–62,76], resulting in a relatively low magnetic volume fraction within the overall complex. Although I do not evaluate specific *in vivo* magnetofection studies in terms of the magnetic forces generated, I provide a comparative analysis of magnetic targeting efficiency in *in vivo* contexts in the following subsection.

Magnetic Targeting of the Retina *in vivo*

The delivery of drugs, stem cells, or genes to retinal cells represents a promising strategy for treating various ophthalmological disorders, as discussed in detail in Chapter 4. Several studies have explored the use of magnetic fields to facilitate such delivery and have reported successful magnetic targeting of the eye in mice *in vivo* [81–83]. In the following, I present a force-based analysis of three representative *in vivo* studies. Due to the frequent lack of detailed magnet specifications, often limited to an image showing the magnet positioned near the target site, I made assumptions regarding the dimensions and grade of the permanent magnets, their distances from the administered magnetic particles, and, where necessary, the magnetization properties of the particles themselves. My analyses consistently consider magnetic particles positioned along the magnet's axial axis. In all cases, I opted to overestimate the magnetic forces, to account for best-case targeting scenarios.

Dengler *et al.* reported an accumulation of cobalt-based magnetic nanoparticles in the posterior segment of the eye following tail vein injection in mice, under the influence of an externally applied magnetic field (see schematic in Fig. 1.6a) [81]. Based on a photograph comparing the magnet size to a C57Bl mouse, I estimated the cylindrical magnet to have a diameter of 4 cm and a height of 7 cm, assuming a high-performance N52-grade NdFeB composition. I further assumed that the injection site was located approximately 8 cm from the magnet, corresponding to the typical body length of a C57Bl mouse (excluding the tail). To illustrate that there can be no effect of the magnet pulling the magnetic nanoparticles from the injection site, I estimated the corresponding magnetic forces using the above geometry. This configuration yields an estimated magnetic field strength of 16 mT and a magnetic field gradient of 0.5 T/m at the injection site. Using the magnetization value derived from the reported magnetic hysteresis data, I calculated the magnetic force acting on a single 100 nm cobalt particle via Eq. (1.7), yielding a maximum value of approximately $7 \cdot 10^{-17}$ N. Assuming the particle moves through water and experiences only viscous drag (via Eqs.(1.4) and (1.5)), the resulting magnetic displacement over one second is only 45 nm. For context, a 100 nm cobalt nanoparticle suspended in water at room temperature exhibits a root mean square displacement of approximately 3 µm over one second due to thermal diffusion, as predicted by Eq. (1.16). This is nearly two orders of magnitude greater than the displacement due to the estimated magnetic force, even under optimistic assumptions. These findings suggest that thermal diffusion overwhelmingly dominates the motion of nanoparticles under the reported conditions. The nanoparticles therefore had to be passively transported via blood flow to regions closer to the magnet, where stronger magnetic forces could become relevant. For instance, if the particles reached the vicinity of the head, assuming the mouse's head to be approximately 1 cm in length, the magnetic field could rise to 384 mT, with a gradient of 26 T/m. Under such conditions, the magnetic force acting on a 100 nm cobalt nanoparticle would increase to around $2.0 \cdot 10^{-15}$ N, resulting in a drift velocity of approximately 4 µm/s in water. This velocity slightly exceeds the root mean square displacement due to Brownian motion, suggesting that magnetic forces could influence nanoparticle accumulation if the particles are brought sufficiently close to the magnet by blood flow. However, as cobalt is not biocompatible and cannot be used in clinical applications, and since, as mentioned previously, magnetofection complexes are not composed solely of magnetic material, the actual magnetic moment in medical scenarios is expected to be considerably lower. This suggests that blood flow must bring the nanoparticles within millimeters of the targeting location before magnetic forces can play a meaningful role in guiding their accumulation.

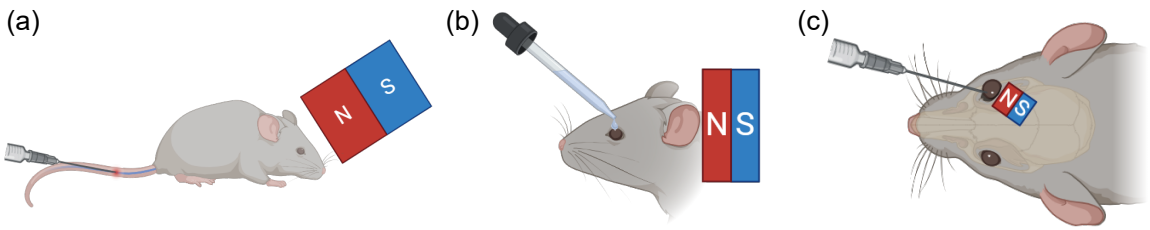

Figure 1.6. Schematic representation of magnetic targeting approaches to the eye reported in the literature: (a) magnet placed anterior to the eye following tail vein injection of magnetic particles [81]; (b) magnet placed posterior to the head in conjuction with topical administration of magnetic particles loaded with therapeutic agents [82]; (c) magnet placed within the ocular orbit following intravitreal injection of stem cells containing internalized magnetic nanoparticles [83].

Bassetto *et al.* presented a study claiming successful delivery of superparamagnetic iron-oxide nanoparticles, loaded with therapeutic agents, to retinal photoreceptor cells following topical administration, using a magnet positioned behind the mouse's head (see schematic in Fig. 1.6b) [82]. The magnetic setup is described merely as a 0.4 T magnet, with no further characterization provided. Based on a photograph in the publication showing a ruler adjacent to the magnet, I estimated its dimensions to be approximately 5 mm in height with a square base of 20 mm per side. However, even assuming a high-grade N52 NdFeB magnet composition, such dimensions would yield a surface magnetic field of only about 0.28 T. To match the reported field strength of 0.4 T, I adjusted the magnet height to 9 mm in the calculations. From the same image, I estimated the mouse's eye to be positioned approximately 15 mm from the magnet's surface. At this distance, the magnetic field generated by the magnet is estimated to be 273 mT, with a corresponding magnetic field gradient of 34 T/m. Using the reported nanoparticle core diameter of 10 nm [82] and adopting a conservative overestimation of their magnetization based on saturation values for iron-oxide nanoparticles from an independent study [84], I calculated the magnetic force on a single particle to be approximately $6 \cdot 10^{-18}$ N. Assuming the particle experiences only Stokes drag in water and neglecting the increased hydrodynamic diameter and the resistance of the tissue, this force would result in a translational velocity of approximately 70 nm/s. In contrast, the root mean square displacement due to Brownian motion, estimated using Eqs. (1.15) and (1.16), exceeds 9 µm. Thus, diffusion dominates over magnetically induced motion by more than two orders of magnitude, suggesting that the magnet had little effect.

Yanai *et al.* demonstrated magnetic targeting by placing a permanent magnet within the orbital cavity, posterior to the rat's eyeball (see Fig. 1.6c) [83]. Mesenchymal stem cells (MSCs) loaded with 200 nm FluidMAG nanoparticles (*Chemicell*) and injected intravitreally were found to accumulate at the retinal surface. The study specifies the use of a NdFeB permanent magnet with dimensions of 3 mm in diameter and 1.5 mm in height, and a maximum energy product of 43.2 MGOe. To estimate the resulting magnetic forces, I considered two representative distances between the injected particles and the magnet: $d_1 = 5\,\mathrm{mm}$, corresponding to the approximate axial length of an adult rat eye, and $d_2 = 200\,\mu\mathrm{m}$, representing an injection very close to the retina. For simplicity, I modeled the magnetic behavior of individual nanoparticles, neglecting potential collective behavior due to their internalization in MSCs. Magnetic properties and particle density were taken from an independent study [85]. At the larger distance d_1, the magnetic field was approximately 34 mT with a field gradient of 14 T/m, resulting in a magnetic force of $1.3 \cdot 10^{-15}$ N per particle. This corresponds to a magnetic drift velocity in water of 0.7 µm/s. In contrast, the root mean square displacement due to Brownian diffusion over 1 second is approximately 2 µm, indicating that magnetic forces contributed to at most 35 % of the motion at this distance. In the close-injection scenario d_2, the magnetic field increases to 290 mT with a field gradient of 76 T/m, yielding a force of $1.5 \cdot 10^{-14}\,\mathrm{N}$ per particle and a drift velocity of 8 µm/s. Given that the magnetized MSCs were observed on the retinal surface following intravitreal injection, it is likely that they were delivered in close proximity to the retina. My analysis shows that a permanent magnet has to be positioned very close to the retina, possibly inside the ocular orbit to exert meaningful magnetic forces on individual nanoparticles (diameter $200\,\mathrm{nm}$).

Despite the physical limitations identified in these force-based estimations, the reviewed studies collectively report successful outcomes in small animal models, such as rodents. Physiological processes, such as blood circulation, must transport magnetic particles into regions with stronger magnetic fields, thereby enabling more effective magnetic targeting than would be predicted when considering only magnetic pulling forces. Nevertheless, it is important to recognize that scaling such approaches to allow applications in humans would require permanent magnets producing significantly stronger magnetic fields and gradients due the substantially larger anatomical dimensions and the rapid spatial decay of magnetic field gradients generated by permanent magnets.

Fortunately, magnetism can be harnessed through alternative means beyond permanent magnets that offer distinct operational advantages. While not all of these approaches are suitable for deep-tissue targeting within the human body, each offers unique advantages that can be tailored for specific biomedical objectives. In the remainder of this chapter, I will introduce these alternative strategies and provide quantitative estimates of the forces they can generate. In the subsequent chapters, I will present representative examples.

1.2.3 Localized Magnetizable Bodies in a Homogeneous Magnetic Field

When a paramagnetic or ferromagnetic material is introduced into an initially homogeneous magnetic field, the magnetic flux lines are distorted by the magnetizable object. This localized perturbation creates a spatially varying magnetic field - *i.e.*, a magnetic field gradient. The characteristics of this gradient, such as its magnitude and spatial decay, can be tuned by adjusting the geometry and dimensions of the magnetizable inclusion, as well as the strength of the applied external magnetic field.

Due to the complexity of the resulting magnetic field distribution, obtaining an analytical solution in such configurations is generally challenging. Therefore, I performed finite element simulations in *COMSOL Multiphysics 6.1*, using the "Magnetic Fields, No Currents" interface. In this analysis, the magnetizable object was modeled as a soft iron cylinder (*e.g.*, a wire) aligned such that its longitudinal axis is parallel to the applied magnetic field (see Fig. 1.7a). To reduce computational costs, I exploited 2D axisymmetry and employed an infinite element domain, with its boundary set to the external magnetic flux density.

I first systematically varied the cylinder's diameter, height, and the amplitude of the external magnetic field to assess the influence of each parameter on the magnetic field gradient:

(i) Height of the magnetizable cylindrical wire element: Increasing the height of the magnetic cylinder leads to a higher maximum magnetic field gradient (see Fig. 1.7b). This effect is a consequence of shape anisotropy, which progressively favors the alignment of magnetic moments in the iron along the applied field as the cylinder's height increases [38]. However, this enhancement saturates beyond a certain cylinder height, as shape anisotropy only influences the orientation, not the magnitude, of the intrinsic magnetic moments. For the presented simulations, the cylinder diameter was fixed at $D = 100\,\mu\mathrm{m}$ and the external magnetic field at $B = 100\,\mathrm{mT}$.

(ii) Diameter of the magnetizable cylindrical wire element: As the diameter increases, the magnetic field gradient near the cylinder surface decreases in magnitude (see Fig. 1.7c). However, it also decays more slowly with distance, with the magnetic field returning to the background homogeneous value at greater distances from the cylinder. This behavior is analogous to the effect observed when increasing the radius of a permanent magnet (see Fig. 1.2b). Here, the cylinder height was fixed at $h = 1\,\mathrm{mm}$ and the external field at $B = 100\,\mathrm{mT}$.

(iii) Magnitude of the magnetic field: An increase in the strength of the externally applied homogeneous magnetic field leads to a corresponding enhancement in the magnitude of the resulting magnetic field gradient (see Fig. 1.7d). This behavior arises from the higher magnetic flux density that becomes available to be focused at the tip of the soft iron cylinder, thereby amplifying the local magnetic field gradient. An increase is possible up to the saturation of the magnetic material. Throughout these simulations, the cylinder dimensions were kept constant, with a diameter of $D = 100\,\mu\mathrm{m}$ and a height of $h = 1\,\mathrm{mm}$.

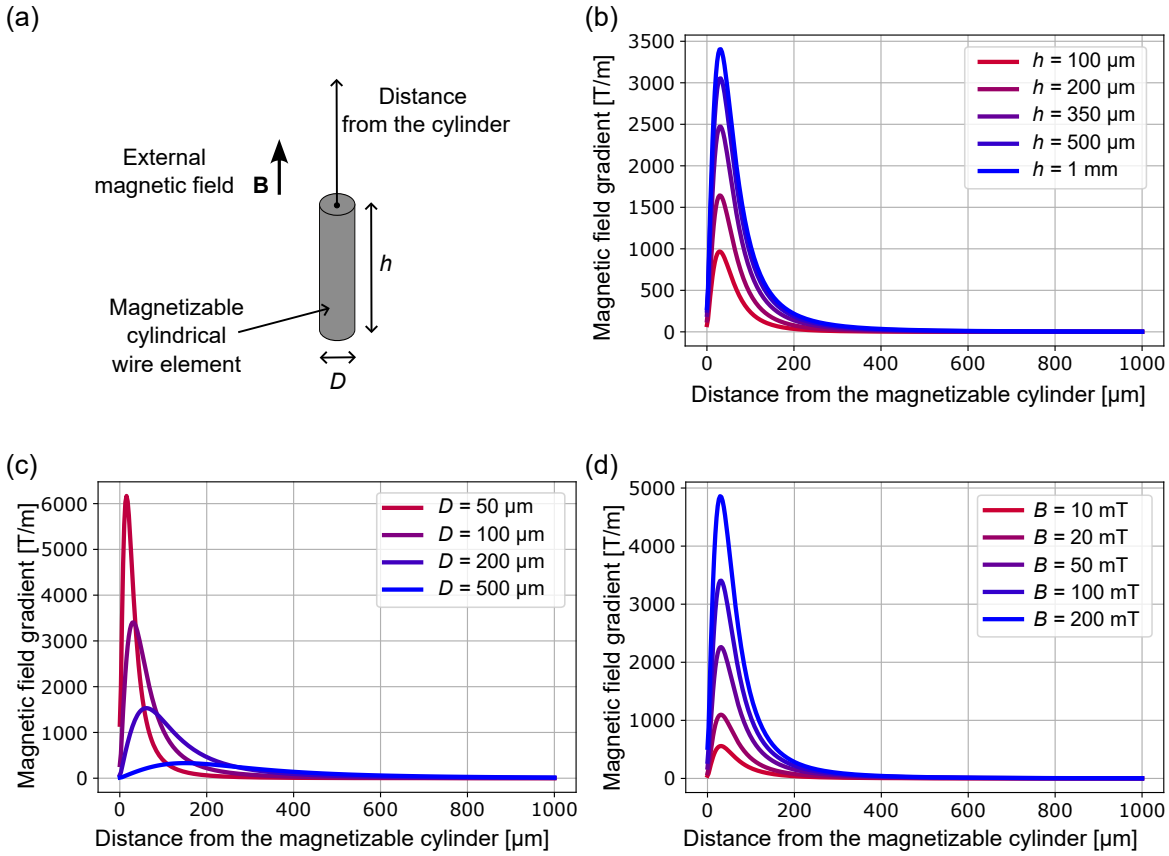

Figure 1.7. Magnetic field gradient as a function of distance from the surface of a soft iron cylindrical wire element placed in a homogeneous external magnetic field oriented along the cylinder's long axis: (a) schematic of the magnetizable cylinder in the external magnetic field, illustrating key parameters; (b) cylinder with fixed diameter $D = 100\,\mu\mathrm{m}$ and varying height, subjected to an external field $B = 100\,\mathrm{mT}$ pointing along the direction of the cylinder's long axis; (c) cylinder with fixed height $h = 1\,\mathrm{mm}$ and varying diameter, subjected to an external field $B = 100\,\mathrm{mT}$; (d) cylinder with fixed diameter $D = 100\,\mu\mathrm{m}$ and height $h = 1\,\mathrm{mm}$, subjected to varying external magnetic field strengths.

Overall, the magnetic field gradient attains very high values several tens of microns away from the iron cylinder (see comparison with the gradient above a permanent magnet in Fig. 1.2a), but it decays rapidly with increasing distance from the iron cylinder. For instance, in the case of a cylinder with a diameter of $D = 100\,\mu\mathrm{m}$ and a height of $h = 1\,\mathrm{mm}$ subjected to an external field of $B = 100\,\mathrm{mT}$, the gradient is around 2 T/m at the distance of 1 mm.

In addition, I present the estimated magnetic force acting on iron particles (see Fig. 1.8a) and iron oxide beads (see Fig. 1.8b) of varying sizes, evaluated as a function of vertical position above a magnetizable cylinder subjected to an external magnetic field. The cylinder had fixed dimensions of $D = 100\,\mu\mathrm{m}$ and $h = 1\,\mathrm{mm}$, and the applied magnetic flux density is $B = 100\,\mathrm{mT}$. These force estimations were based on the corresponding magnetic hysteresis characteristics, shown in Fig. 1.3a for iron and Fig. 1.3b for iron oxide, and were computed using Eq. (1.12), with the magnetic field and its gradient extracted from finite element simulations.

This approach enables the generation of high magnetic forces in a highly localized region, which can be advantageous in scenarios where positioning a permanent magnet close to the area of interest is impractical. Instead, introducing a thin magnetizable wire may offer a less intrusive alternative. Although the effective force generation is restricted to the immediate vicinity of the magnetizable object, typically within tens to a few hundred microns, the resulting forces can significantly exceed those produced by permanent magnets commonly reported in the literature (see Fig. 0.1). This strong microscale localization of the magnetic field gradient, and consequently of the magnetic forces, has significant potential for a range of applications, some of which are explored in more detail in Chapter 3.

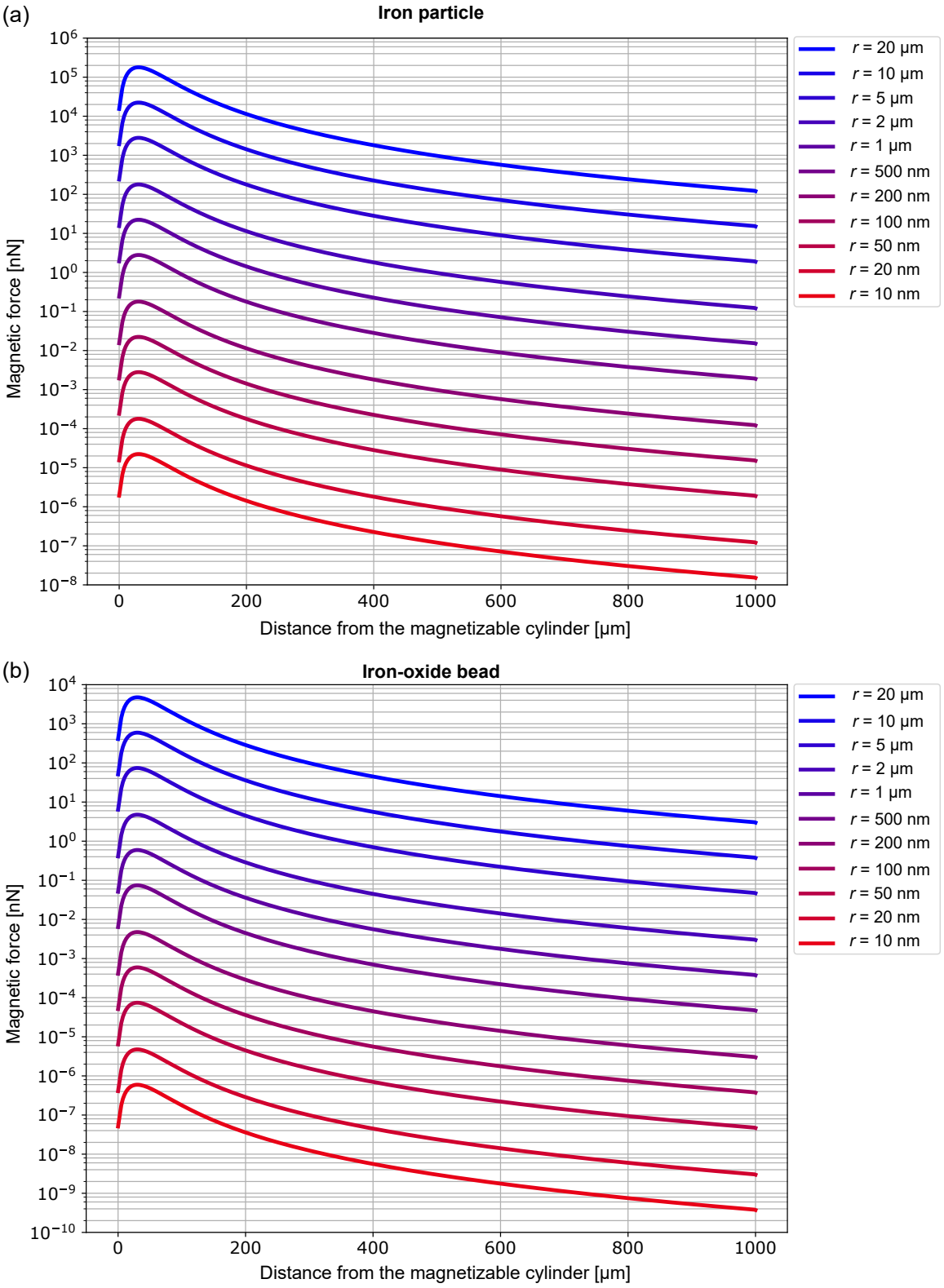

Figure 1.8. Magnetic force acting on (a) an iron particle and (b) an iron-oxide bead, each with radius r, as a function of vertical position above a magnetizable soft iron cylinder under an externally applied homogeneous magnetic field ($D = 100\,\mu\mathrm{m}$, $h = 1\,\mathrm{mm}$, $B = 100\,\mathrm{mT}$).

1.3 Rotating Magnetic Fields

Even in the absence of a magnetic field gradient, force or torque on an object can also be generated through rotating magnetic fields. If the magnetic object of interest exhibits structural chirality, then a rotating homogeneous (i.e. gradient-free) field can also cause translation. Chiral objects are generally defined as those that lack mirror symmetry [86]. For such chiral objects, propulsion can arise from the coupling between rotational and translational motion (see Eq. (1.3)).

In the case of weak, slowly rotating homogeneous magnetic field $\mathbf{B}$, the torque of a chiral magnetic object with the magnetic moment $\mathbf{m}$ is [38]

$$\boldsymbol{\tau} = \mathbf{m} \times \mathbf{B}. \tag{1.17}$$

This external torque can be a source of both rotational and translational movements of the object through Eq. (1.3) [87]. Although the external force $\mathbf{F} = 0$ in Eq. (1.3), the object is propelled with the force

$$\mathbf{F}_{\boldsymbol{\tau}} = -\mathbf{A} \cdot \mathbf{v} = \mathbf{C}^{\intercal} \cdot \boldsymbol{\omega} = \mathbf{C}^{\intercal} \cdot \mathbf{D}_{\text{eff}}^{-1} \cdot (\mathbf{m} \times \mathbf{B}), \tag{1.18}$$

where $\mathbf{D}_{\text{eff}} = \mathbf{D} - \mathbf{C} \cdot \mathbf{A}^{-1} \cdot \mathbf{C}^{\intercal}$ is the renormalized rotation resistance tensor [87].

1.3.1 Resistive force theory for a helix

In the present study, objects propelled via weak rotating homogeneous magnetic fields are helically shaped structures. These helical objects are inspired by flagellated organisms found in nature, which exhibit highly efficient coupling between translation and rotation motions, and thus generate substantial propulsive forces [32, 88].

The drag force opposing the translational motion of the helix along its principal axis with velocity v is often estimated by approximating the shape of the helix by a prolate ellipsoid [88]. In this approximation, the drag force in Eq. (1.5) is given by

$$F_{\mathrm{D},v} = -A_{\mathrm{E}} v \tag{1.19}$$

where A_{E} is the drag coefficient for a prolate ellipsoid, expressed according to the extended Stokes law derived by F. Perrin [89] as

$$A_{\mathrm{E}} = \frac{16\pi\mu\left(a^2 - b^2\right)}{\frac{4a^2-2b^2}{\sqrt{a^2-b^2}} \ln \frac{a+\sqrt{a^2-b^2}}{b} - 2a} \tag{1.20}$$

with a and b denoting the dimensions of the semi-major and semi-minor axes, respectively, and μ representing the dynamic viscosity of the fluid. The assumption of a prolate shape,

however, cannot be used to estimate the force rising from the coupling between the translation and rotation motions for a helical propeller, as the translation-rotation coupling tensor for an ellipsoid $\mathbf{C}_{\mathrm{E}} = \mathbf{0}$.

The resistive force theory predictions developed for helical flagella by Gray and Hancock [90] and by Lighthill [91] are derived by integrating the local forces along small segments of the flagellum. Helical propellers move forward by rotating around their long axis. The theory therefore considers only two degrees of freedom of the isolated propeller: rotation at angular velocity ω around its principal axis and forward translation at velocity v. The set of vector equations (1.3) can be rewritten for a left-handed helix as

$$\begin{aligned} F &= Av + C\omega \\ \tau &= Cv + D\omega, \end{aligned} \tag{1.21}$$

where A, C and D are positive constants [32, 92], also known as friction coefficients. The expressions, originally presented in [91], read

$$A = K_{\mathrm{n}} L \frac{\mathrm{tg}^2\,\theta + \chi}{\sqrt{1 + \mathrm{tg}^2\,\theta}}, \tag{1.22}$$

$$C = K_{\mathrm{n}} L R \frac{\mathrm{tg}\,\theta\,(1 - \chi)}{\sqrt{1 + \mathrm{tg}^2\,\theta}}, \tag{1.23}$$

$$D = K_{\mathrm{n}} L R^2 \frac{1 + \chi\,\mathrm{tg}^2\,\theta}{\sqrt{1 + \mathrm{tg}^2\,\theta}}, \tag{1.24}$$

where $\chi = \frac{K_{\mathrm{t}}}{K_{\mathrm{n}}}$, $K_{\mathrm{n}} = \frac{4\pi\mu}{\ln \frac{cp}{r} + \frac{1}{2}}$ is the normal viscous coefficient, $K_{\mathrm{t}} = \frac{2\pi\mu}{\ln \frac{cp}{r}}$ is the tangential viscous coefficient, L is the length of the helix, R is the radius of the helical coil, r is the radius of the filament, p is the pitch, θ is the pitch angle relative to the principal axis and $c \approx 0.18$ is a constant [91,93]. The force propelling a helix magnetized in-plane (perpendicularly to the principal axis) can be expressed as [87]

$$F_\tau = \frac{C}{D_{\mathrm{eff}}} mB = \frac{AC}{AD - C^2} mB, \tag{1.25}$$

where $D_{\mathrm{eff}} = D - \frac{C^2}{A}$. Assuming $D_{\mathrm{eff}} \approx D$ for $D \gg \frac{C^2}{A}$ [87], Eq. (1.25) can be rewritten using Eq. (1.23) and Eq. (1.24) as

$$F_\tau = \frac{1}{R} \frac{\sin\theta\,(1 - \chi)}{\cos\theta\,(1 + \chi\,\mathrm{tg}^2\,\theta)} mB. \tag{1.26}$$

As we shall see later in the text, helical propellers often comprise a spherical bead on one end of the helical coil as a result of the fabrication procedure. Consequently, the description of their motion must include the propulsion matrix of the bead, in addition to the propulsion matrix of the helical coil. The equation (1.21) can be rewritten as follows [92]

$$\begin{aligned} F &= (A + A_{\mathrm{S}})\, v + C\omega \\ \tau &= Cv + (D + D_{\mathrm{S}})\, \omega, \end{aligned} \tag{1.27}$$

where A_{S} and D_{S} are the non-zero elements from the resistance tensors for a sphere defined in Eq. (1.4). The force driving the propeller forward becomes

$$F_{\tau} = \frac{C}{D_{\mathrm{eff}}} mB = \frac{(A + A_{\mathrm{S}})\, C}{(A + A_{\mathrm{S}})\,(D + D_{\mathrm{S}}) - C^2} mB, \tag{1.28}$$

where $D_{\mathrm{eff}} = D + D_{\mathrm{S}} - \frac{C^2}{(A + A_{\mathrm{S}})}$. Under the assumption $D_{\mathrm{eff}} \approx D + D_{\mathrm{S}}$ for $D + D_{\mathrm{S}} \gg \frac{C^2}{(A + A_{\mathrm{S}})}$, Eq. (1.28) gives

$$F_{\tau} = \frac{LR \operatorname{tg}\theta\,(1 - \chi)}{LR^2\,(1 + \chi \operatorname{tg}^2\theta) + 2R_{\mathrm{S}}^3 \sqrt{1 + \operatorname{tg}^2\theta}\,\left(\ln\frac{cp}{r} + \frac{1}{2}\right)} mB. \tag{1.29}$$

1.3.2 Force estimations based on existing helical propellers

To estimate the typical propulsive forces generated by magnetic helical propellers, I utilized the velocity measurements reported by V. Kadiri *et al.* [31] for propellers fabricated via glancing-angle physical vapor deposition (GLAD) (see Fig. 1.9a–b). For the calculations, I considered the geometrical and magnetic parameters of the propellers shown in Fig. 1.9a: total length $L = 1700\,\mathrm{nm}$, helical coil radius $R = 330\,\mathrm{nm}$, filament radius $r = 100\,\mathrm{nm}$, pitch $p = 950\,\mathrm{nm}$, pitch angle $\theta = 42^{\circ}$, spherical bead radius $R_{\mathrm{S}} = 260\,\mathrm{nm}$, and magnetic moment $m = 2.42 \times 10^{-15}\ \mathrm{Am}^2$ (perpendicular to the propeller's principal axis) [31]. I estimated the forces corresponding to rotating magnetic fields with amplitudes ranging from 1 to $8\,\mathrm{mT}$, which match the range of field values used in the experiments of V. Kadiri *et al.* [31]. From the velocity data shown in Fig. 1.9b, I extracted the maximum reported velocity at each field amplitude to represent the propulsion performance in water.

The forces calculated for one such propeller are plotted in Fig. 1.9c. First, neglecting the presence of the spherical bead, the force propelling the magnetic helix due to the rotating magnetic torque was calculated using Eq. (1.26) (see the blue dots in Fig. 1.9c). In order to account for the presence of the spherical bead at one end of the helical coil (see Fig. 1.9a), I also show the force arising from the magnetic torque as described by Eq. 1.29 (see the green dots in Fig. 1.9c). This thrust force is counterbalanced by the drag force, as stated in Eq. 1.18. Accordingly, I provide a direct comparison of the thrust force with the drag force in Fig. 1.9c as well. The drag force for the helix without the spherical bead is calculated as the contribution proportional to the propulsion velocity v from Eq. (1.21) (see the orange dots in Fig. 1.9c). The drag force considering both the helical and the spherical part of the propeller is estimated as the contribution proportional to the propulsion velocity v from Eq. (1.27) (see the red dots in Fig. 1.9c). In addition, I plot the drag force calculated by approximating the shape of the helix by an ellipsoid with $a = L/2$ and $b = R/2$, as described by Eq. (1.19) (see the purple dots in Fig. 1.9c).

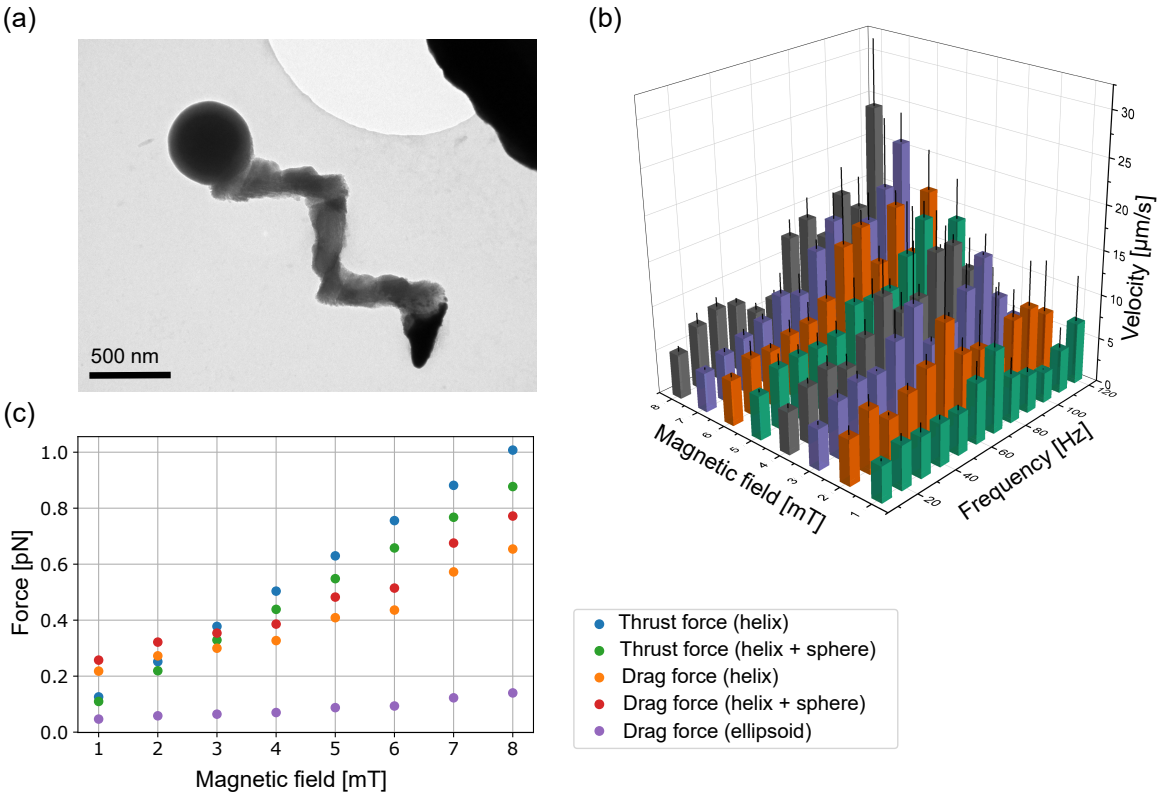

Figure 1.9. Helical propellers fabricated and characterized by V. Kadiri *et al.* [31], along with corresponding force calculations presented in this thesis: (a) transmission electron microscopy micrograph of a helical propeller, acquired by Dr. M. Alarcón-Correa and reproduced from V. Kadiri *et al.* [31]; (b) mean propulsion velocities (measured at 1–8 mT for at least 10 propellers) of magnetically actuated helical swimmers as a function of the rotating magnetic field amplitude and frequency, reported and image reproduced from V. Kadiri *et al.* [31]; (c) calculated thrust and drag forces acting on a magnetic helical propeller as a function of the rotating magnetic field amplitude, as determined in this thesis.

The comparison with the drag force acting on the corresponding ellipsoid shows that the forces calculated using Lighthill's friction coefficients [91] fall within a reasonable range of magnitudes. The thrust and drag forces estimated for a helix without any spherical bead are of a similar magnitude; however, their mutual difference grows with the increasing magnitude of the rotating magnetic field (compare the blue and orange dots in Fig. 1.9c). The thrust and drag forces calculated for a helix with a spherical bead attached to one end are expected to match and indeed show good agreement across most of the examined magnetic field range, except at very low field amplitudes (compare the green and red dots in Fig. 1.9c).

Enhancement of the thrust force can be achieved by increasing the magnetic moment of the helical propeller. For example, using a magnetic moment of $m = 1.64 \times 10^{-14}\,\mathrm{Am}^2$, as reported by V. Kadiri *et al.* in a later study where a thin FePt layer was uniformly deposited onto the entire helical structure [94], instead of the $m = 2.42 \times 10^{-15}\,\mathrm{Am}^2$ used in the present analysis [31], leads to an order-of-magnitude increase in propulsion. Under a rotating magnetic field of 50 mT, this higher magnetic moment yields a thrust force of approximately 40 pN. For comparison, such force magnitudes surpass those achievable using magnetic field gradients above a permanent magnet for iron oxide particles of similar radius (see calculations for a particle of radius 200 nm in Fig. 1.4b). While pure iron particles can experience comparable or greater forces, this is limited to distances below approximately 2.5 mm from the magnet surface (see Fig. 1.4a). Beyond enabling high propulsive forces, rotating magnetic fields offer a significant advantage in scalability. Specifically, low-amplitude fields can be efficiently generated over large volumes, making this approach particularly well-suited for biomedical applications, including potential operation within the human body. A representative application, together with supporting experimental results obtained under laboratory conditions, is presented in Chapter 4.

1.4 Ferrofluid Droplet in a Homogeneous Magnetic Field

As I have shown in Section 1.2, a homogeneous magnetic field does not, on its own, exert a net force on an isolated magnetic particle. However, in a system containing an ensemble of particles, each particle is subjected to an effective magnetic gradient resulting from the presence of its neighboring particles. This phenomenon is analogous to the magnetic gradient induced by localized magnetizable bodies within a homogeneous magnetic field (see Section 1.2), with the distinction that, in this case, the gradient is generated by multiple surrounding particles. An example of such a system is a ferrofluid, a suspension of single-domain ferromagnetic nanoparticles, stabilized by a molecular layer of dispersant in a non-magnetic carrier liquid [95]. Within a homogeneous magnetic field, these nanoparticles act as nanoscale permanent magnets whose orientation can be aligned with the external field. Due to interparticle dipole-dipole interactions, the particles tend to rearrange into a configuration that minimizes the system's overall energy.

Magnetic forces arise at the interface between the ferrofluid and the surrounding immiscible non-magnetic fluid when an external magnetic field is applied. The following is based on Ref. [95]. Assuming both fluids behave as inviscid, isothermal systems of constant composition, the momentum balance at the interface can be expressed as [95]

$$\mathbf{n} \cdot (\mathbf{T}_{\mathrm{M},2} - \mathbf{T}_{\mathrm{M},1}) - \mathbf{n} \cdot p_{\mathrm{C}} = 0, \tag{1.30}$$

where $\mathbf{n}$ is the unit normal vector to the interface, and $p_C = 2\mathcal{H}\gamma$ is the capillary pressure, with $\mathcal{H}$ denoting the arithmetic mean curvature and γ the interfacial tension. The magnetic stress tensors $\mathbf{T}_{M,1}$ and $\mathbf{T}_{M,2}$, which include both magnetic and pressure stress contributions, are evaluated in the magnetic and non-magnetic media adjacent to the interface, and are defined by the following expression [95]

$$\mathbf{T}_M = -\left(p^* + \frac{1}{2}\mu_0 H^2\right)\mathbf{I} + \mathbf{BH}, \tag{1.31}$$

where p^* is the composite pressure, μ_0 is the magnetic permeability of vacuum, $\mathbf{H}$ is the magnetic field strength, $\mathbf{I}$ is the identity matrix and $\mathbf{B}$ is the magnetic flux density. By substituting Eq. (1.31) into Eq. (1.30) for both fluids, applying boundary conditions for the magnetic field, and using the relation $\mathbf{B} = \mu_0(\mathbf{H} + \mathbf{M})$, we obtain the ferrohydrodynamic boundary equation in the absence of viscous stresses [95]

$$p_1^* + p_N = p_0 + p_C, \tag{1.32}$$

where p_0 is the ordinary pressure on the non-magnetic side, and p_N is the magnetic normal traction, defined as [95]

$$p_N = \mu_0 \frac{M_N^2}{2} \tag{1.33}$$

with M_N being the component of the magnetization vector normal to the interface. A schematic representation of the interfacial force balance is shown in Fig. 1.10.

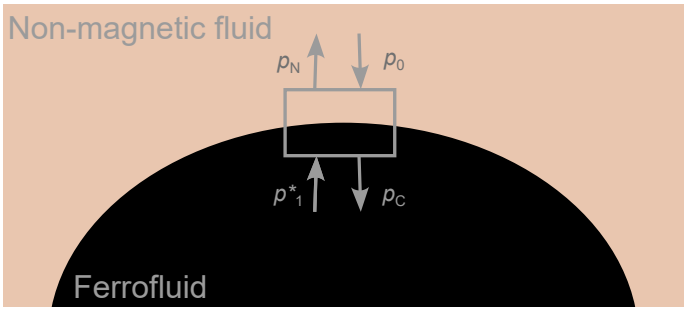

Figure 1.10. Schematic of force balance at the interface between a ferrofluid and a non-magnetic liquid.

When a small ferrofluid droplet is suspended in an immiscible non-magnetic liquid, it adopts a spherical shape at equilibrium to minimize surface free energy (see Fig. 1.11a). Upon application of a uniform external magnetic field, the magnetic nanoparticles within the droplet rearrange to minimize the combined surface and magnetic energies, causing the droplet to deform into an ellipsoid elongated along the field direction [96] (see Fig. 1.11b). This deformation induces a magnetic normal traction, p_N, on the droplet surface, generating

local force $\mathbf{F}$ wherever the magnetization vector $\mathbf{M}$ has a component normal to the interface. According to Eq. (1.33), the magnitude of this force is greatest at regions where the normal component of magnetization, M_{N}, is maximal; specifically where $\mathbf{M}$ aligns parallel or antiparallel to the applied magnetic field $\mathbf{B}$, as illustrated in Fig. 1.11b by the force vectors $\mathbf{F}$. These forces appear symmetrically on opposite sides of the droplet, forming a force dipole rather than producing a net force on the droplet as a whole.

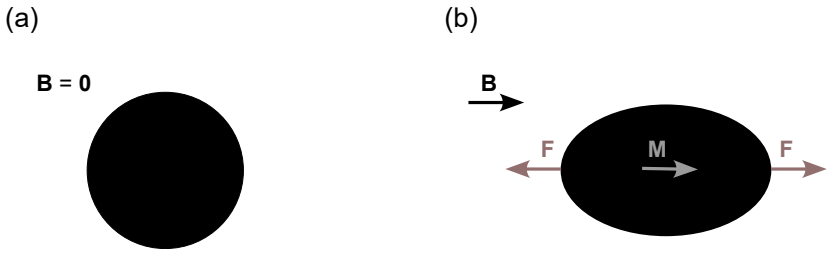

Figure 1.11. Schematics of (a) an undeformed ferrofluid droplet and (b) deformed ferrofluid droplet upon application of a uniform external magnetic field.

In Chapter 3 of this thesis, ferrofluid droplets are introduced into monolayers of biological cells to establish a platform for investigating mechanotransduction. At this stage, we provide theoretical calculations of the maximum forces these droplets can exert on the surrounding cells. In the experiments described in Chapter 3, the ferrofluid droplets generate magnetic traction on adjacent cells across the phase boundary, depicted by the blue-highlighted interface between the droplet and a representative cell in the schematic in Fig. 1.12, acting normal to the interface, as described by Eq. (1.10).

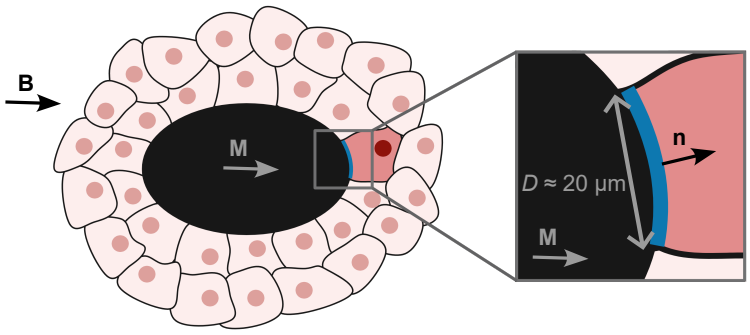

Figure 1.12. Schematic illustration of a ferrofluid droplet deformed under a uniform external magnetic field, exerting magnetic traction on adjacent cells.

To estimate the maximum force exerted on an individual cell, I assume the cell is positioned such that the local interface normal is approximately aligned with the applied magnetic field. For the ferrofluid formulation later used in the experiments (detailed in Chapter 3), the maximum magnetic traction can be calculated from Eq. (1.33), using magnetization data obtained via superconducting quantum interference device (SQUID) measurements (MPMS XL, *Quantum Design Inc.*), shown in Fig. 1.13a. The corresponding force on a single cell is then approximated by $F \approx p_{\mathrm{N}} A$, where $A \approx \pi \left(\frac{D}{2}\right)^2$ represents the estimated cell–droplet contact area, assuming a circular contact region with a cell diameter of $D = 20\,\mu\mathrm{m}$. The resulting force as a function of the applied magnetic field is shown in Fig. 1.13b. It is important to note that the forces shown in Fig. 1.13b represent idealized maximum values, as they are based on the simplifying assumption that the magnetization is normal to the entire cell-droplet interface, without integrating the magnetic normal traction over the interface area. Nevertheless, the estimated forces are substantially higher compared to those generated by magnetic nanoparticles or micropropellers discussed earlier in this chapter, owing also to the larger volume of magnetic material and the stronger magnetic fields involved, highlighting the potential of this platform to apply forces over larger areas on microscale objects.

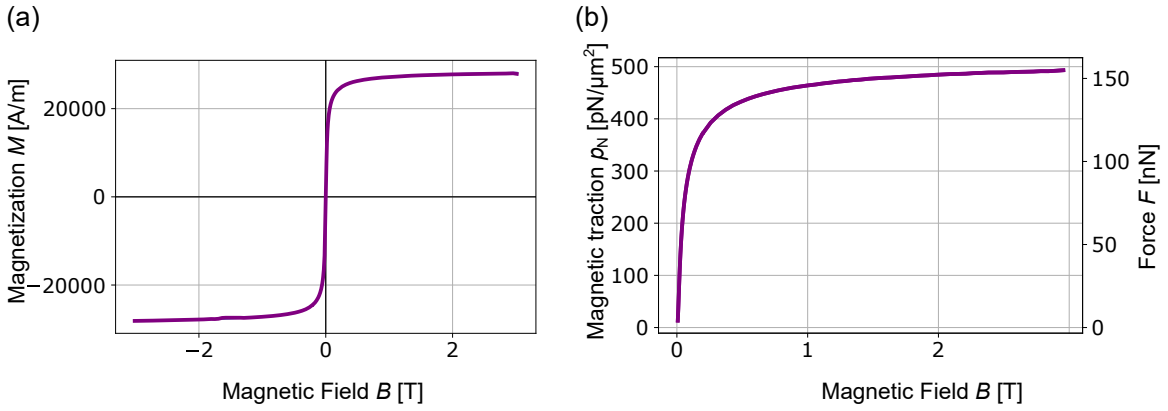

Figure 1.13. Force generation by homogeneous magnetic fields through ferrofluid droplets acting on surrounding cells: (a) magnetic characterization of the ferrofluid phase (ferrofluid silicon oil with lipids, formulation detailed in Chapter 3) used in the experiments of Chapter 3, measured by SQUID magnetometry; (b) calculated magnetic traction and resulting force exerted on a $20\,\mu\mathrm{m}$ cell as a function of the applied magnetic field.

1.5 Overview of Magnetic Force Generation at the Nano-/Microscale for Biomedicine

I have evaluated the magnetic forces achievable using various magnetic strategies and assessed the feasibility of magnetic targeting to cells both *in vitro* and *in vivo*. In particular, I conclude:

(i) Forces generated by magnetic field gradients decay rapidly with distance, making their effective range extremely limited. In particular, when using permanent magnets, the target object, such as a particle, must be positioned very close to the magnet's surface.

(ii) Gradient-based magnetic forces have been widely employed to guide nanoscale objects to cells in both *in vitro* and *in vivo* settings. While such strategies may be effective in carefully designed *in vitro* setups, their translation to *in vivo* applications remains largely unfeasible due to anatomical constraints and the limited scalability of magnetic gradients.

(iii) The proximity constraint to the permanent magnet can be partially bypassed by introducing a magnetizable body within the magnet's field. However, the target object must then be placed even closer to this magnetizable body to experience a significant force.

(iv) Thrust forces on helical propellers, generated by rotating magnetic fields, offer the key advantage of being independent of distance. Since low-amplitude rotating fields can be readily scaled to dimensions relevant to the human body, such systems represent promising candidates for targeted therapeutic applications.

(v) Homogeneous magnetic fields can induce dipole forces on ferrofluid droplets. Although such droplets are not suitable for incorporation into the human body, they can provide a valuable platform for investigating mechanotransduction processes in cell cultures.

Chapter 2

Measurement of the Magnetic Moment of a Single Particle in Liquid

Newtonian fluids provide an ideal system for analyzing and characterizing the motion of nano- and microscale objects, owing to their well-defined and easily quantifiable properties, such as viscosity. Their predictable behavior makes them an ideal medium for developing new measurement techniques and for quantitatively comparing such results with those obtained from other experimental approaches or theoretical models.

Author Contributions

I developed the experimental system to measure the magnetic moment of individual particles described in this chapter. I also fabricated the monodisperse magnetic particles used in this study, performed all magnetometry measurements presented in this chapter using a SQUID magnetometer and acquired the SEM images. I established the full analytical framework, and conducted the measurements and analyses on the monodisperse particles.

Later, together with Dr. N. Moreno Gómez, I extended the experiments to Janus particles functionalized with polymerosomes, which were fabricated by Dr. V. Mihali, Prof. Dr. C. Palivan, and colleagues at the University of Basel. We are currently preparing this work for publication under the title ”Multiplex Modular Nanorobots with Programmable Self-organization and Magnetic Control”.

Scope of the Chapter

In this chapter, I describe a method for quantifying the magnetic moment of single particles, which is based on direct single-particle velocity tracking in a custom-designed setup employing a magnetic field gradient. This method was used to characterize the magnetic moment of commercial magnetic particles, monodisperse microparticles and Janus particles functionalized with polymerosomes. For comparison, I also performed SQUID magnetometry, and converted the result to the average moment per particle.

Motivation

Advancing the mechanistic understanding of biological systems requires a thorough understanding of the relationship between applied forces and biological responses. In this regard, an essential prerequisite for accurately quantifying magnetic forces generated by any magnetic approach is the precise knowledge of the magnetic moment of the object of interest.

In order to establish a well-characterized platform that can support future developments in biomedical applications, I initially acquired commercially available magnetic particles. Specifically, I selected two types of 500-nm particles: SiMAG-Amine magnetic silica particles from *Chemicell* and cross-linked dextran iron oxide fluorescent composite particles from *Micromod*. However, both particle types exhibited considerable variability in size and morphology (Fig. 2.1a-b), resulting in substantial heterogeneity in their magnetic moments at the single-particle level. Conventional magnetic characterization techniques, such as superconducting quantum interference device (SQUID) magnetometry, provide only ensemble-averaged estimates of magnetic properties (see Fig. 2.1c), offering limited insight into particle-to-particle variability.

To develop a robust model system, particularly for use in more complex environments beyond simple Newtonian fluids, two critical components are required: (i) monodisperse magnetic particles with uniform magnetic moments, enabling predictable and reproducible force responses; and (ii) a measurement method capable of determining magnetic moments at the single-particle level, overcoming the limitations of bulk-averaged techniques like SQUID magnetometry.

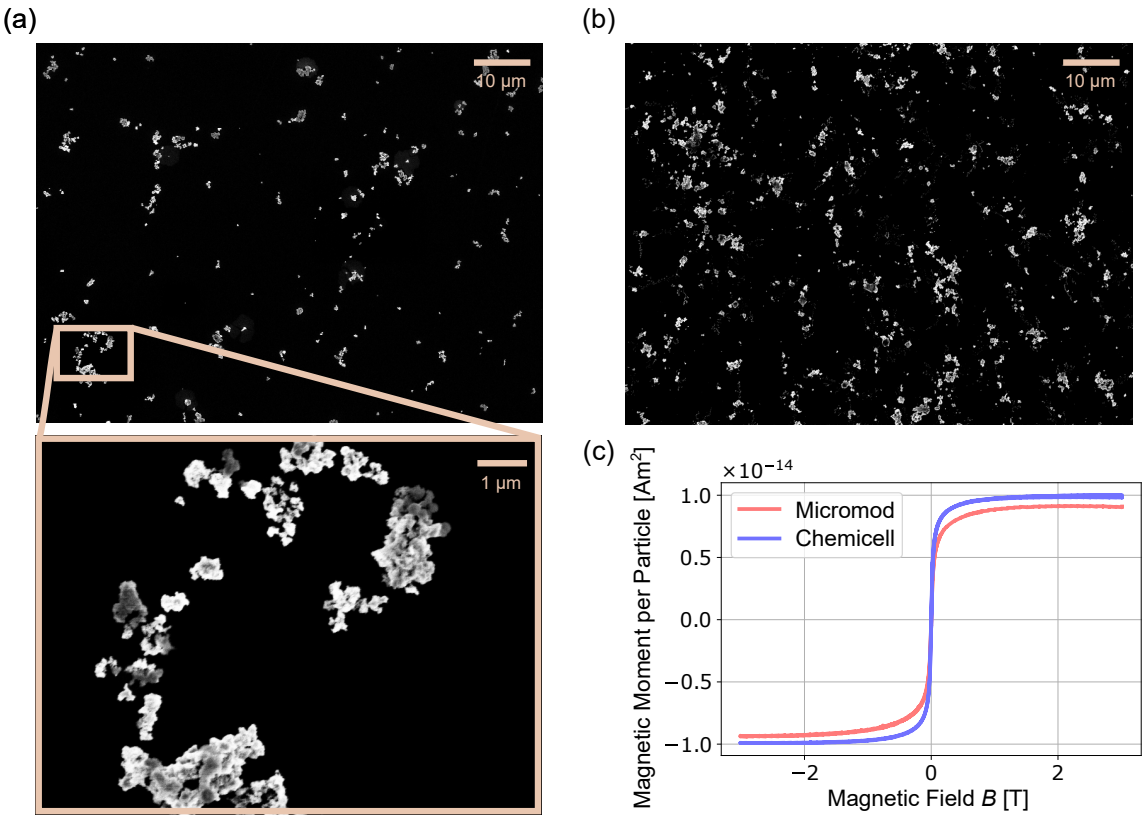

Figure 2.1. Characterization of commercial 500-nm magnetic particles: scanning electron microscopy (SEM) images of (a) SiMAG-Amine magnetic silica particles from *Chemicell* and (b) cross-linked dextran iron oxide fluorescent composite particles from *Micromod*; (c) SQUID measurements showing the average magnetic moment per particle as a function of the applied magnetic field, converted from the bulk magnetometry data using manufacturer-reported particle concentrations.

2.1 Magnetic Particles Fabricated via Glancing Angle Deposition

To ensure uniformity and reproducibility, I fabricated magnetic particles in-house using glancing angle deposition (GLAD).

GLAD is a physical vapor deposition technique in which vapor-phase atoms condense onto a substrate, similar to conventional thin-film deposition, but with the substrate tilted at a steep (glancing) angle α relative to the incoming flux (see Fig. 2.2a), creating an oblique deposition geometry [97, 98]. Upon reaching the substrate, atoms spontaneously form microscopic nuclei, preferentially at sites of defects such as impurities, point defects, and edge defects [97, 98]. Due to the high-vacuum conditions during growth, the atomic flux follows nearly straight, unscattered trajectories, causing regions behind these initial nuclei to receive significantly less material [97, 98]. As a result, the ballistic shadowing confines further deposition to exposed surfaces, producing tilted columnar structures aligned with the incident vapor direction [97, 98]. Moreover, by rotating the substrate (see the angle φ in Fig. 2.2a), the column growth direction can be dynamically manipulated, allowing for the sculpting of nanostructures into a variety of complex shapes [97, 98]. Enhancing structural uniformity of such structures requires precise control over the initial nucleation phase [97, 98]. Predefined nucleation sites and thus periodical shadowed regions can be achieved by introducing a regular microscale topography prior to deposition (see Fig. 2.2b) [97, 98]. Such pre-patterning can be performed on flat substrates using techniques such as Langmuir–Blodgett (LB) deposition, which enables the assembly of monolayers composed of micro- or nanoparticles, most commonly silica or polystyrene. Silica particles employed for LB patterning typically range around $\approx 500\,\mathrm{nm}$, but can be as small as $\approx 20\,\mathrm{nm}$ [99–101], while polystyrene particles are commonly used at sizes around $1\,\mu\mathrm{m}$, with smaller variants available for seeding down to approximately $350\,\mathrm{nm}$ [102, 103]. Alternatively, block copolymer micelle lithography (BCML) enables the fabrication of well-ordered arrays of metal nanoparticles typically ranging from 3 to $15\,\mathrm{nm}$ in size [104, 105], which can be enlarged up to $\approx 50\,\mathrm{nm}$ via an electroless growth step [105–108]. By precisely engineering the geometry and periodicity of these seed layers, one can fabricate highly ordered nanostructure arrays with accurate control over both size and spatial arrangement [109].

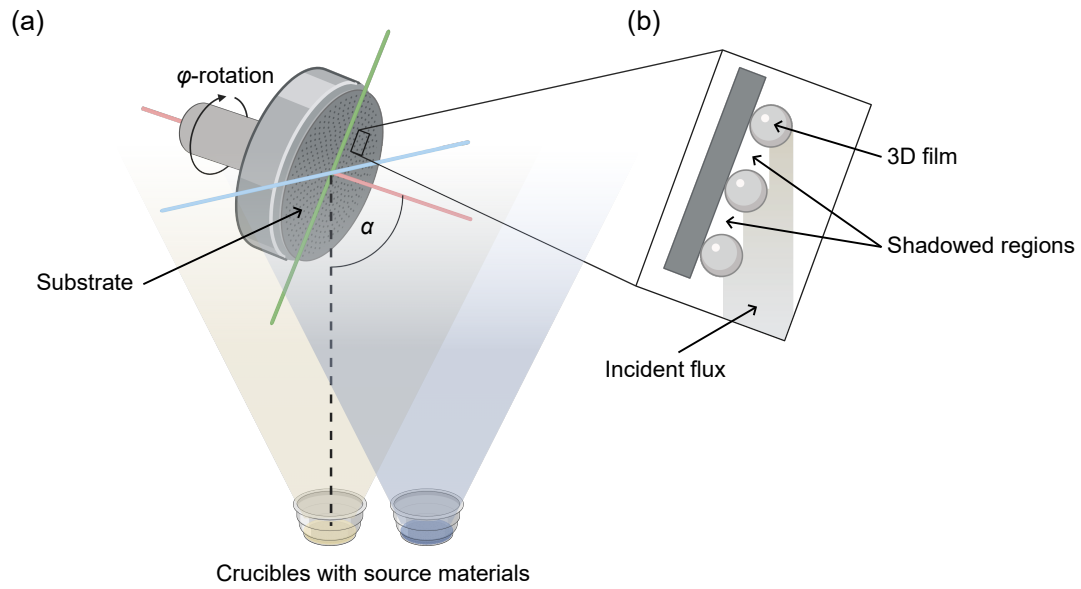

Figure 2.2. Schematic illustration of microstructure fabrication using glancing angle deposition (GLAD): (a) Vapor-phase atoms are emitted from crucibles and condense onto a substrate tilted at a steep angle α with respect to the incident flux; (b) zoom-in of the deposition process on a pre-patterned 3D film. The oblique deposition geometry leads to ballistic shadowing, confining material growth to the upper surfaces of the 3D structures while suppressing deposition in shadowed regions.

To fabricate the monodisperse magnetic particles used in this study, I employed a hexagonally close-packed monolayer of silica beads with a diameter $2b \approx 500\,\mathrm{nm}$ (see Fig. 2.3a) as a templated seed layer, prepared via Langmuir–Blodgett deposition on a Si wafer by C. Miksch, as described elsewhere [99]. The patterned substrate was then transferred to a vacuum chamber for glancing angle deposition (GLAD) at a base pressure of $10^{-6}\,\mathrm{mmHg}$. A thin Ti adhesion layer was first grown, followed by Ni deposition with fast φ-rotation at a glancing incidence angle of $\alpha = 80°$ (see Fig. 2.3b). The nominal Ni deposition length was $800\,\mathrm{nm}$; however, due to the oblique incidence geometry at glancing angle $\alpha = 80°$, this does not correspond to the actual deposited thickness, which is about $420\,\mathrm{nm}$ based on SEM imaging (see Fig. 2.3c). The correction factor between the thickness registered by quartz crystal and the film height is used to determine a ”tooling factor”.

To further investigate the magnetic properties of the sample, I employed SQUID magnetometry. In order to extract the magnetic moment per particle, I utilized the fact that the silica beads are arranged on the substrate in a hexagonal close-packed configuration. In this lattice, each unit hexagonal cell effectively contains three particles, as illustrated in Fig. 2.3a. Given the geometry of the hexagonal lattice, the area of a unit cell is given by $\frac{3\sqrt{3}(2b)^2}{2}$, where $2b \approx 512\,\mathrm{nm}$ is the center-to-center distance between adjacent beads. From this, the areal density of particles,

$$N_\mathrm{A} = \frac{3\ \text{particles}}{\frac{3\sqrt{3}(2b)^2}{2}} \approx 4.4 \cdot 10^6\ \text{particles/mm}^2. \tag{2.1}$$

Using the known area of the sample measured in the SQUID, I computed the average magnetic moment per single particle (see Fig. 2.3d and e). In contrast to the irregular commercial particles (Fig. 2.1), the monodispersity of my fabricated particles eliminates uncertainty associated with size distribution. Nevertheless, due to the large number of particles (millions) measured simultaneously, collective effects such as interparticle interactions are inherently included in the measured response.

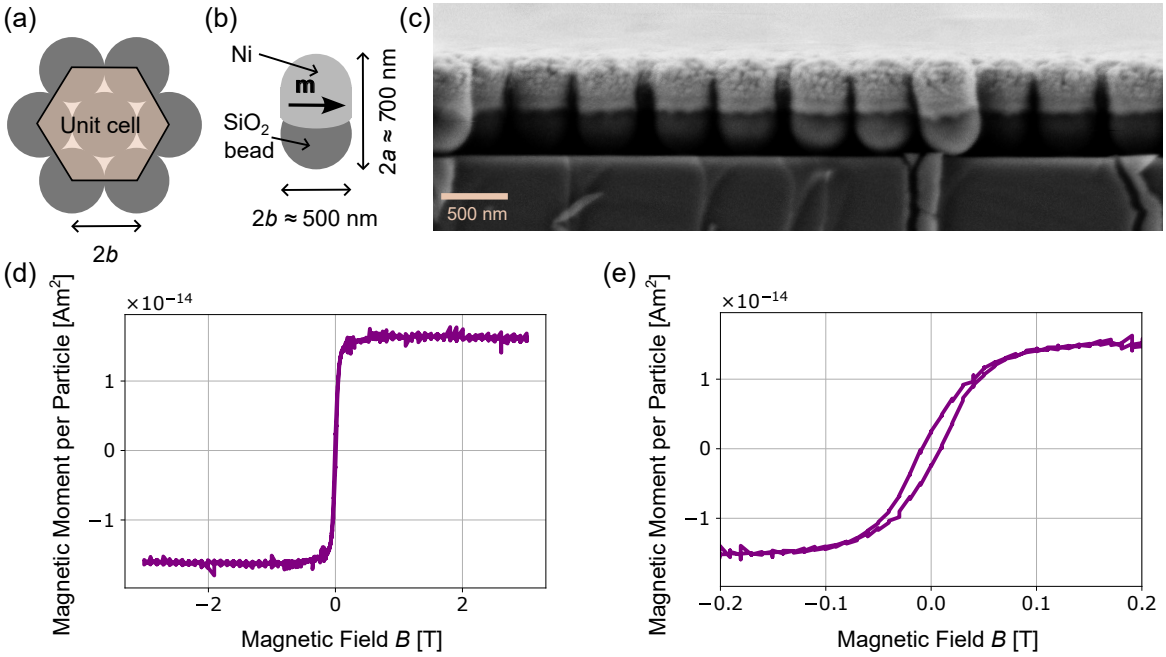

Figure 2.3. Characterization of monodisperse Ni particles fabricated via GLAD: (a) schematic representation of a single Ni particle, consisting of a silica bead and a deposited Ni segment (Ti adhesion layer not shown); (b) SEM image of Ni particles deposited on a Si substrate; (c) SQUID magnetometry data showing the average in-plane magnetic moment per particle as a function of applied magnetic field; (d) magnified view of the hysteresis loop from (c).

To access the magnetic behavior of individual particles while minimizing collective effects, I designed a custom magnetic field gradient setup, fitted onto the microscope stage of an inverted fluorescence microscope. The system consists of a Helmholtz coil pair, which in its basic configuration generates a homogeneous magnetic field between the coils. To introduce a controlled magnetic field gradient, an iron core was inserted into one of the coils (see Fig. 2.4a). The core transitions from a cylindrical shape within the coil to a truncated conical tip directed toward the center between the coils, thereby concentrating the magnetic field and producing a localized gradient at the midpoint. Although the truncation reduces the maximum achievable field gradient, it also ensures a slower spatial variation of the gradient, which facilitates more accurate force calculations during magnetic moment measurements.

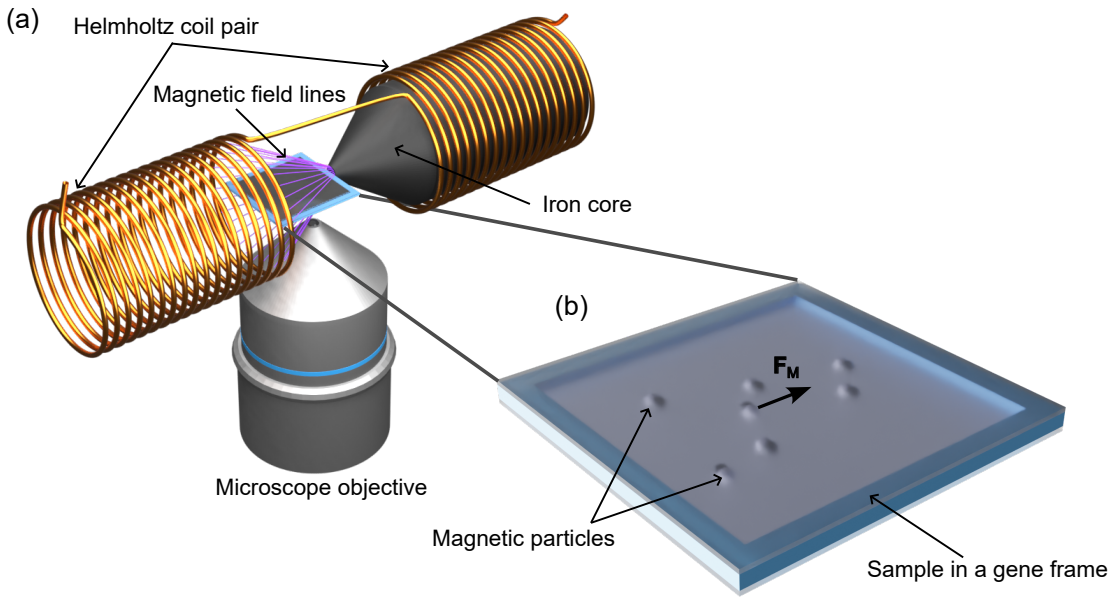

Figure 2.4. Schematic representation of the experimental setup used to determine the magnetic moment of individual particles: (a) a Helmholtz coil pair with an iron core, generating a controlled magnetic field gradient; (b) enlarged view of the sample within the Gene frame, illustrating particle motion along the direction of the applied magnetic gradient.

The magnetic field was generated by applying a DC voltage of 2.5 V to a power supply connected through a 10× voltage amplifier. Characterization of the magnetic field was performed using a Hall probe mounted on a precision mechanical manipulator. The vertical position corresponding to the intended sample location was first identified. Subsequently, the probe was aligned horizontally with the tip of the iron core, and measurements were taken while retracting the probe along the axis of the core. At each position, the magnetic field was recorded. The magnetic field gradient was computed as the finite difference between consecutive field measurements. In addition, a fifth-degree polynomial was fitted to the magnetic field data to produce a smooth, monotonically decreasing profile. This fitted

curve was then also used to compute the gradient. Both the measured data and fitted curves for the magnetic field and its gradient are shown as functions of distance in Fig. 2.5.

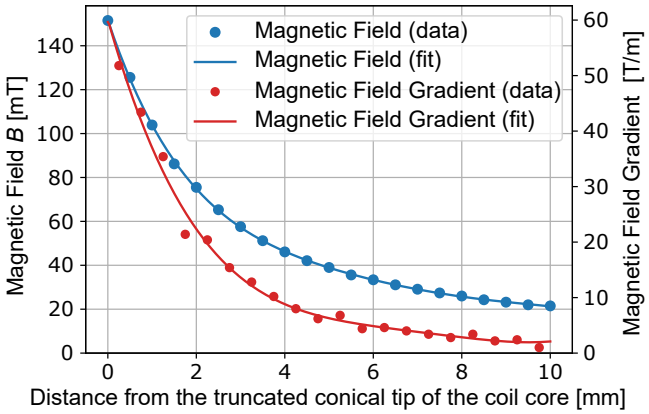

Figure 2.5. Characterization of the magnetic gradient setup depicted in Fig. 2.4. The plot shows the absolute magnitude of the magnetic field and its spatial gradient as functions of the distance from the truncated tip of the iron core. Experimental data points are presented alongside smooth curves obtained through polynomial fitting.

To magnetize the particles, a small section of the wafer was cut and exposed to an in-plane magnetic field of $1.8\,\mathrm{T}$, generated by an electromagnet at its center. This magnetized wafer piece was then placed in water and sonicated for 1 minute, allowing the magnetic particles to detach and disperse into the solution. The particle concentration of such a solution was approximately $2 \cdot 10^4\ \mathrm{particles/\mu l}$ to minimize aggregation. For observation, a chamber was assembled using a base cover slip and a modified Gene frame. The standard (10 × 10 × 0.25) mm^3 Gene frame was trimmed along the sides to reduce the distance between the truncated conical tip and the observation area, yielding a final tip-to-sample spacing of $d = 6.5\,\mathrm{mm}$. A volume of 25 µl of the particle suspension was pipetted into the chamber, after which a second cover slip was placed on top to seal the chamber.

The sample was subsequently mounted between the Helmholtz coil pair, positioned above the microscope objective, using a custom-designed 3D-printed holder. Upon application of the magnetic field, I recorded the directed motion of particles toward the truncated conical tip using bright-field microscopy. Image acquisition was performed with a 63× objective lens and a high-resolution camera at a frame rate of $15\,\mathrm{frames/s}$, integrated into the microscope system.

Particle velocity tracking was performed using the *trackpy* library in *Python 3.10.9*, as described in detail elsewhere [110]. In brief, particle-like features were initially identified in the first frame by estimating a characteristic size of approximately 27 pixels (Fig. 2.6a). Subsequently, feature parameters such as brightness were refined to distinguish genuine particles from artifacts and bigger clusters (Fig. 2.6b). Subpixel localization accuracy was then verified, and similar procedures were applied to detect features in all subsequent frames. To construct particle trajectories, features were linked across frames with a maximum allowed displacement of 15 pixels per frame, while accounting for the possibility of missed detections. Only trajectories persisting for a minimum of 10 consecutive frames were retained for further analysis. Representative trajectories are shown in Fig. 2.6c.

Subsequently, I wrote a custom *Python* script to extract instantaneous velocities from the recorded trajectories. For each particle, the velocity components in the parallel and orthogonal directions to the magnetic field were computed as the frame-to-frame positional differences, multiplied by the frame rate and the conversion factor from pixel units to micrometers. Given that the imaged region is small relative to the spatial scale over which both the magnetic field and its gradient vary at a distance of $d = 6.5\,\mathrm{mm}$ from the truncated conical tip, it is reasonable to approximate both the field and its gradient as uniform within the field of view. The average velocity of each particle was subsequently determined in both directions, and the resulting velocity distributions were visualized as histograms. The histogram of velocity components perpendicular to the magnetic field direction was symmetric about zero (data not shown), indicating no net drift. In contrast, the velocity distribution along the direction of the magnetic field reveals multiple distinct peaks (Fig. 2.6d). The first peak, centered around zero, is attributed to immobile particles and stationary artifacts within the imaging system.

Next, I analyzed the subsequent peaks in the velocity histogram, labeled v_1, v_2, v_3, and v_4 in Fig. 2.6d, which exhibit progressively decreasing heights. These peaks correspond to velocity ranges of 6 µm/s–7 µm/s, 12 µm/s–13 µm/s, 17 µm/s–18 µm/s, and 24 µm/s–25 µm/s, respectively. The consistent velocity differences between successive peaks, approximately 5 µm/s to 7 µm/s, suggest discrete steps in particle mobility. Given the high degree of monodispersity of the magnetic particles, I hypothesize that the secondary peaks v_2, v_3 and v_4 correspond to clusters containing two, three, and four particles, respectively (Fig. 2.6e), with their velocities scaling approximately with the total magnetic moment of the cluster.

To quantify the magnetic moments associated with the velocity peaks and to test this hypothesis, I analyzed the balance of forces acting along the direction of the applied magnetic field, hereafter denoted as the y-axis. At low Reynolds numbers, the magnetic force is balanced by the viscous drag force

$$F_{\mathrm{M},y} + F_{\mathrm{D},v_y} = 0. \tag{2.2}$$

Substituting the expressions for the magnetic and drag forces from Eqs. (1.5),(1.6), and (1.7) into Eq. (2.2), we obtain

$$m\frac{\partial B_y}{\partial y} = Av_y, \tag{2.3}$$

where m is the magnetic moment of the moving object, $\frac{\partial B_y}{\partial y}$ is the magnetic gradient along the magnetic field direction and v_y denotes the velocity associated with a specific peak in the velocity histogram (Fig. 2.6d). The particles are well approximated by ellipsoids, for which the friction coefficient A in Eq. (2.2) has an established analytical expression [89]. In this context, I considered the friction coefficient for a prolate ellipsoid. However, unlike the case of helix motion aligned with the major axis (as in Eq. (1.20)), the Ni particles are magnetized in the in-plane direction, which corresponds to the minor axis of the ellipsoid. As a result, the relevant friction coefficient A is given by [89]

$$A = A_{\mathrm{E}} = \frac{32\pi\mu\,(a^2 - b^2)}{\frac{4a^2-6b^2}{\sqrt{a^2-b^2}}\ln\frac{a+\sqrt{a^2-b^2}}{b} + 2a}, \tag{2.4}$$

where a and b the semi-major and semi-minor axes of the ellipsoid, respectively, and μ the dynamic viscosity of the fluid. Using a magnetic gradient of $\frac{\partial B_y}{\partial y} = 4.3\,\mathrm{T/m}$, obtained from the magnetic field gradient fit in Fig. 2.5 at the distance $d = 6.5\,\mathrm{mm}$ from the truncated conical tip, along with the water viscosity $\mu = 10^{-3}\ \mathrm{Pa\,s}$, and the geometric dimensions $2a = 700\,\mathrm{nm}$ and $2b = 512\,\mathrm{nm}$, the magnetic moment m of the moving object corresponding to each velocity peak can be directly calculated from Eq. (2.2).

In the following analysis, I first focus on the most prominent non-zero peak in the velocity histogram, specifically the bin ranging from 6 µm/s to 7 µm/s, centered at $v_1 \approx 6.75\,\mu\mathrm{m/s}$ (see Fig. 2.6d). Using this velocity in Eq. (2.3), I calculate the corresponding magnetic moment as $m_1 = 8.7 \cdot 10^{-15}\ \mathrm{Am^2}$. This result can be directly compared to the value obtained from SQUID magnetometry, shown in Fig. 2.3e. The average magnetic moment per particle measured at $B = 31.1\,\mathrm{mT}$ (the field magnitude at the distance $d = 6.5\,\mathrm{mm}$ from the truncated conical tip, extracted from the magnetic field fit in Fig. 2.5) acquired using SQUID is $m_{\mathrm{SQUID}} = 9.2 \cdot 10^{-15}\ \mathrm{Am^2}$. Given the close agreement between m_1 and m_{SQUID}, I can reasonably conclude that the velocity peak at $v_1 = 6.75\,\mu\mathrm{m/s}$ corresponds to the motion of a single Ni particle. It is important to remember that while m_{SQUID} is slightly higher, this value represents an ensemble average over more than $> 10^6\ \mathrm{particles}$ and thus includes contributions from interparticle magnetic interactions. In contrast, the magnetic moment m_1, obtained via velocity tracking, reflects the behavior of an individual particle, effectively isolating it from such interactions.

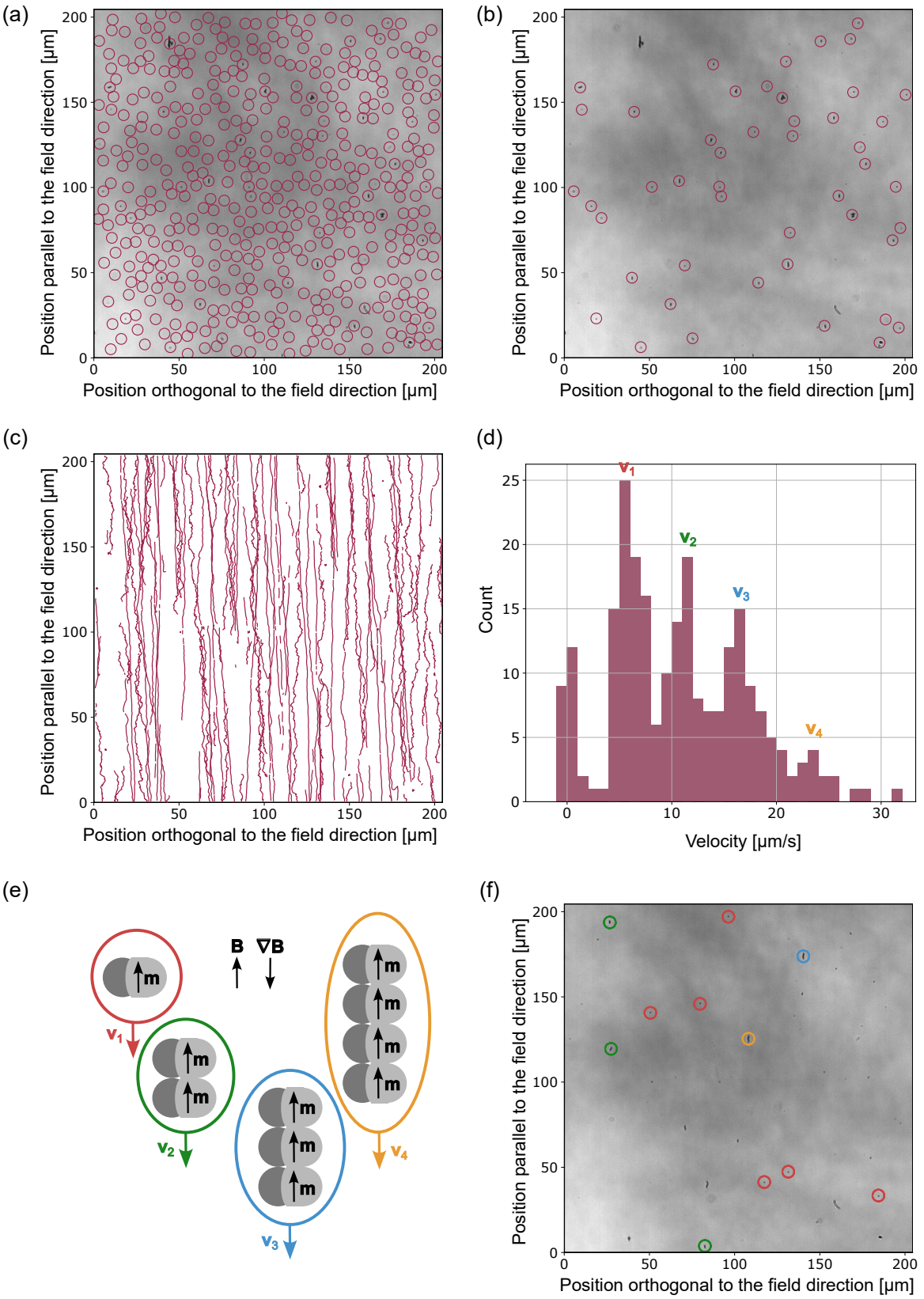

Figure 2.6. Analysis of particle velocity tracking: (a) initial identification of particle-like features in the raw image data; (b) refinement of detected features by filtering out imaging artifacts and larger particle clusters; (c) reconstruction of particle trajectories; (d) histogram of particle velocities along the direction of the magnetic field, with distinct peaks corresponding to different cluster types, color-coded as in (e);

Figure 2.6. (Continued) (e) schematic of a single particle and clusters (doublets, triplets, quadruplets), used for classification and interpretation of velocity data; (f) classification of particles into single units, doublets, triplets, and quadruplets, color-coded as shown in (e).

For the higher-order peaks in the velocity histogram, labeled v_2, v_3, and v_4, Eq. (2.3) shows that the velocity scales linearly with the magnetic moment, assuming a constant magnetic gradient and friction coefficient. Indeed, for elongated particle chains aligned along the magnetic field direction (Fig. 2.6e), the total magnetic force increases proportionally with the number of particles in the cluster, while the hydrodynamic drag remains approximately constant, as it is primarily determined by the cluster's cross-sectional area perpendicular to the flow [111]. This implies that the velocity of such clusters is roughly proportional to their total magnetic moment. The velocity peaks at v_2, v_3, and v_4 thus likely correspond to doublets, triplets, and quadruplets of particles, respectively. This interpretation is further supported by the visual classification in Fig. 2.6f, where colored markers denote clusters of increasing size corresponding to progressively higher velocity bins: 6 µm/s–7 µm/s (red), 12 µm/s–13 µm/s (green), 17 µm/s–18 µm/s (blue), and 24 µm/s–25 µm/s (yellow).

Overall, I demonstrated that monodisperse magnetic particles can be reliably fabricated using GLAD, establishing a robust platform for future studies in complex media where precise control of magnetic forces is essential. Furthermore, I developed and validated a technique for measuring the magnetic moment at the single-particle level. In the following section, this method will be applied to characterize more complex magnetic structures.

2.2 Loaded Polymer Magnetic Janus Particles

Together with Dr. N. Moreno Gómez, I repeated the experiments using Janus particles functionalized with polymerosomes loaded with the fluorescent dye, provided by our collaborators Dr. V. Mihali, Prof. Dr. C. Palivan *et al.*. These polymersomes were engineered by the Palivan's group to encapsulate diverse molecular payloads, including drugs and enzymes, making the resulting hybrid constructs attractive candidates for theranostic applications. The Janus particles feature a dual-lobed core synthesized via seeded emulsion polymerization, allowing selective functionalization of each lobe. One lobe was functionalized with iron oxide nanoparticles to confer magnetic properties, while the other was conjugated with single-stranded DNA. Polymersomes were assembled from amphiphilic block copolymers in the presence of the fluorescent dye Atto488 and functionalized with complementary single-stranded DNA. The final hybrid structures were formed through DNA hybridization, resulting in magnetic Janus particles tethered to dye-loaded polymersomes.

We first characterized the magnetic Janus particles without attached polymersomes. I performed SQUID magnetometry, and the average magnetic moment per particle was estimated based on particle concentrations obtained from dynamic light scattering (DLS) (see Fig. 2.7b). The resulting magnetic moment per particle was approximately $25\times$ lower than that of GLAD-fabricated Ni particles and about $15\times$ lower than that of commercial magnetic particles (compare Figs. 2.1c and 2.3d), presenting a challenge for subsequent velocity tracking. Since the Janus particles exhibited no remanent magnetization, no pre-magnetization step was required; particles were simply sonicated prior to the experiment. The particle motion under a magnetic field gradient was recorded using bright-field microscopy, and subsequent analysis performed in *Python* yielded the velocity distribution shown in Fig. 2.7c. To determine the peak velocity, negative velocities — attributable to noise — were excluded, and the remaining data were fitted with a truncated normal distribution. The peak velocity was found to be $v_{\mathrm{J}} = 1.36\,\mu\mathrm{m/s}$, with a standard deviation of 1.42 µm/s. As the orientation of the particles during motion was unknown (due to the absence of prior magnetization), we considered two cases, both approximating the Janus particles as prolate ellipsoids with dimensions $2a = 350\,\mathrm{nm}$ and $2b = 225\,\mathrm{nm}$. Assuming motion along the minor axis $2b$, similar to the behavior observed for Ni particles (see Fig. 2.6f), the friction coefficient was estimated using Eq. (2.4), yielding a magnetic moment of $m_b = 8.1 \cdot 10^{-16}\,\mathrm{Am}^2$. Alternatively, for motion along the major axis $2a$, the corresponding estimate using Eq. (1.20) resulted in $m_b = 7.3 \cdot 10^{-16}\,\mathrm{Am}^2$. Both estimates exceed the magnetic moment determined by SQUID, $m_{\mathrm{SQUID}} = 2.6 \cdot 10^{-16}\,\mathrm{Am}^2$ at an applied field of $B = 31.1\,\mathrm{mT}$. We attribute this discrepancy primarily to uncertainties in concentration estimates derived from DLS, which are known to exhibit significant variability, often spanning up to an order of magnitude due to factors such as particle aggregation and assumptions regarding scattering properties.

We then repeated the experiment and analysis for Janus particles attached to Atto488-loaded polymersomes. Taking advantage of the fluorescence emitted by Atto488, we tracked particle motion using fluorescence microscopy, which significantly improved signal clarity and reduced background noise compared to the bright-field-based analysis performed previously. Trajectories of five selected tracked particles are shown in Fig. 2.7d, and the corresponding velocity distribution is presented in Fig. 2.7e. The velocity histogram was fitted with a normal distribution, yielding a peak velocity of $v_{\mathrm{J-P}} = 3.45\,\mu\mathrm{m/s}$ and a standard deviation of 1.03 µm/s. Interestingly, the velocity of the Janus–polymersome hybrids ($v_{\mathrm{J-P}}$) exceeds that of the Janus particles alone (v_{J}), which is counterintuitive given the increased hydrodynamic drag associated with the larger particle size and unchanged magnetic driving force. We attribute this effect to pronounced particle clustering, likely caused by the omission of the sonication step prior to the experiment, which was avoided to preserve the structural integrity of the sensitive hybrid particles.

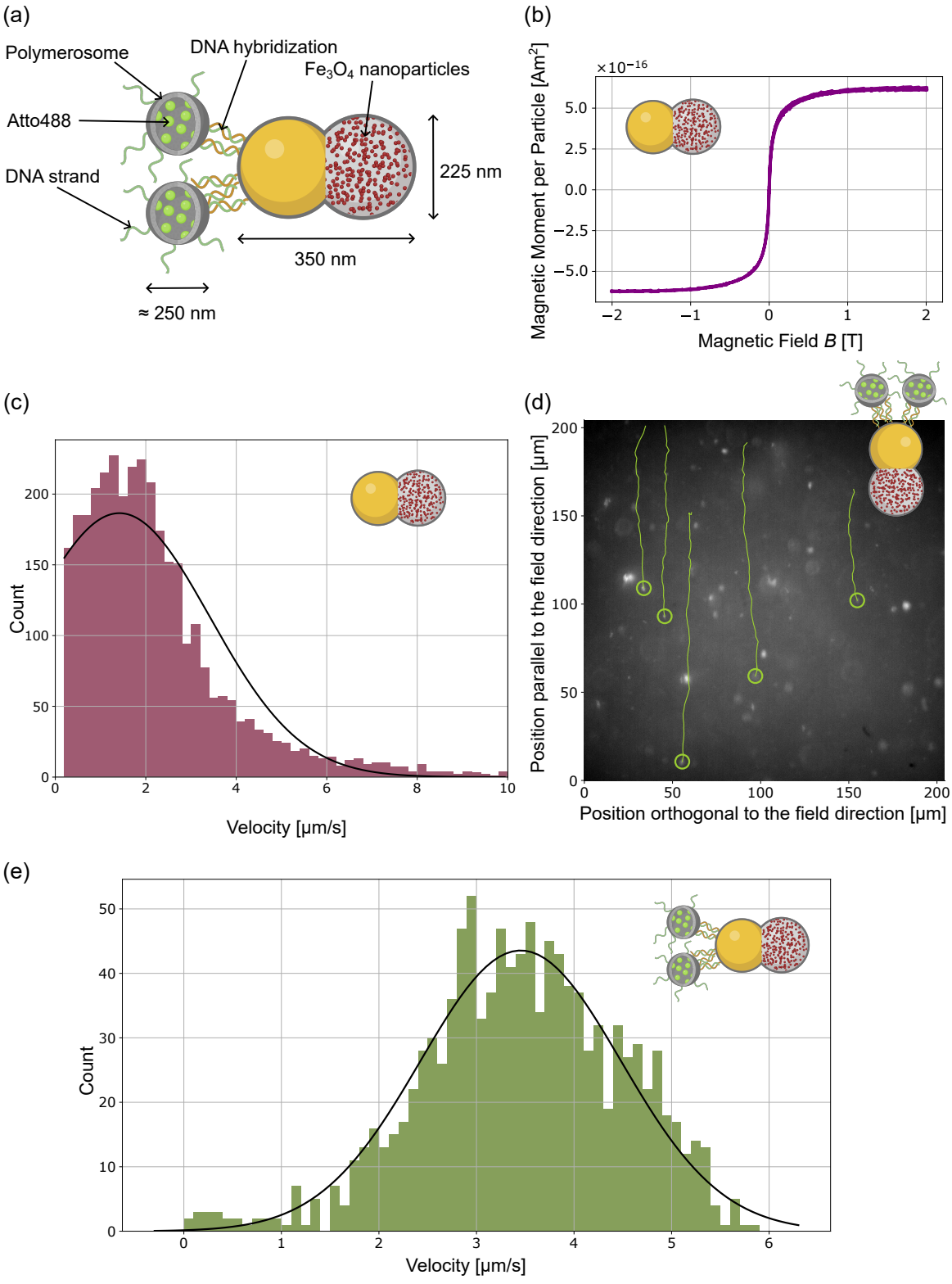

Figure 2.7. Magnetic characterization of Janus particles: (a) schematic illustration of hybrid Janus particles with attached Atto488-loaded polymersomes; (b) magnetometry results showing the average magnetic moment per Janus particle (without polymersomes), measured using SQUID; (c) velocity histogram of Janus particles without polymersomes, fitted with a truncated normal distribution; (d) fluorescence image showing trajectories of five representative Janus particles with attached fluorescent polymersomes; (e) velocity histogram of Janus particles with Atto488-loaded polymersomes, fitted with a normal distribution.

2.3 Overview of Magnetic Moment Measurements at the Single-Particle Level

After investigating methods to deduce the magnetic properties of individual magnetic particles, I conclude that:

(i) The magnetic moment per particle can be evaluated using two complementary approaches. Conventional SQUID magnetometry provides the average magnetic moment per particle, including interparticle interactions. In contrast, the method of velocity tracking in a well-characterized magnetic field gradient that I developed allows estimation of the magnetic moment at the single-particle level. Although this approach yields information at a fixed value of the magnetic field used during the experiment, it is more relevant for motion, as it characterizes particle behavior in solution and accounts for the hydrodynamic radius.

(ii) Commercial magnetic particles exhibit a broad size distribution, and consequently a wide range of magnetic moments. This variability limits their applicability in experiments that require precise control over magnetic forces. The continuous velocity distribution in Fig. 2.8 reflects this heterogeneity, with the absence of discrete peaks indicating the wide spread in magnetic properties among the particles.

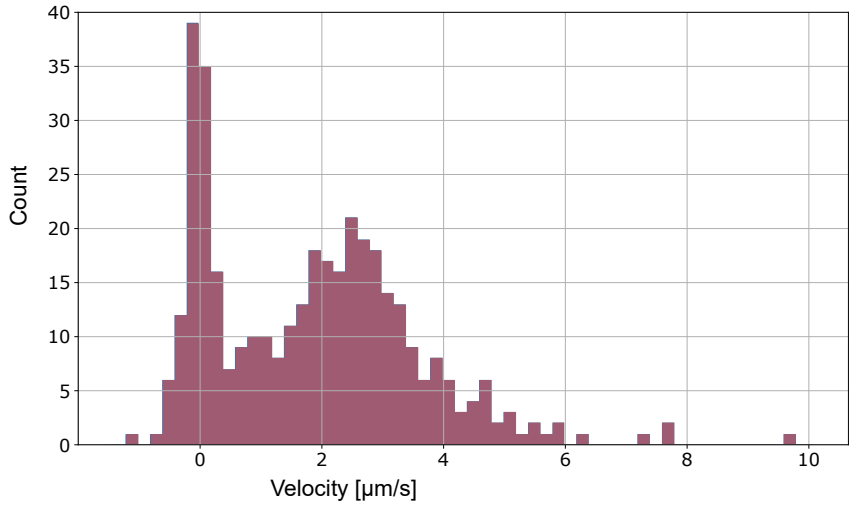

Figure 2.8. Histogram of particle velocities along the magnetic field direction for the cross-linked dextran-coated iron oxide fluorescent composite particles from *Micromod* (refer to Fig. 2.1b). The continuous velocity distribution reflects the polydispersity in size and magnetic moment of the particles.

(iii) I fabricated monodisperse particles fabricated via glancing angle deposition (GLAD) that display discrete velocity distributions, reflecting consistent and uniform magnetic moments across individual particles. This high degree of uniformity enables well-controlled experiments, where applied magnetic forces can be directly correlated with observed particle transport behavior in more complex environments.

(iv) Magnetic velocity tracking remains feasible even for particles with relatively low magnetic loading, such as Janus particles bearing iron oxide nanoparticles on a single lobe. However, the low magnetic signal complicates the separation of magnetically driven motion from experimental artefacts, as the velocity histogram does not clearly separate from zero velocity. Moreover, hybrid organic–inorganic structures, such as Janus particles functionalized with Atto488-loaded polymersomes, are prone to clustering and likely exhibit collective motion, which precludes reliable determination of the magnetic moment at the single-particle level. Nonetheless, we demonstrate that magnetic velocity tracking can still be performed using fluorescence microscopy, which enables selective identification of magnetic, fluorescently labelled particles while excluding non-magnetic debris.

Chapter 3

Magnetic Force Generation in Cell Culture Environments

Externally controlled mechanical cell stimulation and manipulation are garnering interest within the molecular and cell biology community, as they offer a means to advance the mechanistic and physiological understanding of cellular processes. To influence biological processes at the molecular level, particularly those involving membrane proteins, forces on the order of several piconewtons are typically required. Higher force thresholds are necessary for manipulating entire cells, especially within densely packed monolayers. In addition, materials used for force generation must preserve cell viability and seamlessly integrate with conventional cell culture conditions. Therefore, careful consideration must be given to the design of both the actuation stimuli and the materials used for this purpose, ensuring reliable performance without compromising the cellular environment.

Author Contributions

The first section of this chapter, detailing the synthetic magnetic cell platform, was done in collaboration with Dr. S. Pashapour and Dr. J. De Lora, who developed the synthetic magnetic cells used in this study and who were leading the cell-based experiments. Together with Dr. J. De Lora, we carried out droplet deformation experiments in various media and performed measurements of interfacial tension and rheological properties using established techniques. Independently, I adapted and characterized the magnetic setup for our specific applications and microscope, based on an original design and fabrication by Dr. B. Miksch for a different purpose. With assistance from E. Oren, I characterized the temporal response of the magnetic setup. I also performed numerical simulations, carried out the magnetic characterization of the system, performed droplet shape analysis, and analyzed and interpreted material property data obtained through multiple characterization methods.

I also performed estimations of the magnetic force and pressure acting on both the synthetic magnetic cells and neighboring native cells. The manuscript detailing this work is in its final stages and is titled, “Building mechanoresponsive hybrid cell cultures comprising E-Cadherin functionalized synthetic magnetic cells (symcells) and natural cells”.

The second section of this chapter involves clearly defined contributions. The project has been led by H. K. Senapati at the Max Planck Institute (MPI) for Medical Research. Magnetic particles were synthesized and characterized by K. Noh and H. Joo at the Center for Nanomedicine, Institute for Basic Science (IBS), South Korea. I conducted the finite element simulations to evaluate various magnetic configurations, identifying the optimal design based on both macro- and microscale spatial constraints. I also performed quantitative estimations of the magnetic forces acting on cells within the selected configuration. The magnetic setup was fabricated by the mechanical workshop at the MPI in Stuttgart. Magnetometry measurements of the cobalt wire were performed by Prof. Dr. E. Goering at the MPI for Solid State Research. All experiments investigating the control of sprouting behavior using the developed magnetic system, including parylene coating, were carried out by H. K. Senapati. The overall project design and results were discussed with S. Seneca, Prof. Dr. P. Fischer, and, regarding the cellular aspects, with Dr. I. Platzman and Prof. Dr. J. Spatz. This work will be included in a forthcoming manuscript led by H. K. Senapati.

Scope of the Chapter

This chapter explores two magnetic strategies for exerting mechanical stimulation and manipulation of cells *in vitro*.

The first strategy employs homogeneous magnetic fields in combination with ferrofluid-based synthetic magnetic cells integrated within 2D cell culture systems. These synthetic cells generate distributed mechanical forces at the cellular scale, enabling the application of mechanical stress over larger areas. This approach contrasts with the previously described technique using submicron-sized magnetic particles, which induce highly localized forces (see Chapter 2). Initially, by examining droplet deformation within Newtonian fluids or elastic gels under magnetic actuation, we quantitatively extract microscale mechanical properties of the surrounding environment, which are subsequently validated through conventional rheological and interfacial tension measurements. Integration of synthetic magnetic cells into cell cultures then permits the transmission of mechanical forces to neighboring natural cells. Moreover, the introduction of a paramagnetic probe into the homogeneous field amplifies the local magnetic field and generates spatial gradients, further enhancing mechanical stimulation. Collectively, this platform establishes a tool with the potential to probe mechanotransduction and to elucidate cellular responses to controlled mechanical stimuli.

The second strategy aims to design magnetic field gradients to modulate and direct the sprouting behavior of cells that have internalized magnetic nanoparticles. To create a microscale-localized magnetic field gradient, a suitably isolated cobalt wire is introduced into a homogeneous magnetic field generated by a custom cylindrical Halbach array, optimized for integration with confocal microscopy. Furthermore, by incorporating multiple wire segments, the setup enables the simultaneous observation of several independent events. As such, the system provides a versatile platform for our collaborators to spatially guide cellular sprouting to specific locations of interest, thereby advancing potential applications in tissue engineering.

Together, these approaches illustrate the capacity of magnetic fields to facilitate mechanical stimulation and spatial manipulation of cells, advancing the ability to investigate and engineer cellular mechanobiology.

3.1 Synthetic Magnetic Cells

Synthetic cells, in the context of this work, provide a versatile and biocompatible platform for the controlled modulation of cellular behavior. These constructs are designed to replicate selected structural and functional aspects of living cells, often featuring a lipid layer that mimics the native cell surface and an interior for the encapsulation of natural organelles or synthetic components [112]. The surface of synthetic cells can be functionalized with proteins to enable interactions with surrounding cells. Importantly, synthetic cells can be engineered to include remote-actuation mechanisms, such as photosensitive [113], magnetically [114] or temperature-responsive modules [115], allowing precise external control over their behavior.

While the presented study builds upon the work of F. Serwane *et al.* [96], who introduced the use of inert, fluorocarbon-based ferrofluid oil droplets injected into tissue *in vivo* to measure the material properties of such environments, their droplets consisted solely of ferrofluid, fluorocarbon oil, and surfactant. Consequently, they were chemically inert and lacked biological surface functionalization or cell-like adhesive properties, and therefore did not qualify as synthetic cells.

In this work, the synthetic magnetic cells were constructed from ferrofluid-based silicone oil, enabling magnetically controllable actuation, while providing a soft matrix compatible with cell culture environments. A lipid-stabilized surface was essential to form these synthetic cells. To this end, the following protocol was established by Dr. S. Pashapour and Dr. J. De Lora. A lipid mixture containing 85 % 1,2-dioleoyl-sn-glycero-3-phosphocholine (DOPC) or phosphatidylglycerol (PG), 5 % fluorescent Atto488-1,2-Dioleoyl-sn-glycero-3-phosphoethanolamin (Atto488-DOPE), and 10 % Ni^{2+}-NTA functionalized lipids (AvantiLipids) was prepared at a total concentration of 6 mM. The solvent was then evaporated, and the resulting lipid film was dried overnight in a desiccator. This dried film was rehydrated with custom silicone-oil ferrofluid (*Ferrotec*) to form the lipid-ferrofluid phase, maintaining the total lipid concentration of 6 mM. For droplet formation, the lipid-ferrofluid mixture was emulsified into an aqueous phase containing 5 mM TRIS-HCl, 25 % glycerol, and 25 mM cholesterol-polyethylene glycol (PEG) with an average molecular weight of 600 g/mol. The ferrofluid phase and aqueous phase were combined at a 1:100 ratio and emulsified using a high-shear emulsifier, producing droplets ranging $(10 - 50)\,\mu\mathrm{m}$ in diameter. In addition, the droplets were incubated with His-tagged E-cadherin proteins, which bind specifically to the Ni^{2+}-NTA functionalized lipids at the droplet interface. E-cadherin, a well-characterized mechanosensitive adhesion molecule, facilitates the formation of cell–cell junctions and plays a crucial role in transducing mechanical signals across the membrane, thereby influencing cellular behavior and signaling [116–119].

To enable both integration of the synthetic cells with natural cell lines and visualization by fluorescence microscopy, human embryonic kidney (HEK293T) and human epidermal keratinocyte (HaCaT) cell lines were genetically engineered by Dr. S. Pashapour and Dr. J. De Lora to express green fluorescent protein (GFP)-tagged E-cadherin. Through E-cadherin-mediated interactions, the synthetic magnetic cells effectively integrated into these cellular environments (see Fig. 3.1a), forming functional adhesive contacts with living cells that could be visualized via fluorescence imaging.

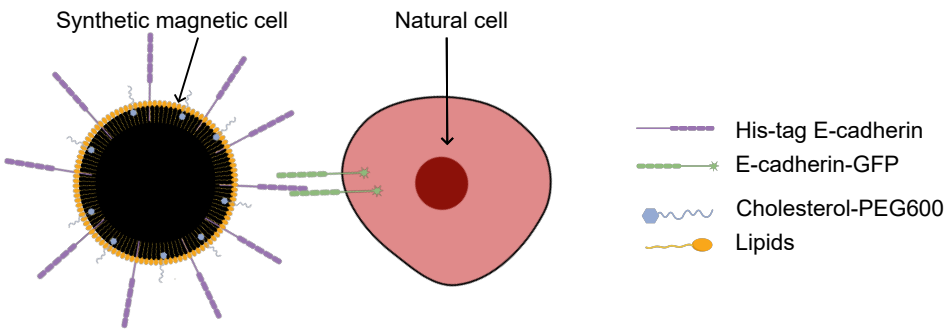

Figure 3.1. A synthetic magnetic cell engaging in E-cadherin-mediated adhesion with a natural cell.

Synthetic magnetic cells were co-seededed with natural cells into the culture to generate mechanical forces within cell monolayers. In a homogeneous magnetic field, the initially spherical synthetic magnetic cells deform into ellipsoids, as detailed in Section 1.4 and previously described by Serwane *et al.* [96]. This deformation generates mechanical stresses on adjacent cells, manifesting as a force dipole aligned parallel and antiparallel to the magnetic field direction. Notably, the ferrofluid-oil formulation with lipid stabilization employed in this study demonstrates nearly twice the magnetic saturation compared to that reported by Serwane *et al.* [96], as illustrated by the hysteresis curve in Fig. 1.13a. Furthermore, unlike the static actuation achieved with a permanent magnet array mounted on a motorized platform in the previous work, our system enables dynamic, real-time actuation of the synthetic magnetic cells, as further elaborated in the following subsection.

3.1.1 Setup to Generate Homogeneous Magnetic Fields

A homogeneous magnetic field was generated using an electromagnet powered by a DC supply. The field was directed horizontally from the iron core through magnetizable steel and two sets of iron pole pieces toward the 35-mm-cell culture dish, which was held in place within the field by a custom 3D-printed holder (see Fig. 3.2). I mounted the whole setup on a custom-built microscope stage on an inverted microscope (*Zeiss* Axio Observer Z1) to enable observation of droplet deformation in real time. To maintain physiological conditions while conducting experiments at long timescales, the setup was placed in a temperature-controlled incubation chamber, with humidity passively maintained by a water-soaked sponge.

The strength of the magnetic field, and consequently the degree of droplet deformation, can be accurately modulated by varying the current supplied to the electromagnet. In the configuration shown in Fig. 3.2, the maximum field reached approximately 63 mT, limited by the saturation magnetization of the steel and iron components. The “first iron pole pair” (see Fig. 3.2) consisted of two iron cylinders, each with a diameter of 40 mm and thickness of 6.5 mm. The field strength could be further increased by modifying the geometry of this pole pair—for instance, by reducing its diameter or reshaping the ends into truncated cones converging toward the sample center. However, such modifications would lead to a trade-off by decreasing the volume over which the field remains homogeneous.

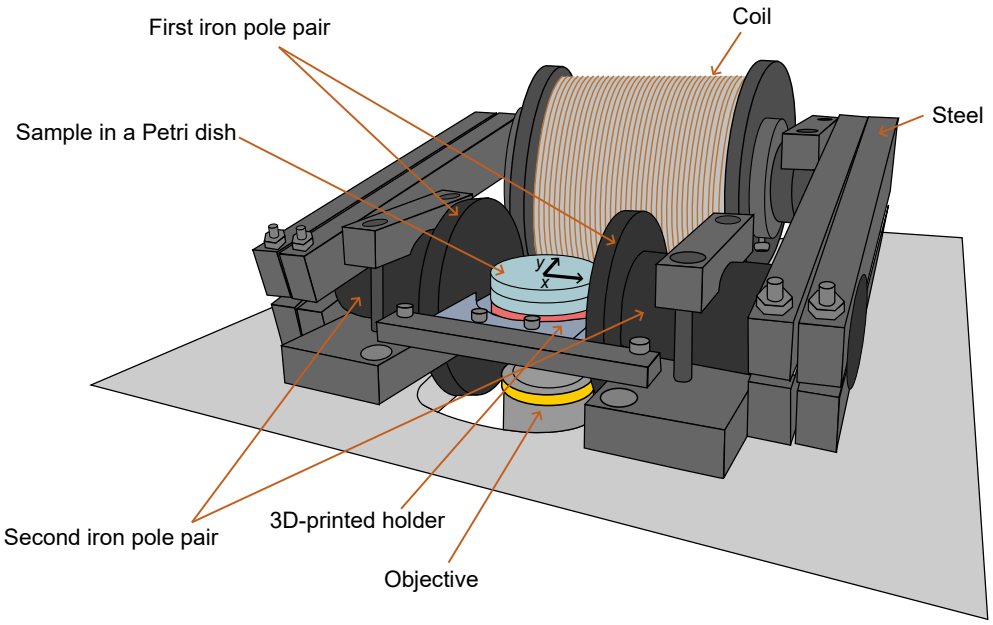

Figure 3.2. Schematic illustration of the experimental setup used to generate a homogeneous magnetic field across the cell culture dish during microscopy.

The spatial uniformity of the magnetic field within the region of interest was assessed through finite element simulations using *COMSOL Multiphysics 6.1*. A 2D axis-symmetric model replicated the experimental geometry, incorporating the exact arrangement and dimensions of the two pairs of iron pole pieces used in the setup. Rather than targeting absolute magnetic field values, which can be inaccurate due to factors like heat dissipation during electromagnet operation, the simulation focused on evaluating field homogeneity. Specifically, I tested whether calibrating the magnetization of the iron components in the simulation to match the experimentally measured magnetic field at the center of the region of interest (measured as $63\,\mathrm{mT}$) would allow accurate predictions of field deviations in other areas. This approach, if validated, would enable reliable magnetic field simulations for other geometries without requiring full experimental mapping. Using the ”Magnetic Fields, No Currents” module in COMSOL, the simulation predicted a field deviation of less than $1\,\%$ within the central 1-cm region (Fig. 3.3a).

Subsequently, experimental mapping of the magnetic field was performed using a magnetometer (*MAGSYS* HGM09s) mounted on a manual micromanipulator (Fig. 3.3c–d). The measured field showed a high degree of uniformity (Fig. 3.3b–d), in strong agreement with the simulation results (Fig. 3.3a). This correspondence confirms that the experimentally calibrated simulation reliably captures the magnetic field distribution and can thus be confidently applied for predicting fields in alternative geometries.

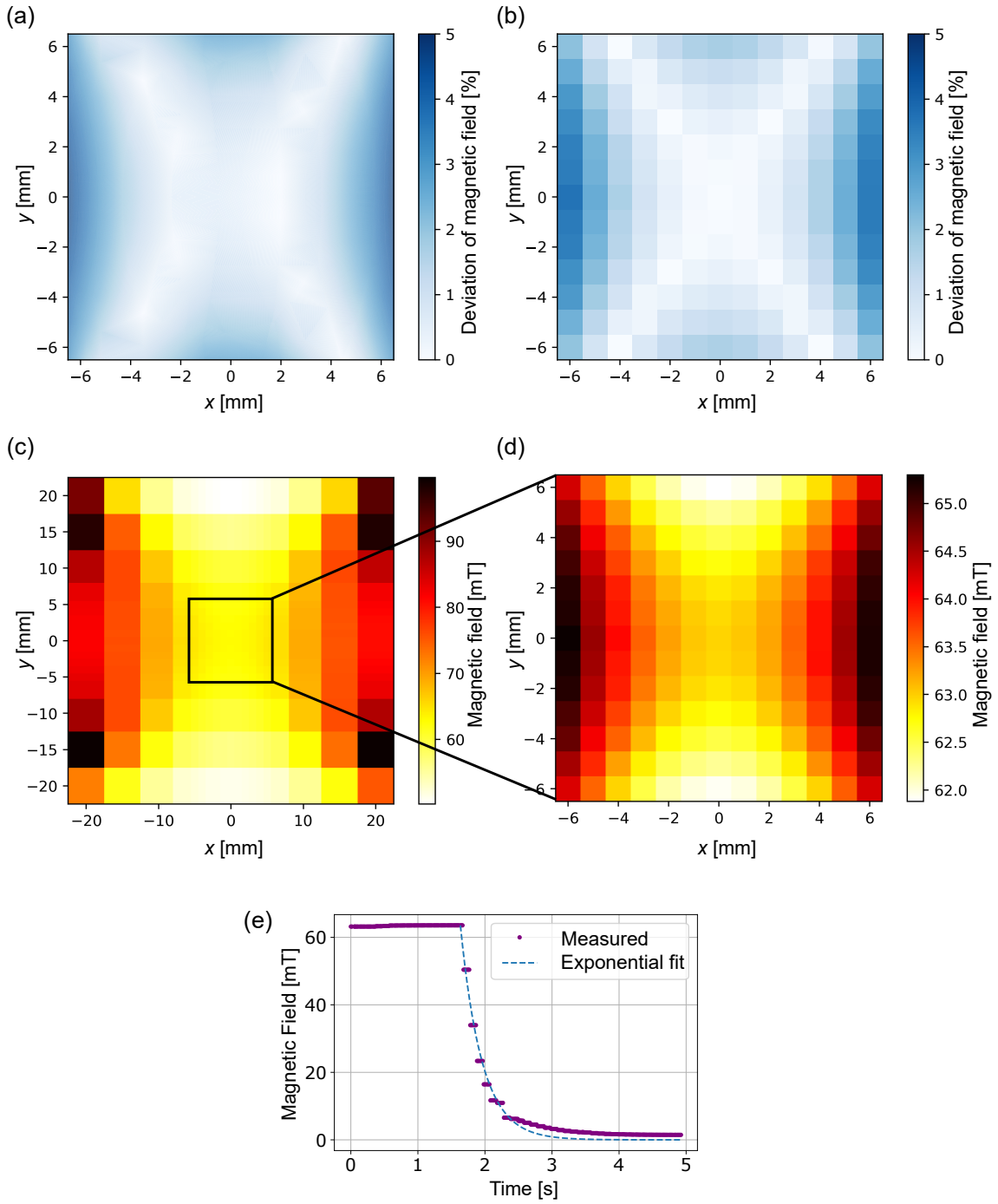

Figure 3.3. Characterization of the setup designed to generate a homogeneous magnetic field: (a) simulated magnetic field deviation across the region of interest, computed in the vertical plane corresponding to the top surface of the glass in the Petri dish using *COMSOL*, (b) experimentally measured magnetic field deviation in the same plane, (c) measured magnetic field, (d) zoomed-in view of the central region shown in (c), and (e) temporal decay of the magnetic field after switching off the voltage, fitted with an exponential curve yielding a time constant $\tau = 0.32\,\mathrm{s}$.

To enable precise control over the magnetic field during stimulation experiments, I calibrated the relationship between the supplied electrical current and the resulting magnetic field at the center of the region of interest. These calibration data were implemented in a *Python 3.10.9* script, which provided automated magnetic field cycling with programmable timing, facilitating periodic activation and deactivation throughout the experiment.

In addition, we characterized the temporal response of the system to assess its suitability for dynamic magnetic stimulation. A magnetometer was positioned at the center of the region of interest to record the magnetic field when the supply voltage was switched off (see Fig. 3.3e). The decay of the magnetic field was fitted with an exponential function of the form $A\mathrm{e}^{-(t-t_0)/\tau}$, where $A = 63.4\,\mathrm{mT}$ is the initial magnetic field amplitude, $t_0 = 1.63\,\mathrm{s}$ marks the onset of the decay, and $\tau = 0.32\,\mathrm{s}$ is the characteristic decay time constant. The system exhibited a response time of just over 1 s from voltage deactivation to effective field removal, thereby establishing the temporal resolution limit for dynamic stimulation experiments.

Overall, the electromagnet configuration enables precise modulation of the magnetic field, combining a high degree of field homogeneity, rapid switching dynamics, and adjustable force application. These capabilities render the system particularly suitable for controlled, dynamic mechanical stimulation in cell-based experiments, offering a robust platform for investigating mechanobiological processes with high spatiotemporal resolution.

3.1.2 Measurements of Interfacial Tension Using Ferrofluid Droplets

Initially, we aimed to test our platform in liquids and elastic gels. For the following experiments, we employed the ferrofluid–silicone oil formulation containing lipids, but excluded additional functional components such as His-tagged E-cadherin proteins. This decision was motivated by both the high cost of the proteins and the practical limitations associated with forming a functionalized interface on injected droplets, as opposed to emulsified droplets used in cell culture experiments. Since the interactive surface characteristic of synthetic magnetic cells arises from post-synthesis functionalization and incubation of preformed droplets, I refrain from referring to these droplets as “synthetic magnetic cells” in the remainder of the text unless they possess such a bioactive interface within a cell culture monolayer.

As a first step, we characterized droplet deformation in Newtonian fluids, where the viscosity remains constant and independent of shear rate [120]. Upon application of a homogeneous magnetic field, a spherical ferrofluid droplet of initial radius R deforms into an ellipsoid characterized by its semi-axes a (minor) and b (major). The uniaxial strain along the major axis of the deformed droplet is defined as $\epsilon = \frac{b-R}{R}$.

Assuming volume conservation during deformation [96] and applying a Taylor expansion around $\frac{b}{a} \to 1$, we obtain an expression for the strain in terms of the ellipsoidal semi-axis [96]

$$\epsilon = \frac{2}{3}\left(\frac{b}{a} - 1\right). \tag{3.1}$$

At mechanical equilibrium, where the deformed droplet shape remains stable, a thorough analysis based on Eq. (1.32) (see also Fig. 1.10) yields the balance between magnetic traction, as described in Eq. (1.33), and the capillary restoring stress p_{C} [121]

$$p_{\mathrm{C}} = p_M, \tag{3.2}$$

where the governing expression p_{C} can be further simplified, based on formulations of Tsebers [122] and Afkhami *et al.* [121] (specifically, Eq.(5) in [122] and Eq.(3.13) in [121]) using a Taylor expansion in the small strain limit $\epsilon \to 0$

$$p_{\mathrm{C}} = \epsilon\frac{6\gamma}{R}, \tag{3.3}$$

where γ is the interfacial tension between the droplet and the surrounding fluid.
Using Eqs. (1.33), (3.2) and (3.3), the surface tension can be expressed as [96]

$$\gamma = \frac{\mu_0 M^2 R}{12\epsilon}. \tag{3.4}$$

Based on Eq. (3.4), we aimed to determine the interfacial tension between a ferrofluid, comprising silicone oil with dispersed lipids, and various Newtonian fluids, including glycerol solutions, glucose solutions, and cell culture medium. For independent validation, we also assessed the suitability by standard techniques, such as pendant drop tensiometry.

Ferrofluid droplets were generated within the continuous liquid phase in glass-bottom cell culture dishes by pressure-driven injection using a microinjector (PLI-100A, *Warner Instruments LLC*) in conjuction with glass microneedles of 20 µm outer diameter (*BioMedical Instruments*). Owing to the higher density of the ferrofluid phase relative to the continuous liquid, the droplets sedimented to the bottom of the dish. The droplet size was regulated by varying the injection pressure between 100 kPa and 170 kPa. An example of a droplet produced using this method is shown in Fig. 3.4a.

Two major challenges were encountered during the experiments. First, the ferrofluid droplets often exhibited negligible deformation upon application of the magnetic field, contrary to expectations based on the fluid's viscosity and magnetic properties. Second, they frequently drifted rapidly toward the nearest iron pole piece once the field was activated, likely due to minor magnetic field gradients present even within an otherwise nominally homogeneous field. This behavior was consistently observed across a range of liquid environments, including 10 %–30 % v/v aqueous glycerol solutions and glucose solutions with concentrations ranging from 2 M to 9 M. In these cases, the increased viscosity was intended to reduce droplet mobility and mitigate drift induced by subtle magnetic gradients.

Further investigation revealed that the lack of deformation in many cases was due to adsorption of the droplets onto the glass bottom of the cell culture dish. This occurred as a result of the interfacial tension balance between the continuous liquid phase, the ferrofluid, and the glass substrate, leading the droplet to adopt a sessile (i.e., surface-adhering and flattened) rather than a spherical shape. While we could influence the initial droplet configuration by adjusting the vertical position of the glass capillary tip relative to the dish bottom during injection, some droplets were still observed to transition into an adsorbed state upon magnetic field activation. To ensure only correctly shaped droplets were included in the analysis, the shape of each droplet was verified both before and after the application of the magnetic field. This was achieved using confocal fluorescence microscopy to visualize the Atto488-DOPE lipids localized at the droplet interface (see Fig. 3.4b), enabling reliable identification of non-spherical or surface-adhering droplets.

To address the second problem, the drift of droplets in response to subtle magnetic field gradients, we explored physical confinement strategies using different chamber designs made of glass and plastic. However, these approaches often introduced new artifacts: droplets in contact with the chamber edge exhibited asymmetric deformation, compromising the analysis of magnetic-induced shape changes. Ultimately, we overcame this issue by employing a high-speed camera (Phantom 7.2, *Vision Research*) operating at 400 frames per second, which allowed us to capture the droplet deformation before the droplet could drift out of the field of view (see Fig. 3.4c). The droplet was considered to have reached equilibrium deformation once its shape stabilized and no longer varied between consecutive frames, despite ongoing drift.

First, droplet deformation experiments were conducted in a 4 M glucose solution. A total of 20 deformation events were recorded for droplets with radii ranging from 42 µm to 59 µm, subjected to magnetic fields between 38 mT and 63 mT. The interfacial tension for each droplet was subsequently calculated using Eq. (3.4). The droplet deformation (major and minor axes) was determined from images acquired with an inverted microscope, while the undeformed droplet radius was measured separately via confocal microscopy to avoid the influence of residual magnetic fields ($< 1\,\mathrm{mT}$) present in the system even in the absence of applied magnetic actuation. The resulting dataset, comprising 20 interfacial tension values, is presented in Fig. 3.4d, where the color of each point corresponds to the radius of the respective droplet. The average interfacial tension across all measurements was found to be $19.2 \pm 0.4 \mathrm{mN/m}$. Within this dataset, no clear dependence of interfacial tension on either the applied magnetic field or droplet size was observed; however, due to the relatively narrow range of both parameters, no definitive conclusions can be drawn.

Subsequently, the same procedure was applied to droplets injected into standard Dulbecco's Modified Eagle Medium (DMEM) supplemented with 1 % Penicillin-Streptomycin and 10 % fetal bovine serum (FBS), as this represents the physiological medium in which cells were cultured in this study. Determining the capillary restoring stress in this biologically relevant environment is critical for understanding droplet mechanics under conditions that closely mimic those used during cellular experiments.

Deformation in DMEM cell culture medium was analyzed for 15 droplets with radii ranging from 70 µm to 500 µm, across applied magnetic fields from 1.4 mT to 28.9 mT. The maximum magnetic field applied in this case was intentionally lower than that used in the 4 M glucose experiments, due to the lower viscosity of DMEM cell culture medium. This precaution was to avoid significant droplet deformation, thereby ensuring that the approximation $\frac{b}{a} \to 1$, a requirement for the validity of Eq. (3.4), remained satisfied. Each droplet was subjected to at least 8 different magnetic field strengths. The resulting dataset, comprising over 140 interfacial tension values, is plotted as a function of magnetic field in Fig. 3.4e. As expected, the interfacial tension exhibited no dependence on droplet radius. However, a clear trend was observed: interfacial tension increased from values slightly above 0 mN/m to approximately 5 mN/m as the magnetic field was raised to 30 mT. In the low-field regime, measurements obtained from larger droplets are considered more accurate due to more pronounced deformations and a higher pixel resolution, which reduced uncertainty in aspect ratio determination and, consequently, the derived interfacial tension.

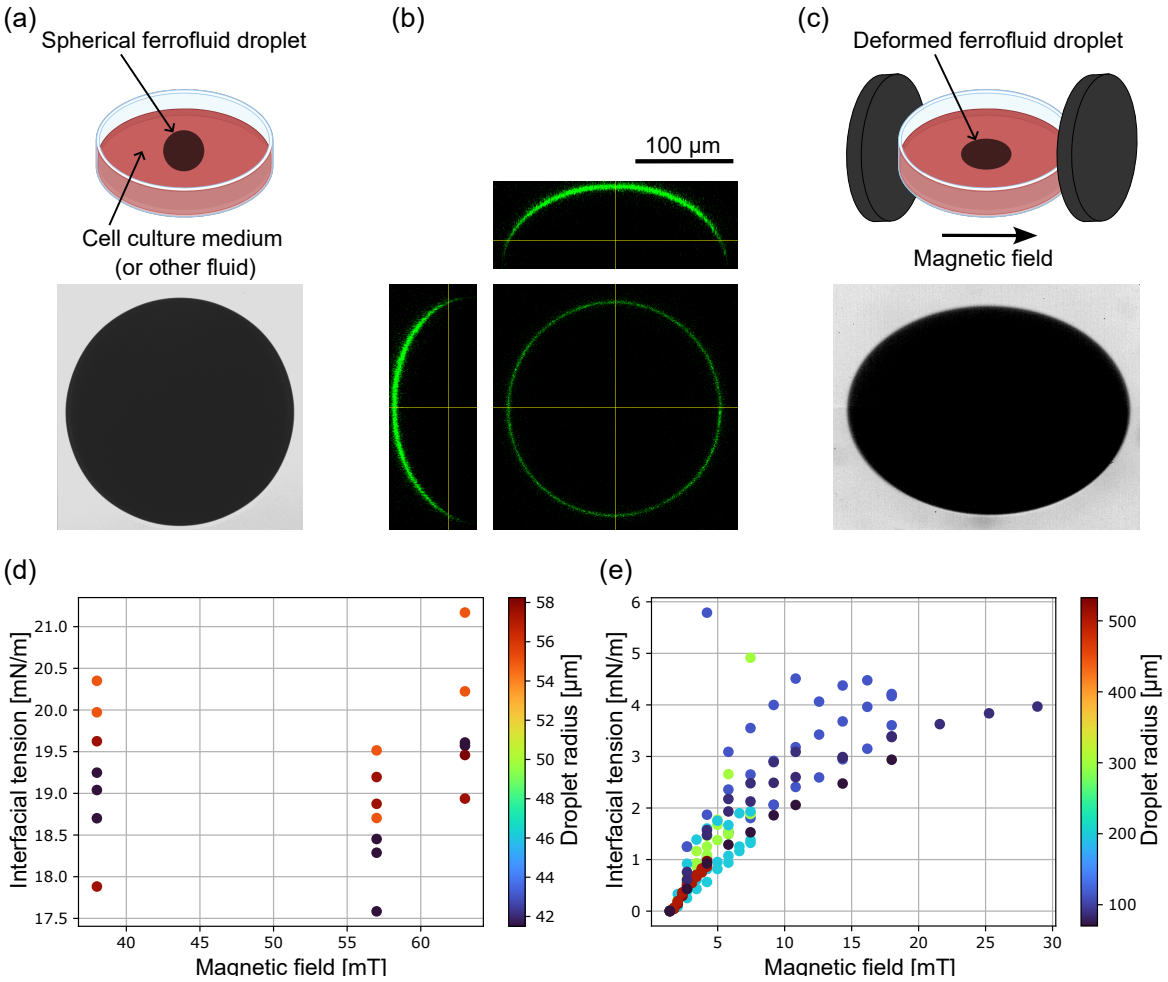

Figure 3.4. Measurement of interfacial tension between the ferrofluid–silicone oil phase containing lipids and Newtonian fluids via magnetic droplet deformation: (a) schematic and confocal image of an undeformed droplet in standard DMEM cell culture medium, (b) radius measurement and verification of non-wetting behavior using confocal fluorescence microscopy, based on the Atto488-DOPE signal at the droplet interface, (c) schematic and corresponding image of a droplet in standard DMEM cell culture medium deformed under a homogeneous magnetic field (11.6 mT), imaged using an inverted microscope, (d) interfacial tension values for 8 droplets in 4 M glucose solution plotted against magnetic field, (e) interfacial tension values for 15 droplets in standard DMEM cell culture medium plotted versus magnetic field. The scale bar shown in (b) applies to images in (a)–(c).

The influence of magnetic fields on interfacial tension has been previously investigated, though the literature presents inconsistent findings. This ambiguity is partly attributed to the confounding effects of magnetic pressure, which deform the magnetic phase along the field direction and can mask genuine variations in surface tension [123, 124]. Many theoretical models continue to assume constant interfacial tension when analyzing the behavior of ferrofluid droplets in magnetic fields [125]. While certain studies suggest negligible dependence on the magnetic field [126], an increasing number of reports indicates that interfacial tension tends to increase with magnetic field strength [121, 123–125, 127]. This trend implies that field-dependent interfacial tension should be incorporated into analytical models of ferrofluid dynamics. The underlying mechanisms for this magnetic influence remain the subject of ongoing investigations. Upon the application of a magnetic field, dipole–dipole interactions among magnetic nanoparticles promote the formation of chain-like aggregates. However, for homogeneous ferrofluids with uniform magnetic properties, the dipole interaction term in the theoretical expressions for interfacial tension is typically deemed negligible and cannot account for the substantial discrepancies between theoretical predictions and experimentally observed values [121, 123, 125]. Furthermore, when ferrofluids are modeled as inhomogeneous composite systems, chain formation that has been shown to alter the effective magnetic susceptibility should be already considered in magnetometry measurements [121, 125]. Beyond changes in susceptibility, magnetic field-induced particle chaining, along with interactions between magnetic nanoparticles and non-magnetic carrier fluid molecules, can result in a redistribution of particles within the ferrofluid [121, 123]. Some studies propose that the magnetic nanoparticles behave similarly to surfactants and move away from the interface in response to an applied field, thus causing an increase in interfacial tension [121, 123]. This idea is supported by evidence showing that the surface of a magnetized ferrofluid is compositionally different from the homogeneous bulk material [128]. In particular, a lower concentration of nanoparticles has been observed at the interface [128], and such surface depletion has been linked to variations in contact angle [129], ultimately impacting the interfacial tension.

3.1.3 Validation of Interfacial Tension Using Standard Methods

To assess the reliability of our interfacial tension measurements obtained via the droplet deformation method, we sought to compare our results with those acquired using established, standardized techniques. Specifically, we aimed to determine the interfacial tension between our ferrofluid droplet formulation (a silicon oil-based ferrofluid containing lipids) and the fluids used for the aforementioned experiments (a 4 M glucose solution and standard DMEM cell culture medium) using a pendant drop tensiometer. In the following, I first discuss the limitations encountered with the pendant drop tensiometer and subsequently address considerations related to the sessile drop method. Both methods were implemented using the Optical Contact Angle 50 instrument in conjunction with the SCA20 software (*DataPhysics Instruments GmbH*), which analyzes droplet shapes by fitting the Young–Laplace equation to extract interfacial tension values. The interfacial tension was calculated from the droplet profile based on fluid densities that we experimentally determined: 1.35 g/ml for the lipid-stabilized silicon oil ferrofluid, 1.23 g/ml for the 4 M glucose solution, and 1.00 g/ml for the supplemented DMEM cell culture medium.

Pendant Drop

The pendant drop method determines interfacial or surface tension by analyzing the shape of a liquid droplet suspended from the tip of a capillary, where the balance between gravitational forces and boundary tension dictates the droplet's profile [130]. For these measurements, the lipid-stabilized silicon oil-based ferrofluid was loaded into a capillary, which was then submerged into a glass cuvette containing the liquid phase to be measured. To prevent the ferrofluid phase from wetting the blunt needle, the needle surface was rendered hydrophilic via oxygen plasma treatment prior to all interfacial tension measurements.

During attempts to quantify the interfacial tension between a 4 M glucose solution and the lipid-stabilized silicon oil-based ferrofluid, we observed an unexpected and pronounced dependence of the measured values on droplet volume. Specifically, interfacial tension decreased from approximately 150 mN/m for a 25 µl droplet to around 25 mN/m for a 3 µl droplet, with a consistent downward trend across five intermediate volumes. To my knowledge, such a strong volume dependence is not reported in the literature, where interfacial tension is expected to remain invariant with droplet size under equilibrium conditions.

Upon visual inspection, all droplets appeared nearly spherical, regardless of their volume. This observation led me to consider the Bond number β, which quantifies the relative importance of gravitational and surface tension forces, and is defined as [131]

$$\beta = \frac{\Delta\rho g R^2}{\gamma}, \tag{3.5}$$

where γ is the interfacial tension between the two fluid phases, $\Delta\rho$ is their density difference, g is the gravitational acceleration, and R is the characteristic droplet radius. When β is small, gravitational effects are negligible compared to surface tension, resulting in a droplet profile that deviates minimally from a perfect sphere. In such cases, the pendant (or sessile) drop technique becomes increasingly unreliable due to insufficient gravitational deformation [132]. Literature suggests that measurements become inaccurate for $\beta < 0.2$ [133]. Using the largest (25 µl) and smallest (3 µl) droplets, and assuming interfacial tensions of approximately 150 mN/m and 25 mN/m, respectively, along with a density difference of $\Delta\rho = 0.12\,\mathrm{g/ml}$, the Bond number in both cases was calculated to be well below 0.1. This confirms that the droplets were in a low-Bond regime, explaining the unreliable and volume-dependent interfacial tension results obtained with the pendant drop method. Although increasing the droplet size could, in principle, enhance the Bond number and improve measurement reliability, the maximum sustainable droplet volume is restricted by gravitational detachment from the needle [132]

$$V_{\max} = \frac{\pi D_{\mathrm{N}} \gamma}{\Delta\rho g}, \tag{3.6}$$

where D_{N} is the needle diameter. For $D_{\mathrm{N}} = 0.8\,\mathrm{mm}$, Eq. (3.6) yields theoretical maximum volumes of approximately 53 µl and 320 µl for interfacial tensions of 25 mN/m and 150 mN/m, respectively. The corresponding Bond numbers, $\beta \approx 0.26$ and $\beta \approx 0.14$, remain at or below the threshold for reliable measurements, highlighting the intrinsic limitations of the method for this system.

In contrast, measurements of the interfacial tension between the standard cell culture medium and the lipid-stabilized silicon oil-based ferrofluid exhibited the opposite challenge: the pendant droplets were excessively elongated under gravity and failed to attain a stable equilibrium shape.

Constrained Sessile Drop

The constrained sessile drop method enables the measurement of interfacial or surface tension by evaluating the equilibrium shape of a liquid droplet positioned on a circular pedestal with a sharp knife edge, where the interplay between gravitational forces and interfacial tension once again governs the droplet's profile [134, 135]. The knife edge acts as a physical constraint, effectively preventing film leakage and allowing for reliable measurements even at very low surface tensions below $1\,\mathrm{mN/m}$ [134, 135].

Using the constrained sessile drop method, attempts to perform measurements in a 4 M glucose solution again failed to produce reliable data. Droplets with volumes ranging from 30 µl to 60 µl exhibited an inverse trend relative to the pendant drop method, with the apparent interfacial tension decreasing from 420 mN/m to 180 mN/m as droplet volume increased. Notably, the Bond number β remained well below 0.1 (see Eq. (3.5)), indicating a regime in which gravitational effects are negligible relative to interfacial forces. Even assuming an interfacial tension of approximately 20 mN/m, as determined via the droplet deformation method, a droplet with a volume of 30 µl would correspond to a Bond number near 0.2, which approaches the limit of measurement reliability [133].

Instead, we focused on quantifying the interfacial tension between the cell culture medium and the lipid-containing silicon oil-based ferrofluid. Due to the dominance of gravitational forces observed during pendant drop measurements, resulting in destabilized droplet shapes for this fluid combination, we employed an alternative approach using a reduced-area pedestal setup. This configuration was implemented with a custom-designed J-shaped needle (Fig. 3.5a), integrated into a tensiometer system (DSA-25 with constrained sessile drop software upgrade for the ADVANCE software package). The reduced-area pedestal facilitated measurements with small droplet volumes, effectively lowering the Bond number β (see Eq. (3.5)), and thereby decreasing the influence of gravity on droplet shape. The J-shaped needle delivered ferrofluid directly from below onto the pedestal surface, significantly reducing mechanical disturbances during droplet deposition. The pedestal featured a sharpened edge that confined the droplet to the platform, enhancing droplet stability. Prior to droplet inflation, the pedestal was fully submerged in at least 20 ml of cell culture medium, which was contained in a precision glass cuvette (SC02, *Krüss Scientific*) featuring a built-in brushed glass diffuser on one side to ensure uniform background illumination.

The exceptionally low interfacial tension between the ferrofluid and the cell culture medium led to pronounced flattening of sessile droplets (see Fig. 3.5b). As a consequence, even a minimal tilt of the suspended pedestal frequently caused the droplets to lose stability and slip off the surface. Measurements were performed across a range of droplet volumes. For each volume, the lowest interfacial tension value obtained from a reliable fit (see a representative image in in Fig. 3.5b) is presented in Fig. 3.5c. The apparent dependence of the

measured interfacial tension on droplet volume likely reflects the fact that larger droplets are more susceptible to sliding off the pedestal, which prevents them from achieving an equilibrium shape. Therefore, I consider the values obtained from smaller, more stable droplets as more accurate representations of the actual interfacial tension. Importantly, these measurements are in good agreement with interfacial tension values independently determined using the droplet deformation method at low magnetic field strengths (see Fig. 3.4e).

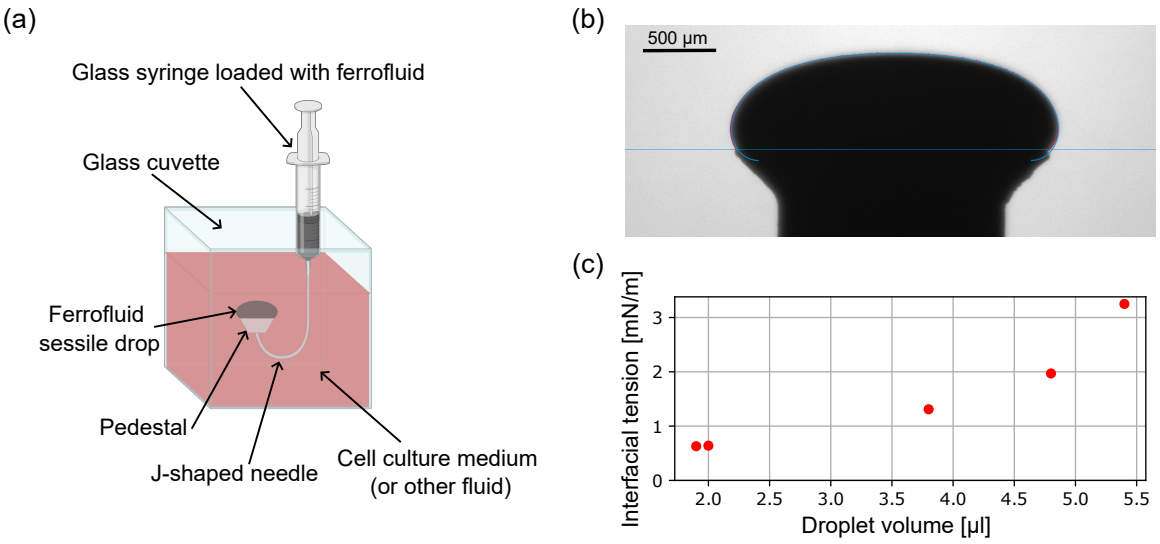

Figure 3.5. Measurement of interfacial tension between a lipid-containing ferrofluid–silicone oil phase and cell culture medium using the constrained sessile drop method: (a) schematic of the experimental setup, showing a droplet supported on a reduced-area pedestal connected to a syringe via a J-shaped needle; (b) representative image of a constrained sessile drop with a volume of $1.9\,\mu\mathrm{l}$, measured to have an interfacial tension of $0.63\,\mathrm{mN/m}$ in cell culture medium; (c) plot showing the minimum reliable interfacial tension values obtained for various droplet volumes.

In experiments involving synthetic magnetic cells in cell culture (discussed in a later section), performed under an applied magnetic field of 63 mT, I adopt an interfacial tension value of 5 mN/m. This value was selected because our data show that interfacial tension increases with magnetic field strength (see Fig. 3.4e), a trend well documented in previous studies [121, 123–125, 127]. Moreover, it has been shown that interfacial tension typically saturates at field strengths well below those required to achieve ferrofluid saturation magnetization [121]. Although our data do not provide direct evidence of interfacial tension saturation, the trend in Fig. 3.4e suggests the onset of a plateau between 4 mN/m and 5 mN/m, supporting the adoption of this value as a reasonable estimate for subsequent analyses.

3.1.4 Measurements of Elastic Modulus Using Ferrofluid Droplets

When a ferrofluid droplet is subjected to a magnetic field within a surrounding medium that exhibits elastic properties, the equilibrium condition for the tension can be expressed as

$$p_M = p_{\mathrm{C}} + p_E, \tag{3.7}$$

where p_E denotes the additional stress due to the elasticity of the surrounding medium. The formulation for the elastic contribution p_E can be adapted from the formulation by R. Style *et al.* [136], particularly from their Eq. (7). In my analysis, I redefine the droplet strain as $\epsilon_{\mathrm{d}} = 2\epsilon$, reflecting the convention adopted in my earlier definition (see the discussion above Eq. (3.1)). I then use the relations $\epsilon_{zz} = \frac{p_M}{E}$ and $L = \frac{\gamma}{E}$, where E denotes the Young's modulus of the surrounding material, and scale the strain term by a factor of $\frac{1}{4}$, following the approach outlined by P. Rowghanian *et al.* [137]. This leads to the final expression for the elastic stress

$$p_E = \epsilon \frac{12E}{5}. \tag{3.8}$$

By substituting the expressions for p_{C} and p_E from Eqs. (3.3) and (3.8), respectively, we obtain

$$\frac{p_M}{\epsilon} = \frac{6\gamma}{R} + \frac{12E}{5} \tag{3.9}$$

which allows the elastic and capillary contributions to be decoupled through linear regression of $\frac{p_M}{\epsilon}$ versus $\frac{1}{R}$, in accordance with the method introduced by F. Serwane *et al.* [96].

To validate this technique, we injected lipid-stabilized silicon oil-based ferrofluid droplets into two different elastic polyacrylamide (PAA) gels. The detailed preparation method followed the procedure outlined in the literature [138] and will be described comprehensively in the forthcoming manuscript. In brief, gels were formulated using either 2 % or 2.5 % acrylamide as the primary monomer, with 0.1 % N,N'-methylene-bis-acrylamide serving as the crosslinker. Polymerization was initiated by the addition of 0.0075 % ammonium persulfate (APS) and 0.0025 % N,N,N',N'-tetramethylethylenediamine (TEMED) [138]. All components were dissolved in Milli-Q water. Droplet deformation measurements were taken for 24 droplets with radii ranging from $106\,\mu\mathrm{m}$ to $133\,\mu\mathrm{m}$ for the 2% gel, and for 14 droplets with radii from $95\,\mu\mathrm{m}$ to $128\,\mu\mathrm{m}$ for the 2.5% gel. The applied magnetic fields ranged from $34\,\mathrm{mT}$ to $63\,\mathrm{mT}$ for both polyacrylamide gels. The relationship between $\frac{p_M}{\epsilon}$ and $\frac{1}{R}$ is shown in Fig. 3.6. From the linear fits, the elastic moduli were determined to be $(310 \pm 40)\ \mathrm{Pa}$ and $(1.0 \pm 0.3)\ \mathrm{kPa}$ for the 2% and 2.5% elastic polyacrylamide gels, respectively. The relatively large uncertainty in the elastic modulus of the 2.5% gel is likely a result of both a limited number of data points and the presence of spatial variations in the gel's elasticity. In particular, three data points around $\frac{p_M}{\epsilon} \approx 4800\,\mathrm{Pa}$, obtained from the same droplet at three different magnetic stresses, significantly influenced the estimated elastic modulus, likely

due to variations in local elastic properties at the measurement location within the gel. It is also noteworthy that the data points in both plots of Fig. 3.6 tend to cluster in groups of two or three. This grouping reflects data from the same droplet, where deformation measurements were taken at two or three distinct magnetic stresses. Overall, this technique enables the quantification of local elastic properties across the sample.

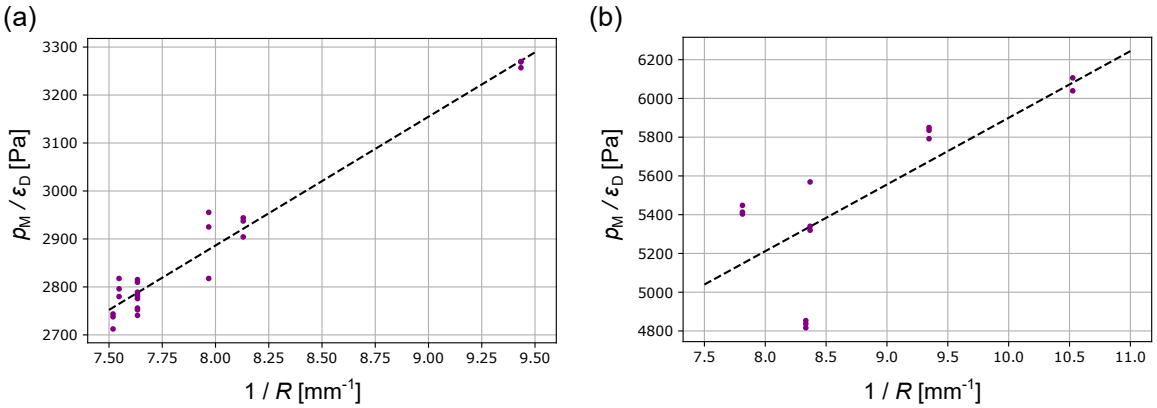

Figure 3.6. Droplet deformation in elastic polyacrylamide gels. The relationship between $\frac{p_M}{\epsilon}$ and the inverse of the droplet radius is shown: (a) the data for the 2% gel are fitted to the equation $\frac{p_M}{\epsilon} = \frac{0.27}{R} + 738$; (b) the data for the 2.5% gel are fitted to the equation $\frac{p_M}{\epsilon} = \frac{0.34}{R} + 2458$.

3.1.5 Validation of Elastic Modulus Using Oscillatory Rheology

The rheological properties of the $2\,\%$ and $2.5\,\%$ polyacrylamide gels used in the droplet deformation experiments were characterized using a rheometer (HAAKE™ MARS™ Rheometer, *Thermo Scientific*) equipped with a C60/1°Ti L cone geometry. Initially, an amplitude sweep was performed at an empirically selected constant normal force of 0.7 N and a frequency of $1\,\mathrm{Hz}$ to determine an appropriate measuring gap. Subsequently, a frequency sweep was conducted (see Fig. 3.7) at the determined measuring gap and a strain amplitude of $10\,\%$, which approximately matches the droplet deformations observed in the polyacrylamide gels during magnetic actuation. Over the frequency range of 0.1 Hz to 10 Hz, both gels exhibited frequency-independent rheological behavior, with the storage modulus G' consistently an order of magnitude greater than the loss modulus G'', thereby confirming their predominantly elastic character. For each gel, a single average value of the storage shear modulus G' was determined and converted to the elastic modulus E using the relation $E = 2G'\,(1+\nu)$, where $\nu = 0.5$ is the Poisson's ratio for incompressible materials, as referenced in Eq. 1.3 of A. F. Liu [139]. The elastic moduli of the 2% and 2.5% polyacrylamide gels were measured to be $(108 \pm 7)\ \mathrm{Pa}$ and $(458 \pm 10)\ \mathrm{Pa}$, respectively. These values are notably 2–-3 times lower than those derived from the droplet deformation approach.

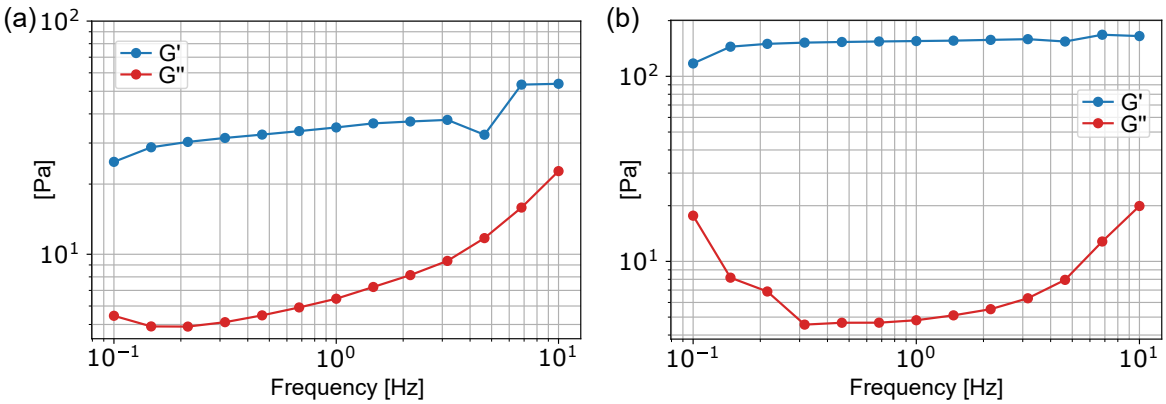

Figure 3.7. The frequency sweep of the storage modulus G' and the loss modulus G'' measured using a rheometer for (a) $2\,\%$ and (b) $2.5\,\%$ polyacrylamide gels.

I primarily attribute this discrepancy to the local compression of the polymer network induced during droplet injection, which leads to a localized increase in the elastic modulus. Analogous phenomena have been observed in fibrous gel networks incorporating stiff inclusions, where the polymer fibers undergo densification and stretching in the vicinity of the inclusions, thereby enhancing the local stiffness [140, 141]. Additionally, other studies have demonstrated that the incorporation of inclusions within soft gels results in a local augmentation of gel stiffness [142], and that increasing the volume fraction of individual inclusions within an elastomer matrix proportionally elevates the overall material stiffness [143]. This stiffening mechanism is exploited to enhance the mechanical performance of composite materials [144].

In addition, the choice of testing methodology and the scale at which the material is analyzed may also influence the measured mechanical properties. At the scale of microstructures and inhomogenities, materials often display scale dependence in their rheological behavior, which is a central topic in the field of microrheology. For instance, within a single tissue type, elastic modulus values can vary by several orders of magnitude depending on the measurement scale (e.g., micro- versus macroscopic) [145]. I hypothesize that the biofunctionalization of ferrofluid droplets with lipids could similarly affect the measured mechanical properties, potentially leading to scale-dependent characteristics. Notably, even polyacrylamide gels of identical formulation exhibit substantial variability in elastic modulus, particularly for very soft gels [146, 147]. While this variability is often attributed to differences in sample preparation required for microscale techniques (e.g., atomic force microscopy) versus macroscale methods (e.g., rheology), significant variations in measured mechanical properties have also been reported despite consistent preparation protocols, when gels are characterized using different microscopic (AFM) and macroscopic indentation techniques [147]. As a result, it has been emphasized that accurate assessment

of cellular mechanosensing and mechanotransduction on soft culture substrates and hydrogels necessitates mechanical characterization at length scales commensurate with cell size, as this scale governs the nature of cell–matrix interactions [148].

3.1.6 Force Generation via Homogeneous Magnetic Fields in Cell Monolayers

We next embedded synthetic magnetic cells into monolayer cell cultures. J. De Lora and S. Pashapour established transient E-Cadherin-GFP reporter cell lines (Hek293T-EGFP referred to as HEKE and HaCaT-EFGP referred to as HEE). Integration of synthetic magnetic cells into the cell monolayers required surface grafting with E-Cadherin, as ungrafted synthetic cells remained only on top of the natural cell monolayer. The hybrid co-culture was seeded onto an elastic polyacrylamide traction hydrogel substrate, with a Young's modulus of 35 kPa, functionalized with fibronectin, prepared in 35-mm glass-bottom dishes compatible with our 3D-printed holder of our custom microscope (see Fig. 3.2). The cell coculture on this poly-acrylamide substrate in this configuration thus potentially enables combination of our droplet deformation force generation with established techniques such as traction force microscopy (TFM) and monolayer stress microscopy (MSM), highlighting the potential to quantitatively assess mechanical responses under magnetic actuation.

I present a proof of principle for the remote application of mechanical forces to cells via embedded synthetic magnetic cells. The undeformed, relaxed synthetic cell within the HEKE cell monolayer is presented in Fig. 3.8a. Upon application of a homogeneous magnetic field of 63 mT, the synthetic magnetic cell underwent uniaxial elongation (see Fig. 3.8b), corresponding to a material strain of approximately $\epsilon \approx 0.07$. The applied magnetic field induces a magnetic traction at the surface of the synthetic cell, with the highest traction $p_{\mathrm{M}} \approx 213\,\mathrm{Pa}$ occurring at locations where the surface normal aligns with the direction of the magnetic field. Based on the measured strain ϵ and an estimated interfacial tension of $\gamma \approx 5\,\mathrm{mN/m}$ (see the interfacial tension measurements between the ferrofluid phase and cell culture medium presented earlier in this Section), I determined a corresponding capillary stress of $p_{\mathrm{C}} \approx 62\,\mathrm{Pa}$. After subtracting this capillary contribution from the total magnetic traction, we obtain a residual stress of approximately $p_{\mathrm{M}} - p_{\mathrm{C}} \approx 150\,\mathrm{Pa}$, which I ascribe to the elastic response of the surrounding cells resisting deformation, including the contributions from E-cadherin-mediated interactions. It is important to note that this estimation assumes the synthetic magnetic cell is fully embedded within the cell monolayer, with a height at least comparable to that of the surrounding cells —a premise that may be challenged by observations in Fig. 3.8. Consequently, a more comprehensive characterization is essential to confirm the extent of embedding and mechanical interaction between

synthetic and natural cells. Interestingly, despite applying a higher normal magnetic traction compared to F. Serwane *et al.* [96], the measured strain ϵ is smaller. This discrepancy is complex to resolve, I propose that it may arise from the additional elastic component contributed by the interaction between the synthetic magnetic cells and the surrounding cells, a factor not present in F. Serwane's study with inert ferrofluid droplets [96].

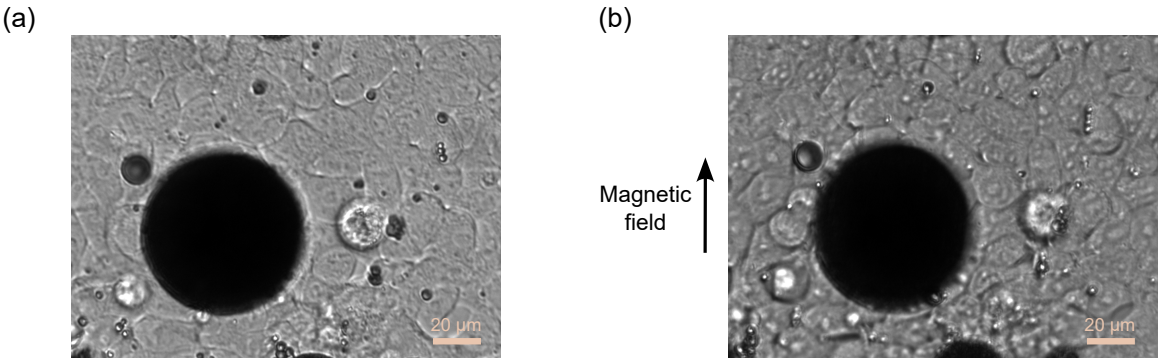

Figure 3.8. Magnetically induced deformation of a synthetic magnetic cell within a cellular monolayer: (a) the synthetic magnetic cell in its initial, relaxed state; (b) upon application of a homogeneous magnetic field of 63 mT, the synthetic magnetic cell deforms along the direction of the field, thus inducing mechanical stress on the adjacent natural cells.

We employed confocal laser scanning microscopy to show that the synthetic magnetic cells are part of the monolayer and to examine various cellular components after longer magnetic field stimulation on 35-mm glass bottom dishes. Specifically, we imaged nuclei (Fig. 3.9a), E-Cadherin-EGFP expression in natural cells (Fig. 3.9b), and the actin cytoskeleton (Fig. 3.9c). Synthetic magnetic cells were actuated with a 63 mT magnetic field, applied for 1 min and followed by 4 min off, over a total culture duration of 6h. Although we did not observe significant changes in cellular organization following magnetic field actuation, this approach demonstrates that HEE cells co-cultured with synthetic magnetic cells remain viable. Notably, the spatial arrangement of synthetic magnetic cells within the monolayer is visualized in the Z-projections shown in Fig. 3.9d. There is an indication that natural cells may partially extend beneath the synthetic magnetic cells. Nevertheless, this work provides the first demonstration of synthetic cell integration into natural cellular assemblies via E-Cadherin-mediated interactions, known to mediate mechanical forces at intercellular junctions, and thus influence cell behavior and tissue organization [149, 150].

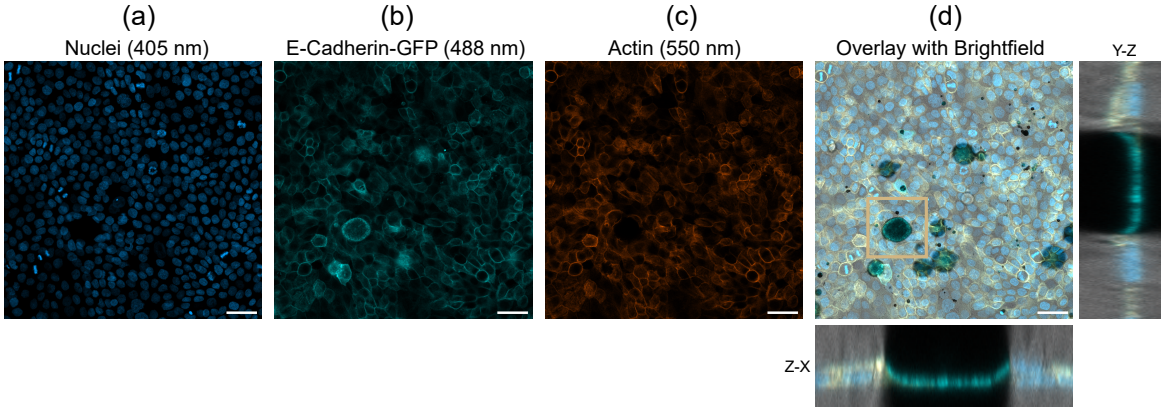

Figure 3.9. Confocal micrographs showing the integration of synthetic magnetic cells within a natural cell monolayer following actuation with a homogeneous magnetic field: (a) nuclei staining; (b) E-Cadherin-GFP expression; (c) actin staining; (d) overlay with bright-field image, including Z-projections for the beige box, with Z-X horizontal and Y-Z vertical inlays. Scale bar: $50\,\mu\mathrm{m}$.

The magnitude of mechanical stress required to modulate cellular behavior within monolayers remains an open question in the current literature. A stress of approximately 200 Pa applied to a cell within a confluent monolayer slightly exceeds the range of traction forces typically exerted by individual cells during collective processes such as migration, where values generally peak around 100 Pa, as determined through traction force microscopy [151–153]. However, in confluent monolayers, mechanical stresses accumulate with increasing distance from the leading edge due to force transmission through intercellular junctions. This results in cumulative stresses that can rise to several kilopascals when integrated across multiple rows of cells [151]. Importantly, it was reported that external mechanical cues sufficient to elicit cellular responses often represent only a small fraction of the internal cytoskeletal pre-stress, with threshold strains around $1 - 5\ \%$ for intracellular structures such as proteins and chromatin [154]. For example, applying a low-strength electric field of 0.5 V/cm was sufficient to initiate collective migration in an epithelial monolayer, accompanied by a modest increase in traction forces of a few pascals and a rise in monolayer stress of approximately 150 Pa [155], suggesting that the level of mechanical input we apply may indeed be biologically relevant. To further evaluate the effect of magnetic actuation, we attempted to detect stress patterns in the surrounding monolayer using monolayer stress microscopy. However, the induced forces were below the detection threshold, indicating that higher mechanical inputs may be necessary to reveal discernible mechanobiological responses, such as localized changes in E-cadherin expression.

Although our current experimental configuration did not reveal significant changes in cell behavior within a confluent monolayer, alternative cellular arrangements may provide increased sensitivity to mechanical perturbations. In particular, the ability of cells to exert or endure mechanical stress is strongly dependent on both the cell type and the mechanical properties of their substrate [156]. Moreover, the mechanical properties of cells are profoundly influenced by their collective organization; for example, epithelial monolayers exhibit elastic moduli that are nearly two orders of magnitude greater than those of individual, isolated cells [157, 158]. At the single-cell level, even relatively subtle mechanical loads can induce substantial biological responses. For example, extremely small forces corresponding to stresses of just a few pascals, applied via techniques such as optical tweezers, are sufficient to activate mechanosensitive signaling pathways, including intracellular calcium fluxes [159]. Similarly, applying an external stress of approximately 20 Pa to mouse embryonic stem cells was found to enhance their spreading behavior, increase cytoskeletal prestress, augment substrate traction forces, and promote cell differentiation [154, 156]. Remarkably, single leukocytes exposed to mechanical stresses in the tens-of-pascals range exhibit marked changes in morphology and motility [160]. Furthermore, stresses near 100 Pa have been shown to induce structural rearrangements in the cytoskeleton, such as actin filament alignment in the direction of applied force [161]. Consequently, a more pronounced mechanobiological response could be induced by targeting a limited number of cells instead of the entire cell monolayer. To further influence processes such as collective migration of a cell monolayer, positioning the stimulated synthetic cells at the leading edge would be beneficial.

To enhance the mechanical stimulus delivered to surrounding cells, it would be advantageous for the synthetic magnetic cells to closely match the height of the epithelial monolayer. This alignment would allow greater stress transmission, particularly from the droplet center, where deformation is maximal. Furthermore, magnetic traction could be increased—potentially by up to a factor of two, as suggested by the magnetic hysteresis measurements shown in Fig. 1.13a and estimations in Fig. 1.13b, through the application of a stronger external magnetic field. Such an enhancement could be achieved, for instance, by modifying the geometry of the ”first iron pole pair”, as previously discussed. In addition, increasing the magnetic nanoparticle concentration in the ferrofluid would further raise its magnetization, thereby enabling even higher levels of applied stress.

3.1.7 Setup to Generate Microscale Magnetic Field Gradients

We further explore the potential for enhancing mechanical stress exerted by synthetic magnetic cells by introducing a paramagnetic element within the homogeneous magnetic field in proximity to the region of interest, thus creating a localized magnetic field gradient at the microscale. The resulting increase in mechanical stress exerted by the synthetic magnetic cell onto adjacent natural cells arises from two distinct mechanisms: (i) the presence of a magnetic field gradient generates a magnetic force on the nanoparticles within the ferrofluid phase, as described by Eq. (1.6), and (ii) the local perturbation of the otherwise uniform magnetic field enhances its intensity near the paramagnetic body, thereby amplifying the force dipole acting on the synthetic magnetic cell according to Eq. (1.33).

The magnetic field gradient was generated using a 75–µm thick iron wire affixed to a diamagnetic copper probe, which was mechanically supported by a carbon fiber reinforcement (see Fig. 3.10). The probe was mounted on a precision mechanical manipulator, allowing controlled adjustment of its position and thereby enabling spatial modulation of the localized magnetic field gradient. In the absence of the probe, the setup generated a baseline homogeneous magnetic field of up to 83 mT, achieved by employing a thicker (15 mm) pair of "first iron poles" relative to the configuration illustrated in Fig. 3.2.

Before proceeding with the demonstration involving cells, I first evaluated whether COMSOL simulations could reliably predict the magnetic field gradient and thus the magnetic force exerted on a synthetic magnetic cell. For this validation, I utilized 5 µm magnetic polystyrene beads from *microParticles GmbH*. The motion of the beads was observed in an 80 % (v/v) glycerol solution, which served to slow down their movement, within a magnetic field gradient generated by perturbing an initially homogeneous 83 mT field (see Fig. 3.11a).

In contrast to the analysis in Chapter 2, the magnetic field gradient in this setup varies on the microscale across $\approx 200\,\mu\mathrm{m}$. As a result, the assumption of a constant magnetic field gradient, and thus uniform velocities along the direction of the homogeneous field and the inserted wire, is no longer valid. Instead, I calculated the velocity of each particle at its specific location, and interpolated these values across a grid covering the entire imaging area. The magnetic force on each particle was determined by balancing magnetic and viscous drag forces (see Eqs. (2.2) and (2.3)), using the friction coefficient for a sphere, $A = 6\pi\mu R_{\mathrm{S}}$ (Eq. (1.4)). This allowed calculation of the magnetic force at every observed location. The resulting force profile along the axis of the wire is shown in purple in Fig. 3.11b. Areas near the actual particle trajectories are evaluated with higher confidence, while regions further away rely more on interpolation and thus have greater uncertainty. Notably, due to the high velocities near the tip of the wire, particle tracking was not feasible in this region (see the absence of trajectories near the tip in Fig. 3.11a). Thus, the magnetic force within $\approx 45\,\mu\mathrm{m}$ from the tip (delineated by the dashed line in Fig. 3.11b) cannot be determined reliably.

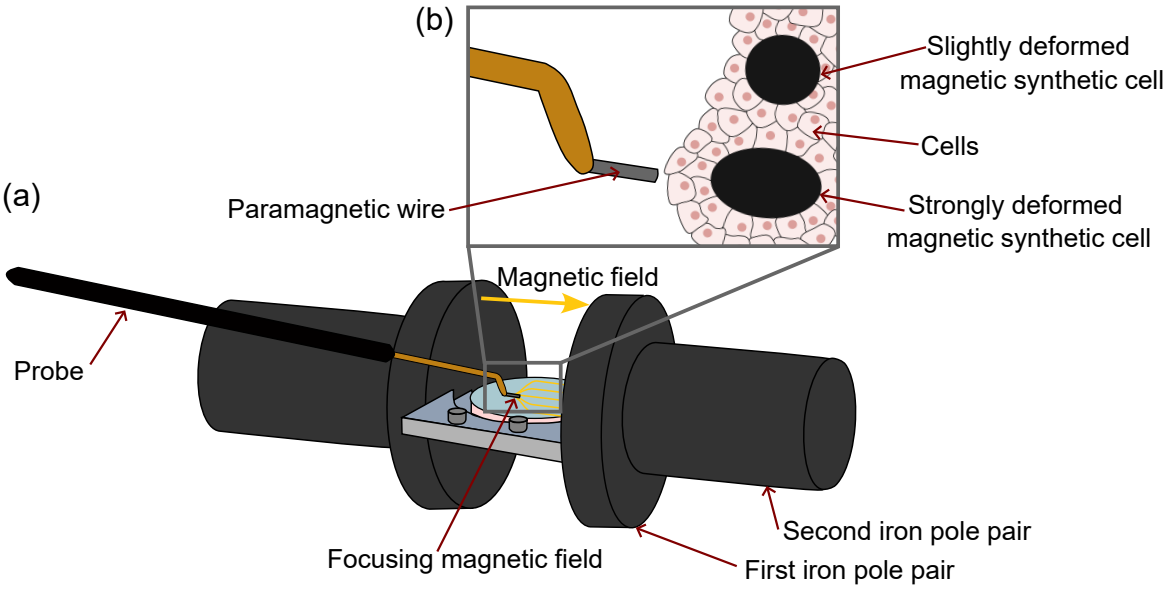

Figure 3.10. Schematic representation of the experimental setup used to introduce a microscale magnetic field gradient into an initially homogeneous magnetic field, as described in Fig. 3.2: (a) a paramagnetic wire is attached to an otherwise diamagnetic probe, locally focusing the magnetic field (field lines shown in yellow) and generating a gradient upon application of the external homogeneous field.; (b) the resulting magnetic gradient is confined to the microscale: a synthetic magnetic cell near the wire is attracted toward the wire tip due to the gradient and undergoes enhanced deformation as a result of the locally augmented magnetic field, whereas a synthetic magnetic cell positioned farther from the tip is influenced only by the uniform magnetic field, as discussed in Section 1.4.

In addition, I repeated the analysis without neglecting particle acceleration (see the discussion on velocity tracking in Chapter 2). As anticipated under low Reynolds number conditions, the results were consistent, indicating that inertial effects are negligible and supporting the validity of my force calculations under these experimental conditions.

Next, I performed magnetic simulations in *COMSOL* using a 2D axisymmetric geometry and the ”Magnetic Fields, No Currents” module. As with the configuration used to generate a homogeneous magnetic field, the magnetization of the ”second iron pole pair” was adjusted to reproduce the same initial homogeneous field observed experimentally. Subsequently, a paramagnetic wire with a thickness of 75 µm and a length of 1 mm was introduced into the geometry, aligned with the direction of the homogeneous field. Using a refined mesh around the wire, I calculated the magnetic field, the magnetic field gradient, and the resulting magnetic force acting on a single 5 µm bead. In this analysis, I employed an approximation by not integrating the force over the entire volume of the magnetic bead. Instead, I estimated the force by multiplying the bead’s volume with its magnetization and the magnetic field gradient evaluated at its center. I argue that this simplification does not significantly affect

the accuracy of the calculated force. Although the magnetic field gradient varies considerably with distance from the tip, this approximation is justified given the bead's size relative to the spatial scale of gradient variation. The resulting force on a 5 µm bead is shown in green in Fig. 3.11b.

A comparison between the results from velocity tracking (purple curve in Fig. 3.11b) and the *COMSOL* simulation (green curve in Fig. 3.11b) reveals that that the simulation predicts a higher magnetic force, approximately five times greater at a distance of 100 µm where the experimental velocity measurements are considered reliable (in contrast to regions near the wire tip, as discussed previously). This discrepancy can be attributed in part to experimental imperfections. Specifically, the wire in the experimental setup is not perfectly horizontal, and therefore not fully aligned with the external magnetic field. Moreover, the wire tip is not ideally sharp but rather irregularly shaped (see Fig. 3.11a), which leads to asymmetrical field gradients and enhanced particle accumulation on one side. Additional sources of deviation may include inaccuracies in the material properties used in the simulation, particularly the hysteresis behavior of soft iron used for both the magnetic pole pieces and the wire model. Furthermore, the magnetic properties of the particles were approximated using a hysteresis curve of similar materials, introducing further uncertainty. In conclusion, for the subsequent experiments in cell culture, it is important to account for the possibility that the actual magnetic force may be up to five times lower than the simulated values.

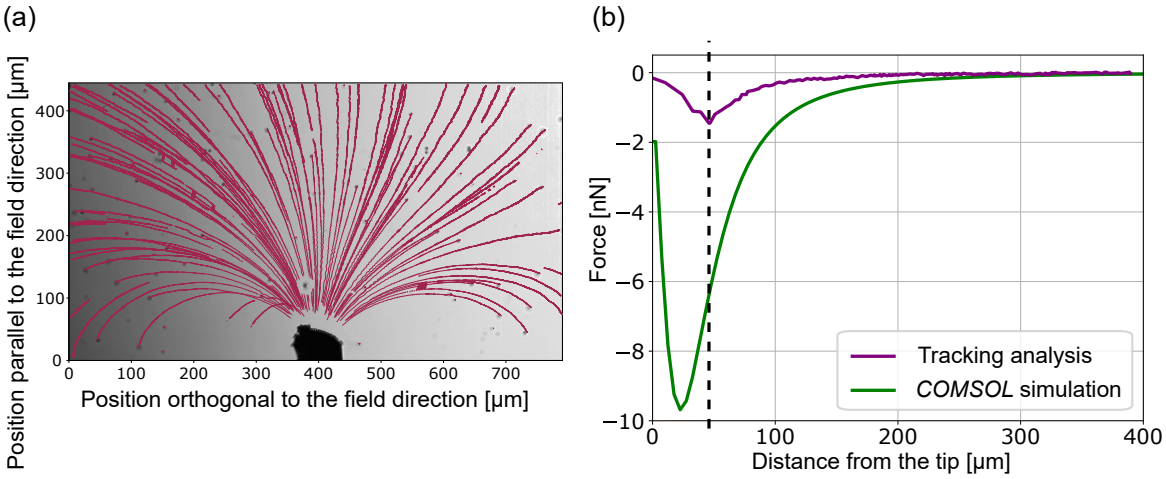

Figure 3.11. Behavior of 5 µm magnetic beads in a microscale magnetic gradient generated by a paramagnetic wire exposed to a homogeneous magnetic field of 83 mT. (a) Representative image showing bead trajectories overlaid on a tracking frame, illustrating the directed motion of the beads toward the wire tip. (b) Quantitative comparison of the magnetic force acting on the beads, derived from velocity tracking (purple) and numerical simulation using *COMSOL* (green). The dashed line delineates the region near the wire tip where experimental force estimation is unreliable.

3.1.8 Force Generation via Magnetic Field Gradient in a Cell Monolayer

Next, we demonstrate targeted magnetic actuation of synthetic magnetic cells embedded within a HEKE monolayer using a microscale magnetic field gradient. To achieve effective magnetic actuation, it is essential to position the wire tip in close proximity to the target synthetic magnetic cell. To facilitate this, we seeded the hybrid culture into a removable two-well culture insert from *ibidi*, which, upon removal, created a defined cell-free gap commonly used in migration assays. This setup enabled us to approach the wire, attached to the probe, from a region free of cells, thereby minimizing disruption to the surrounding cell monolayer (see Fig. 3.12a–c). Owing to spatial constraints imposed by the adaptation of the system to a standard 35-mm culture dish, the maximum achievable initial homogeneous magnetic field in this configuration was 72 mT.

In this experiment, an external homogeneous magnetic field of 29 mT was applied. As the wire tip was incrementally brought closer to the selected synthetic magnetic cell, we observed a corresponding increase in droplet deformation, along with a lateral displacement of the cell within the monolayer toward the wire tip (Fig. 3.12a–c). The original circular contour of the droplet at its initial position is indicated in red in each corresponding image. The precise distance between the wire tip and the targeted synthetic magnetic cell is annotated in each panel, enabling direct correlation between proximity and the extent of deformation.

I adapted the *COMSOL* simulations previously used for 5 µm magnetic beads. Fig. 3.12d and its detailed view provided in Fig. 3.12e illustrate the spatial profiles of both the magnetic field and its gradient as a function of position along the central axis of the wire. For both the 29 mT field used in the cell deformation experiments (Fig. 3.12a–c) and the maximum achievable homogeneous field of 72 mT, the simulations reveal a pronounced enhancement of the magnetic field in the immediate vicinity of the wire tip. This localized amplification rapidly decays with increasing distance, approaching the baseline value of the applied uniform field within approximately 400 µm. Similarly, the magnetic field gradient exhibits a sharp peak within the first few tens of micrometres from the wire tip and diminishes to negligible levels beyond the same spatial range.

The magnetic force acting on a synthetic magnetic cell with a diameter of $2R = 47\,\mu\mathrm{m}$, such as the one depicted in Fig. 3.12a–c, under both field configurations is shown in Fig. 3.12f, with a detailed view in Fig. 3.12g (solid lines). It is important to note that, for simplicity, the calculations were performed using the magnetic field and field gradient values at the center of the droplet, rather than integrating these values over the entire cell volume. This simplification does not account for the spatial variation of the field and gradient across the droplet, which is significant given that the droplet size is comparable to the scale over which

these quantities change. As a result, when assessing the force at a given distance y from the wire tip (see Fig. 3.12h), it is more accurate to interpret the results as representative for the interval $(y-25\,\mu\mathrm{m}, y+25\,\mu\mathrm{m})$, rather than as an exact value at a single point. Additionally, based on previous experimental observations (see discussion in Fig. 3.11b), the actual force experienced by the synthetic cell in practice is expected to be up to five times lower than the simulated values, due to experimental factors and limitations of the model.

In this context, I quantify the maximum pressure p_M exerted on the cells located immediately in front of the synthetic magnetic cell, on the side facing the wire. This pressure is estimated to act on a plane orthogonal to both the principal axis of the wire and the plane of the glass substrate (see solid lines in Fig. 3.12f and the detailed view in Fig. 3.12g). The value of p_M is estimated by dividing the force by an effective area, defined as $\frac{1}{3} \cdot 4\pi R^2$. Here, the factor $\frac{1}{3}$ is used to estimate the portion of the cell surface that is perpendicular to the applied force, under the assumption that the synthetic cell is surrounded on all sides by native cells. Due to intercellular adhesion mediated by E-cadherin, the synthetic magnetic cell remains mechanically coupled to its neighboring native cells. As a result, the applied force is transmitted not only to the cells directly in front of the synthetic cell (relative to the wire) as a compressive load, pushing them toward the wire, but also to the cells behind it as a tensile load, effectively pulling them toward the wire. Thus, the $\frac{1}{3}$ factor accounts for the fact that, in three dimensions, two out of six possible surface orientations will be aligned to experience the force from the wire, providing a practical approximation of the effective area over which the pressure is applied. At close proximity to the wire tip (approximately $25\,\mu\mathrm{m}$), the pressure p_M reaches its maximum, indicating a highly localized mechanical effect. However, as the distance increases, the magnetic normal traction p_N (see Eq. (1.33)), which results from the enhanced magnetic field rather than its gradient, becomes the dominant mechanical factor (compare dashed and solid lines in Fig. 3.12f–g). This is also the case for the situation captured in Fig. 3.12a–c. The directionality of the corresponding forces is distinct: p_M is oriented toward the wire, whereas p_N acts outward from the surface of the synthetic magnetic cell (see schematic in Fig. 3.12h). Furthermore, the relative magnitudes of these pressures depend on the local values of the magnetic field and its gradient at each specific position. The superposition of these two pressure components leads to asymmetric deformation of the magnetic synthetic cell, reflecting the complex interplay of mechanical forces generated by the localized magnetic field and its gradient.

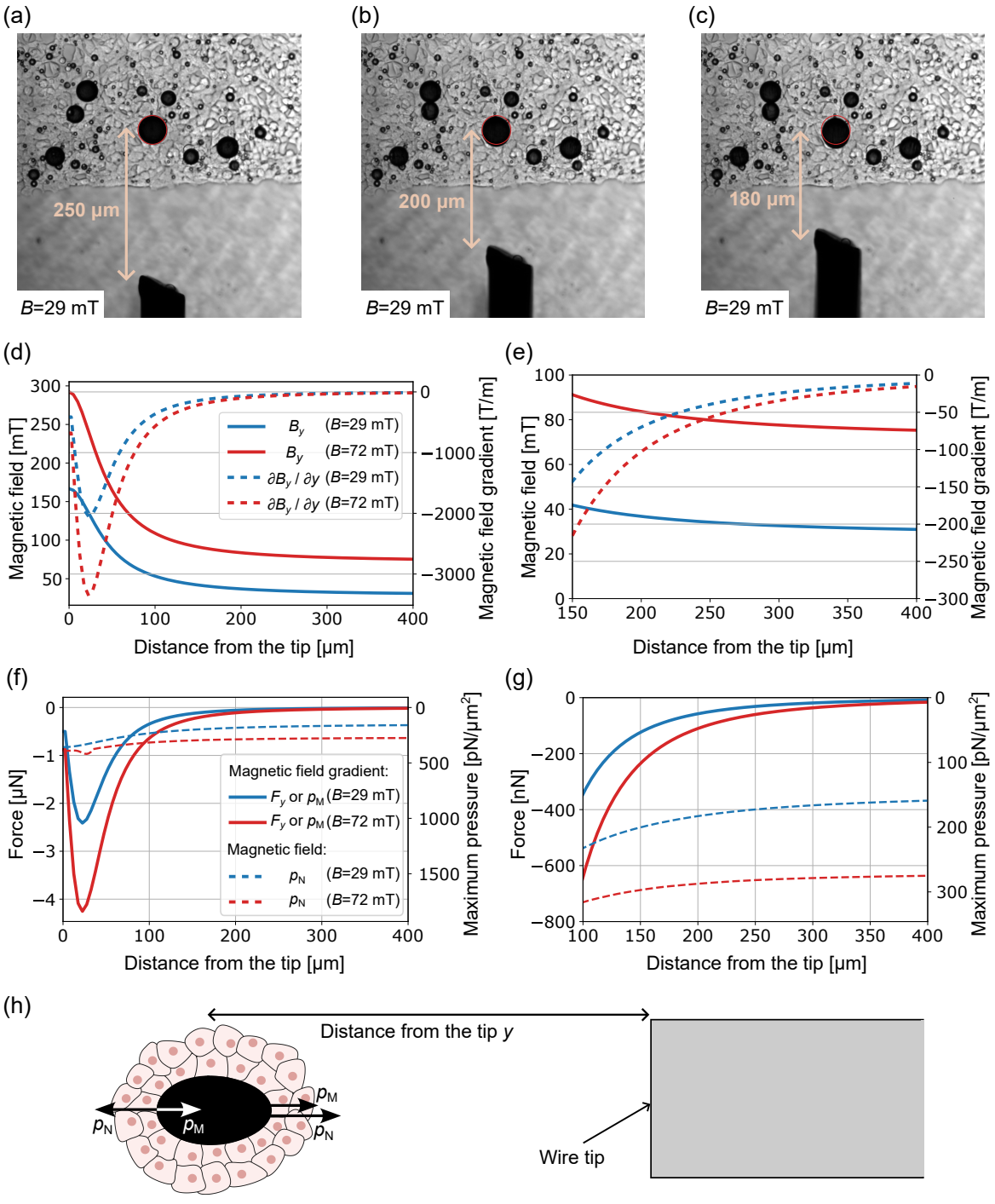

Figure 3.12. Characterization of magnetic synthetic cell behavior in a microscale-localized magnetic field gradient setup, as described in Fig. 3.10: (a)–(c) microscopy images showing the 75–µm thick wire approaching the selected magnetic synthetic cell (its original, undeformed shape at its initial position is indicated in red for reference); (d) magnetic field and magnetic field gradient as a function of distance from the wire tip, measured for the configurations within external homogeneous magnetic fields of 29 mT and 72 mT; (e) magnified view of (d); (f) estimated magnetic force acting on the selected synthetic cell from (a)–(c), along with the corresponding maximum pressure p_{M} exerted on adjacent cells and the maximum magnetic normal traction p_{N}; (g) magnified view of (f);

Figure 3.12. (Continued) (h) schematic illustration of the deformed synthetic magnetic cell, indicating the directions of the maximum pressure p_{M} (arising from the magnetic field gradient) and the magnetic normal traction p_{N} (arising from the enhanced magnetic field).

In summary, we have demonstrated that a microscale-localized magnetic field gradient can be used to selectively exert a larger force on an individual synthetic magnetic cell, provided it is spatially isolated from other synthetic cells in the vicinity. The interplay between this localized pressure and the magnetic normal traction, arising from the enhanced magnetic field, produces a greater mechanical effect on cells situated directly in front of the targeted cell, on the side facing the wire. This approach offers a powerful tool for spatially precise mechanical actuation within cell monolayers, and could be leveraged to control collective behaviors such as cell migration in engineered tissue systems.

3.2 Guidance of Cellular Sprouts

The vascular system is composed of a complex, branched network of blood vessels that ensures the delivery of oxygen and nutrients, thereby maintaining the physiological function of all tissues and organs [162, 163]. The formation of new blood vessels occurs predominantly through sprouting angiogenesis, a process in which endothelial cells from pre-existing vessels undergo a series of coordinated events, including basement membrane degradation, sprout initiation, proliferation, migration, lumen formation, and stabilization [162, 164]. Sprouting angiogenesis plays a central role not only in embryonic and organ development but also in wound healing, tissue regeneration, and the integration of engineered tissues [165–167]. Consequently, gaining control over this process is a major goal in tissue engineering and regenerative medicine. By manipulating angiogenic mechanisms, it may become possible to control the formation of complex vascularized tissue structures and restore function in damaged organs [167, 168]. At the same time, abnormal angiogenesis contributes to numerous pathological conditions, including cancer and retinal diseases such as diabetic retinopathy and age-related macular degeneration [169–171]. In these cases, targeted control of abnormal sprouting could lead to more effective treatments. Effective therapeutic strategies targeting these diseases require a deeper understanding of how to inhibit or normalize excessive sprouting [169–171]. Achieving such control over sprouting angiogenesis requires a comprehensive understanding of the intracellular mechanisms that govern critical processes such as the initiation of new sprouts, the selection of leading tip cells, the regulation of sprout number, and the collective migratory behavior of endothelial populations [164]. While it is established that angiogenesis is regulated by an interplay

between biochemical and biophysical cues, the precise signaling pathways and molecular mechanisms underlying these processes remain incompletely understood [166]. In this context, studying mechanotransduction, the conversion of mechanical signals from the cellular microenvironment, including neighboring cells, into biochemical responses, may offer valuable insights into the regulatory pathways involved in endothelial sprouting [166].

In this study, we investigated the ability to guide sprouting behavior using controlled magneto-mechanical forces. Specifically, magnetic field gradients were applied to endothelial cells that had internalized superparamagnetic nanoparticles, allowing for spatially defined mechanical stimulation.

3.2.1 3D *in vitro* Cellular Models to Study Sprouting Dynamics

To investigate sprouting behavior using magneto-mechanical forces as a guiding stimulus, two well-defined *in vitro* models were implemented, both employing cells pre-incubated with magnetic nanoparticles:

(i) Collagen 3D invasion assay: Endothelial cells were seeded on top of a 3D collagen matrix and allowed to invade the gel, following the model developed by Bayless *et al.* [164]. This was accomplished using an imaging chamber (inner diameter of 9 mm) with two openings, where collagen was injected through one hole and, after polymerization, cells were seeded onto the matrix surface via the second opening (see Fig. 3.14b; wire insertion is discussed later).

(ii) Spheroids embedded in collagen: Spheroids were generated from human umbilical vein endothelial cell using Aggrewell microwell plates (*Stemcell Technologies*) and subsequently embedded in collagen matrices to allow outgrowth of endothelial cell sprouts originating from each spheroid (see Fig. 3.14c; wire insertion is discussed later). The protocol was adapted from established methods previously reported in the literature [172, 173].

3.2.2 Characterization of Nanoparticle-Loaded Cells

To enable magnetic manipulation, endothelial cells were incubated with superparamagnetic nanoparticles provided by collaborators at the Center for Nanomedicine, South Korea. The nanoparticles consisted of a zinc-doped ferrite core ($Zn_{0.4}Fe_{2.6}O_4$) with a diameter of approximately 15 nm. The core was encapsulated in a silica (SiO_2) shell, followed by surface functionalization with fluorescein and a final polyethylene glycol (PEG) coating. The resulting hydrodynamic diameter was approximately 22 nm.

For the purpose of evaluating magnetic forces acting on individual cells within a magnetic field gradient, magnetometry data obtained from a nanoparticle ensemble was converted to represent the average magnetic moment per single nanoparticle (see Fig. 3.13). This value was then scaled to estimate the magnetic moment per cell (see Fig. 3.13), based on an estimated internalization of $2 \cdot 10^6$ nanoparticles per cell, as quantified by H. K. Senapati using inductively coupled plasma mass spectrometry.

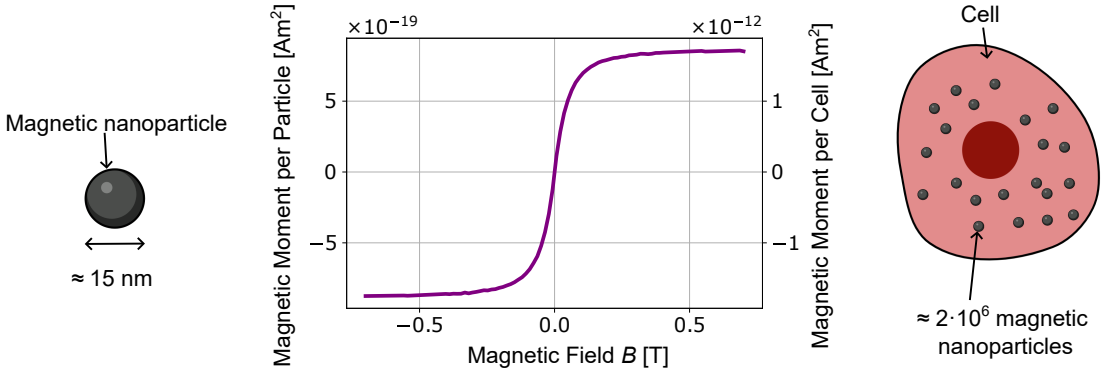

Figure 3.13. Magnetometry measurements showing the average magnetic moment per nanoparticle and per cell, assuming an internalization of $2 \cdot 10^6$ nanoparticles per cell.

3.2.3 Magnetic Gradient Setup to Guide Sprouting

The magnetic setup used to generate the magnetic field gradient was designed to meet several key criteria:

(i) Sufficient force: The magnetic setup was required to accommodate both 3D *in vitro* models and generate a magnetic field gradient strong enough to exert biologically relevant forces on endothelial sprouts. The magnitudes of mechanical forces reported to influence cellular behavior vary widely across the literature. For example, Bongaerts *et al.* [174] demonstrated that forces within the low piconewton regime are sufficient to induce migratory responses. In contrast, Kunze *et al.* [175] observed that cellular migration in response to mechanical cues can require forces on the order of several hundred piconewtons per cell. In addition, the polarization of key biochemical pathways within cells, linked to the regulation of directed cell behaviors, has been achieved using mechanical forces ranging from a few piconewtons [176] to several nanonewtons [177]. Based on these findings, the setup needed to be capable of producing tunable forces up to several hundred piconewtons per cell.

(ii) Microscale dimensions: To enable live-cell imaging under a microscope, the magnetic field gradient had to be generated in the horizontal direction. This imposed constraints on the microscale geometry of the setup, as direct contact between the cells and magnetic components had to be avoided to preserve cell viability.

(iii) Macroscale dimensions: The setup needed to accommodate a standard 35 mm Petri dish commonly used for cell culture. Additionally, to ensure compatibility with the incubated confocal laser scanning microscope (*Zeiss* LSM 980), the outer diameter of the setup was constrained to a maximum of 60 mm.

(iv) Experiment scalability: After the initial fabrication of the main setup, only minimal preparation should be required before each individual experiment, enabling efficient and reproducible operation across multiple experiments.

To meet these criteria, I evaluated a variety of designs for generating magnetic field gradients using finite element simulations in *COMSOL Multiphysics*. The analyzed designs included permanent magnets of various shapes and wires of differing diameters, introduced into external magnetic fields produced by distinct methods. Due to the spatial limitations imposed by the microscope stage and the mismatch in scale between conventional magnets and microscale biological systems, I selected a configuration that produces a homogeneous magnetic field using a Halbach array, with a magnetic gradient introduced by placing a wire within this field. The Halbach array is composed of 12 cubic neodymium magnets (grade N50), each with a side length of 8 mm, arranged in a circular configuration (see Fig. 3.14a). This design accommodates a standard 35 mm Petri dish at its center while remaining compact enough to fit within the constraints of the Zeiss LSM 980 confocal microscope stage. Simulation results indicate that the magnetic field at the center of the dish reaches approximately 88 mT and is highly uniform before the wire is introduced (see magnetic field lines in Fig. 3.14a).

The magnetic field gradient is established by incorporating a cobalt wire with a diameter of 500 µm. Cobalt was selected for its superior magnetization under the total magnetic field present in the setup compared to nickel, as well as its greater corrosion resistance relative to iron. To mitigate cytotoxic effects, the wire was coated with a 10 µm layer of parylene directly within the Petri dish [178]. This coated wire can then be embedded into the collagen matrix for use in both 3D *in vitro* cellular models (see Fig. 3.14b–c), allowing the distance to the targeted cells to be minimized to less than 200 µm.

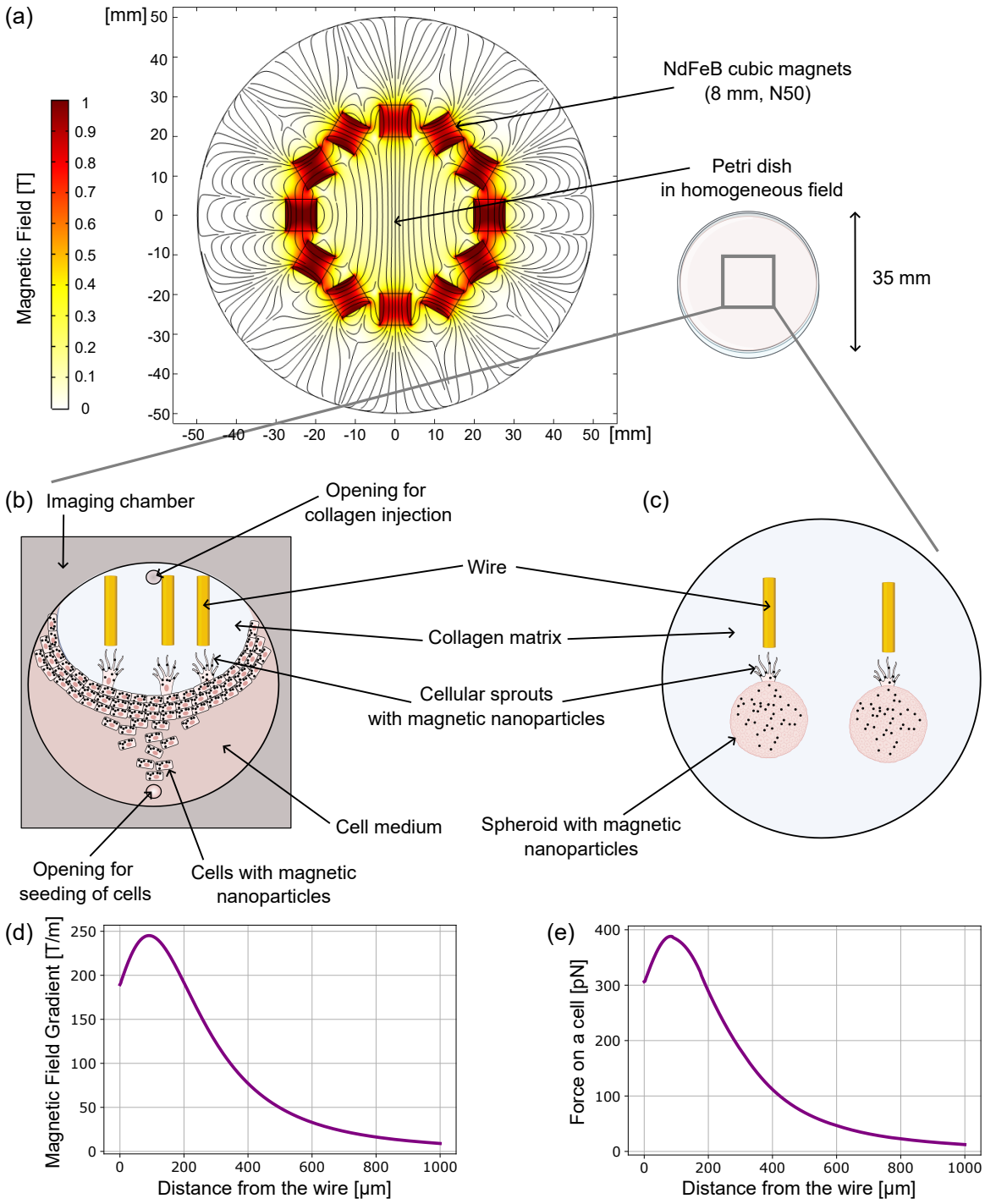

Figure 3.14. Magnetic gradient setup for guiding cellular sprouting: (a) magnetic field and field lines generated by a Halbach array designed to fit the confocal microscope and accommodate a 35 mm Petri dish in the central homogeneous field region; (b) 3D *in vitro* model with surface-seeded cells invading a collagen matrix, with a cobalt wire used to guide sprout direction; (c) 3D *in vitro* model with endothelial spheroids embedded in collagen, also guided by a cobalt wire; (d) magnetic field gradient as a function of distance from a 500 µm thick cobalt wire, based on magnetometry measurements of the actual wire; (e) calculated magnetic force acting on a single cell versus distance from the wire tip in this configuration.

For the calculations of the magnetic field gradient presented in Fig. 3.14d, I used magnetometry data measured from the actual cobalt wire. This approach yielded a magnetic gradient approximately two times lower than simulations based on bulk cobalt properties with high magnetic remanence (data not shown). According to simulations using the measured magnetic properties of the cobalt wire, the magnetic field gradient remains above $\approx 200\,\mathrm{T/m}$ within 200 µm of the wire tip. This gradient corresponds to magnetic forces exceeding 300 pN on a single cell (see Fig. 3.14e), as calculated using the magnetization data shown in Fig. 3.13. In these calculations, I assumed, as a simplification, that all nanoparticles are located at the same position within the cell. By incorporating multiple wire segments, it is possible to observe several independent events simultaneously (see Fig. 3.14b–c). Moreover, the magnetic forces can be increased by using thinner wires, provided the distance to the target cells can be further reduced. As discussed previously, decreasing the wire diameter results in a higher magnetic field gradient, but the peak of the gradient magnitude shifts closer to the wire tip (see also Fig. 1.7b).

While the magnetically induced drift of an individual nanoparticle remains significantly smaller than its thermally driven displacement over the same time period (*e.g.*, in water: drift velocity $\approx 1.4\,\mathrm{\mu m/s}$ as estimated from Eq. (1.4), compared to a root mean square displacement of $\approx 8\,\mathrm{\mu m}$ due to diffusion over 1 s from Eq. (1.16)), our objective is not to manipulate isolated particles. Rather, we are interested in the collective mechanical stress arising from a large ensemble of magnetic nanoparticles within the cell. Under our experimental conditions, the total magnetic force per cell reaches the hundreds of piconewtons range, which has previously been shown to be sufficient to influence cellular behavior [174–176]. Although these forces are lower than the nanonewton-scale forces reported by Tseng *et al.* [177], our system offers the advantage of high throughput due to straightforward sample preparation and the ability to perform live observations using a confocal microscope. If compatibility with live confocal imaging were not required, the magnetic forces could be substantially increased, for example by using larger magnets in the Halbach array. This could result in approximately a fivefold increase in magnetic force at an external field of 0.5 T, while keeping the microscale experimental configuration unchanged.

3.3 Overview of Magnetic Manipulation of Cells

After reviewing the literature and designing several magnetic setup configurations intended for cell stimulation and manipulation, the main findings of generating stimuli on cells can be summarized as follows:

(i) Mechanical forces required to elicit cellular responses span several orders of magnitude in existing literature, ranging from a few piconewtons to nanonewtons per cell.

(ii) Maximum magnetic force generated in presented experimental setups:

- Synthetic magnetic cells + homogeneous magnetic field (electromagnet coil):
  The maximum pressure exerted at the region of highest droplet curvature is $\approx 200\,\mathrm{pN}/\mu\mathrm{m}^2$.
- Synthetic magnetic cells + magnetic field gradient and field enhancement (iron wire, electromagnet coil):
  At distance 100 µm from the wire, the maximum pressure reaches $\approx 600\,\mathrm{pN}/\mu\mathrm{m}^2$ (due to gradient attraction) and $\approx 700\,\mathrm{pN}/\mu\mathrm{m}^2$ (due to field enhancement), both measured at the region of maximal droplet deformation.
- Cells with internalized magnetic nanoparticles + magnetic field gradient (cobalt wire, Halbach array):
  At distance 100 µm from the wire, forces around 350 pN per cell are expected.

(iii) While synthetic magnetic cells are theoretically capable of generating forces up to several tens of nanonewtons per natural cell at the region of highest droplet curvature, the actual mechanical stimulus delivered to the cell monolayer is likely substantially reduced in practice. This reduction is primarily attributed to geometric mismatches, as the synthetic magnetic cells employed in this study were typically much taller than the cell monolayer, thereby limiting efficient force transmission across the monolayer.

(iv) The design of the magnetic setups in this study was primarily constrained by the requirement that all components be compatible with specific inverted microscope platforms used for real-time cellular observation. These spatial and geometric limitations substantially restricted the range of possible magnetic configurations, making it challenging to achieve the force magnitudes reported in studies, where real-time observation is not required.

Chapter 4

Transport Through Vitreous Substitutes and Native Ocular Tissue

The transport of nanoscale materials within tissue presents significant challenges due to the intricate and inhomogeneous tissue environment. Beyond the intrinsic viscoelastic properties of the tissue, the movement of any nanoobject is influenced by a range of additional factors, such as molecular adhesion, including mechanisms like electrostatic interactions, as well as the presence of biological barriers with a microstructure that prevents transport of objects above a critical size. The complexity is further compounded by the frequent reliance on various animal *ex vivo* models, which introduce species-specific and experimental variables that may not accurately reproduce the physiological conditions of the human tissue *in vivo*. Specifically, in the field of ophthalmology, critical questions remain regarding the effective transport of nanoscale therapeutics and the precise constraints imposed by tissue architecture and barrier properties, highlighting the need for further systematic studies.

In pathological conditions or following surgical procedures, the replacement of native biological structures with biomimetic substitutes may be necessary to restore anatomical and functional integrity. The eye is one example, where substitutes such as hydrogels can be used to mimic the properties of the vitreous body. Efficient drug delivery through these materials post-implantation necessitates a comprehensive understanding of material transport at the micro- and nanoscale. Although hydrogels typically provide a more homogeneous and predictable medium compared to native tissue, they still impose significant constraints on transport due to factors such as higher viscosity compared to water, surface adhesion and porosity. These properties directly impact the mobility of therapeutic agents and must be carefully characterized to optimize their delivery.

Author Contributions

The work presented in Section 4.2 was carried out in collaboration with Dr. med. M. Hammer from Heidelberg University Hospital and the DJ Apple Laboratory, under the mentorship of JunProf. Dr. P. Uhl from Heidelberg University. The novel hydrogels were developed by Dr. med. M. Hammer's research group and fabricated by Dr. S. Wohlfart. I fabricated the monodisperse magnetic particles and helical propellers via GLAD. I imaged most of the structures using SEM, with Dr. M. Alarcón-Correa and Dr. F. Peter contributing additional imaging. I designed the experimental setup and protocol for pore size characterization, with a contribution to the final procedure from F. Hecht. I also developed the experimental protocol for investigating propulsion through the hydrogels using helical micropropellers. The experiments, covering preparation of the various gel formulations, as well as testing different particle types and microswimmer geometries, were performed by I. Wittmann and F. Hecht, following my guidance. I regularly discussed progress with Dr. M. Alarcón-Correa.

The work presented in Section 4.3 was carried out in close collaboration with Dr. F. Peter, Dr. M. Alarcón-Correa, and Dr. D. Missirlis. The Ussing chamber experiments were conducted by myself and E. Schmitt during his bachelor's thesis, with help from Dr. F. Peter. Nuclear magnetic resonance measurements were performed by I. S. Bochert. Together with Dr. F. Peter and Dr. M. Alarcón-Correa, we developed the sclero-retinal explant model. The preparation of samples using this model was performed by myself and Dr. M. Alarcón-Correa, with help from M. I. Real de Asúa Pérez-Serrano. I conducted the cryotome sectioning. Functionalization of silica beads with collagenase was developed by Dr. F. Peter and Dr. M. Alarcón-Correa. Throughout the project, microscopy imaging and post-processing were conducted by Dr. F. Peter and Dr. D. Missirlis. For the purpose of this thesis, I processed the microscopy images, with initial support from Dr. A. Song for intensity profile plotting. High-resolution scanning electron microscopy was conducted and analyzed by Dr. I. Wacker and E. R. Curticean from the research group of Prof. Dr. R. Schröder. Throughout the project, I benefited from discussions with Dr. F. Peter, Dr. M. Alarcón-Correa and Dr. D. Missirlis.

Scope of the Chapter

The first part of this chapter, Section 4.1, provides an overview of ocular anatomy, current therapeutic approaches for a range of ophthalmological disorders, and emerging treatment strategies along with their associated challenges. It also reviews the state of the art in research closely aligned with the focus of our work presented later in the chapter.

The second part of this chapter, Section 4.2, focuses on hydrogels composed of hyaluronic acid, a promising class of vitreous humor substitutes. We begin by evaluating their porosity using two sizes of monodisperse magnetic particles I fabricated, whose penetration is driven by magnetic field gradients generated by permanent magnets. Subsequently, we employ rotating magnetic fields to propel various microhelices through these hydrogels, demonstrating the theoretical feasibility of targeted drug delivery within such biomimetic environments.

In the third part of this chapter, Section 4.3, we shift focus to native ocular tissue and advance the development of an innovative therapeutic strategy, envisioned for non-viral and minimally invasive delivery of genetic material to retinal cells. We propose the use of helical magnetic micropropellers as a novel delivery vector. We envision that these micropropellers could be introduced into the vitreous humor and guided precisely towards the retina. To successfully reach the target retinal cells, the micropropellers must traverse several ocular barriers, with the inner limiting membrane (ILM) presenting the most significant challenge. We first address the permeability of this layer and its size exclusion limit as discussed in the existing literature by investigating the range of sizes supposedly capable of permeating the ILM. Experimentally, we investigate retinal explants mounted in diffusion chambers, known as Ussing chambers, to assess passive and electrically enhanced diffusion. Although high voltage can enhance diffusion across the retinal tissue, the combined effects of electrical stimulation and mechanical stress associated with mounting the explants in the chamber was found to result in substantial tissue damage, indicating that electric fields and ionic currents may compromise tissue integrity. We therefore developed a new sclero-retinal explant model that minimizes retinal damage during handling. Following this, we first determined the size threshold of nanocomponents capable of crossing the ILM unaided. Subsequently, we studied their penetration after enzymatic ILM digestion, introduced also as a part of Dr. F. Peter's doctoral thesis [179]. To promote the transport of larger nanoparticles while maintaining tissue integrity, we show that conjugating collagenase enzymes to microbeads allows for a localized and controlled enzymatic activity, thereby lowering the total enzyme dosage required to degrade the ILM. By bringing these collagenase-functionalized particles into direct contact with the ILM, we achieve targeted and localized enzymatic degradation of the membrane, enhancing the transport of larger particles through the ILM. We envision that integrating all these findings will ultimately enable the development of micropropellers capable of delivering therapeutic cargo across the ILM to retinal cells.

4.1 Ophthalmic Background and Therapeutic Challenges

Vision loss is a rapidly growing public health concern. More than 1.1 billion people across the globe are currently living with some form of vision impairment, including 43 million with complete blindness and 295 million with moderate to severe vision loss [180, 181]. These numbers have more than doubled over the past three decades and the projections indicate that they will continue to increase within the next three decades, impacting up to 1.8 billion people by 2050 [180–182], in part due to a global increase in diabetes and an aging population.

The treatment of vision-threatening ocular diseases varies based on the underlying pathology and typically involves pharmacological therapies, laser interventions, or surgical procedures. Although these methods have led to significant advances in disease management, they frequently offer only partial or transient therapeutic benefit, may be associated with adverse effects or procedural risks, and are often insufficient to reverse established tissue damage. As a result, clinical outcomes remain suboptimal in many cases. There is a pressing need for innovative therapeutic strategies that extend beyond current treatment paradigms. Although clinical needs are well recognized and promising therapeutic concepts exist in theory, their practical implementation remains limited by unresolved technical, biological, and translational challenges.

For context, I begin with a concise overview of the ocular anatomy.

4.1.1 Eye Anatomy

The anatomy of the eye, illustrated in Fig. 4.1, highlights the key structures involved in visual perception. Light first encounters the cornea, a transparent, curved structure that plays a crucial role in refracting it [183, 184]. The light then passes through the pupil, an adjustable aperture controlled by the iris, which modulates its diameter to optimize light intake based on ambient conditions [183, 184]. Following this, the lens further refines the focus to project a sharp image onto the retinal surface [183, 184]. The neurosensory retina is located deep within the eye, shielded by multiple anatomical layers, specifically the sclera, choroid, and retinal pigment epithelium (RPE), the latter serving as a critical barrier maintained by its intercellular tight junctions. Within the retina, photoreceptors (rods and cones) absorb incoming photons and convert them into electrical impulses [185]. The macula, which spans only $\approx 4\,\%$ of the total retinal area, is densely populated with cone photoreceptors and is essential for most human vision [186]. These electrical signals are processed through a network of retinal interneurons and ultimately transmitted by retinal ganglion cells, whose axons converge to form the optic nerve [187]. This neural pathway conveys all visual information from the eye to the brain, shaping our perception of the visual world [187].

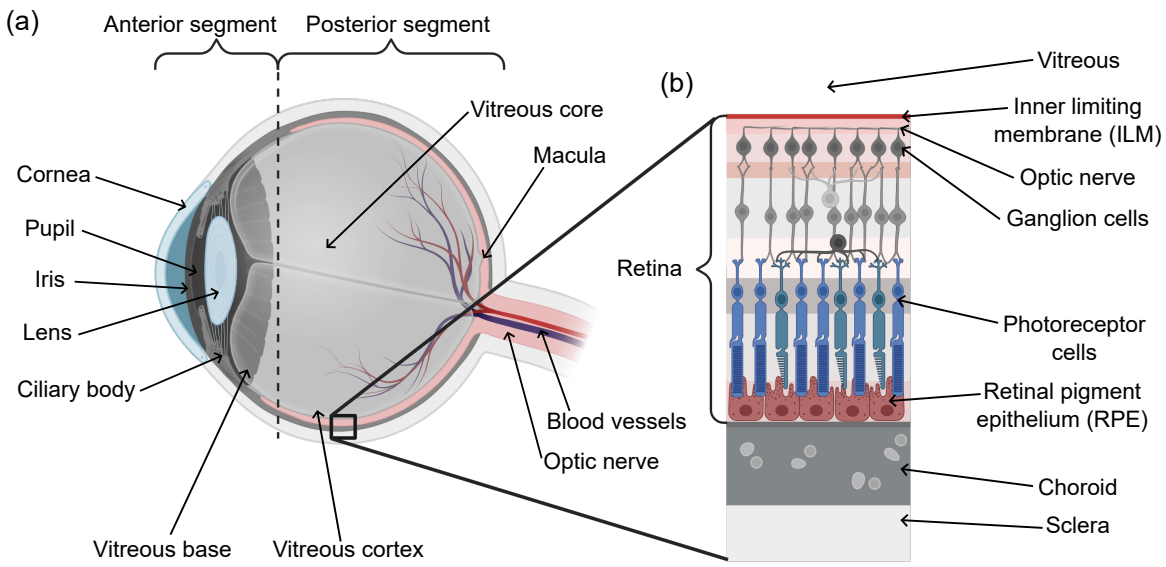

Figure 4.1. Anatomy of the human eye: (a) schematic overview of the eye globe and (b) magnified cross-sectional view illustrating the spatial organization of ocular layers and internal structures.

The vitreous body, while not active in light perception beyond permitting light transmission, contributes significantly to maintaining the eye's mechanical and molecular homeostasis [188]. Composed predominantly of water (98–99%), the vitreous body also contains collagen fibers noncovalently bound to hyaluronic acid, forming a polymer scaffold [188]. This structure stabilizes the lens and retina, while dissipating external mechanical forces [188, 189]. Additionally, the vitreous facilitates molecular exchange with adjacent structures, which is essential for maintaining its metabolic function and integrity [188].

The inner limiting membrane (ILM) is a basement membrane at the vitreoretinal interface and consists of a dense, three-dimensional matrix of extracellular proteins, including collagen IV, laminin, and proteoglycans [190, 191]. The ILM undergoes age-related thickening, measuring approximately $(300 - 350)\,\mathrm{nm}$ in individuals around 20 years of age and exceeding 1500 nm by the age of 80 [192]. Although the ILM is essential during early retinal development, its physiological function in the adult eye remains unclear [193]. Consequently, ILM peeling has become a common surgical practice in the treatment of conditions such as macular holes [193]. The impact of ILM removal on retinal function remains a subject of debate: whereas some studies report no significant changes post-peeling, others have observed reductions in retinal sensitivity [194].

4.1.2 Vitreous Replacement After Vitrectomy

Vitrectomy is a common surgical intervention involving the removal of the vitreous body and is employed in the treatment of various vision-threatening ocular conditions [188, 189, 195]. Indications include retinal pathologies (e.g., retinal detachment, diabetic retinopathy, macular holes), intraocular infections and inflammation, ocular trauma, vitreous opacification, and age-related vitreous liquefaction [188, 189, 196–199].

Following vitrectomy, the vitreous does not regenerate. Instead, the vitreous cavity fills with aqueous fluid, which lacks the structural and biochemical properties of the native vitreous [188]. To preserve ocular homeostasis and function, an appropriate vitreous substitute is therefore required [188].

An ideal vitreous substitute should closely mimic the native vitreous in both structure and function. Essential characteristics include optical transparency, biocompatibility, chemical inertness and the ability to maintain intraocular pressure for preserving the anatomical positioning of ocular structures [188, 189, 200, 201]. It should also exhibit viscoelasticity similar to the natural vitreous for effective buffering of mechanical forces, long-term stability, and hydrophilicity to ensure uniform tamponade throughout the vitreous cavity [188, 189, 201]. Additionally, sufficient surface tension is important for facilitating retinal break closure, along with injectability through small-gauge instruments, physiological pH, and a porous microstructure that supports nutrient diffusion and may enable targeted drug delivery [188, 189, 200].

Currently used vitreous substitutes in clinical practice provide temporary mechanical support but lack key physiological properties of the natural vitreous [201]. Gases offer temporary tamponade through surface tension and expansion but are quickly absorbed and lack viscoelasticity, sufficient density, and optical clarity [188]. Silicone oils provide longer-lasting tamponade but are limited due to their significantly different refractive index compared to water, causing reduced visual acuity, and because they provide insufficient tamponade in the inferior retina [188]. Their hydrophobic nature increases the risk of emulsification and related complications, requiring removal within months [188, 189]. Perfluorocarbon liquids are limited to intraoperative use due to their high density, mismatched refractive index, lack of elasticity, and risk of inflammation [188].

Polymer-Based Vitreous Substitutes

As none of the vitreous substitutes currently employed in clinical practice adequately replicate the structure and function of the native human vitreous, significant research efforts have focused on the development of polymer-based alternatives. These materials offer several compelling advantages, including high water content, the potential for uniform retinal tamponade via controlled viscosity and swelling pressure, and tunable rheological and porous properties [188]. Particularly, the adjustable porous matrix presents a significant improvement over traditional vitreous substitutes by enabling the encapsulation and controlled release of therapeutic agents, such as bioactive molecules and therapeutic cells [200]. An additional benefit of hydrogel-based substitutes is that they typically do not require surgical removal after implantation, thereby addressing a major drawback of many conventional vitreous substitutes [202]. A wide range of natural and synthetic polymers has been investigated for this purpose, including hyaluronic acid, collagen, gellan, chitosan, alginate, polyvinyl alcohol methacrylate, poly(ethylene glycol), acrylic acid and acrylamide [189]. However, the clinical translation of many polymeric vitreous substitutes developed in the past decade has been limited by challenges such as insufficient optical transparency, refractive index mismatch, degradation, limited biocompatibility, and cytotoxicity associated with certain crosslinking agents [189].

Among natural polymers, hyaluronic acid and collagen have received particular attention due to their excellent biocompatibility and their presence as key components of the native vitreous [200, 202, 203]. However, these materials generally provide poor tamponade and short residence times *in vivo*, primarly due to rapid degradation and low viscosity [202]. Hyaluronic acid has been employed in its native form, as well as in derivatives such as sodium hyaluronate, or in combination with other natural compounds like gellan or silk [200, 202, 203]. Depending on the formulation, it has been used without crosslinking, chemically crosslinked via methods such as UV irradiation and dihydrazide chemistry, or incorporated into thermoresponsive systems—particularly in conjunction with gellan—where *in situ* gelation is induced by physiological temperature and ionic conditions [188,202,203]. Nevertheless, rapid degradation and the consequent changes in mechanical and optical properties remain a major limitation for hyaluronic acid-based hydrogels [200, 202, 203]. This drawback is particularly critical, as ideal vitreous substitutes require long-term stability to ensure sustained functionality [202]. To address this, enzymatically crosslinked hyaluron acid–silk composite hydrogels have been developed, demonstrating improved stability and slower degradation profiles in situ [204].

4.1.3 Retinal Gene Therapy

A substantial proportion of the visual impairments causing blindness, including age-related macular degeneration and diabetic retinopathy, originate from pathological changes in the retina, particularly affecting photoreceptor cells and RPE cells (see Fig. 4.1) [205–207]. While gene and cell therapies offer significant promise for treating retinal diseases at their genetic roots, including recent advances in pediatric patients [208], achieving efficient, targeted and safe delivery to the affected retinal cells remains a major obstacle [209]. These delicate retinal layers are protected by several anatomical barriers, which both shield them from external harm and pose challenges for therapeutic intervention [210]. Among these, the RPE itself forms a critical barrier, and, together with the underlying choroid and sclera, limits the penetration of substances from outside the eye. Coming from the other side, the penetration is limited by the vitreous humor and particularly by the ILM [190, 191].

Current clinical trials for retinal gene therapy predominantly employ subretinal injection, a surgical procedure that introduces therapeutic agents into the space between the photoreceptors and the underlying RPE (see Fig. 4.2a), with viral vectors most commonly used as the delivery vehicles [209]. This approach results in a partial retinal detachment and carries risks of serious complications, including permanent retinal detachment or the formation of retinal holes [211]. Furthermore, the therapeutic effect is generally limited to the immediate vicinity of the injection site, thereby restricting the extent of the treated retina [212]. Beyond the risks associated with the procedure, the use of viral vectors can provoke adverse immune responses, posing significant safety concerns. Therefore, advancing research into non-viral vectors and exploring less invasive delivery methods is essential to improve the safety, efficacy, and accessibility of gene therapy for retinal diseases.

In this context, intravitreal injection has gained attention as a promising less invasive alternative to subretinal delivery (see Fig. 4.2b), aiming to reduce procedural risks while providing broader retinal access [213]. However, its efficacy is significantly limited by intraocular barriers. Our group has previously shown that magnetic helical micropropellers can successfully traverse the vitreous humor [214], yet the ILM remains a principal obstacle. Its densely organized extracellular matrix significantly impedes the penetration of nanoscale therapeutics, thereby restricting access to underlying retinal cells [190, 191].

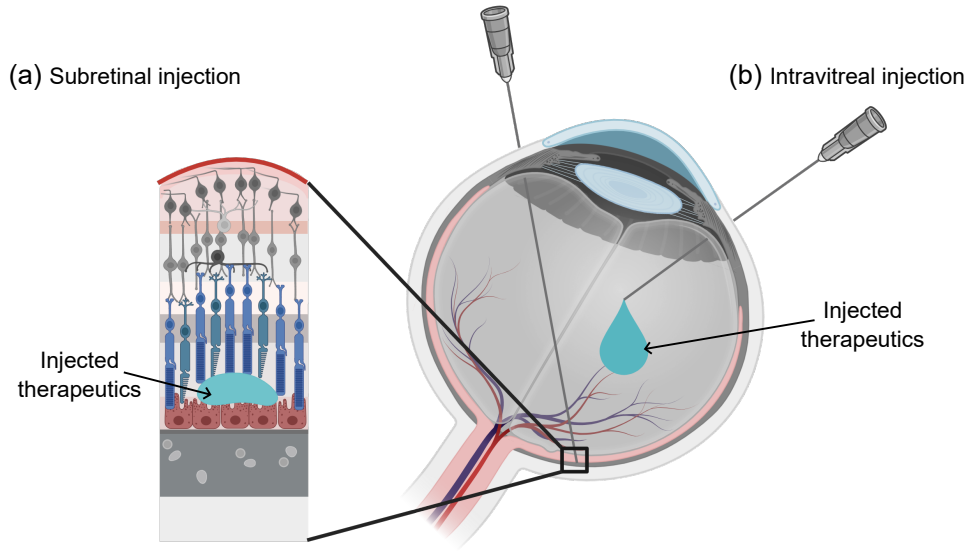

Figure 4.2. Schematic depiction of principal therapeutic strategies for retinal diseases: (a) subretinal injection of therapeutics into the space between the retinal pigment epithelium (RPE) and the photoreceptor layer; (b) intravitreal injection of therapeutics directly into the vitreous body.

4.1.4 Nanoscale Crossing of the Inner Limiting Membrane

Although retinal gene delivery has garnered considerable scientific interest, the characteristics, such as size and type, of nanoscale materials capable of crossing the human ILM remain inconclusive in the existing literature. Multiple factors account for this ambiguity:

(i) The poor correlation between *in vitro* experiments and *in vivo* conditions [215].

(ii) *Post-mortem* tissue degradation and the cessation of physiological functions in *ex vivo* experiments [216, 217].

(iii) Structural differences in the ILM across species, which challenge the direct translation of results from animal models to humans [218].

Some of these limitations can be partially addressed, yet complete elimination remains beyond reach. Current guidelines therefore recommend prioritizing large animal models that more closely replicate human ocular structure, as well as integrating *ex vivo* approaches during early experimental stages [215]. Nonetheless, *in vivo* experimentation at these stages is often constrained by ethical concerns, limited access to suitable models, and high financial costs. Therefore, *ex vivo* approaches remain essential in the field, with particular emphasis on reducing the *post-mortem* interval to better maintain physiological relevance [219].

In this context, the following discussion focuses on findings from large animal models, including both *ex vivo* and *in vivo* results.

The determination of the ILM size cut-off has been explored using a range of experimental models; however, despite its importance for retinal drug delivery, the findings remain inconclusive. The vitreous contains a high concentration of negatively charged molecules, which retain positively charged nanomaterials and hinder their diffusion, thus restricting their effectiveness [220–222]. Consequently, most research has shifted towards assessing the permeability of negatively charged molecules or nanoparticles, as they are capable to traverse these electrostatic traps.

Based on standard 8-mm porcine retinal explants, P. S. Apaolaza *et al.* found that while the majority of 20 nm gold nanoparticles accumulated on the surface of the ILM, those conjugated to hyaluronan could traverse the ILM and reach deeper retinal layers [223]. In interpreting such findings, it is crucial to account for the possibility that particles could inadvertently move around the explant and diffuse through the retina from the opposite, more permeable RPE side, which could complicate the interpretation of results. This is particularly relevant in the context of retinal explant experiments, where nanoscale materials are typically applied to the surface of the explant in culture medium and are therefore not prevented from diffusing around the tissue.

To address this limitation, several research teams have adopted the use of the Ussing chamber, which allows retinal explants to be placed between two isolated compartments, thereby controlling the diffusion direction. For example, T. L. Jackson *et al.* used this system with FITC-dextrans of different molecular sizes, consistently identifying a size barrier of about 6 nm across ILMs from humans, pigs, cows, and rabbits [224]. Likewise, a custom-designed Ussing chamber was employed by Y. Tao *et al.* to quantitatively evaluate the permeability thresholds of different porcine retinal layers, and their findings indicate that the ILM restricts the passage of nanomaterials larger than approximately 8 nm [225]. In addition, studies conducted by H. M. Kim *et al.* utilizing the Ussing chamber indicated that brimonidine, with a molecular weight of 292 Da (about 2 nm), successfully crossed the rabbit ILM; in contrast, bevacizumab, a larger molecule at 149 kDa (approximately 10 nm), was largely impeded from permeating this membrane [226].

To preserve the integrity of the vitreoretinal interface, K. Peynshaert *et al.* proposed an alternative *ex vivo* model that retains the vitreous attached to the retinal explants [227]. Using this approach, they determined an ILM permeability size threshold of approximately 40 nm using carboxylated polystyrene particles, thus substantially lower than the 100 nm cut-off observed in their conventional retinal explants [227]. In subsequent work, the same research group demonstrated that although hyaluronic acid functionalization improved the intravitreal mobility of 125 nm lipoplexes, this coating did not enable these larger complexes to traverse the ILM in bovine vitreoretinal explants [228]. Consistent with these

observations, S. Tavakoli *et al.* demonstrated that 50 nm liposomes with either negative or neutral surface charge were able to penetrate bovine vitreoretinal interface, whereas 100 nm liposomes failed to cross this barrier [229].

In an *in vivo* experiments conducted on rhesus monkeys, J. Mordenti *et al.* reported that following intravitreal administration, a 48 kDa antibody ($\approx 7\,\mathrm{nm}$) reached the RPE layer [230]. In contrast, a larger 148 kDa antibody ($\approx 10 - 15\,\mathrm{nm}$) did not diffuse to this region [230].

Overall, these findings indicate that there is no consistent agreement regarding the ILM size exclusion cut-off in large animal models as the results indicate thresholds ranging from below $\approx 10\,\mathrm{nm}$ to below $\approx 100\,\mathrm{nm}$. It should also be noted that several experiments were conducted on explants over many hours, which is likely to cause additional degradation effects or may damage the ILM through handling the explant.

4.1.5 Enhancing Transport Across the Inner Limiting Membrane

The smallest transfection agents employed in retinal gene therapy fall within the broad and uncertain permeability range of the ILM, estimated between 2 nm and 100 nm. Among these, adeno-associated viral vectors are a widely used platform for delivering genetic material to retinal cells, with capsid sizes measuring about 22 nm [231–236]. Non-viral delivery systems, including compacted DNA nanoparticles created by complexing a single DNA molecule with a pegylated CK30 peptide, have been have been tailored to similar size range [179, 237]. These nanoparticles, which can accommodate larger genetic sequences, measure between 8 and 45 nm depending on the cargo and the conformation of the nanoparticle [179, 237]. Given that even the smallest of these vectors approach or surpass the estimated size exclusion limit of the ILM, passive diffusion across this barrier is unlikely to enable efficient delivery. This emphasizes the need for sophisticated delivery approaches to achieve effective transfection of retinal cells.

A range of strategies has been explored to improve the delivery of particles across the ILM. Some methods are designed to apply external forces, such as magnetic or electrical fields, to drive particles through the ILM. Other approaches focus on increasing the permeability of the ILM itself, either through physical means (e.g., light-based disruption) or biochemical methods (such as enzymatic digestion). Surgical removal of the ILM is another technique that has been shown to substantially increase transfection efficiency [235]. However, this method requires a vitrectomy, making it less desirable due to its invasiveness.

In one example of force-based delivery, S. Ahn *et al.* used permanent magnets to guide adeno-associated viruses that were conjugated to commercially available particles ($\approx 200\,\mathrm{nm}$ in diameter) in *ex vivo* porcine retinal explants and whole eyes [238]. Nevertheless, the relatively weak magnetic forces generated by the magnets raise questions about the actual contribution of magnetic guidance to the observed delivery efficiency. Another approach, described by E. Eljarrat-Binstock *et al.*, involved applying a low electric current to enhance the penetration of positively charged nanoparticle suspensions (20–45 nm) into rabbit retinas *in vivo* [239].

More recently, K. Peynshaert *et al.* developed a light-based method for ILM ablation by irradiating indocyanine green (ICG) bound to the ILM with short laser pulses [240]. This technique enabled effective ILM disruption in both bovine and human retinal explants, facilitating the entry of 126 nm pegylated carboxylated nanoparticles and lipid nanoparticles containing luciferase mRNA in bovine tissue. In a subsequent study, the same group encapsulated ICG within nanoparticles to achieve more localized ILM disruption in bovine retinal explants [241].

Enzymatic digestion of the ILM is another investigated method, employing enzymes such as pronase E, hyaluronan lyase, chondroitin ABC lyase, heparinase III, and collagenase VII [231,242,243]. While these enzymes can increase ILM permeability, higher concentrations have been associated with damage to nerve fibers and ganglion cells, and most studies to date have been limited to rodent models. Among enzymatic agents, ocriplasmin (brand name Jetrea), a recombinant protease derived from human plasmin, was the only one approved for intraocular use [244,245]. Although not primarily intended for ILM degradation, it aimed to facilitate vitreous liquefaction and posterior vitreous detachment to treat symptomatic vitreomacular adhesion and traction [245]. Despite initial clinical promise, ocriplasmin was later withdrawn from the market for commercial reasons, likely compounded by low success rates, which limited its widespread clinical adoption [244,246].

Although these approaches show promise for improving the delivery of therapeutic agents to the retina, further research is necessary to optimize their effectiveness and, importantly, to minimize potential damage to surrounding retinal tissue.

4.2 Transport Through Vitreous Substitutes

We first address the need for improved vitreous substitutes, which are implanted following vitrectomy for various clinical indications. In this context, we investigate hyaluronic acid-based hydrogels as model materials, evaluating their suitability for potential targeted delivery within the vitreous cavity. Specifically, we assess whether active transport through these substitutes is feasible using magnetically actuated helical nano- and micropropellers. While no drugs are involved in this study, such propellers could, in future applications, serve as carriers for therapeutic agents.

The hyaluronic acid-based gels utilized in this study are currently in preparation for patent filing by our clinical collaborators (Dr. med. M. Hammer's research group). Three different stock compositions, differing in hyaluronic acid concentration and molecular weight, were tested, no further information can be disclosed due to the ongoing patenting process. For the purpose of this thesis, I will refer to these stock compositions as follows:

(i) Lower hyaluronic acid concentration with a lower molecular weight (low c, low M_{w});

(ii) Higher hyaluronic acid concentration (twice that of the low-c compositions) with a lower molecular weight (high c, low M_{w});

(iii) Lower hyaluronic acid concentration with a higher molecular weight (low c, high M_{w}).

Subsequent experiments were conducted on diluted forms of these stock gels in order to investigate transport behavior across a range of viscosities and structural properties.

4.2.1 Porosity Examination Using Magnetic Field Gradients

Before evaluating the ability of helical propellers to generate sufficient thrust for propulsion through hyaluronic acid-based gels, we first examined the penetrability of the gel matrix using monodisperse magnetic particles of comparable sizes, mobilized via strong magnetic field gradients. Although magnetic field gradients are not ideally suited for actuation *in vivo*, they offer a more straightforward method *in vitro* compared to helical propellers. This investigation based on magnetic field gradients was designed to characterize the effective pore size within the gel network and to determine whether structures on the order of hundreds of nanometers could be transported through the matrix.

Monodisperse Magnetic Particles

To enable a reliable assessment of porosity, we employed monodisperse magnetic particles that I fabricated via glancing angle deposition (GLAD) at a glancing angle $\alpha = 80°$. Two distinct particle sizes were utilized:

(i) Particles with a diameter of $\approx 500\,\mathrm{nm}$, as presented in Section 2.1 and characterized in Fig. 2.3. Briefly, $500\,\mathrm{nm}$ silica beads were initially coated with a thin titanium adhesion layer, followed by nickel deposition, resulting in a total Ni thickness of $\approx 420\,\mathrm{nm}$.

(ii) Particles with a diameter of $\approx 250\,\mathrm{nm}$, their smaller counterparts. These were fabricated using a hexagonally close-packed monolayer of $\approx 250\,\mathrm{nm}$ silica beads, prepared via Langmuir–Blodgett deposition by C. Miksch. Both the titanium adhesion layer and the nickel layer were deposited using GLAD with rapid azimuthal (φ) rotation. Due to the glancing incidence angle of $80°$, the resulting vertical Ni thickness was $\approx 230\,\mathrm{nm}$.

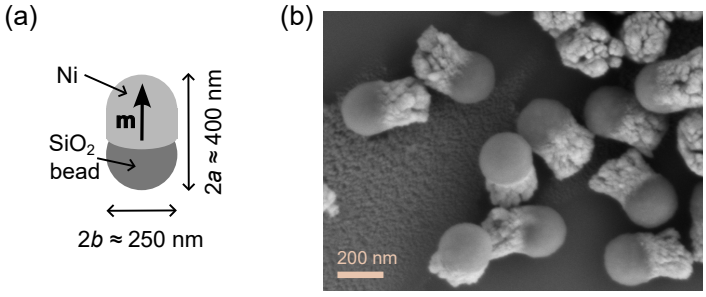

Figure 4.3. Characterization of the smaller monodisperse Ni particles fabricated via GLAD: (a) Schematic illustration of a single Ni particle composed of a $250\,\mathrm{nm}$ silica bead and a deposited Ni segment (Ti adhesion layer not shown); (b) SEM image of sonicated Ni particles on a silicon substrate. The SEM image acquired by Dr. F. Peter.

Experimental Setup Based on a Permanent Magnet

In order to generate magnetic force on the magnetic particles, we utilized a NdFeB permanent magnet (grade N48, height $h = 8\,\mathrm{mm}$, radius $R = 1.5\,\mathrm{mm}$) sourced from *Webcraft GmbH* [43] (see Fig. 4.4a and Section 1.2.1). The magnetic field and its gradient along the vertical axis z were analytically calculated using Eqs. (1.10) and (1.11), with the results shown as the beige curves in Fig. 4.4b–c.

Complementing the theoretical calculations, I conducted experimental measurements of the magnetic field above two identical magnets of the specified grade and dimensions using a Hall probe affixed to a precision mechanical manipulator. Starting with the probe in contact with the magnet surface, it was retracted along the magnet's axis. Because the Hall sensor's active element is located approximately $0.715\,\mathrm{mm}$ from the probe surface, the recorded

measurements were offset accordingly, beginning at $z = 0.715\,\mathrm{mm}$ (see the purple curves in Fig. 4.4b). I determined this offset distance of 0.715 mm experimentally by identifying the zero magnetic field position between two identical magnets oriented antiparallel to each other (i.e., repelling configuration). Subsequently, I calculated the magnetic field gradient data as the finite difference between consecutive magnetic field measurements, with the results shown as purple curves in Fig. 4.4c. The experimental results are in good agreement with the analytical calculations.

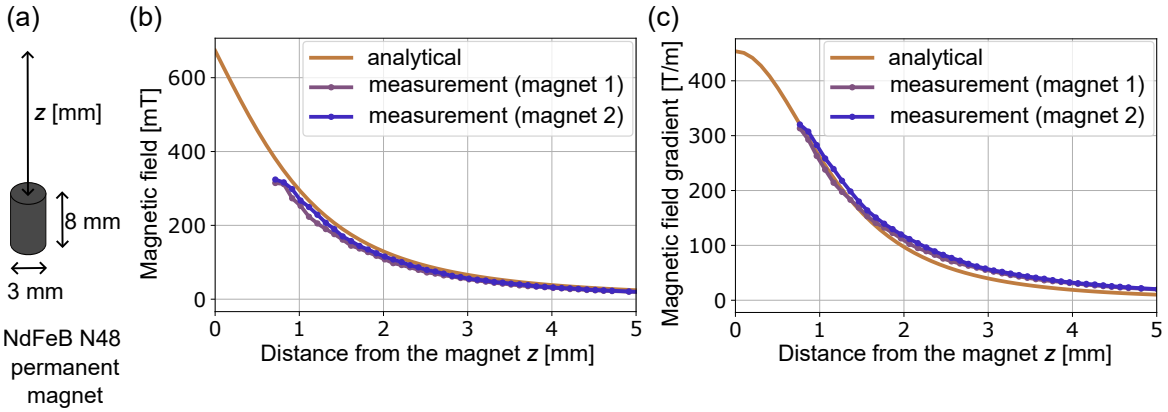

Figure 4.4. Characterization of the permanent magnet used for porosity assessment in hyaluronic acid-based gels: (a) schematic illustration of the magnet with specified dimensions; (b) magnetic field above the magnet obtained from both analytical calculations and experimental measurements; (c) magnetic field gradient above the magnet, derived analytically and from experimental data.

Due to the rapid decay of the magnetic field gradient with increasing distance from the magnet, it was essential to develop an experimental setup that allows the magnetic particles to be positioned in close proximity to the magnet while enabling assessment of their penetration through the hyaluronic acid-based gels. To achieve this, a thin #0 precision coverslip from *Thorlabs*, with the nominal thickness of $(100 \pm 15)\,\mu\mathrm{m}$, was used as a base substrate (see Fig. 4.5a). A Gene frame (1 cm × 1 cm, thickness 250 µm) was then affixed onto the coverslip to create a sample chamber. A small section (approximately $3\,\mathrm{mm} \times 5\,\mathrm{mm}$) of a wafer containing magnetic particles was cut and magnetized in an out-of-plane magnetic field of 1.8 T generated by an electromagnet at its center. This magnetization aligned the individual dipole moments within each particle to produce a net magnetic moment $\mathbf{m}$ oriented along their longest dimension (see schematic in Fig. 4.3a), thereby ensuring directed particle motion along this axis. The magnetized wafer piece was then immersed in $\approx 200\,\mu\mathrm{l}$ of Milli-Q water and sonicated for one minute, facilitating detachment and dispersion of the magnetic particles into the solution. The sonicated magnetic particle suspension was subsequently mixed, in varying ratios, with one of the three ungelled stock hyaluronic acid-based

compositions, resulting in samples with varying final concentrations derived from the original stocks. A total volume of 25 µl of the resulting suspension was pipetted into the Gene frame, after which the chamber was sealed with another cover slip (Fig. 4.5a). The assembled sample underwent gelation under controlled conditions (see Fig. 4.5b). Upon gelation, the gel-containing sample was placed directly atop a permanent magnet (see Fig. 4.5c), stabilized within a 3D-printed holder (not depicted in the schematic). The holder ensured direct contact between the magnet and the coverslip, thereby minimizing the gap between the magnet and the embedded particles. Exposure durations varied depending on gel concentration, ranging from 30 min for lower concentrations to 180 min for higher concentrations.

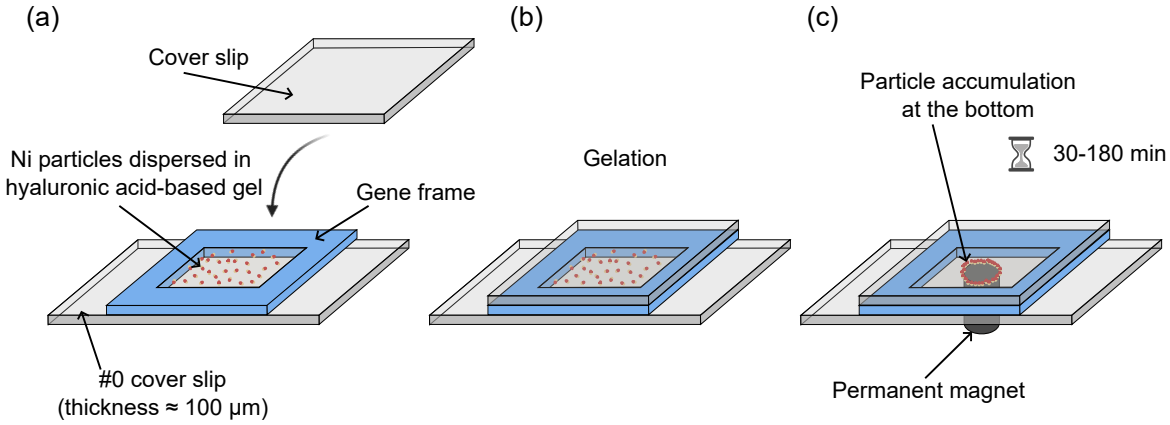

Figure 4.5. Step-by-step schematic of sample preparation for porosity assessment: (a) magnetic particles dispersed in the two components of the hyaluronic acid-based gel are pipetted into an observation chamber formed by a #0 coverslip and a Gene frame, and subsequently sealed with a second coverslip; (b) the sample undergoes gelation under controlled conditions; (c) a permanent magnet is placed in contact with the sample. If the gel's porosity permits, magnetic particles migrate and accumulate along the rim of the magnet.

Particle penetration through the gel was evaluated using an inverted microscope after removal of the magnet. Successful penetration was evidenced by particle accumulation in a circular pattern at the bottom of the gel, immediately above the coverslip, mirroring the shape of the underlying magnet (see Fig. 4.5c and Fig. 4.6a–b). This accumulation arises due to the presence of both vertical and lateral components of the magnetic field gradient. While the vertical component drives particles downward through the gel, the lateral component acts on particles located away from the magnet's central axis, drawing them radially toward the magnet's edge where the horizontal gradient is strongest. Additionally, the particles assembled into linear chains, a characteristic behavior resulting from dipolar interactions between individual particles (see Fig. 4.6c). This chaining effect further confirms that all particles possess a uniform magnetization direction following their initial alignment in the applied magnetic field.

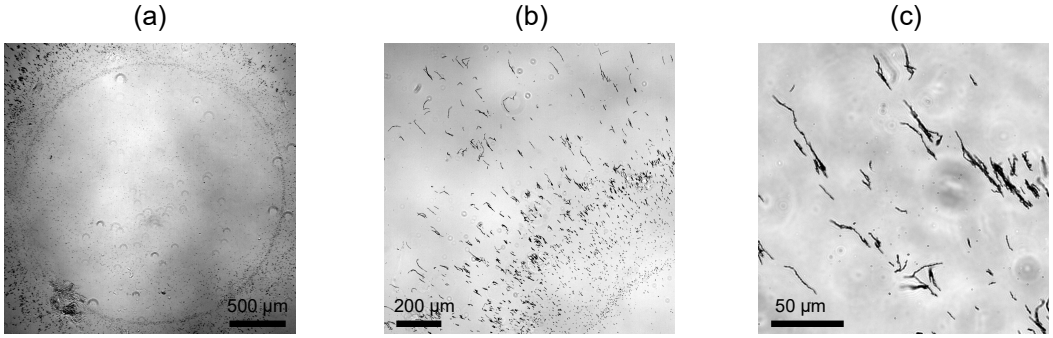

Figure 4.6. Representative bright-field images showing successful penetration of 250 nm particles through the 10 % formulation of the high c, low M_{w} hyaluronic acid-based gel (notation used to describe the formulation is explained later in the text): (a) accumulation of particles in a circular pattern defined by the magnet's shape, imaged with a $5\times$ objective; (b) magnified view of a section of the pattern, imaged with a $10\times$ objective; (c) chain-like structures formed by particles due to dipolar interactions, imaged with a $63\times$ objective. Images acquired by F. Hecht and I. Wittmann.

Assessment of Particle Penetration Across Diluted Gel Formulations

To evaluate particle penetration, we examined a series of diluted formulations derived from the three stock hyaluronic-acid gels described earlier in this chapter. For example, a formulation designated as 30 % (low c, low M_{w}) refers to a mixture in which 30 % of the total pre-gelation volume consisted of the stock composition with lower hyaluronic acid concentration and lower molecular weight. The remaining 70 % of the volume consisted of magnetic particles suspended in Milli-Q water. The two components (the ungelled hyaluronic acid-based composition and the magnetic particle suspension) were thoroughly mixed just prior to sample preparation and subsequent gelation.

The results of particle penetration across the various gel formulations are summarized in Table 4.1. Penetration was assessed qualitatively and is reported as "yes," "no," or "–" (not tested due to the time-intensive nature of the experiments).

For the stock low c, low M_{w} hyaluronic acid-based gel, 500 nm particles were able to penetrate formulations up to 60 %, whereas 250 nm particles penetrated up to 70 %. While the absence of penetration beyond these thresholds could result from either insufficient magnetic force relative to viscous drag or reduced pore size, we attribute it primarily to pore size limitations. This interpretation is supported by the observation that smaller particles, despite experiencing a lower magnetic-to-drag force ratio, penetrated denser formulations more efficiently than the larger ones. This can be rationalized by considering that the drag force in a homogeneous medium scales linearly with particle radius (Eqs.(1.4) and (1.5)), whereas the magnetic force scales with the cube of the radius of the magnetic component (Eq. (1.7)).

	low c, low M_w		high c, low M_w	low c, high M_w
Gel content	Particles 500 nm	Particles 250 nm	Particles 250 nm	Particles 250 nm
10%	-	-	yes	-
20%	-	-	yes	-
25%	-	-	yes	-
30%	yes	-	yes	yes
35%	-	-	yes	-
40%	yes	yes	yes	no
45%	-	-	yes	-
50%	yes	yes	no	no
60%	yes	yes	-	-
70%	no	yes	-	no
80%	no	no	-	-
90%	no	no	-	-

Table 4.1. Summary of particle penetration results for two particle sizes (250 nm and 500 nm) across various dilutions prepared from three hyaluronic acid-based stock gel formulations. Dilution percentages refer to the volume fraction of the stock gel in the final formulation, which also includes the magnetic particle suspension. Particle penetration was evaluated qualitatively and reported as ”yes”, ”no”, or not tested (”-”).

Based on this, we anticipated that 250 nm particles would penetrate the high c, low M_w stock gel formulation up to 35 %, corresponding to the same absolute hyaluronic acid content as the 70 % formulation of the low c, low M_w stock gel. Interestingly, penetration was observed up to the 45 % formulation, suggesting that factors beyond total concentration of hyaluronic acid also influence the final pore size.

In the case of the low c, high M_w hyaluronic acid gel, penetration of 250 nm particles was observed only up to the 30 % formulation, consistent with the expectation that higher molecular weight polymers form denser networks with smaller effective pore sizes.

Overall, these threshold values define the maximum gel concentrations that remain permeable to 500 nm and 250 nm particles, which correspond to typical sizes of potential drug delivery vectors for vitreous substitutes. In the following subsection, we investigate the directed motion of helical propellers with comparable dimensions through these, or less concentrated, gel formulations.

4.2.2 Directed Motion of Helical Propellers

Actuation by rotating magnetic fields offers particular advantages for *in vivo* applications, as such fields can be readily generated over larger length scales (tens of cm), unlike magnetic field gradients, which are technically challenging to maintain across similar distances. Magnetically actuated helical propellers thus present a compelling strategy for the targeted delivery of therapeutic agents within the human body. Our group has previously demonstrated that such propellers can effectively navigate the native vitreous humor in porcine eyes [214]. Since vitreous substitutes are implanted after vitrectomy to restore ocular structure and function, it is desirable that these materials also allow for controlled transport to support post-surgical treatment. Demonstrating effective navigation of helical propellers through these vitreous substitutes would thus enhance their potential by enabling magnetically guided drug delivery in clinical scenarios involving vitreous replacement.

Magnetic Helical Propellers

To investigate propulsion through hyaluronic acid-based gels, three distinct magnetic helical propellers were fabricated, varying in both composition and size (see Fig. 4.7a–c). The propeller dimensions perpendicular to the direction of motion matched the particle sizes used in the porosity assessment described previously. All propellers were fabricated via GLAD at a glancing angle of 85°, employing hexagonally close-packed monolayers of silica spheres with diameters of 250 nm or 500 nm. The studied propellers are described as follows:

(i) Nickel-containing propellers with a diameter of $\approx 500\,\mathrm{nm}$ (see Fig. 4.7a, d). The helical structures were grown from silica, resulting in a two-turn helix. Subsequently, a titanium adhesion layer was deposited, followed by a nickel layer deposited with rapid azimuthal rotation. This process yielded monodisperse propellers, with the magnetic nickel layer reaching a thickness of approximately 200 nm and a total propeller length of 2000 nm.

(ii) Iron-platinum-containing propellers with a diameter of $\approx 500\,\mathrm{nm}$ (see Fig. 4.7b, e). These propellers incorporate the magnetically superior $\mathrm{L1_0}$ phase of FePt instead of nickel. FePt is biocompatible [31], unlike many magnetic materials such as cobalt or nickel, and the $\mathrm{L1_0}$ phase exhibits exceptional nanoscale magnetic properties, including an energy product exceeding that of NdFeB magnets [247] and significantly higher remanent magnetization than nickel or iron [31]. Since propulsion experiments utilize low rotating magnetic fields ($< 10\,\mathrm{mT}$), remanent magnetization critically dictates the magnetic moment and thereby influences the propulsion behavior as described by Eq. (1.25). Our group previously fabricated $\mathrm{L1_0}$ phase FePt propellers [31, 103]. In this study, I fabricated FePt propellers on silica beads with a diameter of $\approx 500\,\mathrm{nm}$ by first growing the silica helix body, producing approximately 1.4 helical turns. Subsequently, a titanium adhesion layer was added, followed by co-deposition of Fe and Pt at a 1:1 atomic ratio, maintaining the same azimuthal rotation as for the helical body. This yielded propellers approximately 1800 nm in length with a FePt layer thickness near 200 nm. To induce the ordered $\mathrm{L1_0}$ phase, the wafers were cut into thin pieces upon removal from the deposition chamber. Dr. F. Peter sealed these pieces in quartz ampules under argon atmosphere, and annealed them at 700 °C for one hour with subsequent rapid cooling in an ice bath [179].

(iii) Nickel-containing propellers with a diameter of $\approx 250\,\mathrm{nm}$ (see Fig. 4.7c, f). For these smaller structures, I used silica beads with a diameter of 250 nm and implemented several design optimizations. To prevent fusion of neighboring propellers, previously observed due to closely spaced helical tails, I deposited the magnetic material at the propeller head. This configuration was achieved by first depositing a titanium adhesion layer, followed by nickel with high azimuthal rotation, and then capped with an additional titanium layer to support subsequent helical growth. To enhance visibility under optical microscopy, I replaced silica with titanium dioxide as the helical material, owing to its significantly higher refractive index [248]. The $\mathrm{TiO_2}$ thickness was deposited with increased azimuthal rotation to suppress the formation of broad, merging helices encountered in earlier attempts, resulting in approximately 2.2 helical turns. The final propellers exhibited a total length of 1000 nm, with a nickel layer thickness of approximately 100 nm.

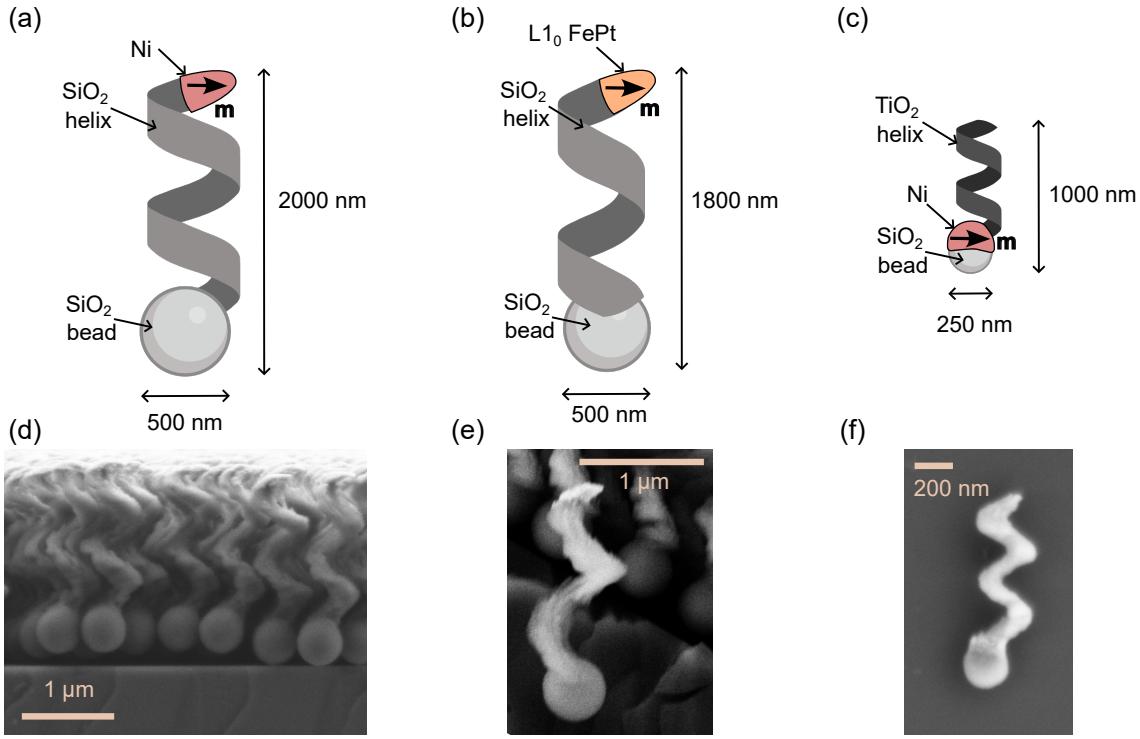

Figure 4.7. Characterization of magnetic helical propellers used in propulsion experiments within various hyaluronic acid-based vitreous substitute formulations: (a) schematic of a Ni propeller with a diameter of $\approx 500\,\mathrm{nm}$, with (d) showing a corresponding SEM image of multiple such Ni propellers prior to release from the wafer; (b) schematic of an FePt propeller with a diameter of $\approx 500\,\mathrm{nm}$, with (e) showing its corresponding SEM image; (c) schematic of a smaller Ni propeller with a diameter of $\approx 250\,\mathrm{nm}$, with (f) showing its corresponding SEM image acquired by Dr. M. Alarcón-Correa. Thin titanium adhesion layers are not depicted in the schematics.

Propulsion Experiments Across Diluted Gel Formulations

The objective of these experiments was to identify which hyaluronic acid-based gel formulations allow effective propulsion of magnetic helical propellers, and to determine the most efficient propeller design for navigation through such environments. These findings aim to guide the selection of suitable formulations for use as vitreous substitutes.

For each selected gel formulation and propeller type, propellers on a small wafer piece ($\approx 2\,\text{mm} \times 2\,\text{mm}$) were first magnetized in-plane using an electromagnet producing a central magnetic field of 1.8 T. The magnetized propellers were then immersed in Milli-Q water and released from the wafer via sonication. Gel formulations were prepared following the same protocol as in the magnetic particle penetration experiments, with propellers suspended in water instead of particles. Experiments were conducted using formulations based on the low c, low M_w and low c, high M_w hyaluronic acid stock compositions. For each experiment, 25 µL of the ungelled composition containing suspended propellers was pipetted into an observation chamber composed of a standard cover slip and a Gene frame (1 cm × 1 cm, thickness 250 µm), and sealed with a second cover slip. The assembled chamber was then subjected to gelation under controlled conditions.

Actuation experiments were performed using three orthogonally arranged pairs of custom-built Helmholtz coils, as described previously [249]. These coils, mounted on the stage of an inverted optical microscope, allowed generation of rotating magnetic fields in three dimensions. The fields were controlled via a *Matlab*-based custom program interfaced through a DAC and a $10\times$ amplifier. All propellers were initially tested in water to verify their propulsion ability before being evaluated in hyaluronic acid-based gel formulations. Magnetic field strengths ranged from 5 mT to 8 mT, with rotation frequencies between 5 Hz and 70 Hz. When subjected to rotating magnetic fields, the propellers advance forward up to the so-called step-out frequency, beyond which the viscous drag exceeds the magnetic torque, resulting in a loss of synchronous rotation [249]. As step-out frequency inversely correlates with medium viscosity [249], a reduction in the maximum frequency supporting propulsion was expected in more viscous gel environments.

We first investigated the propulsion of magnetic micropropellers in hydrogel formulations based on a low c, low M_w hyaluronic acid composition (see Table 4.2). Propulsion tests were performed using all three propeller geometries (see Fig. 4.7), revealing four distinct types of behavior within the gels: (i) active propulsion under rotating magnetic fields, (ii) alignment of the propeller's magnetic moment with the applied magnetic field without propulsion—indicating that the generated magnetic torque was insufficient to overcome viscous drag, (iii) minimal motion without a clear response to the magnetic field, and (iv) complete immobilization within the gel. In the most dilute formulation (10 % of the stock composition), all propeller types exhibited active propulsion. However, significant differences emerged at higher concentrations, particularly in the 30 % formulation. The 250 nm Ni propellers were unable to align with the magnetic field, while the 500 nm Ni propellers could align but were unable to propel. Only the 500 nm FePt propellers achieved effective propulsion in this gel formulation, driven by a rotating magnetic field of 7 mT at 45 Hz.

low c, low M_w	Propellers		
gel content	500 nm Ni	500 nm FePt	250 nm Ni
10%	Propulsion	Propulsion	Propulsion
30%	Alignment to the field	Propulsion	Minimal motion
50%	Minimal motion	Minimal motion	No motion
70%	-	-	No motion
90%	No motion	-	-

Table 4.2. Summary of propulsion performance in various hydrogel formulations, all based on a low c, low M_w hyaluronic acid-based stock composition. Results are presented for three distinct propeller geometries. The reported dilution percentages indicate the volume fraction of the ungelled low c, low M_w stock hyaluronic-acid based solution in the final formulation, which also contains the magnetic propeller suspension. The table categorizes the behavior into four conditions: active propulsion; alignment of the propeller's magnetic moment with the external magnetic field without propulsion; minimal motion without systematic response to the magnetic field; and no observable motion. Cells marked with "–" indicate conditions that were not tested.

A representative propulsion experiment in the 30 % formulation was recorded, and five selected frames are shown in Fig. 4.8, with the trajectory of the propeller overlaid using particle tracking in *ImageJ*. Initially, the FePt propeller reorients along the *x*-axis when the magnetic fields are applied in the *y*- and *z*-directions (Fig. 4.8a). It subsequently aligns with the *y*-axis as the fields are applied in the *x*- and *z*-directions (Fig. 4.8b), propelling along the *y*-axis during continuous field rotation about the *y*-axis (Fig. 4.8c). Finally, the field is rotated about the *x*-axis (Fig. 4.8d), resulting in propulsion along the *x*-axis (Fig. 4.8e).

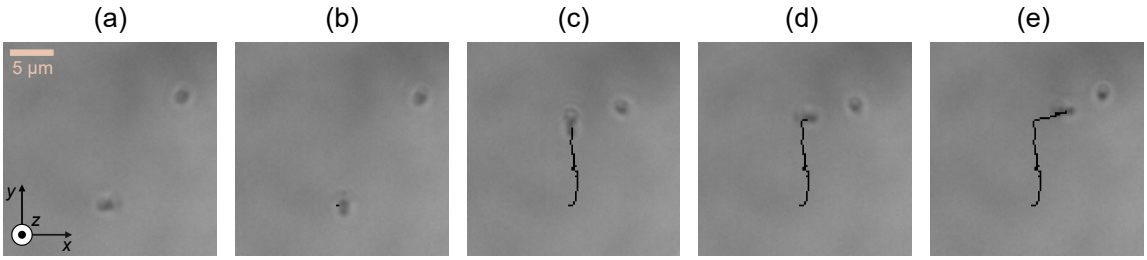

Figure 4.8. Propulsion of a 500 nm FePt propeller in a 30 % dilution of the low c, low M_w hyaluronic acid-based gel, driven by a rotating magnetic field of 7 mT at 45 Hz: (a) alignment along the *x*-axis; (b) alignment along the *y*-axis; (c) propulsion along the *y*-axis; (d) reorientation along the *x*-axis; (e) propulsion along the *x*-axis. Video acquired by I. Wittmann and F. Hecht.

These results indicate that the inability of the 500 nm and 250 nm Ni propellers to achieve directed motion in the 30 % dilution of the low c, low M_w hyaluronic acid-based gel is not due to restricted pore size, as the 500 nm FePt propeller can still propel under these conditions. Instead, we attribute this behavior to insufficient magnetic moments in the Ni propellers, which fail to generate enough magnetic torque to overcome viscous drag. Effective propulsion is achieved only with the superior magnetic properties of the $L1_0$ FePt propellers.

We next investigated propulsion in hydrogel formulations based on a low c, high M_w hyaluronic acid stock composition (see Table 4.3). Given the comparable size but superior performance of the 500 nm FePt propellers over their Ni counterparts, experiments were conducted only with 500 nm FePt and 250 nm Ni propellers. While the 500 nm FePt propellers were unable to propel even in the least concentrated 5 % formulation, the smaller 250 nm Ni propellers successfully navigated both the 5 % and 10 % dilutions.

low c, high M_w	Propellers	
gel content	500 nm FePt	250 nm Ni
5%	Alignment to the field	Propulsion
10%	Alignment to the field	Propulsion
15%	-	Minimal motion
20%	No motion	-

Table 4.3. Summary of propulsion performance in various hydrogel formulations, all based on a low c, high M_w hyaluronic acid-based stock composition. Results are presented for two distinct propeller geometries. The reported dilution percentages indicate the volume fraction of the ungelled low c, high M_w stock hyaluronic-acid based solution in the final formulation, which also contains the magnetic propeller suspension. The table categorizes the behavior into four conditions: active propulsion; alignment of the propeller's magnetic moment with the external magnetic field without propulsion; minimal motion without systematic response to the magnetic field; and no observable motion. Cells marked with "–" indicate conditions that were not tested.

A representative propulsion experiment with the 250 nm Ni propellers in the 10 % formulation was recorded under rotating magnetic fields of 7 mT at 60 Hz. Five selected frames are shown in Fig. 4.9, with the trajectory overlaid via particle tracking in *ImageJ*. The propeller follows a square-like path: moving from its initial position (see Fig. 4.9a) along the *y*-axis (Fig. 4.9b), then the *x*-axis (see Fig. 4.9c), followed by motion along the negative *y*-axis (see Fig. 4.9d), and finally along the negative *x*-axis (see Fig. 4.9e). As expected, the maximum effective frequency in the gel (60 Hz) was lower than that observed in water (70 Hz), consistent with the increased viscosity.

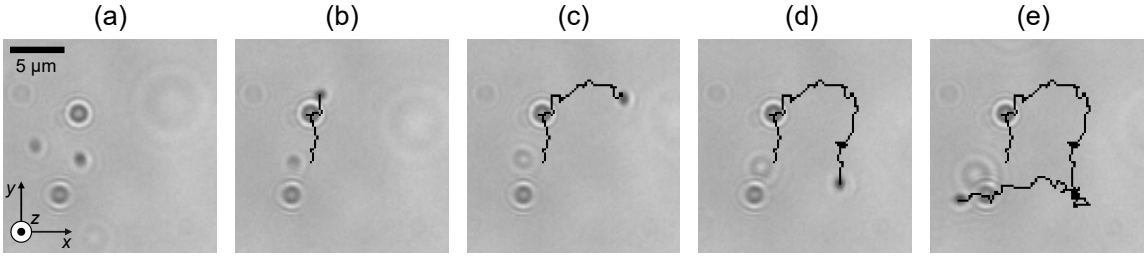

Figure 4.9. Propulsion of a 250 nm Ni propeller in a 10 % dilution of the low c, high M_w hyaluronic acid-based gel, driven by a rotating magnetic field of 7 mT at 60 Hz, following a square-like trajectory: (a) initial position; (b) propulsion along the *y*-axis; (c) along the *x*-axis; (d) along the negative *y*-axis; (e) along the negative *x*-axis. Video acquired by I. Wittmann and F. Hecht.

The ability of the 250 nm Ni propellers to propel in the 10 % formulation, while the larger and magnetically stronger 500 nm FePt propellers remained immobile, only aligning with the magnetic field, suggests that propulsion of the 500 nm FePt propellers is limited by the gel pore size, not the magnetic torque. As the 250 nm propellers exhibited motion without responding to the magnetic field in the 15 % formulation, we anticipate that propulsion in this and denser gels may be enabled by 250 nm propellers with higher magnetic moments, such as those based on the $L1_0$-phase FePt.

Overall, these findings demonstrate that for the low c, low M_w hyaluronic acid-based gel, targeted propulsion, and thus potential drug delivery, can be achieved in formulations with up to 30 % dilution using 500 nm FePt propellers. In contrast, for the low c, high M_w gel, effective propulsion is feasible up to 10 % dilution using 250 nm Ni propellers. Propulsion at higher dilutions may be attainable with 250 nm propellers incorporating the high-moment $L1_0$-phase FePt.

4.3 Transport Through Retina

The overarching vision of this research is to enable non-invasive gene delivery to the retina via the intravitreal route, using non-viral vectors. In this long-term perspective, beyond the scope of the present study, we propose the use of helical magnetic micropropellers as delivery vehicles. Our group has previously demonstrated several steps toward achieving this goal:

(i) Helical microrobots can be guided through the porcine vitreous body via weak rotating magnetic fields, as shown by Z. Wu *et al.* [214].

(ii) Magnetic actuation can be achieved with biocompatible FePt alloys, which exhibit excellent magnetic properties, surpassing conventional hard magnetic materials such as NdFeB [247]. The fabrication and propulsion of FePt-based micropropellers have been shown by V. Kadiri *et al.* [31].

(iii) The helical structures of these microrobots can be fabricated from biodegradable MgZn alloys, which gradually dissolve into magnesium and zinc ions, naturally occurring elements in the human body. The propulsion of such degradable microrobots has been demonstrated by F. Peter *et al.* [103].

While these design strategies for propulsion and material selection are well-developed, a significant challenge remains. The size exclusion limit of the ILM, estimated between 2 nm and 100 nm, may prevent these microrobots from crossing this barrier to deliver therapeutic cargo to retinal cells. Additionally, the propulsion forces generated, estimated to be on the order of a few piconewtons, as discussed in Chapter 1, are insufficient to mechanically penetrate the ILM [179]. To address these constraints, the present study first focused on systematically investigating the size range of particles capable of traversing the ILM. Establishing this threshold is a critical first step in assessing the feasibility of microrobotic delivery systems for retinal applications. Looking ahead, we envision combining microrobotic transport with localized enzymatic disruption of the ILM, as suggested in Dr. F. Peter's doctoral work [179]. To minimize the risk of retinal damage from high enzyme concentrations, a targeted approach is conceptualized, involving the attachment of collagenase IV directly to the surface of the micropropellers [179]. As a proof of concept, we investigate enzyme-functionalized microbeads to assess their ability to facilitate ILM digestion and enhance nanomaterial penetration. Altogether, this long-term vision combines targeted enzymatic modulation with magnetic propulsion and degradable materials, aiming to develop microrobotic systems capable of crossing the ILM and delivering therapeutic payloads to retinal cells.

4.3.1 Transport Across the ILM in Ussing Chamber Experiments

To advance the understanding of the ILM permeability to nanoscale materials, our initial objective was to establish a robust and reproducible system for assessing the penetration of materials of varying sizes. To closely replicate the physiological conditions of gene delivery to human retinal cells, we employed a porcine eye model due to its anatomical similarity to the human eye. The Ussing chamber was selected as our starting platform due to its promise to maintain distinct environments on either side of the tissue sample, thereby enabling controlled and quantitative analysis of transmembrane transport.

Porcine retinal explants with a diameter of 8 mm were prepared based on established protocols [250, 251]. In brief, fresh porcine eyes were collected from a local slaughterhouse and kept at 4°C immediately after enucleation, ensuring that all dissections were performed within four hours *post-mortem*. Following eye desinfection, a scleral incision permitted gentle removal of the cornea, lens, and vitreous. The eyecup was divided into three to four sectors, and circular explants were punched out in supplemented Neurobasal-A medium (*Life Technologies*). Each explant was placed with the ILM facing upward on a Millicell insert and cultured in a 12-well plate until Ussing-chamber experiments, initiated within 48 h of culture.

The next step involved mounting the retinal explants in the Ussing chamber in a way that ensured a secure seal between the two compartments while minimizing mechanical pressure on the tissue, as direct compression was found to compromise retinal integrity. To address this, we developed a sealing approach where the retina's periphery was sealed using wax and a plastic foil rather than mechanical clamping. First, filter paper with a pore size of $(3-5)\,\mu\mathrm{m}$ was coated by applying a ring of molten wax, leaving the central area free of wax (see Fig. 4.10a). The Millicell insert containing the retinal explant was trimmed precisely around the tissue, and the retinal explant was transferred onto the wax-coated filter paper so that the center of the retina rested within the wax-free center (see Fig. 4.10b). Next, a plastic foil with a $4\,\mathrm{mm}$ central aperture was placed over the explant (see Fig. 4.10c). This assembly was mounted into the Ussing chamber such that only the waxed filter paper and the foil were clamped between the chamber halves, avoiding any direct pressure on the retina itself (see Fig. 4.10d). Each chamber compartment was filled with 5 ml of fluid, as described later. To promote transretinal transport, the setup was further equipped with electrodes allowing the application of an electrical potential across the explant, thereby offering the possibility to enhance diffusion rates when desired (Fig. 4.10d).

Some of our results have been published as part of the bachelor's thesis of E. Schmitt [252].

Passive Transretinal Diffusion in the Ussing Chamber System

We initially investigated passive diffusion across the retinal explant using materials spanning several orders of magnitude in diameter:

(i) Water (molecular diameter ≈ 2.8 Å): One chamber compartment, flushed with argon to reduce exposure to atmospheric water vapor, was filled with heavy water (D_2O), while the opposing compartment contained Milli-Q water. At defined intervals, aliquots were collected from both sides, and samples from the D_2O compartment were transferred into argon-flushed NMR tubes. The concentration of H_2O in the D_2O-filled compartment was quantified by Nuclear Magnetic Resonance (NMR) spectroscopy, exploiting the distinct resonance frequencies of ^1H and ^2H nuclei [253]. The experiment was conducted in duplicate, yielding consistent results with a diffusion rate of $\approx 0.5\,\mathrm{M/h}$ over the first 10 hours (Fig. 4.10e). Given a compartment volume of 5 ml and a circular exposed retinal area with a diameter of 4 mm, this corresponds to a rate of $\approx 0.2\,\mathrm{mmol/(mm^2 h)}$. A more detailed analysis of the water diffusion experiments is provided in the bachelor's thesis of E. Schmitt [252]. It should be noted that using water instead of a physiological medium such as phosphate-buffered saline (PBS) may have affected retinal cell viability.

(ii) Rhodamine B (molecular diameter $\approx 1.6\,\mathrm{nm}$): One chamber compartment was filled with a $\approx 420\,\mu\mathrm{M}$ Rhodamine B solution in PBS, while the opposing compartment contained pure PBS. At various time points, aliquots were collected from both sides and analyzed via UV-Vis spectrophotometry. Absorbance values were converted to concentration. The experiment was repeated nine times, consistently yielding an initial diffusion rate of $\approx 0.5\,\mu\mathrm{M/h}$ (Fig. 4.10f), corresponding to a rate of $\approx 0.2\,\mathrm{nmol/(mm^2 h)}$.

(iii) FITC-dextrans (molecular weights: 3–5 kDa, 10 kDa, 40 kDa and 150 kDa; corresponding hydrodynamic diameters of approximately 2.8 nm to 9 nm): A 125 µM FITC-dextran solution in PBS was added to one compartment of the chamber, with the opposing side filled with PBS alone. Samples were collected at various time points and analyzed using either fluorometry or UV-Vis spectrophotometry, with fluorescence intensity or absorbance values converted to concentration (Fig. 4.10g). No consistent correlation between molecular weight and diffusion rate was observed; in some cases, larger molecules exhibited unexpectedly higher diffusion rates. The integrity of the retinal explant may have been compromised in some experiments.

(iv) Fluorescent carboxylated polymethacrylate particles, micromer®-redF from *micromod Partikeltechnologie* (diameter 25 nm): A $100\,\mu\mathrm{g/ml}$ suspension in PBS was added to one chamber compartment, with PBS alone in the opposite side. The experiment was repeated six times. The resulting diffusion profiles, analyzed via fluorometry, are shown as blue curves in Fig. 4.10h.

Across most passive diffusion experiments, we observed a recurring phenomenon: after an initial period of slow, gradual or even negligible transport, the measured concentration exhibited a sudden and pronounced increase, contrary to the expected trend of decreasing diffusion rate over time. We ascribe these abrupt jumps to mechanical rupturing of the retinal explant, resulting in compromised tissue integrity that resulted in uncontrolled passage of material. This explanation was supported by visual inspection after opening the chamber.

Overall, for small molecules such as water and Rhodamine B, diffusion through the intact retina could be consistently detected prior to any rupture, confirming their ability to permeate the tissue under passive conditions. In contrast, for 25 nm carboxylated nanoparticles, the signal increase was typically abrupt, with minimal or no evidence of gradual transport beforehand. This suggests that the intact retina, particularly the ILM, acts as a strong barrier to particles of this size. Even in rare cases where particle passage appeared to occur, the transport was markedly slow, highlighting the need for alternative strategies to facilitate effective delivery of therapeutic gene vectors across the ILM.

Electrically Facilitated Transretinal Diffusion in the Ussing Chamber System

To enhance and control the diffusion of nanoscale materials across the ILM, we introduced an externally applied electric field in the Ussing chamber setup (see Fig. 4.10d). This approach aimed to generate a tunable driving force for charged particles across the retinal explant.

We selected 25 nm fluorescent carboxylated polymethacrylate nanoparticles (micromer®-redF, *micromod Partikeltechnologie*) for these experiments, which carry a net negative charge due to their surface carboxylation—a modification previously shown to facilitate intravitreal mobility [220–222]. The presence of surface charge is also a critical factor enabling their response to the applied electric field. Zeta potential measurements in Milli-Q water confirmed their negative surface charge at physiological pH, yielding values around −40 mV [252]. Due to the presence of ions in phosphate-buffered saline (PBS), which interfere with the applied field, all electrically assisted experiments were performed in Milli-Q water. It should be again noted that the pure water may in itself also affect the integrity of the retina. A 100 µg/ml particle suspension was introduced into one compartment, while the opposing side contained only Milli-Q water. The electric field was generated using a high-voltage power supply, with the positive electrode positioned behind the compartment containing Milli-Q water and the negative electrode behind the suspension of negatively charged particles, thereby directing electrophoretic movement across the explant (see Fig. 4.10d). As a proof of concept, we first verified that application of the electric field promoted particle migration across a simple filter membrane in the absence of retinal tissue [252], confirming the basic functionality of the setup.

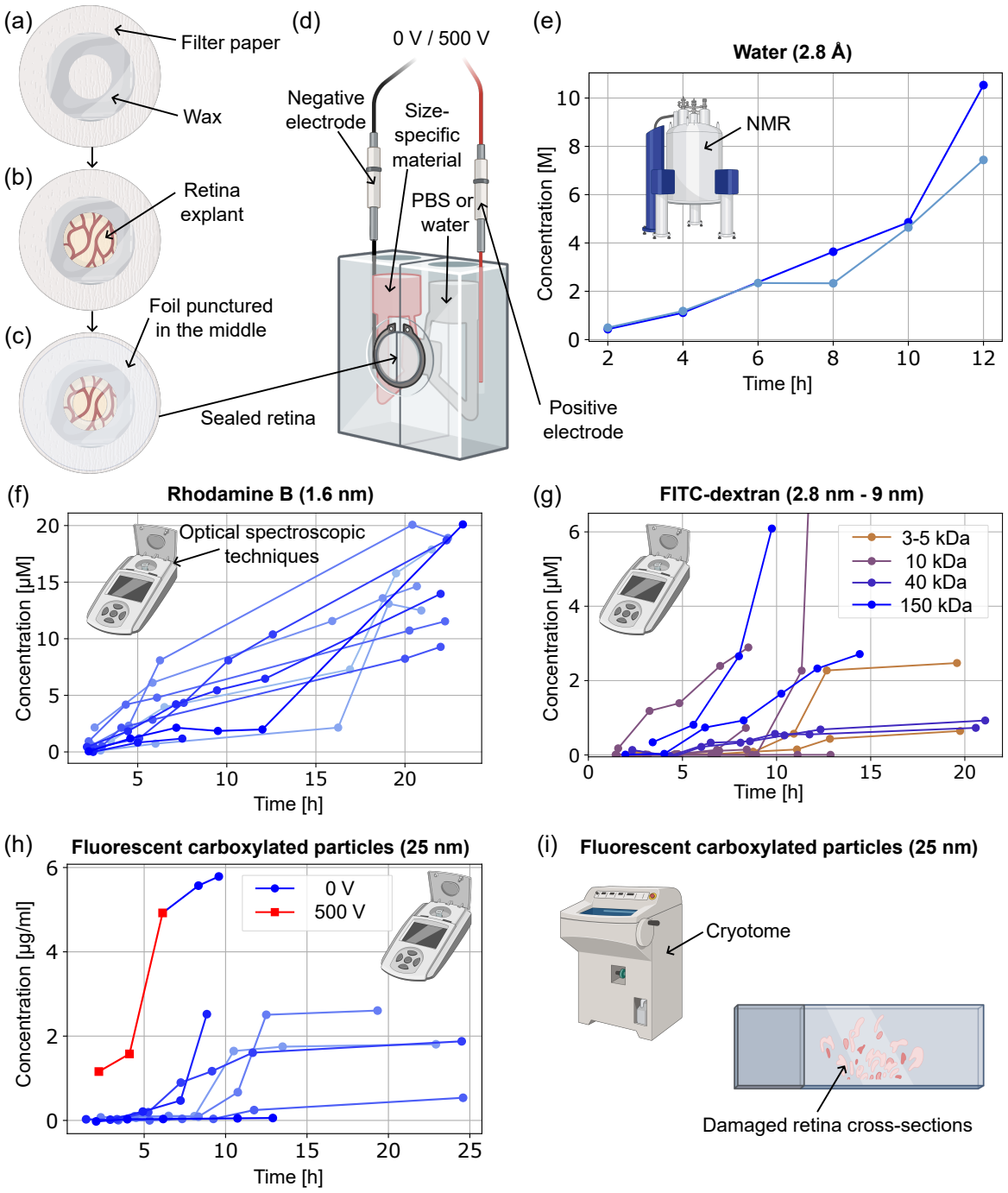

Figure 4.10. Retinal permeability, including the ILM, assessed using the Ussing chamber system: (a)–(c) schematic representation of the sealing protocol: (a) filter paper is coated with a peripheral wax ring to define the sealing region; (b) the retinal explant is carefully placed onto the center of the filter paper; (c) a plastic foil with a central aperture is positioned above the explant; (d) schematic illustration of the Ussing chamber setup, enabling voltage generation across the membrane via inserted electrodes; (e) time-dependent penetration of water through the retina, quantified by NMR spectroscopy (data also reported in Ref. [252]); (f) time-dependent penetration of Rhodamine B through the retina, measured using a UV-Vis spectrophotometer (data also partially reported in Ref. [252]);

Figure 4.10. (Continued) (g) time-dependent penetration of FITC-dextran molecules of varying molecular weights through the retina over time, assessed via fluorometry or UV-Vis spectrophotometry; (h) time-dependent penetration of 25 nm fluorescent carboxylated polymethacrylate nanoparticles through the retina, measured using a fluorometer; (i) cryosectioning and imaging of post-experiment tissue reveals significant structural disruption of the retina.

In retinal experiments, a voltage of 500 V was applied across electrodes spaced 5 cm apart, producing an electric field strength of $\approx 100\,\mathrm{V/cm}$. Most explants subjected to this field exhibited significant tissue damage. In one rare case where structural integrity appeared preserved, solution samples were collected at three time points during field application (see the red curve in Fig. 4.10h), followed by continued sampling after the field was turned off (see the adjoining blue curve in Fig. 4.10h). While the application of the electric field appeared to enhance transretinal transport, post-experimental cryosectioning followed by DAPI staining and fluorescence imaging revealed significant tissue disruption (see schematic in Fig. 4.10i), likely caused by the high field strength. Comparable tissue damage was also observed at lower field strengths, suggesting that the retina is highly sensitive to electrical stress.

Histology of Retinas Following Passive Diffusion in the Ussing Chamber System

In parallel, we examined retinal tissue from passive diffusion experiments using the same histological methods. While some level of tissue disruption was also evident, it was generally less severe than in the electrically assisted cases. However, interpretation of these results is complicated by the mechanical stress introduced during sample disassembly, particularly the removal of the sealing foil in direct contact with the retinal periphery prior to sectioning. This procedural step introduces artifacts that hinder reliable assessment of ILM permeability at the cellular level. These methodological limitations highlight the need for alternative experimental models that allow accurate and reproducible evaluation of transretinal permeability with cellular resolution while minimizing mechanical perturbation of the tissue.

4.3.2 Transport Across the ILM Using a Novel Sclero-Retinal Model

To address these challenges, we developed an experimental model designed to preserve the retina in its native structural context for as long as possible. This model facilitates the controlled application of nanomaterials to the vitreal side of the ILM and enables reliable *post hoc* evaluation at cellular resolution. Specifically, we established a porcine sclero-retinal model in which the retina remains attached to the underlying sclera throughout the experiment. This configuration maintains the integrity of a large eye segment, thereby providing a more physiologically relevant platform for assessing nanomaterial penetration. Importantly, this approach limits diffusion from the retinal pigment epithelium (RPE) side, known to be more permeable, thus mitigating potential artifacts and improving the assessment of the results.

Eye Dissection and Sample Preparation

As with our previous experiments, fresh porcine eyes were collected from a local slaughterhouse and stored at 4°C after enucleation until dissection, which was carried out within four hours *post-mortem*. Extraocular tissues were carefully removed, followed by disinfecting the eyes in 70% ethanol and rinsing with sterile PBS. The dissection was initiated by puncturing the sclera with a surgical scalpel (Fig. 4.11a), creating an entry point for the insertion of surgical scissors, which were then used to excise the anterior segment of the eye (Fig. 4.11b). The vitreous humour was gently removed by tilting the eye cup and carefully extracting it with tweezers (Fig. 4.11c). The posterior segment of the eye cup was then bisected, with particular care taken to ensure that the optic nerve remained at the margin of one of the resulting sections (Fig. 4.11d), thus resulting in two *ex vivo* sclero-retinal models from each eye (Fig. 4.11e). Each sclero-retinal model was secured onto a Styrofoam plate using needles, ensuring preservation of the central tissue architecture and preventing structural collapse (Fig. 4.11f). A suspension containing nanomaterials or enzyme-functionalized beads in Hank's balanced salt solution (HBSS) supplemented with Ca^{2+} ions was administered to the tissue surface using a pipette (Fig. 4.11g), ensuring that the pipette tip did not come into contact with the tissue. Calcium ions were essential for enzyme activity; to maintain consistency, HBSS containing Ca^{2+} was also used in control experiments without enzymes. The samples were placed for 1 h (unless stated otherwise) in an incubator set to 37°C to mimic *in vivo* physiological temperature conditions (Fig. 4.11h). After incubation, a central section of each model was carefully cut out with surgical scissors (Fig. 4.11i), transferred into an aluminum foil mold containing Tissue-Tek O.C.T. compound (*Sakura Finetek*), and subsequently embedded with an additional layer of Tissue-Tek (Fig. 4.11j). For rapid and uniform freezing, molds containing eye sections were placed on an aluminum

foil raft floating atop liquid nitrogen, thereby preventing direct contact between the molds and the liquid nitrogen (Fig. 4.11k). After freezing, the samples were kept at −80 °C until further processing by cryosectioning.

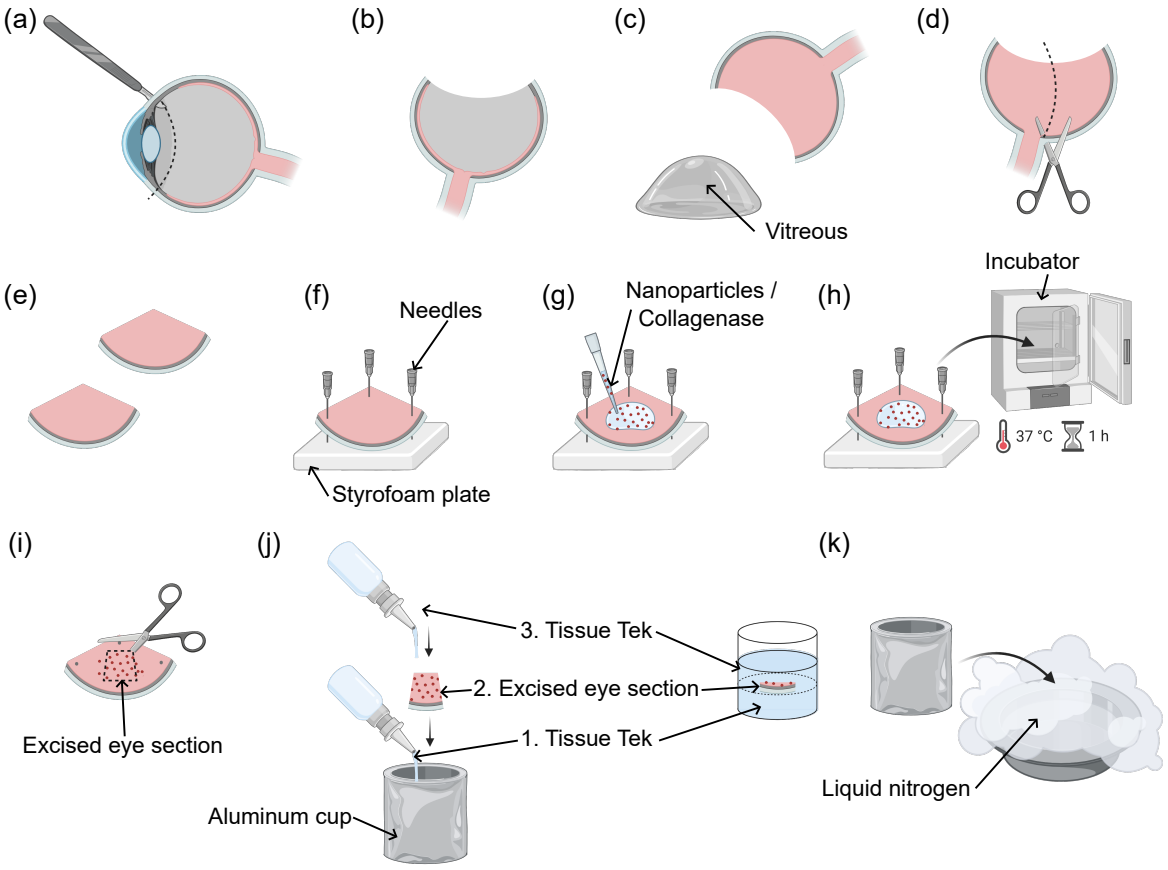

Figure 4.11. Step-by-step schematic overview of the eye dissection and sample preparation protocol: (a) initial incision of the eyeball; (b) removal of the anterior segment; (c) extraction of the vitreous humor; (d) bisection of the posterior eye cup; (e) generation of two *ex vivo* models from each eye; (f) stabilization of the tissue sample on a Styrofoam plate using needles; (g) application of nanomaterials or collagenase; (h) incubation of the sample; (i) excision of the central tissue region; (j) embedding of the sample in Tissue-Tek O.C.T. compound within an aluminum foil mold; (k) rapid freezing of the embedded sample in liquid nitrogen.

Cryosectioning, Fixation, Staining and Confocal Imaging of Sclero-Retinal Explants

Sclero-retinal explants embedded in molds were sectioned at a thickness of 12 µm, unless stated otherwise, using a CryoStar NX50 cryostat (*Thermo Scientific*). The resulting sections were collected onto SuperFrost® Plus adhesion glass slides (*R. Langenbrinck GmbH*). Immediately after sectioning, tissue slices were fixed in methanol for 10 minutes. Next, the slides were washed in Tris-buffered saline for at least 10 minutes. Cell nuclei were stained with DAPI, and fluorescence preservation was ensured by applying FluorSave™ reagent prior to coverslip mounting. Imaging was carried out using either a standard fluorescence and bright-field microscope DMi8 (*Leica*) with a $10\times$ air objective or a $63\times$ oil-immersion objective, or an LSM 880 confocal microscope (*Zeiss*) with a $20\times$ air objective.

Retention and Permeability of Size-Defined Nanomaterials at the ILM

We investigated the transport properties of various negatively charged nanomaterials using the *ex vivo* sclero-retinal model:

(i) Fluorescent carboxylated polystyrene and polymethacrylate particles (micromer®-redF, *micromod Partikeltechnologie*) with diameters of 25 nm (polymethacrylate) and 50 nm, 100 nm, and 250 nm (polystyrene).

(ii) Carboxylated gold nanoparticles conjugated with Alexa Fluor 555 (*Nanopartz Inc*) in sizes of 5 nm, 15 nm, and 25 nm.

(iii) Carboxylated quantum dots (Qdot™ 655 ITK™ Carboxyl, *Invitrogen*) with core sizes 2–10 nm.

(iv) Goat anti-Rabbit IgG secondary antibody labeled with Alexa Fluor 488 (*Invitrogen*), with approximate dimensions of 14 nm × 8 nm (dimensions depicted in a schematic shown later; see Fig. 4.15).

For the polystyrene and polymethacrylate particles, no penetration through the ILM was observed under any of the tested conditions. As shown in Fig. 4.12a, particles, depicted in red to represent their fluorescence signal, remained localized at the ILM, with cell nuclei shown in blue due to DAPI staining. For polystyrene particles (50–250 nm), experiments included an extended pre-incubation period of 4 h prior to particle exposure for 1 h, a condition expected to increase retinal permeability. In contrast, polymethacrylate particles were incubated directly with the sclero-retinal explants for 1 h. All images were acquired using an inverted Leica DMi8 microscope equipped with a $10\times$ air objective, with fluorescence signals overlaid on phase contrast images as shown in Fig. 4.12. In all cases, however, the detected fluorescence signal within the retinal tissue appeared as a uniform band approximately 12 µm thick, consistent across all particle sizes (25–250 nm). We believe that

genuine nanoparticle penetration through the ILM and subsequent diffusion into the retina would likely result in a more dispersed signal rather than a sharply defined band that correlates with the edge of the ILM. Notably, a fluorescent signal was observed in the lower regions of some sections, between the retina and choroid, particularly for the 50 nm and 100 nm particles (Fig. 4.12c–d). However, this signal likely originates from particles entering through the lateral edges of the explant or potentially via the puncture sites where the tissue was pinned to the Styrofoam during incubation. This signal can be clearly distinguished from the targeted ILM penetration, as no fluorescence was detected within the retinal layers between the ILM and choroid, where it would otherwise be expected if the particles had penetrated from the ILM side.

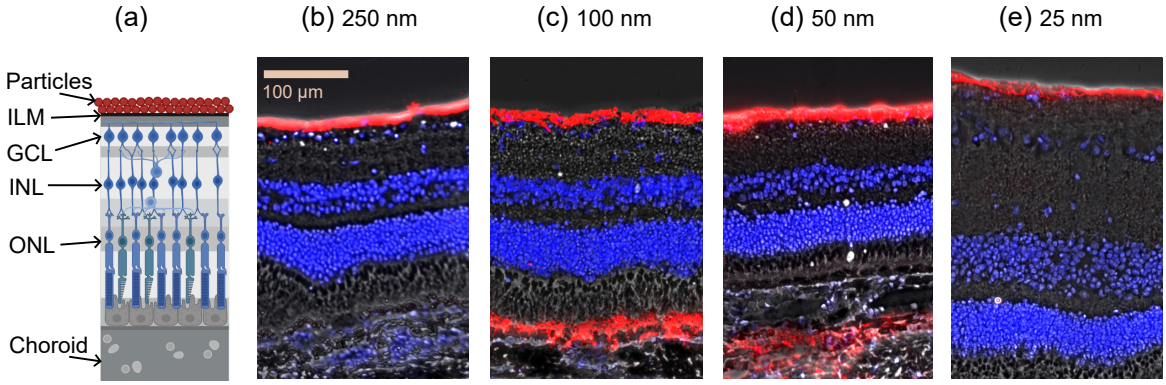

Figure 4.12. Retention of fluorescent carboxylated polystyrene and polymethacrylate particles at the ILM across a size range from 250 nm to 25 nm: (a) schematic illustration showing particles (red) localized on the ILM surface, with cell nuclei stained by DAPI (blue), GCL indicating ganglion cell layer, INL inner nuclear layer, ONL outer nuclear layer; representative fluorescence micrographs overlaid on phase contrast images depicting the absence of particle penetration through the ILM for: (b) polystyrene particles of 250 nm, (c) 100 nm, (d) 50 nm, and (e) polymethacrylate particles of 25 nm diameter. The scale bar shown in (b) applies to all images.

We further investigated the origin of the uniform fluorescent band, approximately 12 µm thick, consistently observed across all particle sizes. We hypothesized that the band arises from the cryosectioning process rather than particle penetration through the ILM. To test this hypothesis, sections of the same sample were prepared at varying thicknesses (6 µm, 12 µm and 30 µm). Upon imaging using an inverted *Leica* DMi8 microscope equipped with a $60\times$ oil immersion objective, the apparent depth of the fluorescent signal was found to correspond directly with the section thickness (see Fig. 4.13). This clear correlation supports the hypothesis that the observed fluorescent band results from the sectioning procedure itself, likely due to compression of the particle layer on the ILM during sectioning, rather than from genuine particle infiltration into the retinal tissue. Consequently, our findings demonstrate

that carboxylated polystyrene and polymethacrylate particles do not spontaneously traverse the ILM under the experimental conditions tested.

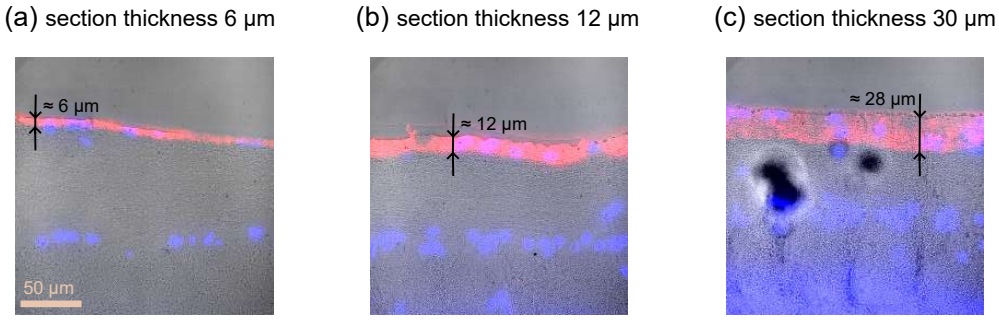

Figure 4.13. Representative fluorescence micrographs overlaid on phase contrast images demonstrating the correlation between the thickness of the observed red fluorescent band at the ILM (arising from particle fluorescence) and the section thickness: (a) 6 µm section; (b) 12 µm section; and (c) 30 µm section. The scale bar shown in (a) applies to all images.

Subsequently, we tested even smaller nanomaterials, specifically carboxylated quantum dots with core sizes in the 2–10 nm range. No penetration through the ILM was observed (Fig. 4.14). Instead, the quantum dots were retained at the ILM surface, as visualized by fluorescence signals overlaid on phase contrast images acquired with an inverted *Leica* DMi8 microscope equipped with a $10\times$ air objective.

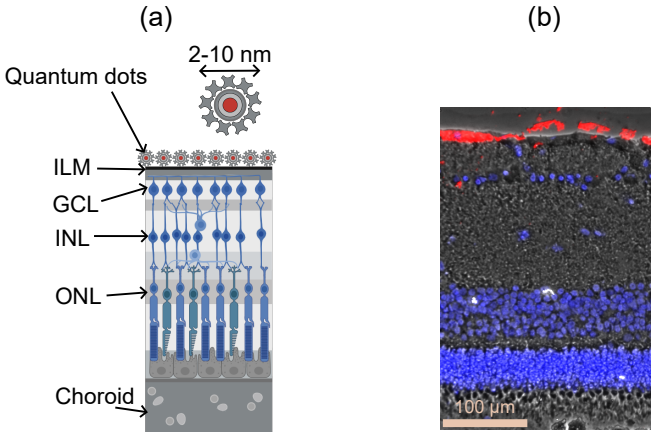

Figure 4.14. ILM retention of carboxylated quantum dots: (a) schematic illustration showing carboxylated quantum dots (red) localized at the ILM surface, with cell nuclei stained by DAPI (blue); GCL, INL, and ONL denote the ganglion cell layer, inner nuclear layer, and outer nuclear layer, respectively; (b) representative fluorescence micrograph overlaid on a phase contrast image demonstrating the absence of quantum dot penetration through the ILM.

In contrast, the fluorophore-labeled goat anti-rabbit IgG secondary antibody (size ≈ 14 nm × 8 nm, as depicted in Fig. 4.15a) traversed the ILM and diffused throughout the retinal layers within 1 h of incubation. This is clearly visualized in the confocal microscopy image in Fig. 4.15b, where the green fluorescence corresponds to the labeled antibody.

To minimize interference from tissue autofluorescence, which was found to vary between samples and can obscure detection of weak fluorescence signals, an additional detection channel was employed during imaging. This channel captured emissions at significantly longer wavelengths than those of the fluorophore of interest, using the same excitation laser. Since the autofluorescent background signal should be largely independent of the detection wavelength, the difference between the channel intensities was used to subtract the background, allowing isolation of the specific fluorescence signal associated with the antibody. The resulting signal is displayed in green in Fig. 4.15b.

To verify that the green fluorescence observed within the retina originated from ILM penetration rather than from diffusion through the lower layers, we analyzed the fluorescence distribution across the retinal depth in more detail. In earlier experiments (Fig. 4.12c–d), signals above the choroid were attributed to particle entry through the lateral edges of the explant or at puncture sites. Similarly, in Fig. 4.15, fluorescence above the choroid appears stronger than in the ganglion cell layer (GCL) and inner nuclear layer (INL), necessitating a careful analysis to discern whether the signal within the GCL and INL results from true ILM penetration or from diffusion originating at the choroid side. To determine the direction of the antibody penetration, the average fluorescence intensity across the retinal depth from Fig. 4.15b, including both the DAPI signal and the background-corrected antibody fluorescence, normalized to their respective maxima, is plotted in Fig. 4.15c. The antibody signal exhibited a prominent peak at the ILM, while DAPI fluorescence peaked at the inner (INL) and outer nuclear layer (ONL). Notably, the antibody fluorescence beneath the ILM (at GCL) was higher than at the ONL, confirming penetration from the ILM side. The antibody signal observed beyond the ONL likely reflects entry through lateral edges or puncture sites, without significant diffusion into inner retinal layers such as the ONL, INL, or GCL.

Overall, these findings suggest that the ILM imposes a size exclusion threshold for negatively charged particles between approximately 8 nm and 25 nm. However, particle size alone does not fully determine the ability to penetrate the retina from the vitreoretinal interface, suggesting that additional factors, such as chemical interactions, may also influence retinal entry. Notably, the smallest transfection agents currently available for gene therapy approach or exceed this threshold, implying that passive diffusion is unlikely to enable efficient delivery. These results highlight the necessity for advanced, targeted delivery strategies to facilitate the transport of transfection agents across the ILM and to enhance the overall efficacy of retinal gene therapy.

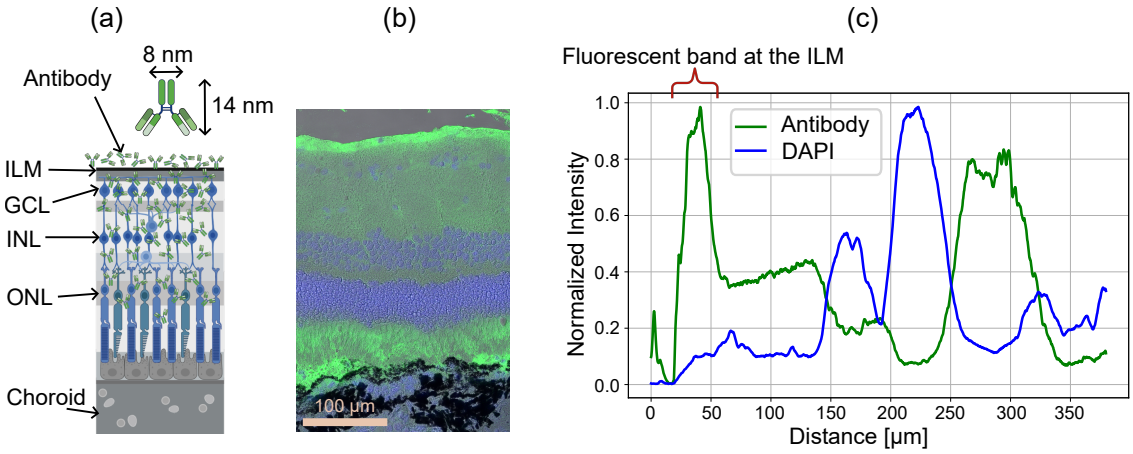

Figure 4.15. Investigation of ILM permeability to a fluorescently labeled goat anti-rabbit IgG secondary antibody: (a) schematic illustration depicting antibody (green) penetration into deeper retinal layers, with cell nuclei stained by DAPI (blue); GCL, INL, and ONL indicate the ganglion cell layer, inner nuclear layer, and outer nuclear layer, respectively; (b) representative fluorescence micrograph overlaid on a bright field image showing antibody penetration throughout the retinal layers; (c) normalized fluorescence intensity profiles, with green representing the fluorescently labeled antibody signal and blue indicating DAPI-stained nuclei.

4.3.3 Enhanced Transport across the ILM after Enzymatic Digestion

To enable the delivery of larger nanoscale materials (approximately $> 10\,\mathrm{nm}$) across the ILM, we explored the strategy to increase ILM permeability through enzymatic digestion, as initially described in Dr. F. Peter's doctoral work [179]. Specifically, we employed collagenase type IV (*Sigma-Aldrich*), an enzyme known to selectively degrade type IV collagen [179, 254], the principal structural constituent of the ILM [190, 191].

As demonstrated in Dr. F. Peter's thesis [179], incubation of sclero-retinal models with 50 µg and 100 µg of collagenase IV in Hank's balanced salt solution (HBSS) supplemented with Ca^{2+} for 1 h led to effective ILM digestion. This increased permeability allowed the passage of 25 nm carboxylated polymethacrylate nanoparticles [179], which are otherwise unable to cross the ILM under passive conditions (see Fig. 4.12e). However, as discussed in Dr. F. Peter's thesis and reported in other studies, high concentrations of enzymes may not only digest the ILM, but also negatively impact the structural integrity and function of the underlying retinal tissue [179, 242]. Additionally, the use of such high enzyme concentrations in human eyes *in vivo* would likely cause deleterious effects on the vitreous body, which contains collagen fibers.

To enhance the transport of larger nanoparticles while preserving retinal integrity, we explored minimizing the required collagenase IV dose by immobilizing the enzyme on silica beads. These collagenase-functionalized beads were co-incubated with 25 nm carboxylated polymethacrylate nanoparticles atop sclero-retinal explants (Fig. 4.16a). As established previously, the 25 nm nanoparticles are unable to penetrate the intact ILM unaided (Fig. 4.16b). Therefore, by delivering collagenase to the ILM surface via the functionalized beads, we aimed to achieve targeted, localized enzymatic digestion of the ILM (Fig. 4.16c). This localized enzymatic digestion was anticipated to selectively enhance ILM permeability, thereby promoting the subsequent diffusion of nanoparticles into the retinal tissue (Fig. 4.16d).

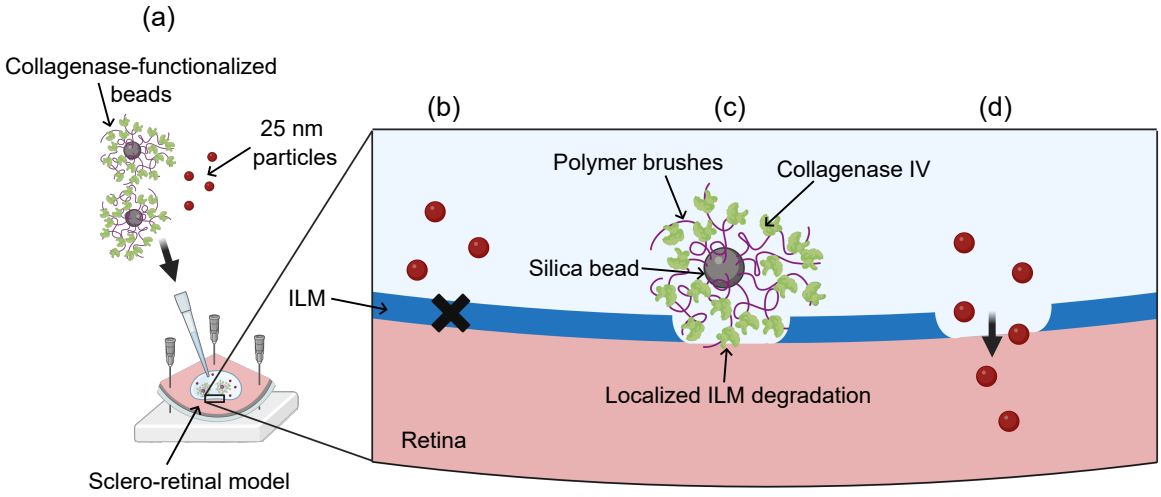

Figure 4.16. Schematic illustration of localized enzymatic degradation of the ILM: (a) collagenase-functionalized beads are incubated together with 25 nm carboxylated polymethacrylate nanoparticles atop sclero-retinal explants; (b) 25 nm particles cannot penetrate the retina unaided; (c) localized ILM degradation mediated by collagenase immobilized on silica beads via polymer brushes; (d) enhanced diffusion of 25 nm particles into the retina.

The collagenase IV was immobilized onto silica beads (1.5 µm diameter) by Dr. F. Peter and Dr. M. Alarcón-Correa, and only a brief description is provided here. Collagenase was localized to silica beads via surface-grafted polymer brushes, prepared according to the protocol described by Marcelino *et al.* [255]. Briefly, silica particles were dispersed in ethanol and functionalized with an APTES-ATRP initiator by refluxing with APTES for 1 h. After sequential washing with ethanol/toluene mixtures of increasing toluene content, the particles were redispersed in toluene and reacted overnight with triethylamine and α-Bromoisobutyryl bromide. Subsequent washes with toluene/ethanol mixtures of increasing ethanol content were performed before final redispersion in ethanol. Polymerization was achieved by combining the functionalized particles with $CuSO_4$, (+)-sodium L-ascorbate, tris[2-(dimethylamino)ethyl]amine and 2-(diethylamino)ethyl methacrylate, fol-

lowed by agitation for 6 h. The resulting particles were dialyzed into water (MWCO 12 500 Da) for 3 days, washed in pH 1 phosphate buffer, sonicated, and resuspended in pH 6 phosphate buffer. For enzyme immobilization, the particles were incubated with collagenase IV (100 µg enzyme/mg particles) for 1 h or overnight at 4 °C, followed by multiple washes.

To evaluate the efficacy of localized enzymatic ILM degradation to facilitate nanoparticle transport, we examined the transport of 25 nm fluorescent carboxylated polymethacrylate nanoparticles co-incubated with polymer brush-grafted silica beads carrying immobilized collagenase (Fig. 4.17c). These findings were directly compared to two control conditions, specifically nanoparticles applied alone without beads (Fig. 4.17a), and nanoparticles co-incubated with silica beads grafted with polymer brushes but lacking immobilized enzymes (Fig. 4.17b). For this purpose, sclero-retinal *ex vivo* models were prepared as previously described (see Fig. 4.11) and incubated for 1 h with the respective materials (i.e., 25 nm nanoparticles alone or in combination with 2 mg beads, with or without collagenase). Following incubation, central regions of the samples were excised, cryofixed, cryosectioned, and stained with DAPI. Confocal microscopy was then used to evaluate nanoparticle penetration (Fig. 4.17d–f). In both control conditions, the red fluorescence from the nanoparticles remained confined to a superficial 12 µm region adjacent to the ILM (Fig. 4.17d–e). In contrast, samples treated with collagenase-functionalized beads demonstrated deeper penetration of red fluorescence into the retinal tissue, indicating facilitated trans-ILM permeability (see representative image in Fig. 4.17f).

Closer inspection of the sections treated with collagenase-functionalized beads revealed multiple beads retained at the retinal interface, corresponding to the ILM location (Fig. 4.18a). Additionally, the interface in these samples appeared visibly roughened, consistent with localized enzymatic degradation and the associated increase in trans-ILM nanoparticle penetration. This contrasts with the smooth ILM profile observed in control samples (compare Fig. 4.18a with Fig. 4.17d–e, Fig. 4.13, and Fig. 4.12e).

To characterize the retinal interface at higher resolution, high-resolution electron microscopy was performed and analyzed by Dr. I. Wacker and E. R. Curticean from the research group of Prof. Dr. R. Schröder. Explants incubated with 1.5 µm silicon beads, with or without immobilized collagenase, were prepared as previously described (up to step (i) in Fig. 4.11). Subsequent processing by E. R. Curticean and Dr. I. Wacker involved fixation of the central explant region, dehydration, resin infiltration, embedding in molds, and polymerization. Sample blocks were then sectioned with diamond knives to obtain individual sections averaging 100 nm in thickness, which were mounted on silicon wafers and imaged using a *Zeiss* ULTRA 55 electron microscope.

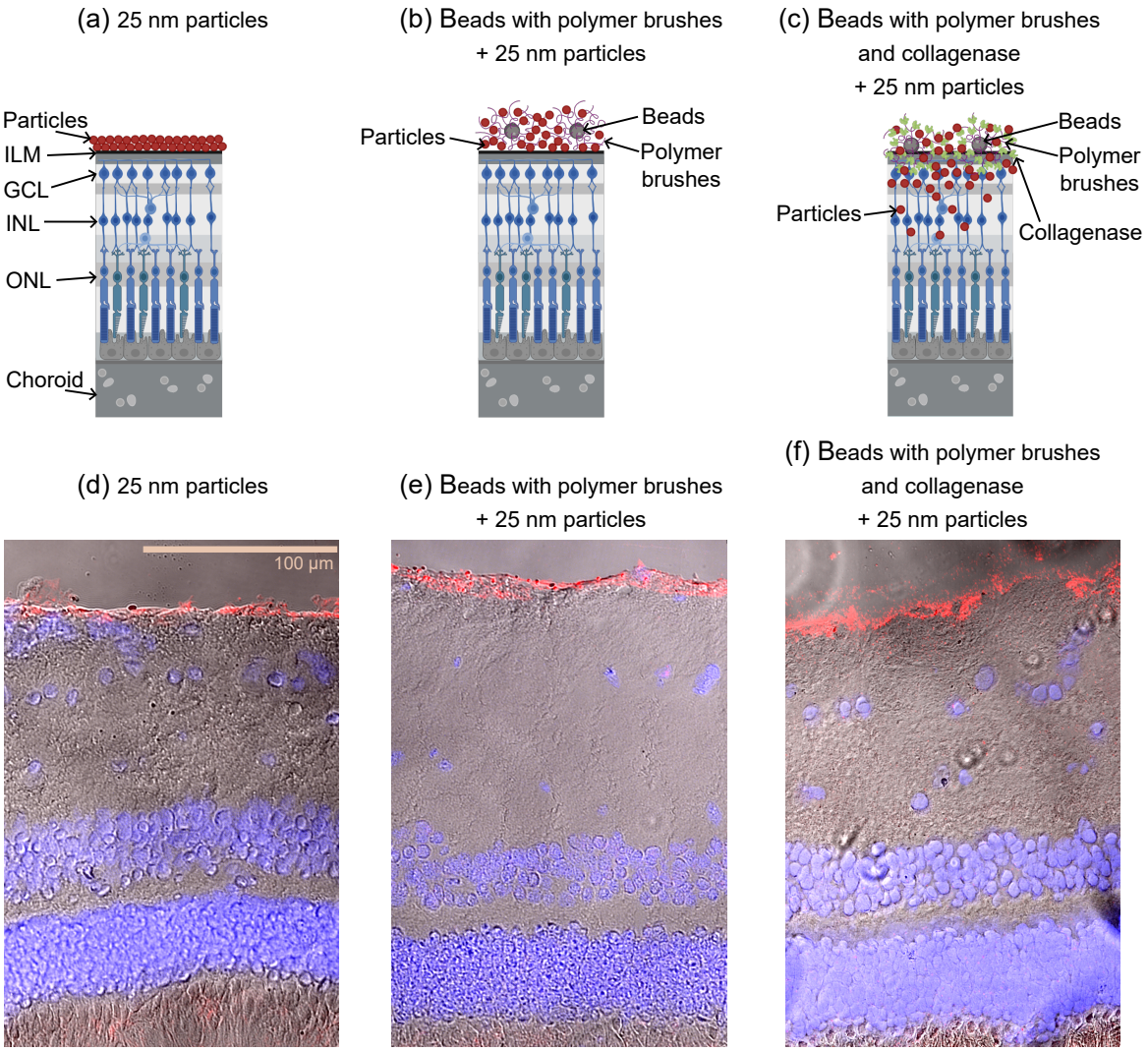

Figure 4.17. Localized enzymatic degradation of the ILM facilitates nanoparticle penetration into retinal tissue: (a) schematic illustrating nanoparticles alone, which remain confined to the ILM, with the corresponding representative microscopy image shown in (d); (b) schematic depicting nanoparticles co-incubated with silica beads grafted with polymer brushes but lacking collagenase, which also remain localized at the ILM, alongside the representative microscopy image in (e); (c) schematic showing nanoparticles incubated with silica beads grafted with polymer brushes carrying immobilized collagenase, resulting in enhanced nanoparticle diffusion into the retina, with the corresponding representative microscopy image in (f). The scale bar shown in (d) applies to all microscopy images. Two of the microscopy images were preselected from our extensive image dataset by Dr. F. Peter.

Electron microscopy of explants treated with collagenase-functionalized beads revealed multiple beads retained at the retinal surface, specifically at the ILM (Fig. 4.18b). In contrast, no beads were detected at the interface in control samples lacking collagenase. Although no beads were observed within the retinal layers in either condition, the consistent retention of collagenase-functionalized beads at the ILM, unlike the non-functionalized beads, provides further support for localized enzymatic activity. While the 1.5 µm beads themselves did not penetrate the retina, we argue that their accumulation at the ILM facilitated localized degradation, thereby promoting transport of smaller, 25 nm nanoparticles across the ILM, as previously shown in Fig. 4.18a.

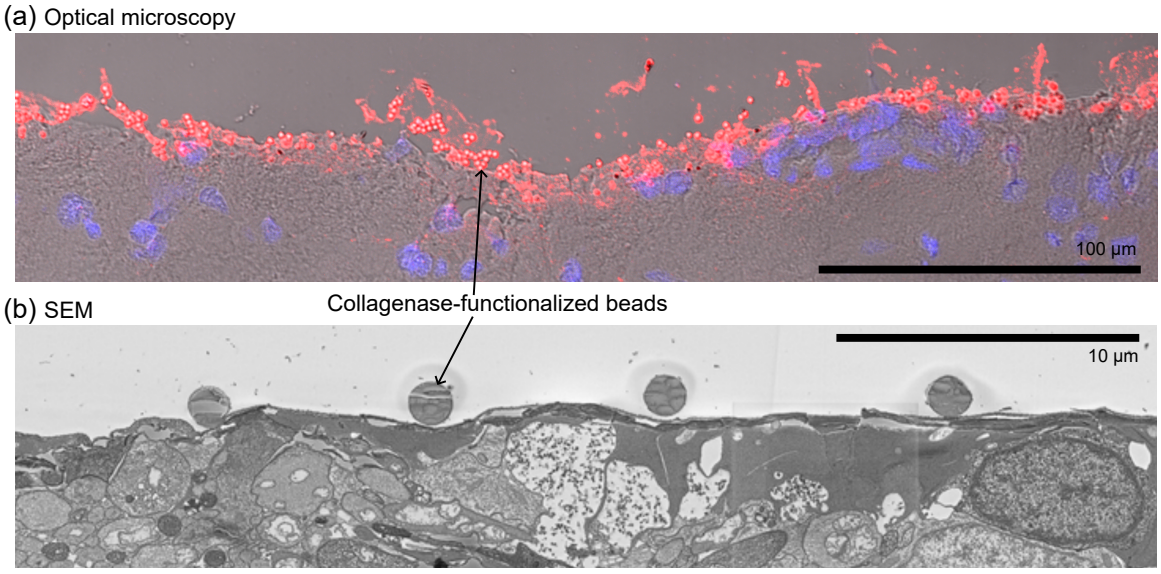

Figure 4.18. Retinal interface following localized ILM degradation by collagenase immobilized on 1.5 µm silica beads: (a) optical microscopy image showing red fluorescence from co-incubated 25 nm nanoparticles penetrating the retina (preselected from our extensive image dataset by Dr. F. Peter); (b) SEM image depicting collagenase-functionalized beads adhered to the retinal surface (acquired by Prof. Dr. R. Schröder's group).

Overall, these results demonstrate the promising potential of a non-invasive strategy for delivering nanomaterials into retinal cells. Unlike the detrimental effects observed with enzyme application in bulk solution for ILM degradation, localized enzymatic activity is achieved by immobilizing collagenase on microscale beads. Importantly, using the same total amount of enzyme ($\approx$1 µg per sclero-retinal explant) dispersed in solution without localization did not enhance nanoparticle diffusion across the ILM. This contrast highlights that collagenase immobilization on beads enables more efficient ILM degradation, particularly when compared to the substantially higher enzyme concentrations (50 µg and 100 µg) required in our previous ILM digestion experiments using collagenase solution, as detailed in Dr. F. Peter's thesis [179].

4.4 Overview of Nano-/Microscale Transport for Opthalmological Applications

A range of strategies to study and enhance nanoparticle transport within ocular substitutes and native tissue have been explored. These included magnetic techniques, methods for characterizing passive diffusion, as well as electrical and chemical approaches to actively promote penetration through tissue. In particular, my key conclusions are as follows:

(i) Directed transport using helical propellers actuated via rotating magnetic fields is feasible in various hyaluronic acid-based gels developed as a replacement for the vitreous. We identified compatible gel formulations and optimal propeller designs, paving the way for smart vitreous substitutes suitable for targeted drug delivery.

(ii) In lower molecular weight hyaluronic acid-based gels, larger FePt propellers enabled propulsion at higher polymer concentrations than smaller Ni propellers, limited primarily by magnetic torque rather than pore size.

(iii) In contrast, in higher molecular weight hyaluronic acid-based gels, smaller Ni propellers performed better, suggesting pore size restrictions dominate. Further improvements may be achieved using smaller propellers with enhanced magnetic moments, such as those made from FePt in the $L1_0$-phase.

(iv) Although intravitreal injection is less invasive than subretinal delivery, nanoparticle transport is limited by the ILM, whose permeability remains unclear. Using Ussing chambers, we confirmed passive diffusion of small molecules (e.g., water, rhodamine B $\approx$1.6 nm) but observed inconsistent or negligible diffusion for larger probes (e.g., FITC-dextran, 25 nm particles). Mechanical stress and tissue damage from high-voltage enhancement further indicated that Ussing chambers are unsuitable to reliably assess ILM permeability.

(v) We developed *ex vivo* sclero-retinal models for assessing trans-ILM diffusion. While negatively charged nanoparticles (25 nm–250 nm) and quantum dots (2 –10 nm) failed to penetrate the ILM, goat anti-rabbit IgG secondary antibody (14 nm × 8 nm) did. This suggests a size threshold between 8 nm and 25 nm, with chemical interactions also influencing ILM permeability.

(vi) Since most transfection agents exceed this ILM's permeability limit, strategies to enhance penetration are essential. We showed that immobilizing collagenase IV on silica microbeads enables localized ILM degradation, allowing 25 nm particles to enter retinal tissue. Unlike a solution of free enzymes at high concentration, this approach improves delivery while minimizing tissue damage.

Conclusion and Outlook

This thesis explored various magnetic strategies for generating forces at the nano- and microscale, aiming to characterize the magnetic properties of objects at this scale, probe the mechanical properties of surrounding media, stimulate and manipulate cells, and enable transport through complex environments such as vitreous substitute materials. Forces were applied through magnetic field gradients, deformation of elastic magnetic bodies by homogeneous magnetic fields, and rotating magnetic fields, each tailored to specific experimental contexts. In addition to magnetic approaches, this thesis addressed nanoscale transport through ocular tissues by investigating passive diffusion and introducing an enzymatically driven strategy to enhance the penetration of nanomaterials across the inner limiting membrane of the eye, a major barrier to effective retinal delivery.

Magnetic field gradients generated by permanent magnets can exert forces on nanoscale and microscale objects; however, these forces decay rapidly with increasing distance from the magnet. Despite this limitation, such gradients are predictable and straightforward to produce, thus particularly well-suited for quantitative studies under controlled laboratory conditions. In this thesis, magnetic field gradients were employed to develop a reliable method for evaluating the mesh size of hydrogels proposed as smart vitreous substitutes. This approach enabled the identification of hydrogel formulations that could, in principle, permit the penetration of materials with defined sizes.

For applications where placing a permanent magnet in close proximity to the biological target is impractical due to spatial constraints and rapid decrease of the gradient, the use of magnetizable microscale bodies introduced into a homogeneous magnetic field offers a compelling alternative. These bodies locally perturb the field to produce strong gradients in their immediate vicinity, enabling localized force application. This concept was implemented using a paramagnetic probe to exert magnetic forces on ferrofluid droplets embedded in cell cultures within a coil-generated magnetic field, thereby enhancing their capability to mechanically stimulate cells. Although cellular biochemical responses were not analyzed, the platform presents a promising tool for investigating mechanotransduction. A similar approach, using a Halbach array to generate the external field, was designed to study the sprouting behavior of cells that had internalized magnetic nanoparticles. This tool is cur-

rently being used in biological experiments by our collaborators and may provide insights into cellular signaling pathways, thereby advancing research in tissue engineering and regenerative medicine.

Homogeneous magnetic fields can also serve as a source of magnetic stimuli in systems containing ensembles of magnetic particles, such as ferrofluid droplets in diamagnetic environments. Although the droplet material and size are not suitable for *in vivo* applications, these constructs can be effectively used to probe material properties and elicit cellular responses to mechanical cues in *in vitro* or *ex vivo* settings. In this thesis, the platform was initially employed to characterize the mechanical properties of fluids and gels by integrating the electromagnetic coil generating the homogeneous field onto a microscope stage. Subsequently, the system was adapted for use with cell monolayers, enabling simultaneous mechanical stimulation at multiple sites within the culture dish. Although the applied stimulus did not produce detectable changes in cell behavior, potential improvements, such as reducing the ferrofluid droplet height or employing stronger magnetic fields, are expected to enhance mechanical stimulation.

Rotating magnetic fields can generate relatively strong propulsive forces on chiral objects, such as helical propellers. The low-amplitude rotating fields required for their actuation can be produced over relatively large distances, making this approach particularly well-suited for biomedical applications within the human body. In this work, helical propellers are proposed as targeted drug delivery vehicles capable of navigating through vitreous substitute materials, which are essential for treating various eye diseases. Targeted delivery through these novel materials has the potential to significantly improve treatment efficacy and enhance the patient quality of life. This thesis demonstrates the feasibility of directed transport using helical propellers in these gels and identifies the most suitable hyaluronic acid-based formulations along with optimal propeller designs for efficient propulsion.

Retinal gene therapy could also benefit from targeted delivery using helical propellers actuated by rotating magnetic fields. A major challenge in this context is the safe and effective transport of therapeutic genes to retinal cells, whose pathological changes underlie many forms of vision loss. Delivery via magnetically driven helical propellers injected into the vitreous humor could offer a less invasive and safer alternative to the surgical procedure currently used in clinical practice. While transport through vitreous using helical propellers has been previously demonstrated by our group, the major obstacle in reaching the retinal cells has been the inner limiting membrane, separating the vitreous from neurosensory retina. To address this, the thesis first examined the permeability of this barrier to nanoscale materials. After determining that the materials capable of passive diffusion are smaller than transfection agents available for retinal gene therapy, we demonstrated that localized degradation of the inner limiting membrane can be achieved by immobilizing the enzyme collagenase IV

onto silica microbeads, thereby facilitating the passage of larger nanoscale materials. We envision that functionalizing helical propellers with both collagenase IV and therapeutic genes could enable safe, targeted delivery to retinal cells (see Fig. 5.1). Additionally, fabricating these propellers from degradable MgZn alloy and incorporating biocompatible magnetic FePt alloy (see Fig. 5.1), as previously demonstrated by our group, would further enhance the system's suitability for *in vivo* applications. To support this development, collagenase-functionalized silica beads and magnesium–zinc helical propellers are currently undergoing long-term biocompatibility testing in pigs *in vivo* in a collaboration with Dr. med. M. Hammer's research group.

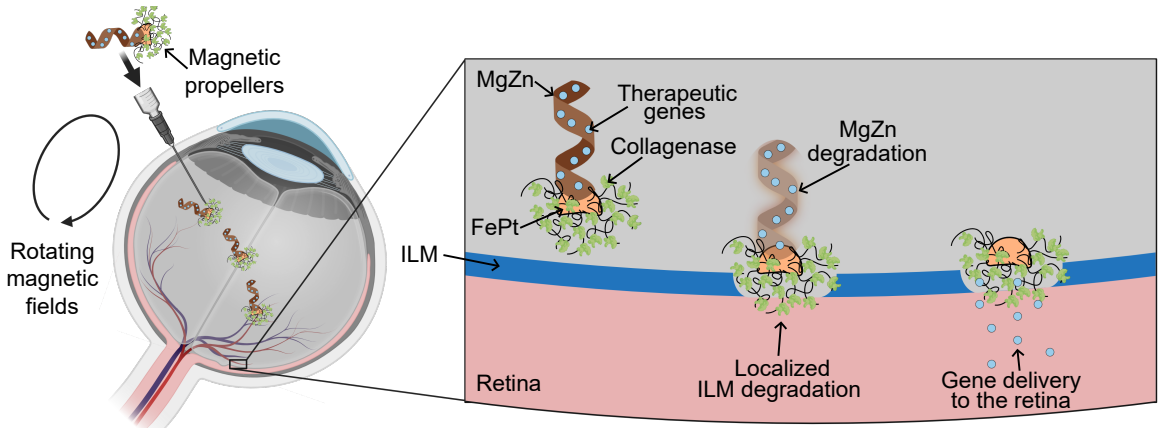

Figure 5.1. Illustration of a conceptual approach for targeted retinal gene therapy using helical micromagnetic propellers. Therapeutic genes and the enzyme collagenase IV are envisioned to be co-functionalized onto the surface of the propellers, which would be fabricated from a degradable MgZn alloy [103] and incorporate biocompatible FePt as the magnetic component [31]. Following intravitreal injection, the propellers would be guided to the diseased retinal region using externally applied rotating magnetic fields. Upon reaching the inner limiting membrane (ILM), collagenase IV would induce localized degradation of the barrier, while the MgZn structure gradually dissolves. This process would facilitate the diffusion of therapeutic genes across the ILM, allowing for targeted transfection of retinal cells. Figure concept adapted from a presentation by Dr. F. Peter.

Overall, by integrating physical principles and chemical approaches with biomedical applications, this work introduces novel strategies that advance both the tools for investigating mechanobiology, as well as micro- and nanoscale tools for targeted delivery in ophthalmology.

Bibliography

[1] Dance, A. The secret forces that squeeze and pull life into shape. *Nature* **589**, 186 (2020).

[2] Steward, A. J. & Kelly, D. J. Mechanical regulation of mesenchymal stem cell differentiation. *J. Anat.* **227**, 717 (2015).

[3] Manokawinchoke, J. *et al.* Mechanical loading and the control of stem cell behavior. *Arch. Oral Biol.* **125**, 105092 (2021).

[4] Gebhardt, J. C. M. & Rief, M. Force signaling in biology. *Science* **324**, 1278 (2009).

[5] Shiraishi, K. *et al.* Biophysical forces mediated by respiration maintain lung alveolar epithelial cell fate. *Cell* **186**, 1478 (2023).

[6] Carter, D. R., Orr, T. E., Fyhrie, D. P. & Schurman, D. J. Influences of mechanical stress on prenatal and postnatal skeletal development. *Clin. Orthop. Rel. Res.* **219**, 237 (1987).

[7] Naqvi, S. M. & Mcnamara, L. M. Stem cell mechanobiology and the role of biomaterials in governing mechanotransduction and matrix production for tissue regeneration. *Front. Bioeng. Biotechnol.* **8**, 597661 (2020).

[8] Molnar, K. & Manneville, J.-B. Emerging mechanobiology techniques to probe intracellular mechanics. *npj Biol. Phys. Mech.* **2**, 12 (2025).

[9] Rodriguez, M. L., McGarry, P. J. & Sniadecki, N. J. Review on cell mechanics: Experimental and modeling approaches. *Appl. Mech. Rev.* **65**, 060801 (2013).

[10] Moreno-Flores, S. Hallmarks of life in single cell contact mechanics: Outstanding challenges and perspectives. *Front. Mech. Eng.* **6**, 58 (2020).

[11] Tian, Z., Wang, X. & Chen, J. On-chip dielectrophoretic single-cell manipulation. *Microsyst. Nanoeng.* **10**, 117 (2024).

[12] Ozcelik, A. *et al.* Acoustic tweezers for the life sciences. *Nat. Methods* **15** (2018).

[13] Bongrand, P. Ligand-receptor interactions. *Rep. Prog. Phys.* **62**, 921 (1999).

[14] Angle, M. R., Wang, A., Thomas, A., Schaefer, A. T. & Melosh, N. A. Penetration of cell membranes and synthetic lipid bilayers by nanoprobes. *Biophys. J.* **107**, 2091 (2014).

[15] Grandbois, M., Beyer, M., Rief, M., Clausen-Schaumann, H. & Gaub, H. E. How strong is a covalent bond. *Science* **283**, 1727 (1999).

[16] Beyer, M. K. The mechanical strength of a covalent bond calculated by density functional theory. *J. Chem. Phys.* **112**, 7307 (2000).

[17] Ishijima, A. *et al.* Multiple-and single-molecule analysis of the actomyosin motor by nanometer-piconewton manipulation with a microneedle: Unitary steps and forces. *Biophys. J.* **70**, 383 (1996).

[18] Finer, J. T., Simmons, R. M. & Spudicht, J. A. Single myosin molecule mechanics: piconewton forces and nanometre steps. *Nature* **368**, 113 (1994).

[19] Bo, G. D. Mechanochemistry of the mechanical bond. *Chem. Sci.* **9**, 15 (2018).

[20] Markin, V. S. & Hudspeth, A. J. Gating-spring models of mechanoelectrical transduction by hair cells of the internal ear. *Annu. Rev. Biophys. Biomol. Struct.* **24**, 59 (1995).

[21] Strick, T., Allemand, J. F., Croquette, V. & Bensimon, D. The manipulation of single biomolecules. *Phys. Today* **54**, 46 (2001).

[22] Pal, S. K., Jeong, S., Otoufat, T., Bae, H. & Kim, G. Adaptive cooling strategy via human hair: High optothermal conversion efficiency of solar radiation into thermal dissipation. *Proc. Natl. Acad. Sci. U.S.A.* **121**, e2312297121 (2024).

[23] Yang, S. *et al.* Acoustic tweezers for high-throughput single-cell analysis. *Nat. Protoc.* **18**, 2441 (2023).

[24] Fan, Z. *et al.* Acoustic actuation of integrin-bound microbubbles for mechanical phenotyping during differentiation and morphogenesis of human embryonic stem cells. *Small* **14**, e1803137 (2018).

[25] Shi, M., Fischer, P. & Melde, K. Acoustic holographic assembly of cell-dense tissue constructs. *Biofabrication* **17**, 035009 (2025).

[26] Arbore, C., Perego, L., Sergides, M. & Capitanio, M. Probing force in living cells with optical tweezers: from single-molecule mechanics to cell mechanotransduction. *Biophys. Rev.* **11**, 765 (2019).

[27] Mierke, C. T. Magnetic tweezers in cell mechanics. *Methods Enzymol.* **694**, 321 (2024).

[28] Shapiro, B. *et al.* Open challenges in magnetic drug targeting. *Wiley Interdiscip. Rev. Nanomed. Nanobiotechnol.* **7**, 446 (2014).

[29] Aram, E. *et al.* Smart and multi-functional magnetic nanoparticles for cancer treatment applications: Clinical challenges and future prospects. *Nanomaterials* **12**, 3567 (2022).

[30] Polyak, B. & Friedman, G. Magnetic targeting for site-specific drug delivery: applications and clinical potential. *Expert Opin. Drug Deliv.* **6**, 53 (2009).

[31] Kadiri, V. M. *et al.* Biocompatible magnetic micro- and nanodevices: Fabrication of FePt nanopropellers and cell transfection. *Adv. Mater.* **32**, 2001114 (2020).

[32] Purcell, E. M. The efficiency of propulsion by a rotating flagellum. *Proc. Natl. Acad. Sci. U.S.A.* **94**, 11307 (1997).

[33] Trombley, C. I. & Ekiel-Jeżewska, M. L. Basic concepts of Stokes flows. In Toschi, F. & Sega, M. (eds.) *Flowing Matter*, 35–50 (Springer International Publishing, Cham, Switzerland, 2019).

[34] Happel, J. & Brenner, H. *Low Reynolds Number Hydrodynamics: With Special Applications to Particulate Media* (Springer Netherlands, Dordrecht, Netherlands, 1983).

[35] Sun, X., Lin, T. & Gezelter, J. D. Langevin dynamics for rigid bodies of arbitrary shape. *J. Chem. Phys.* **128**, 234107 (2008).

[36] Carrasco, B. & De La Torre, J. G. Hydrodynamic properties of rigid particles: Comparison of different modeling and computational procedures. *Biophys. J.* **76**, 3044 (1999).

[37] Pankhurst, Q. A., Connolly, J., Jones, S. K. & Dobson, J. Applications of magnetic nanoparticles in biomedicine. *J. Phys. D: Appl. Phys.* **36**, 167 (2003).

[38] Coey, J. M. D. *Magnetism and Magnetic Materials* (Cambridge University Press, New York, New York, USA, 2009).

[39] Goldfarb, R. B. The permeability of vacuum and the revised international system of units. *IEEE Magn. Lett.* **8**, 1 (2017).

[40] Camacho, J. M. & Sosa, V. Alternative method to calculate the magnetic field of permanent magnets with azimuthal symmetry. *Rev. Mex. Fis. E* **59**, 8 (2013).

[41] Mladenović, A. N. & Slavoljub, R. A. Block permanent magnet system magnetic field determination. In *Proceedings of the 54th Internationales Wissenschaftliches Kolloquium* (Ilmenau, Germany, 2009).

[42] Webcraft GmbH. Physical magnet data (2006). URL `https://www.supermagnete.de/eng/physical-magnet-data`. Accessed 30.01.2025.

[43] Webcraft GmbH. Neodymium magnets: the super-strong ones (2023). URL `https://www.supermagnete.de/eng/supermagnete-strong-neodymium-magnets`. Accessed 30.01.2025.

[44] Webcraft GmbH. Which magnet coatings are there? (2016). URL `https://www.supermagnete.de/eng/faq/Which-magnet-coatings-are-there`. Accessed 30.01.2025.

[45] Derks, R., Dietzel, A., Wimberger-Friedl, R. & Prins, M. W. Magnetic bead manipulation in a sub-microliter fluid volume applicable for biosensing. *Microfluid. Nanofluidics* **3**, 141 (2007).

[46] Meister, M. Physical limits to magnetogenetics. *eLife* **5**, e17210 (2016).

[47] Qin, S. *et al.* A magnetic protein biocompass. *Nat. Mater.* **15**, 217 (2016).

[48] Stanley, S. A., Sauer, J., Kane, R. S., Dordick, J. S. & Friedman, J. M. Remote regulation of glucose homeostasis in mice using genetically encoded nanoparticles. *Nat. Med.* **21**, 92 (2015).

[49] Wheeler, M. A. *et al.* Genetically targeted magnetic control of the nervous system. *Nat. Neurosci.* **19**, 756 (2016).

[50] Xu, F. X. *et al.* Magneto is ineffective in controlling electrical properties of cerebellar Purkinje cells. *Nat. Neurosci.* **23**, 1041–1043 (2020).

[51] Wang, G. *et al.* Revaluation of magnetic properties of Magneto. *Nat. Neurosci.* **23**, 1047 (2020).

[52] Widder, K. J., Senyei, A. E. & Scarpelli, D. G. Magnetic microspheres: A model system for site specific drug delivery in vivo. *Proc. Soc. Exp. Biol. Med.* **158**, 141 (1978).

[53] Scherer, F. *et al.* Magnetofection: Enhancing and targeting gene delivery by magnetic force in vitro and in vivo. *Gene Ther.* **9**, 102 (2002).

[54] Plank, C., Zelphati, O. & Mykhaylyk, O. Magnetically enhanced nucleic acid delivery. ten years of magnetofection-progress and prospects. *Adv. Drug Deliv. Rev.* **63**, 1300 (2011).

[55] Mykhaylyk, O. *et al.* Magnetic nanoparticle and magnetic field assisted siRNA delivery in vitro. In Sioud, M. (ed.) *RNA Interference: Challenges and Therapeutic Opportunities*, 53–106 (Springer New York, New York, New York, USA, 2015).

[56] Zhang, T. Y. *et al.* Design of magnetic gene complexes as effective and serum resistant gene delivery systems for mesenchymal stem cells. *Int. J. Pharm.* **520**, 1 (2017).

[57] Wang, Z. *et al.* Shape-controlled magnetic mesoporous silica nanoparticles for magnetically-mediated suicide gene therapy of hepatocellular carcinoma. *Biomaterials* **154**, 147 (2018).

[58] Yang, Z. *et al.* Superparamagnetic iron oxide nanoparticles modified with polyethylenimine and galactose for siRNA targeted delivery in hepatocellular carcinoma therapy. *Int. J. Nanomed.* **13**, 1851 (2018).

[59] Cen, C. *et al.* Improving magnetofection of magnetic polyethylenimine nanoparticles into MG-63 osteoblasts using a novel uniform magnetic field. *Nanoscale Res. Lett.* **14**, 1 (2019).

[60] Cui, Y. *et al.* Effect of PEGylated magnetic PLGA-PEI nanoparticles on primary hippocampal neurons: Reduced nanoneurotoxicity and enhanced transfection efficiency with magnetofection. *ACS Appl. Mater. Interfaces* **11**, 38190 (2019).

[61] Huang, R.-Y. *et al.* Magnetic ternary nanohybrids for nonviral gene delivery of stem cells and applications on cancer therapy. *Theranostics* **9**, 2411 (2019).

[62] Gong, M. *et al.* Polyethylenimine-dextran-coated magnetic nanoparticles loaded with miR-302b suppress osteosarcoma in vitro and in vivo. *Nanomedicine* **15**, 711 (2020).

[63] Cristofolini, T. *et al.* Multifunctional hybrid nanoparticles as magnetic delivery systems for siRNA targeting the HER2 gene in breast cancer cells. *Mater. Sci. Eng. C* **109**, 110555 (2020).

[64] Rejman, J., Oberle, V., Zuhorn, I. S. & Hoekstra, D. Size-dependent internalization of particles via the pathways of clathrin- and caveolae-mediated endocytosis. *Biochem. J.* **377**, 159 (2004).

[65] Kirkham, M. & Parton, R. G. Clathrin-independent endocytosis: New insights into caveolae and non-caveolar lipid raft carriers. *Biochim. Biophys. Acta* **1745**, 273 (2005).

[66] Chaudhary, N. *et al.* Endocytic crosstalk: Cavins, caveolins, and caveolae regulate clathrin-independent endocytosis. *PLoS Biol.* **12**, e1001832 (2014).

[67] Smolders, S. *et al.* Magnetofection is superior to other chemical transfection methods in a microglial cell line. *J. Neurosci. Methods* **293**, 169 (2018).

[68] Gao, J. *et al.* Magnetic field promotes migration of Schwann cells with Chondroitinase ABC (ChABC)-loaded superparamagnetic nanoparticles across astrocyte boundary in vitro. *Int. J. Nanomed.* **15**, 315 (2020).

[69] AlSadek, D. M. *et al.* Cancer cell death induced by nanomagnetolectin. *Eur. J. Cell Biol.* **96**, 600 (2017).

[70] Bassetto, M. *et al.* New method for efficient siRNA delivery in retina explants: Reverse magnetofection. *Bioconjug. Chem.* **32**, 1078 (2021).

[71] Sen, M. *et al.* Efficient ocular delivery of VCP siRNA via Reverse Magnetofection in RHO P23H rodent retina explants. *Pharmaceutics* **13**, 225 (2021).

[72] Can, M. M., Coşkun, M. & Fırat, T. A comparative study of nanosized iron oxide particles; magnetite (Fe_3O_4), maghemite (γ-Fe_2O_3) and hematite (α-Fe_2O_3), using ferromagnetic resonance. *J. Alloys Compd.* **542**, 241 (2012).

[73] Hirano, N. *et al.* Magnetic vortex structure for hollow Fe_3O_4 spherical submicron particles. *Appl. Phys. Lett.* **119**, 132401 (2021).

[74] Nomura, E. *et al.* Magnetization process of cubic Fe_3O_4 submicron particles studied by polarized small-angle neutron scattering. *AIP Adv.* **12**, 035034 (2022).

[75] Atkins, P. & de Paula, J. *Physical Chemistry* (W. H. Freeman and Company, New York, New York, USA, 2006), 8th edn.

[76] Prosen, L. *et al.* Magnetic field contributes to the cellular uptake for effective therapy with magnetofection using plasmid DNA encoding against Mcam in B16F10 melanoma in vivo. *Nanomedicine* **11**, 627 (2016).

[77] Singh, J., Mohanty, I. & Rattan, S. In vivo magnetofection: A novel approach for targeted topical delivery of nucleic acids for rectoanal motility disorders. *Am. J. Physiol. Gastrointest. Liver Physiol.* **314**, G109 (2018).

[78] Pereyra, A. S. & Mykhaylyk, O. Magnetofection enhances adenoviral vector-based gene delivery in skeletal muscle cells. *J. Nanomed. Nanotechnol* . **7**, 1000364 (2016).

[79] Heun, Y. *et al.* HIF-1α dependent wound healing angiogenesis in vivo can be controlled by site-specific lentiviral magnetic targeting of SHP-2. *Mol. Ther.* **25**, 1616 (2017).

[80] Rieck, S. *et al.* Local anti-angiogenic therapy by magnet-assisted downregulation of SHP2 phosphatase. *J. Control. Release* **305**, 155 (2019).

[81] Dengler, M. *et al.* Targeted delivery of magnetic cobalt nanoparticles to the eye following systemic administration. *AIP Conf. Proc.* **1311**, 329 (2010).

[82] Bassetto, M. *et al.* Magnetically assisted drug delivery of topical eye drops maintains retinal function in vivo in mice. *Pharmaceutics* **13**, 1650 (2021).

[83] Yanai, A. *et al.* Focused magnetic stem cell targeting to the retina using superparamagnetic iron oxide nanoparticles. *Cell Transplant.* **21**, 1137 (2012).

[84] Karaagac, O., Hasirci, C. & Köçkar, H. Optimum saturation magnetization of superparamagnetic iron oxide nanoparticles for versatile applications. *Acta Phys. Pol. A* **146**, 154–164 (2024).

[85] Angelakeris, M. *et al.* Can commercial ferrofluids be exploited in ac magnetic hyperthermia treatment to address diverse biomedical aspects? *EPJ Web Conf.* **75**, 08002 (2014).

[86] Sachs, J. *Motion, Symmetry Spectroscopy of Chiral Nanostructures*. PhD thesis, University of Stuttgart, Stuttgart, Germany (2020).

[87] Morozov, K. I. & Leshansky, A. M. The chiral magnetic nanomotors. *Nanoscale* **6**, 1580 (2014).

[88] Dasgupta, D., Pally, D., Saini, D. K., Bhat, R. & Ghosh, A. Nanomotors sense local physicochemical heterogeneities in tumor microenvironments**. *Angew. Chem. Int. Ed.* **59**, 23690 (2020).

[89] Perrin, F. Mouvement brownien d'un ellipsoide - i. dispersion diélectrique pour des molécules ellipsoidales. *J. Phys. Radium.* **5**, 497 (1934).

[90] Gray, J. & Hancock, G. J. The propulsion of sea-urchin spermatozoa. *J. Exp. Biol.* **32**, 802 (1955).

[91] Lighthill, J. Flagellar hydrodynamics. *SIAM Rev.* **18**, 161 (1976).

[92] Chattopadhyay, S., Moldovan, R., Yeung, C. & Wu, X. L. Swimming efficiency of bacterium Escherichia coli. *Proc. Natl. Acad. Sci. U.S.A.* **103**, 13712 (2006).

[93] Hu, J., Yang, M., Gompper, G. & Winkler, R. G. Modelling the mechanics and hydrodynamics of swimming E. coli. *Soft Matter* **11**, 7867 (2015).

[94] Kadiri, V. M. *et al.* Light- and magnetically actuated FePt microswimmers. *Eur. Phys. J. E* **44**, 74 (2021).

[95] Rosensweig, R. E. *Ferrohydrodynamics* (Dover Publications, Mineola, New York, USA, 2014).

[96] Serwane, F. *et al.* In vivo quantification of spatially varying mechanical properties in developing tissues. *Nat. Methods* **14**, 181 (2017).

[97] Hawkeye, M. M. & Brett, M. J. Glancing angle deposition: Fabrication, properties, and applications of micro- and nanostructured thin films. *J. Vac. Sci. Technol. A: Vac. Surf. Films* **25**, 1317 (2007).

[98] Hawkeye, M. M., Taschuk, M. T. & Brett, M. J. *Glancing Angle Deposition of Thin Films: Engineering the Nanoscale*. Wiley Series in Materials for Electronic and Optoelectronic Applications (John Wiley & Sons, Chichester, UK, 2014).

[99] Schamel, D. *et al.* Chiral colloidal molecules and observation of the propeller effect. *J. Am. Chem. Soc.* **135**, 45 (2013).

[100] Deák, A., Bancsi, B., Tóth, A. L., Kovács, A. L. & Hórvölgyi, Z. Complex Langmuir–Blodgett films from silica nanoparticles: An optical spectroscopy study. *Colloids Surf. A Physicochem. Eng. Asp.* **278**, 10 (2006).

[101] Szekeres, M. *et al.* Ordering and optical properties of monolayers and multilayers of silica spheres deposited by the Langmuir-Blodgett method. *J. Mater. Chem.* **12**, 3268 (2002).

[102] Thangamuthu, M., Santschi, C. & Martin, O. J. Reliable Langmuir Blodgett colloidal masks for large area nanostructure realization. *Thin Solid Films* **709**, 138195 (2020).

[103] Peter, F. *et al.* Degradable and biocompatible magnesium zinc structures for nanomedicine: Magnetically actuated liposome microcarriers with tunable release. *Adv. Funct. Mater.* **34**, 2314265 (2024).

[104] Khullar, P. *et al.* Block copolymer micelles as nanoreactors for self-assembled morphologies of gold nanoparticles. *J. Phys. Chem. B* **117**, 3028 (2013).

[105] Mark, A. G., Gibbs, J. G., Lee, T.-C. & Fischer, P. Hybrid nanocolloids with programmed three-dimensional shape and material composition. *Nat. Mater.* **12**, 802 (2013).

[106] Kruss, S., Srot, V., Aken, P. A. V. & Spatz, J. P. Au-Ag hybrid nanoparticle patterns of tunable size and density on glass and polymeric supports. *Langmuir* **28**, 1562 (2012).

[107] Li, H. *et al.* Precise electrokinetic position and three-dimensional orientation control of a nanowire bioprobe in solution. *Nat. Nanotechnol.* **18**, 1213 (2023).

[108] Alarcón-Correa, M., Lee, T. C. & Fischer, P. Dynamic inclusion complexes of metal nanoparticles inside nanocups. *Angew. Chem. Int. Ed.* **127**, 6834 (2015).

[109] Jensen, M. O. & Brett, M. J. Periodically structured glancing angle deposition thin films. *IEEE Trans. Nanotechnol.* **4**, 269 (2005).

[110] Trackpy Contributors. Walkthrough — trackpy 0.6.3+2.ga65a2a6 documentation. `https://soft-matter.github.io/trackpy/dev/tutorial/walkthrough.html` (2019). Accessed 23.04.2025.

[111] Baubigny, J. D. D. *et al.* AFM study of hydrodynamics in boundary layers around micro- and nanofibers. *Phys. Rev. Fluids* **1**, 044104 (2016).

[112] Rothschild, L. J. *et al.* Building synthetic cells - from the technology infrastructure to cellular entities. *ACS Synth. Biol.* **13**, 974 (2024).

[113] Bartelt, S. M., Steinkühler, J., Dimova, R. & Wegner, S. V. Light-guided motility of a minimal synthetic cell. *Nano Lett.* **18**, 7268 (2018).

[114] Zhu, K. K. *et al.* Magnetic modulation of biochemical synthesis in synthetic cells. *J. Am. Chem. Soc.* **146**, 13176 (2024).

[115] Monck, C., Elani, Y. & Ceroni, F. Genetically programmed synthetic cells for thermoresponsive protein synthesis and cargo release. *Nat. Chem. Biol.* **20**, 1380 (2024).

[116] Roy, F. V. & Berx, G. The cell-cell adhesion molecule E-cadherin. *Cell. Mol. Life Sci.* **65**, 3756 (2008).

[117] Wu, Y., Kanchanawong, P. & Zaidel-Bar, R. Actin-delimited adhesion-independent clustering of E-cadherin forms the nanoscale building blocks of adherens junctions. *Dev. Cell* **32**, 139 (2015).

[118] Collins, C., Denisin, A. K., Pruitt, B. L. & Nelson, W. J. Changes in E-cadherin rigidity sensing regulate cell adhesion. *Proc. Natl. Acad. Sci. U.S.A* **114**, E5835 (2017).

[119] Koirala, R. *et al.* Inside-out regulation of E-cadherin conformation and adhesion. *Proc. Natl. Acad. Sci. U.S.A* **118**, e2104090118 (2021).

[120] George, H. F. & Qureshi, F. Newton's law of viscosity, Newtonian and non-Newtonian fluids. In Wang, Q. J. & Chung, Y.-W. (eds.) *Encyclopedia of Tribology*, 2416 (Springer US, Boston, Massachusetts, USA, 2013).

[121] Afkhami, S. *et al.* Deformation of a hydrophobic ferrofluid droplet suspended in a viscous medium under uniform magnetic fields. *J. Fluid Mech.* **663**, 358 (2010).

[122] Tsebers, A. O. Virial method of investigation of statics and dynamics of drops of magnetizable liquids. *Magnetohydrodynamics* **21**, 19 (1985).

[123] Romanenko, M. G., Shagrova, G. V. & Drozdova, V. I. Computer simulation system for oscillations of magnetizable microdroplets taking into account the dependence of the interfacial tension on the strength of an external magnetic field. *J. Math. Sci.* **260**, 210 (2022).

[124] Khokhryakova, C., Shmyrov, A. & Mizeva, I. Does magnetic field influence the surface tension of ferrofluid? *Langmuir* **40**, 4285 (2024).

[125] Tyler, A. J. *Ferrofluid Droplets in Uniform Magnetic Fields: Evidence for Field-dependent Interfacial Tension*. PhD thesis, The University of Western Australia, Perth, Australia (2010).

[126] Flament, C. *et al.* Measurements of ferrofluid surface tension in confined geometry. *Phys. Rev. E* **53**, 4801 (1996).

[127] Ivanov, A. S. Anomalous interfacial tension temperature dependence of condensed phase drops in magnetic fluids. *Phys. Fluids* **30**, 052001 (2018).

[128] Vorobiev, A., Gordeev, G., Konovalov, O. & Orlova, D. Surface structure of sterically stabilized ferrofluids in a normal magnetic field: Grazing-incidence x-ray study. *Phys. Rev. E* **79**, 031403 (2009).

[129] Guba, S., Horváth, B. & Szalai, I. Examination of contact angles of magnetic fluid droplets on different surfaces in uniform magnetic field. *J. Magn. Magn. Mater.* **498**, 166181 (2020).

[130] Ambwani, D. S. & Fort, T. Pendant drop technique for measuring liquid boundary tensions. In Good, R. J. & Stromberg, R. R. (eds.) *Surface and Colloid Science: Volume 11: Experimental Methods*, 93–119 (Springer US, Boston, Massachusetts, USA, 1979).

[131] Alvarez, N. J., Walker, L. M. & Anna, S. L. A non-gradient based algorithm for the determination of surface tension from a pendant drop: Application to low Bond number drop shapes. *J. Colloid Interface Sci.* **333**, 557 (2009).

[132] Berry, J. D., Neeson, M. J., Dagastine, R. R., Chan, D. Y. & Tabor, R. F. Measurement of surface and interfacial tension using pendant drop tensiometry. *J. Colloid Interface Sci.* **454**, 226 (2015).

[133] Seneviratne, K. N., Hughes, T. J., Johns, M. L., Marsh, K. N. & May, E. F. Surface tension and critical point measurements of methane + propane mixtures. *J. Chem. Thermodyn.* **111**, 173 (2017).

[134] Yu, L. M. *et al.* Constrained sessile drop as a new configuration to measure low surface tension in lung surfactant systems. *J. Appl. Physiol.* **97**, 704 (2004).

[135] GmbH, K. Constrained sessile drop (2022). URL `https://www.kruss-scientific.com/en/know-how/glossary/constrained-sessile-drop`. Accessed 26.05.2025.

[136] Style, R. W., Wettlaufer, J. S. & Dufresne, E. R. Surface tension and the mechanics of liquid inclusions in compliant solids. *Soft Matter* **11**, 672 (2015).

[137] Rowghanian, P., Meinhart, C. D. & Campàs, O. Dynamics of ferrofluid drop deformations under spatially uniform magnetic fields. *J. Fluid Mech.* **802**, 245 (2016).

[138] Charrier, E. E. *et al.* A novel method to make viscoelastic polyacrylamide gels for cell culture and traction force microscopy. *APL Bioeng.* **4** (2020).

[139] Liu, A. F. *Mechanics and Mechanisms of Fracture: An Introduction* (ASM International, Materials Park, Ohio, USA, 2005).

[140] Carroll, B., Thanh, M. T. H. & Patteson, A. E. Dynamic remodeling of fiber networks with stiff inclusions under compressive loading. *Acta Biomater.* **163**, 106 (2023).

[141] Shivers, J. L. *et al.* Compression stiffening of fibrous networks with stiff inclusions. *Proc. Natl. Acad. Sci. U.S.A.* **117**, 21037 (2020).

[142] Wen, D., Lin, Z., Tjiptowidjojo, Y. & tak Wan, K. Indenting a thick gel with a solid spherical inclusion. *Eur. J. Mech. A/Solid.* **106**, 105343 (2024).

[143] Heyden, S., Style, R. W. & Dufresne, E. R. Strain stiffening elastomers with swelling inclusions. *Soft Matter* **19**, 4385 (2023).

[144] Zidek, J., Polacek, P. & Jancar, J. Deformation of gels with spherical auxetic inclusions. *Gels* **8**, 698 (2022).

[145] Wahlsten, A. *et al.* Multiscale mechanical analysis of the elastic modulus of skin. *Acta Biomater.* **170**, 155 (2023).

[146] Denisin, A. K. & Pruitt, B. L. Tuning the range of polyacrylamide gel stiffness for mechanobiology applications. *ACS Appl. Mater. Interfaces* **8**, 21893 (2016).

[147] Megone, W., Roohpour, N. & Gautrot, J. E. Impact of surface adhesion and sample heterogeneity on the multiscale mechanical characterisation of soft biomaterials. *Sci. Rep.* **8** (2018).

[148] Norman, M. D., Ferreira, S. A., Jowett, G. M., Bozec, L. & Gentleman, E. Measuring the elastic modulus of soft culture surfaces and three-dimensional hydrogels using atomic force microscopy. *Nat. Protoc.* **16**, 2418 (2021).

[149] Sullivan, B. *et al.* Mechanical disruption of E-cadherin complexes with epidermal growth factor receptor actuates growth factor–dependent signaling. *Proc. Natl. Acad. Sci. U.S.A.* **119**, e2100679119 (2022).

[150] Yang, Y. A. *et al.* Local contractions regulate E-cadherin rigidity sensing. *Sci. Adv.* **8**, 387 (2022).

[151] Trepat, X. *et al.* Physical forces during collective cell migration. *Nat. Phys.* **5**, 426 (2009).

[152] Tambe, D. T. *et al.* Collective cell guidance by cooperative intercellular forces. *Nat. Mater.* **10**, 469 (2011).

[153] Vishwakarma, M. *et al.* Mechanical interactions among followers determine the emergence of leaders in migrating epithelial cell collectives. *Nat. Commun.* **9**, 1 (2018).

[154] Chowdhury, F., Huang, B. & Wang, . N. Cytoskeletal prestress: The cellular hallmark in mechanobiology and mechanomedicine. *Cytoskeleton* **78**, 249 (2021).

[155] Cho, Y., Son, M., Jeong, H., & Shin, J. H. Electric field-induced migration and intercellular stress alignment in a collective epithelial monolayer. *Mol. Biol. Cell* **29**, 2292 (2018).

[156] Chowdhury, F. *et al.* Material properties of the cell dictate stress-induced spreading and differentiation in embryonic stem cells. *Nat. Mater.* **9**, 82 (2009).

[157] Wang, H. *et al.* Static and dynamic mechanics of cell monolayers: A multi-scale structural model. *Acta Mech. Sin.* **38**, 222006 (2022).

[158] Harris, A. R. *et al.* Characterizing the mechanics of cultured cell monolayers. *Proc. Natl. Acad. Sci. U.S.A.* **109**, 16449 (2012).

[159] Falleroni, F., Torre, V. & Cojoc, D. Cell mechanotransduction with piconewton forces applied by optical tweezers. *Front. Cell. Neurosci.* **12**, 130 (2018).

[160] Guilford, W. H., Lantz, R. C. & Gore, R. W. Locomotive forces produced by single leukocytes in vivo and in vitro. *Am. J. Physiol.* **268**, C1308 (1995).

[161] Li, X. *et al.* Tensile force-induced cytoskeletal remodeling: Mechanics before chemistry. *PLoS Comput. Biol.* **16**, e1007693 (2020).

[162] Hiepen, C. *et al.* Endothelial tip-cell position, filopodia formation and biomechanics require BMPR2 expression and signaling. *Commun. Biol.* **8**, 1 (2025).

[163] Potente, M. & Carmeliet, P. The link between angiogenesis and endothelial metabolism. *Annu. Rev. Physiol.* **79**, 43 (2017).

[164] Bayless, K. J., Kwak, H.-I. & Su, S.-C. Investigating endothelial invasion and sprouting behavior in three-dimensional collagen matrices. *Nat. Protoc.* **4**, 1888 (2009).

[165] Sano, T. *et al.* Image-based crosstalk analysis of cell–cell interactions during sprouting angiogenesis using blood-vessel-on-a-chip. *Stem Cell Res. Ther.* **13**, 532 (2022).

[166] Flournoy, J., Ashkanani, S. & Chen, Y. Mechanical regulation of signal transduction in angiogenesis. *Front. Cell Dev. Biol.* **10**, 933474 (2022).

[167] Peak, C. W., Cross, L., Singh, A. & Gaharwar, A. K. Microscale technologies for cell engineering. In Singh, A. & Gaharwar, A. K. (eds.) *Microscale technologies for engineering complex tissue structures*, 3–25 (Springer International Publishing, Cham, Switzerland, 2016).

[168] Novosel, E. C., Kleinhans, C. & Kluger, P. J. Vascularization is the key challenge in tissue engineering. *Adv. Drug Deliv. Rev.* **63**, 300 (2011).

[169] Carmeliet, P. & Jain, R. K. Molecular mechanisms and clinical applications of angiogenesis. *Nature* **473**, 298 (2011).

[170] Cheng, Y. *et al.* Endothelial AGGF1 promotes retinal angiogenesis by coordinating TNFSF12/FN14 signalling. *Nat. Commun.* **16**, 1 (2025).

[171] Choi, Y. & Jung, K. Normalization of the tumor microenvironment by harnessing vascular and immune modulation to achieve enhanced cancer therapy. *Exp. Mol. Med.* **55**, 2308 (2023).

[172] Wang, W. *et al.* Collagen density regulates tip-stalk cell rearrangement during angiogenesis via cellular bioenergetics. *APL Bioeng.* **8**, 26120 (2024).

[173] Pfisterer, L. & Korff, T. Spheroid-based in vitro angiogenesis model. In Martin, S. G. & Hewett, P. W. (eds.) *Angiogenesis Protocols*, 167–177 (Springer New York, New York, New York, USA, 2016).

[174] Bongaerts, M. *et al.* Parallelized manipulation of adherent living cells by magnetic nanoparticles-mediated forces. *Int. J. Mol. Sci.* **21**, 6560 (2020).

[175] Kunze, A. *et al.* Engineering cortical neuron polarity with nanomagnets on a chip. *ACS Nano* **9**, 3664 (2015).

[176] Cho, S. *et al.* Tension exerted on cells by magnetic nanoparticles regulates differentiation of human mesenchymal stem cells. *Biomater. Adv.* **139**, 213028 (2022).

[177] Tseng, P., Judy, J. W. & Carlo, D. D. Magnetic nanoparticle-mediated massively parallel mechanical modulation of single-cell behavior. *Nat. Methods* **9**, 1113 (2012).

[178] Menzel, R. *et al.* Parylene C coating efficacy studies: Enhancing biocompatibility of 3D printed polyurethane parts for biopharmaceutical and CGT applications. *ACS Appl. Bio Mater.* **7**, 5369 (2024).

[179] Peter, F. R. *Biocompatible active microcarriers*. PhD thesis, Heidelberg University, Heidelberg, Germany (2024).

[180] Bourne, R. R. A. *et al.* Trends in prevalence of blindness and distance and near vision impairment over 30 years: An analysis for the global burden of disease study. *Lancet Glob. Heal.* **9**, e130 (2021).

[181] Stern, J., Yasmin, S., Qureshi, M. B. & Bourne, R. 2030 in sight: the future of global eye health. *Eye* **38**, 1979 (2023).

[182] Fricke, T. R. *et al.* Global prevalence of visual impairment associated with myopic macular degeneration and temporal trends from 2000 through 2050: systematic review, meta-analysis and modelling. *Br. J. Ophthalmol.* **102**, 855 (2018).

[183] Sharp, P. F. & Philips, R. Physiological optics. In Hendee, W. R. & Wells, P. N. T. (eds.) *The Perception of Visual Information*, 1–29 (Springer New York, New York, New York, USA, 1993).

[184] Artal, P. The eye as an optical instrument. In Al-Amri, M. D., El-Gomati, M. & Zubairy, M. S. (eds.) *Optics in Our Time*, 285–297 (Springer International Publishing, Cham, Switzerland, 2016).

[185] Yao, X. & Wang, B. Intrinsic optical signal imaging of retinal physiology: a review. *J. Biomed. Opt.* **20**, 090901 (2015).

[186] Okano, K. *et al.* Retinal cone and rod photoreceptor cells exhibit differential susceptibility to light-induced damage. *J. Neurochem.* **121**, 146 (2012).

[187] Sanes, J. R. & Masland, R. H. The types of retinal ganglion cells: Current status and implications for neuronal classification. *Annu. Rev. Neuosci.* **38**, 221 (2015).

[188] Schulz, A. & Szurman, P. Vitreous substitutes as drug release systems. *Transl. Vis. Sci. Technol.* **11**, 14 (2022).

[189] Confalonieri, F. *et al.* Vitreous substitutes from bench to the operating room in a translational approach: Review and future endeavors in vitreoretinal surgery. *Int. J. Mol. Sci.* **24**, 3342 (2023).

[190] Zhang, K. Y. & Johnson, T. V. The internal limiting membrane: roles in retinal development and implications for emerging ocular therapies. *Exp. Eye Res.* **206**, 108545 (2021).

[191] Candiello, J. *et al.* Biomechanical properties of native basement membranes. *FEBS J.* **274**, 2897 (2007).

[192] Candiello, J., Cole, G. J. & Halfter, W. Age-dependent changes in the structure, composition and biophysical properties of a human basement membrane. *Matrix Biol.* **29**, 402 (2010).

[193] Lai, C.-C. Internal limiting membrane: Making the decision to peel. *Retina Today* 35 (2015).

[194] Qi, Y. *et al.* Effect of internal limiting membrane peeling on normal retinal function evaluated by microperimetry-3. *BMC Ophthalmol.* **20**, 1 (2020).

[195] Evans, D. Vitrectomy: Understanding the eye surgery for retinal disorders. *Ophthalmol. Case Rep.* **9**, 255 (2025).

[196] Shao, E. H., Yates, W. B., Ho, I.-V., Chang, A. A. & Simunovic, M. P. Endophthalmitis: Changes in presentation, management and the role of early vitrectomy. *Ophthalmol. Ther.* **10**, 877 (2021).

[197] Yu, H. *et al.* Optimal timing of vitrectomy for severe mechanical ocular trauma: A retrospective observational study. *Sci. Rep.* **9**, 18016 (2019).

[198] Lumi, X. *et al.* Ageing of the vitreous: From acute onset floaters and flashes to retinal detachment. *Ageing Res. Rev.* **21**, 71 (2015).

[199] Khoshnevis, M., Rosen, S. & Sebag, J. Asteroid hyalosis—a comprehensive review. *Surv. Ophthalmol.* **64**, 452 (2019).

[200] Su, X. *et al.* Recent progress in using biomaterials as vitreous substitutes. *Biomacromolecules* **16**, 3093 (2015).

[201] Alovisi, C., Panico, C., Sanctis, U. D. & Eandi, C. M. Vitreous substitutes: Old and new materials in vitreoretinal surgery. *J. Ophthalmol.* **2017**, 3172138 (2017).

[202] Mondelo-García, C. *et al.* Current situation and challenges in vitreous substitutes. *Macromol. Biosci.* **21**, 2100066 (2021).

[203] Wang, T., Ran, R., Ma, Y. & Zhang, M. Polymeric hydrogel as a vitreous substitute: current research, challenges, and future directions. *Biomed. Mater.* **16**, 042012 (2021).

[204] Raia, N. R. *et al.* Enzymatically crosslinked silk-hyaluronic acid hydrogels. *Biomaterials* **131**, 58 (2017).

[205] GBD 2019 Blindness and Vision Impairment Collaborators and Vision Loss Expert Group of the Global Burden of Disease Study. Causes of blindness and vision impairment in 2020 and trends over 30 years, and prevalence of avoidable blindness in relation to VISION 2020: the Right to Sight: an analysis for the Global Burden of Disease Study. *Lancet Glob. Health* **9**, e144 (2021).

[206] Wang, S. *et al.* The retinal pigment epithelium: Functions and roles in ocular diseases. *Fundam. Res.* **4**, 1710 (2024).

[207] Schnichels, S. *et al.* Retina in a dish: Cell cultures, retinal explants and animal models for common diseases of the retina. *Prog. Retin. Eye Res.* **81**, 100880 (2021).

[208] Michaelides, M. *et al.* Gene therapy in children with AIPL1-associated severe retinal dystrophy: an open-label, first-in-human interventional study. *Lancet* **405**, 648 (2025).

[209] Dalkara, D., Goureau, O., Marazova, K. & Sahel, J. A. Let there be light: Gene and cell therapy for blindness. *Hum. Gene Ther.* **27**, 134 (2016).

[210] Ramsay, E. *et al.* Selective drug delivery to the retinal cells: Biological barriers and avenues. *J. Control. Release* **361**, 1 (2023).

[211] Irigoyen, C. *et al.* Subretinal injection techniques for retinal disease: A review. *J. Clin. Med.* **11**, 4717 (2022).

[212] Ducloyer, J. B. *et al.* Intravitreal air tamponade after AAV2 subretinal injection modifies retinal EGFP distribution. *Mol. Ther. Methods Clin. Dev* . **28**, 387 (2023).

[213] Ghasemi Falavarjani, K. & Nguyen, Q. D. Adverse events and complications associated with intravitreal injection of anti-VEGF agents: a review of literature. *Eye* **27**, 787 (2013).

[214] Wu, Z. *et al.* A swarm of slippery micropropellers penetrates the vitreous body of the eye. *Sci. Adv* **4**, eaat4388 (2018).

[215] Peynshaert, K., Devoldere, J., Smedt, S. D. & Remaut, K. Every nano-step counts: a critical reflection on do's and don'ts in researching nanomedicines for retinal gene therapy. *Expert Opin. Drug Deliv.* **20**, 259 (2023).

[216] De-Giorgio, F., Grassi, S., d'Aloja, E. & Pascali, V. L. Post-mortem ocular changes and time since death: Scoping review and future perspective. *Leg. Med.* **50**, 101862 (2021).

[217] Johnson, N. F. & Grierson, I. Post-mortem changes in the rabbit retina. *Acta Ophthalmol.* **54**, 529 (1976).

[218] Bohley, M., Dillinger, A. E., Tamm, E. R. & Goepferich, A. Targeted drug delivery to the retinal pigment epithelium: Untapped therapeutic potential for retinal diseases. *Drug Discov. Today* **27**, 2497 (2022).

[219] Klettner, A. K. & Dithmar, S. *Retinal Pigment Epithelium in Health and Disease* (Springer, Cham, Switzerland, 2020).

[220] Pitkänen, L., Ruponen, M., Nieminen, J. & Urtti, A. Vitreous is a barrier in nonviral gene transfer by cationic lipids and polymers. *Pharm. Res.* **20**, 576 (2003).

[221] Martens, T. F. *et al.* Measuring the intravitreal mobility of nanomedicines with single-particle tracking microscopy. *Nanomedicine* **8**, 1955 (2013).

[222] Kim, H., Robinson, S. B. & Csaky, K. G. Investigating the movement of intravitreal human serum albumin nanoparticles in the vitreous and retina. *Pharm. Res.* **26**, 329 (2009).

[223] Apaolaza, P. S. *et al.* Hyaluronic acid coating of gold nanoparticles for intraocular drug delivery: Evaluation of the surface properties and effect on their distribution. *Exp. Eye Res.* **198**, 108151 (2020).

[224] Jackson, T. L., Antcliff, R. J., Hillenkamp, J. & Marshall, J. Human retinal molecular weight exclusion limit and estimate of species variation. *Investig. Ophthalmol. Vis. Sci.* **44**, 2141 (2003).

[225] Tao, Y. *et al.* Diffusion of macromolecule through retina after experimental branch retinal vein occlusion and estimate of intraretinal barrier. *Curr. Drug Metab.* **8**, 151 (2007).

[226] Kim, H. M. *et al.* Permeability of the retina and RPE-choroid-sclera to three ophthalmic drugs and the associated factors. *Pharmaceutics* **13** (2021).

[227] Peynshaert, K. *et al.* Toward smart design of retinal drug carriers: A novel bovine retinal explant model to study the barrier role of the vitreoretinal interface. *Drug Deliv.* **24**, 1384 (2017).

[228] Devoldere, J. *et al.* The obstacle course to the inner retina: Hyaluronic acid-coated lipoplexes cross the vitreous but fail to overcome the inner limiting membrane. *Eur. J. Pharm. Biopharm.* **141**, 161 (2019).

[229] Tavakoli, S. *et al.* Ocular barriers to retinal delivery of intravitreal liposomes: Impact of vitreoretinal interface. *J. Control. Release* **328**, 952 (2020).

[230] Mordenti, J. *et al.* Comparisons of the intraocular tissue distribution, pharmacokinetics, and safety of 125I-labeled full-length and Fab antibodies in rhesus monkeys following intravitreal administration. *Toxicol. Pathol.* **27**, 536 (1999).

[231] Dalkara, D. *et al.* Inner limiting membrane barriers to AAV-mediated retinal transduction from the vitreous. *Mol. Ther.* **17**, 2096 (2009).

[232] Yin, L. *et al.* Intravitreal injection of AAV2 transduces macaque inner retina. *Investig. Ophthalmol. Vis. Sci.* **52**, 2775 (2011).

[233] Cehajic-Kapetanovic, J., Milosavljevic, N., Bedford, R. A., Lucas, R. J. & Bishop, P. N. Efficacy and safety of glycosidic enzymes for improved gene delivery to the retina following intravitreal injection in mice. *Mol. Ther. Methods Clin. Dev* . **9**, 192 (2018).

[234] Takahashi, K. *et al.* Improved intravitreal AAV-mediated inner retinal gene transduction after surgical internal limiting membrane peeling in cynomolgus monkeys. *Mol. Ther.* **25**, 296 (2017).

[235] Teo, K. Y. C. *et al.* Surgical removal of internal limiting membrane and layering of AAV vector on the retina under air enhances gene transfection in a nonhuman primate. *Investig. Ophthalmol. Vis. Sci.* **59**, 3574 (2018).

[236] Gonçalves, M. A. Adeno-associated virus: from defective virus to effective vector. *Virol. J.* **2**, 43 (2005).

[237] Liu, G. *et al.* Nanoparticles of compacted DNA transfect postmitotic cells. *J. Biol. Chem.* **278**, 32578 (2003).

[238] Ahn, S. *et al.* Magnetically guided adeno-associated virus delivery for the spatially targeted transduction of retina in eyes. *Adv. Healthc. Mater.* **13**, e2401577 (2024).

[239] Eljarrat-Binstock, E., Orucov, F., Aldouby, Y., Frucht-Pery, J. & Domb, A. J. Charged nanoparticles delivery to the eye using hydrogel iontophoresis. *J. Control. Release* **126**, 156 (2008).

[240] Peynshaert, K. *et al.* ICG-mediated photodisruption of the inner limiting membrane enhances retinal drug delivery. *J. Control. Release* **349**, 315 (2022).

[241] Clerck, K. D. *et al.* Photodisruption of the inner limiting membrane: Exploring ICG loaded nanoparticles as photosensitizers. *Pharmaceutics* **14**, 1716 (2022).

[242] Zhang, K. Y. *et al.* Role of the internal limiting membrane in structural engraftment and topographic spacing of transplanted human stem cell-derived retinal ganglion cells. *Stem Cell Rep.* **16**, 149 (2021).

[243] Cehajic-Kapetanovic, J., le Goff, M. M., Allen, A., Lucas, R. J. & Bishop, P. N. Glycosidic enzymes enhance retinal transduction following intravitreal delivery of AAV2. *Mol. Vis.* **17**, 1771 (2011).

[244] European Medicines Agency. Jetrea (2025). URL `https://www.ema.europa.eu/en/medicines/human/EPAR/jetrea`.

[245] Syed, Y. Y. & Dhillon, S. Ocriplasmin: a review of its use in patients with symptomatic vitreomacular adhesion. *Drugs* **73**, 1617 (2013).

[246] Grinton, M. & Steel, D. H. Cochrane corner: Ocriplasmin-why isn't it being used more? *Eye* **33**, 1195 (2019).

[247] Son, K. *et al.* Superior magnetic performance in FePt $L1_0$ nanomaterials. *Small* **15**, 1902353 (2019).

[248] Mazur, M. *et al.* TiO_2/SiO_2 multilayer as an antireflective and protective coating deposited by microwave assisted magnetron sputtering. *Opto-electron. Rev.* **21**, 233 (2013).

[249] Walker, D. T. *Magnetically actuated micro- and nanopropellers*. PhD thesis, University of Stuttgart, Stuttgart, Germany (2015).

[250] Kuehn, S. *et al.* The novel induction of retinal ganglion cell apoptosis in porcine organ culture by NMDA - an opportunity for the replacement of animals in experiments. *ATLA Altern. Lab. Anim.* **44**, 557 (2016).

[251] Kuehn, S. *et al.* Degenerative effects of cobalt-chloride treatment on neurons and microglia in a porcine retina organ culture model. *Exp. Eye Res.* **155**, 107 (2017).

[252] Schmitt, E. *Characterization of diffusion through the porcine retina*. Bachelor's thesis, Heidelberg University, Heidelberg, Germany (2023).

[253] Massachusetts Institute of Technology, Department of Chemistry. NMR frequency table. `https://chemistry.mit.edu/wp-content/uploads/2018/08/NMR-Frequency-Table.pdf` (2018). Accessed 17.05.2025.

[254] Huhtala, P., Chow, L. T. & Tryggvason, K. Structure of the human type IV collagenase gene. *J. Biol. Chem.* **265**, 11077 (1990).

[255] Marcelino, T. *et al.* Surfaces coated with polymer brushes work as carriers for histidine ammonia lyase. *Macromol. Biosci.* **23**, 2200528 (2023).

Acknowledgements

I would love to thank the many wonderful people without whom this PhD might never have been completed — or if it had, it would have been a far lonelier and more difficult path. There were moments when I came close to giving up, not just on my work, but on my life in Germany altogether, during one of the most difficult personal chapters I have faced. And yet, also thanks to you and the little moments we have shared, I was able to find a sense of joy and fulfillment deeper than I ever imagined. You created a warm and safe space around me, and this work is as much a result of that environment as it is of the research itself — full of experimentation, setbacks, and discovery. Though I have been in Germany just a little over 4.5 years, it feels as if an entire lifetime unfolded here. Thank you for walking — and sometimes running — this journey with me, one that has been both hard and beautiful, as only life can be.

First, I would like to express my sincere and deep gratitude to **Prof. Dr. Peer Fischer** for his patient and thoughtful mentoring. No matter how complex the scientific challenges or difficult the situations, you always found a way forward and offered guidance with kindness and wisdom. I am especially thankful for your caring and support beyond the realm of science, far more than anyone could ever expect.

I would also like to sincerely thank **Prof. Dr. Christine Selhuber-Unkel**, **JunProf. Dr. Philipp Uhl**, and **Dr. Venera Weinhardt** for kindly agreeing to evaluate this thesis.

I am thankful to **Dr. Irene Wacker**, **Prof. Dr. Rasmus Schröder**, **Dr. med. M. Hammer**, **Dr. Jacqueline De Lora**, **Dr. Voichita Mihali**, **Prof. Dr. Cornelia Palivan**, and **Senne Seneca** for many invaluable scientific discussions. I am also grateful to **the research group of Dr. Sven Schnichels** for teaching me the eye dissection technique.

I would like to express my deepest gratitude to **Mariana Alarcón-Correa** for her unwavering encouragement and support during moments when the scientific work felt overwhelming. I am especially thankful for the openness and trust that allowed me to share everything with you — whether scientific, joyful, funny, serious, or sad. Thank you for always listening, for helping in countless ways, and for your careful corrections of my thesis.

I wish to thank all my **friends and colleagues from work**. In particular, I am deeply grateful to **Florian Peter** for being there during some of the darkest moments in my life — always ready to join for a run, a yoga session, or a dinner conversation. I sincerely thank **Nikhilesh Murty** for always being open to talk about life and for showing genuine understanding and interest in my situation, despite the challenges he himself faced. I thank **Oscar Demeulenaere** for many enjoyable evenings speaking in French and for offering his support at work many times, often without being asked. I am also grateful to **Nicolás Moreno Gómez** for our deep conversations about both work and life. To **Corinna Scalet**, I am grateful for teaching me how to stay positive despite health struggles—your smile has helped me more than you can imagine. My big thanks go to **Dimitris Missirlis** for his constant readiness to help with work-related matters, for his feedback on sections of this thesis, and for bringing a sense of humor and positivity to the work environment. To **Ida Bochert**, thank you for your thoughtfulness and for always being in such a good mood. I would also like to thank **Lovish Gulati** for his optimism and for the shared runs that brought balance to busy days. To all my other work friends, thank you for your smiles, encouragement, and the many great lunch discussions — especially **Athanasios Athanassiadis**, **Kai Melde**, and **Jan-Philipp Günther**. My sincere thanks also go to **Hyunah Kwon** for generously sharing her knowledge in the lab, as well as for her exceptional kindness and understanding during moments when I shared personal challenges. I am also grateful to **Hannah-Noa Barad** for generously sharing her expertise in the lab and for the many engaging conversations we shared over lunch. I would like to thank **Björn Miksch** for the many enjoyable days spent together in the lab and for sharing his knowledge during our experiments. I wish to thank **Rahul Goyal** for his consistent helpfulness at work, and **Jutta Heß** for her reliable support whenever needed. I would like to sincerely thank **Eldin Schmitt**, **Inga Wittmann**, and **Felix Hecht** for their motivation, dedicated work and nice conversations. I thank **Inma Real** for her efforts to ease my workload. I am also grateful to **Cornelia Miksch** for her support and positive attitude in the workplace. I am grateful to **Sadaf Pashapour** for her kind help in difficult moments at work and for proofreading parts of this thesis, as well as to **Harish Kumar Senapati** for proofreading one of the sections.

My endless gratitude goes to **my parents**, whose love and support have made it possible for me to follow this path. Knowing that I can always turn to you, no matter what, gives me deep comfort. To **my brothers**, among the kindest people I know, thank you for your gentle words when I needed them most, the laughter we have shared, and the bond that always brings me home. To **my grandfather**, thank you for always being so proud of me, it means more than I can say.

I am very grateful to **Lukas Stadler** for being there for me during the intense final weeks before submission — cooking countless meals, helping with anything I needed, and taking care of the little things so I could focus fully on my work. Thank you for bringing laughter into even the most stressful days, for our walks and honest conversations, and for being such an amazing friend.

With all my heart, I would like to thank **Naomi Ellenbogen**. No matter what we do together, we always share such wonderful moments. Thank you for being a kind, thoughtful, and supportive person in my life — someone I can always rely on. Your positivity toward life and remarkable endurance inspire me immensely.

My deep appreciation also goes to **my dancing friends**, especially **Emre Ekinci**, **Mirjam Düben**, **Lotti Weidner**, and **Isabel Schuldlos**. Thank you for thinking of me and for your incredible support — from surprise cards and thoughtful treats to always being ready to brainstorm solutions to my challenges. Somehow, problems always felt smaller after talking with you. I would also like to express my gratitude to **Janik Fechtelpeter** for our captivating conversations. Thank you for creating a space where we could openly share life's updates and for always listening with such genuine care and attentiveness. Many thanks to the entire **Swing community** in Heidelberg for the cheerful conversations and the happiness that dancing with you has brought into my life.

A big thank you to **my entire French community** around Montpellier-Haus in Heidelberg for brightening my days through joyful conversations in French. I am especially grateful to **Julia Schöfthaler** for her honest reflections on life, her contagious love for the French language, and for being so patient and supportive as the submission deadline approached.

To **Simon Frey** and **Cata Bahamon**, I am truly grateful for the inspiration your healthy lifestyle provides me, as well as for all the fun times we always share together.

To **Mostafa Elyamany**, thank you for our coffee talks and for your empathy.

To all my other great friend circles in Heidelberg — **my gym community**, **my bouldering** and **running friends**, and anyone I might have unintentionally forgotten — thank you all for your support and the much-needed moments of distraction.

To **my Czech friends** — though we see each other only a few times a year, it feels like nothing ever changes between us; instead, our connection grows even stronger. I especially want to thank **Teri Brůžová** for sharing every joy and sorrow, for standing by me in my darkest moments, for our deep conversations through the night before our 40 km hikes, and for staying close despite the distance, time apart, and my sporadic texting. I am also deeply grateful to **Iva Turanová** and **Miriam Zelenková** for laughing with me about the tough moments in life.

To **Joni Ander Arregi**, thank you for teaching me the basics of experimental work that helped me so much during my PhD. Above all, thank you for being such a great friend during one of the hardest moments in my life. I'm so grateful for your kindness and for all the laughter we share whenever we meet.

To **Erika Fontana**, thank you for supporting me across the distance and for welcoming me into your home when I needed comfort the most.

Last but by no means least, I wish to thank **Justus Heinze** for bringing even more joy and laughter into my life over the past few weeks and months — just when I least expected it. Thank you for your boundless optimism and your wonderful sense of humor, your gentle empathy, as well as your deep understanding of my busy life.